WEAK LENSING MEASUREMENTS FOR

THE APEX-SZ CLUSTER SURVEY

Dissertation
zur
Erlangung des Doktorgrades (Dr. rer. nat)
der
Mathematisch-Naturwissenschaftlichen Fakultät
der
Rheinischen Friedrich-Wilhelms-Universität Bonn

vorgelegt von
Matthias Klein
aus
Lahnstein

Bonn, September 2013

Angefertigt mit Genehmigung der Mathematisch-Naturwissenschaftlichen Fakultät der
Rheinischen Friedrich-Wilhelms-Universität Bonn

1. Gutachter:	Prof. Dr. Frank Bertoldi
2. Gutachter:	Prof. Dr. Peter Schneider
Tag der Promotion:	18. Dezember 2013
Erscheinungsjahr:	2014

ABSTRACT

The formation of structures in the universe, such as galaxy clusters, depends sensitively on cosmological parameters. Measuring the abundance of clusters as a function of mass and redshift therefore yields a way to constrain those parameters at high accuracy. In this context a major task is to reliably constrain the scaling relation between the observables used to estimate the cluster mass and the true mass.

Gravitational lensing is the deflection of light from distant galaxies by the mass of a cluster. Observations of this deflection allow to measure the total mass distribution of galaxy clusters without making assumptions about the dynamical state of the cluster.

This thesis describes the weak gravitational lensing observations of all redshift $z < 1$ clusters that were previously detected via the Sunyaev-Zel'dovich (SZ) effect with the APEX-SZ instrument on the APEX telescope. The combination of archive data and follow-up observations with the 2.2m telescope at La Silla, Chile, provided sensitive imaging of 39 galaxy clusters in three optical filters.

The redshift distribution of galaxies in color and magnitude space was investigated using a deep photometric reference catalog and allows us to derive individual distance estimates for each galaxy in the observed field. The individual distance estimates are used to select a signal to noise optimized galaxy catalog suitable for weak lensing measurements. This new method reduces the scatter and the systematic effects that arise from cosmic variance in the cluster and the reference fields. The individual distance estimates allow to map the distribution of cluster galaxies, providing important insights to the cluster dynamics and matter distribution. A modified version of the method was used to derive accurate estimates of cluster redshifts. The comparison of these redshift estimates with spectroscopic redshifts of eleven clusters showed a scatter that is four times smaller than that found for commonly used methods.

The derived lensing masses were used to study the scaling relation between mass and integrated Compton-y parameter, Y_{SZ}, using preliminary results of 29 clusters observed with APEX-SZ. Measurements of 17 clusters by the Planck satellite are used furthermore to analyze the mass-Y_{SZ} scaling relation for the Planck SZ measurements. The scaling relations found for APEX-SZ and Planck measurements are in agreement with each other and with prior published work. Excluding two potential outliers yields slope parameters that are in good agreement with self-similar evolution.

Five clusters were studied in greater detail, using weak lensing, SZ and X-ray maps. The developed methods to map cluster member galaxies were used to verify the mass distribution found in the lensing convergence maps. The newly developed method to derive cluster redshifts was applied to the observed substructures to verify their physical proximity. Two clusters are recognized as undergoing a major merger event, showing either shock fronts in the intracluster medium (ICM), or a large spatial separation between the ICM and the position of the main dark matter concentrations. One of these clusters may show the largest offset between dark matter and ICM known so far.

CONTENTS

Part I

INTRODUCTION

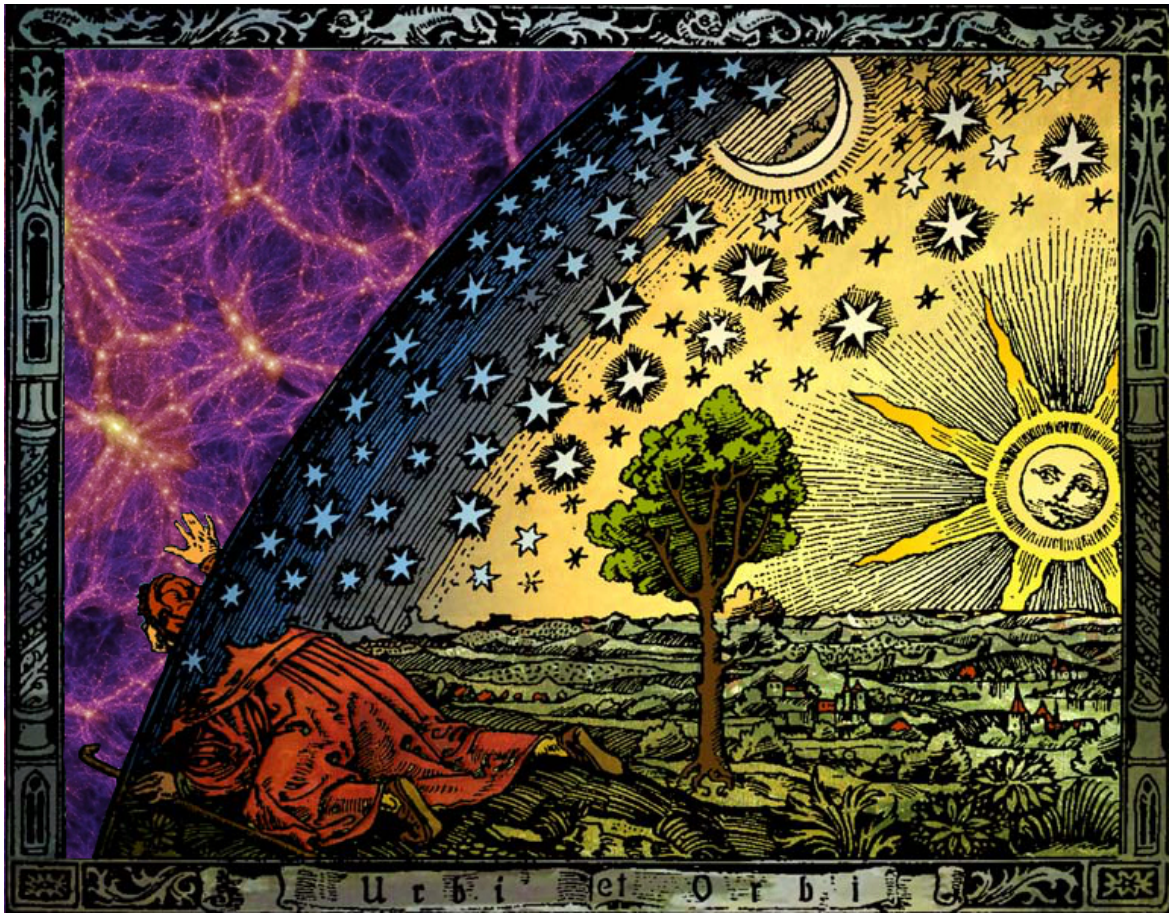

Figure 1: "The curious human", my personal interpretation of the woodcarving "Au pèlerin" from C. Flammarion 1888. Background image taken from Springel et al. (2005)

1

HISTORY OF COSMOLOGY

Cosmology aims to describe the structure, the evolution and the contents of the universe. In this role it was subject of religion and metaphysics since the beginning of human being. It is therefore astonishing that the basis of modern cosmology was founded within a period of only 20 years, from 1910 to 1930.

The beginning of modern cosmology can be dated to 1912 with the observation of the redshifts of 'Spiral nebulae' by Vesto Slipher, which he interpreted to be caused by Doppler shifts due to peculiar motion. In the same year, Henrietta S. Leavitt published her observations of the period-luminosity relationship of Cepheid variables, the key tool to derive distances of sources much further away than measurable with the parallax method.

About ten years later, with the availability of the 100 inch (2.5m) Hooker Telescope, Edwin Hubble was able to identify Cepheids in nearby galaxies, such as Andromeda or Triangulum. Based on the period-luminosity relationship, he showed that these 'nebulae' are too distant to be part of the Milky Way Galaxy. This resulted in a change of paradigm, giving up the assumption that the Universe is just populated by the Milky Way, towards an Universe populated by an 'uncountable' number of galaxies.

Only four years later, in 1929 Edwin Hubble combined his distance estimates with the redshifts measurements of Vesto Slipher and Milton L. Humason to derive the redshift-distance relation now known as Hubble's Law.

During the same time period where the observations started to change our view of the universe, also the theory and therefore the explanation of the observations evolved. In 1915 Albert Einstein published his work on General Relativity. Two years later he applied his theory to model the structure of the universe. He included an additional term in his equations called the "cosmological constant" or "Λ-term", to allow his equations to describe a static universe. Despite it was driven by his own belief in a static universe, it was also completely allowed by his equations.

In the following years Willem de Sitter, Alexander Friedmann, Georges Lemaître and others explored Einsteins field equations. They found various solutions, describing a dynamic and curved universes and showed that a static universe is only one solution to the equations. In 1927, two years before the result of Edwin Hubble, Georges Lemaître predicted the redshift-distance relation based on his solutions of an expanding universe.

After this phase of 20 years, the basic theory of modern cosmology was established. In the following time period, observations more and more favored this theory of a expanding universe against a static or "steady state" universe. The final breakthrough can be settled to the year 1965 where Robert Wilson and Arno Penzias observed the 2.7 K cosmic microwave background (CMB), which then was interpreted as the remaining radiation from the big bang by James Peebles, Robert Dicke and others.

After 1965 the theory of an expanding universe became broadly accepted as the most plausible theory of describing the universe. During the 1970s and 1980s, as the observational capabilities improve, some tensions arose to describe the observed structure of the universe with the evolution of the observed (or non observed) anisotropies in the CMB. This problem could be solved by the introduction of another type of matter which does not interact with electromagnetic fields but via gravity. The existence of such type of matter was also supported by other observations. First announced in 1975 and published in

1980, Vera Rubin and colleges stated that the rotation curves of galaxies suggest six times more invisible matter than visible matter in galaxies.

Another evidence for the existence of dark matter came from observations of galaxy clusters. Fritz Zwicky observed in 1933 the velocity dispersion of galaxies within the Coma cluster and used the virial theorem to derive a cluster mass which is 400 times larger then the visible matter. He also introduced the name "dark matter" for this type of matter. Despite the fact that his estimate of the ratio of dark matter to visible matter was significantly off (due to wrong assumptions of the mass of luminous matter and the ignorance of the existence of intergalactic hot gas) galaxy clusters play an important role of supporting the existence of dark matter.

The last two major changes in the standard model of cosmology were driven by space based telescopes. The precise all sky observations of Cosmic Background Explorer (COBE) and the Wilkinson Microwave Anisotropy Probe (WMAP), both measuring the CMB, could put tight constraints on cosmological parameters such as total matter density, baryon density and curvature of the universe. It supported the theory of cosmic inflation, a period of extremely fast exponential expansion of the universe in the early phase of the universe, which results in the observation of a flat universe.

The observations of supernovae type 1a yielded the first evidence that the universe is undergoing an accelerated expansion. This observation could be explained with a cosmological constant as introduced by Einstein in 1917.

This current standard cosmological model is called the Λ cold dark matter (ΛCDM) model.

Current and upcoming experiments such as Planck, eROSITA or Euclid are designed to probe the standard model in detail. Due to their statistical power the systematic errors become a dominant source of error and their understanding are crucial to archive the full constraining power of these experiments.

A recent example for that are the results of CMB measurements by the Planck satellite (Planck Collaboration et al., 2013a), which has shown excellent agreement with the current standard model, but also highlighted some tensions. For example the best fit ΛCDM model to the CMB power spectrum shows a 2.5σ difference of the Hubble constant compared to SN 1a and direct estimates using multiple images of lensed Quasars.

There is also disagreement between Planck CMB and Planck cluster count estimates of σ_8 using the Sunyaev-Zel'dovich (SZ) effect. This disagreement might be the result of a lack of knowledge of the scaling between SZ observable and cluster mass and their systematics.

Studying the scaling between SZ observables and other mass proxies is one of the major project goals of the APEX-SZ project. In this context, I present in this thesis the cluster masses derived from weak gravitational lensing for all SZ detections of APEX-SZ below $z = 0.9$. I also derive a first scaling relation between lensing based cluster masses and integrated Compton Y parameter based on preliminary results from APEX-SZ.

The structure of this work follows roughly the chronological way of my work and should guide the interested reader from the theoretical basics, over observations and data reduction to the advanced analysis and application of the measurements. It also highlights additional aspects and side results that come with a rich data sets, such as that presented in this work. As an example for that, this thesis presents two cluster mergers with exceptional features between their intra cluster gas and dark matter distribution.

Part II

THEORETICAL FRAMEWORK

This part of the thesis describes the theoretical framework that builds that basis necessary to understand this work. The first chapter gives an introduction of the cosmological model used in this thesis. The second chapter describes galaxy clusters and how they can be used for deriving cosmological parameters. The last chapter of this part explains the measurement method used to obtain masses of galaxy clusters.

2

COSMOLOGY

Since cosmology is by definition a large field in science, it is almost impossible and also not useful to give a detailed introduction in all of its subfields in this thesis work.

We therefore focus on the large-scale structure and evolution of the Universe and leave other aspects such as the primordial nucleosynthesis out of focus.

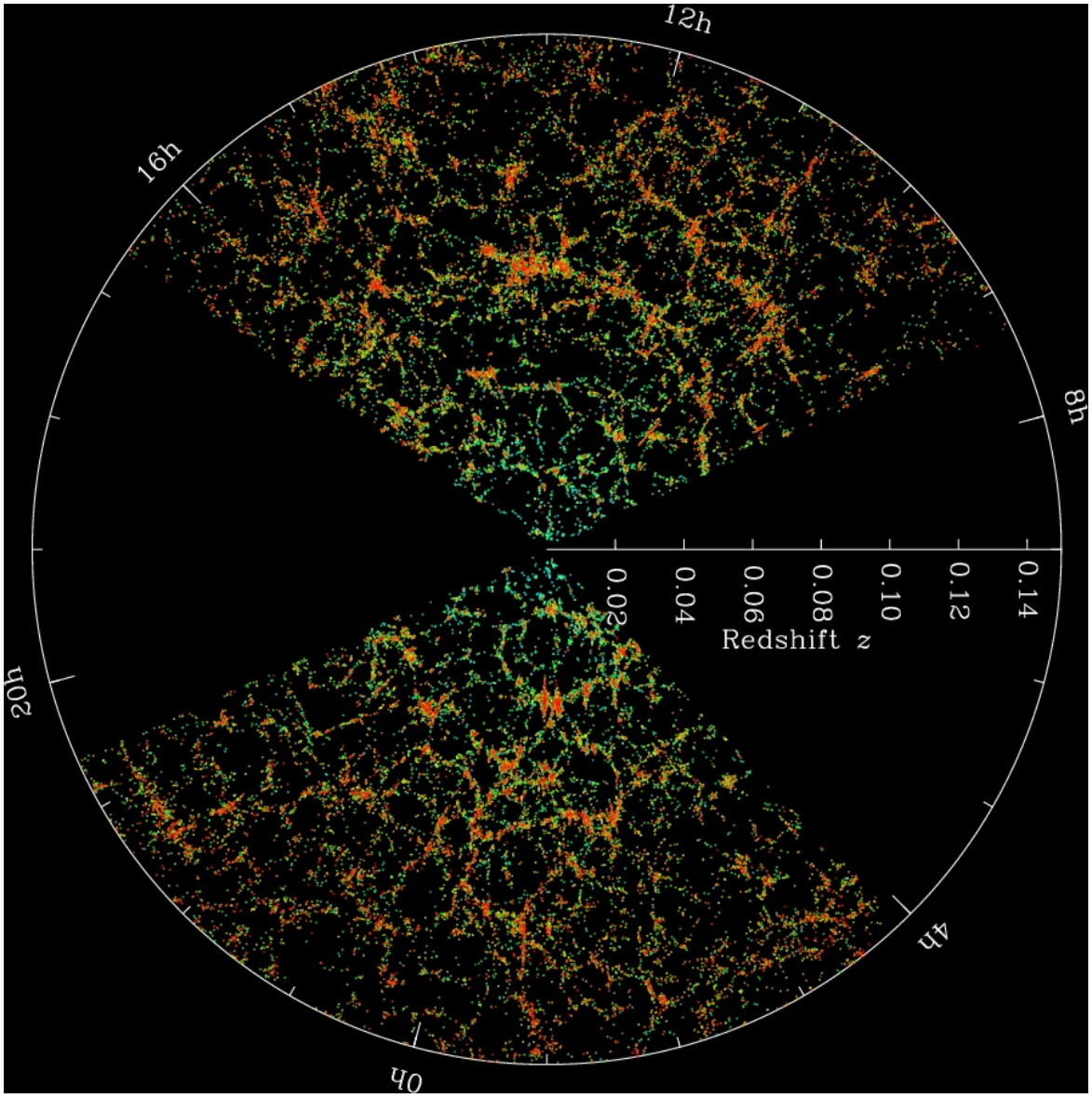

Figure 2: Galaxy distribution of a thin slice of the local universe as measured by the Sloan Digital Sky Survey (SDSS). Image credit: M. Blanton and the Sloan Digital Sky Survey

This short introduction into cosmology is based on lecture notes of the cosmology lecture course held by Matthias Bartelmann and on two textbooks by Peter Schneider (Schneider, 2006a,c).

2.1 BASIC ASSUMPTIONS OF THE STANDARD MODEL

To build a theoretic model of the universe, one has to make some basic assumptions. The two fundamental ones are:

- Isotropy;
- The cosmological principle.

The first says, that averaged over sufficient large scales, the observable properties of the universe appears to be the same, independent of the direction it is observed. The second means that no position in the universe is preferred to any other position. Both combined means, that the Universe has to appear isotropic at any position in the Universe, which requires the universe to be homogeneous. It can therefore be rephrased as: the universe has to be homogeneous and isotropic.

These assumptions seem to be easy acceptable for young astronomers but it took a long time to move from a Earth centered, via the Sun centered, to the uncentered point of view. The assumptions are not beyond any doubt, since there is some evidence from large quasar groups (Clowes et al., 2013) or an 'anomaly' in the CMB power spectrum at $20 < l < 40$ measured by WMAP as well as by Planck that these assumptions may have to be partially reconsidered (Planck Collaboration et al., 2013a).

Other important assumptions are:

- Fundamental constants stay constant over the life time of the Universe;
- The strong and weak force act only on short length scales, typical for particle interactions;
- The electromagnetic force is limited in range by the shielding by opposite charged particles;
- Magnetic fields are negligible on large scales;
- General relativity (GR) is the correct description of the gravitational force on large scales;
- The four dimensional space-time, as described in GR, is the right description of space and time;
- The existence of small deviations of homogeneity in the early phase of the Universe.

Assuming a constant being constant does not appear to be a great thing, but it has to be verified that this is the case over the time scale of 13.8 billion years. For most of the important constants no experimental evidence of a time dependency exist, but some evidence for a variation of the fine-structure constant, α, was found based on high resolution quasar absorption line spectra (Webb et al., 2001; Murphy et al., 2003). Recent results from Planck (Planck Collaboration et al., 2013a) constrained a possible variation of fine structure constant between $z \approx 1000$ ($\sim 13.8 \times 10^9$ years) and $z = 0$ (now) to be less than 0.4%.

The remaining assumptions, except of the last one, ensure that the evolution of the universe can be described in the framework of GR. This is additionally supported by (Planck Collaboration et al., 2013a) results, which are consistent with no primordial magnetic fields, which could affect the structure formation.

The last assumption arise from the obvious reason that we observe structure in the universe, whereas a perfectly homogeneous medium would not form structure. It is assumed that quantum fluctuations in the early universe are the cause of these inhomogeneities, but for this work it is enough to assume the existence of these perturbations.

2.2 FRIEDMANN-LEMAÎTRE-ROBERTSON-WALKER METRIC

To describe the Universe, we fist define a metric and scales. We therefore start with the metric tensor $g_{\mu\nu}$ of Einsteinian Space-Time and the line element ds called Eigentime. The line element is

$$\mathrm{d}s^2 = g_{\mu\nu}\mathrm{d}x^\mu \mathrm{d}x^\nu. \tag{1}$$

The metric tensor $g_{\mu\nu}$ is a symmetric 4×4 tensor, which has ten independent elements. The three space-time components g_{0j}, the time-time component g_{00} and the six space-space components.

For a co-moving observer, described by the coordinates $\mathrm{d}x^j = 0$, the Eigentime equals the coordinate time $\mathrm{d}t$. It follows for the time-time component of the metric tensor

$$\mathrm{d}s^2 = g_{00}\mathrm{d}t^2 = c^2\mathrm{d}t^2 \Longrightarrow g_{00} = c^2. \tag{2}$$

From isotropy follows, that the space-time components have to be $g_{0j} = 0$, which reduces the line element to the form

$$\mathrm{d}s^2 = c^2\mathrm{d}t^2 + g_{ij}\mathrm{d}x^i\mathrm{d}x^j. \tag{3}$$

This shows that space-time can be decomposed in hyper-surfaces with constant time. This hyper-surfaces can be scaled by the function $a(t)$, which depends only on time,

$$\mathrm{d}s^2 = c^2\mathrm{d}t^2 + a^2(t)\mathrm{d}l^2, \tag{4}$$

where $\mathrm{d}l$ is the line element of an isotropic and homogeneous three-space. It simplifies, if we express $\mathrm{d}l$ in polar coordinates (χ,θ,ϕ), since isotropy requires spherical symmetry. We can express $\mathrm{d}l$ as

$$\mathrm{d}l^2 = \mathrm{d}\chi^2 + f_K^2(\chi)(\mathrm{d}\theta^2 + \sin^2\theta\mathrm{d}\phi^2). \tag{5}$$

We can introduce the radial function $f_K(\chi)$ since the relation between χ and the area of spheres of constant χ are still arbitrary. Homogeneity requires $f_K(\chi)$ to be either trigonometric, hyperbolic or linear in χ. Therefore we can express this function as

$$f_K(\chi) = \begin{cases} \sin(\chi\sqrt{K})/\sqrt{K} & (K > 0) \\ \chi & (K = 0) \\ \sinh(\chi\sqrt{-K})/\sqrt{-K} & (K < 0). \end{cases} \tag{6}$$

If we now insert Equation (5) in Equation (4) we get the Friedmann-Lemaître-Robertson-Walker (FLRW) metric

$$\mathrm{d}s^2 = c^2\mathrm{d}t^2 + a^2(t)[\mathrm{d}\chi^2 + f_K^2(\chi)(\mathrm{d}\theta^2 + \sin^2\theta\mathrm{d}\phi^2)]. \tag{7}$$

2.3 EINSTEIN AND FRIEDMANN EQUATIONS

One of the central pillars of GR are the Einstein field equations, which connect energy and pressure with metric and curvature:

$$G_{\mu\nu} + \Lambda g_{\mu\nu} = \frac{8\pi G}{c^4} T_{\mu\nu}. \tag{8}$$

Here, $G_{\mu\nu}$ is the Einstein tensor, which is constructed from the metric tensor via the Ricci curvature tensor and scalar

$$G_{\mu\nu} = R_{\mu\nu} - \frac{1}{2} R g_{\mu\nu}. \tag{9}$$

The second term on the left side of Equation (8) is the term Einstein included to obtain a static Universe, where Λ is called cosmological constant. On the right hand side G denotes the gravitational constant and $T_{\mu\nu}$ is the energy-momentum tensor. In our case this is the stress-energy tensor of a perfect fluid, which is characterized by a time dependent pressure $p = p(t)$ and energy density $\rho = \rho(t)$. The assumption of homogeneity on large scales, prohibits a spatial dependence on pressure and density. If we now specialize the Einstein's equations to the FLRW metric, we end up with the Friedmann's equations:

$$\begin{aligned} \left(\frac{\dot{a}}{a}\right)^2 &= \frac{8\pi G}{3}\rho - \frac{Kc^2}{a^2} + \frac{\Lambda c^2}{3}, \\ \frac{\ddot{a}}{a} &= -\frac{4\pi G}{3}\left(\rho + \frac{3p}{c^2}\right) + \frac{\Lambda c^2}{3}. \end{aligned} \tag{10}$$

The first equation of Equation (10) describes the expansion rate of the universe and its left hand side can be expressed in terms of the *Hubble parameter* using the definition $H(t) = (\dot{a}/a)$. The value of the Hubble parameter today is called *Hubble constant* $H_0 = H(t_0)$. Based on the curvature parameter K, we distinguish between three cases describing three fundamental geometries. For $K < 0$ it has a hyperbolic geometry, which its 3-space pendant is a saddle-shaped surface. We call this case an *open* universe. For $K > 0$ we get a *closed* universe similar to a 3-sphere. The third case is $K = 0$, which is called a *flat* universe, corresponds to an Euclidean geometry. Current results by Planck are consistent with a flat universe.

We can combine the two Friedmann equations resulting in the adiabatic equation

$$\frac{\mathrm{d}}{\mathrm{d}t}\left[a^3(t)\rho(t)c^2\right] + p(t)\frac{\mathrm{d}a^3(t)}{\mathrm{d}t} = 0. \tag{11}$$

The left summand describe the change of internal energy, the right one is the pressure work. This equation states energy conservation and represents the first law of thermodynamics without a heat flow. A potential heat flow would violate isotropy and is therefore not considered in our cosmological model.

2.4 PARAMETERS

To reflect the different properties of matter, one can modify the acceleration equation in Equation (10) to allow several perfect fluids

$$\frac{\ddot{a}}{a} = -\frac{4\pi G}{3}\sum_i \left(\rho_i + \frac{3p_i}{c^2}\right) + \frac{\Lambda c^2}{3}. \tag{12}$$

We can broadly distinguish two different kinds of matter: relativistic and non-relativistic. The relativistic one is usually associated with electromagnetic radiation, where as non-relativistic matter are particles with a significant rest mass energy compared to their kinetic energy. For relativistic bosons and fermions the pressure is

$$p = \frac{\rho c^2}{3}. \tag{13}$$

For non-relativistic matter the pressure can be set to zero since the rest mass energy ρc^2 is huge in comparison with the pressure. Therefore Equation (11) simplifies for non-relativistic mater to

$$\frac{\mathrm{d}}{\mathrm{d}t}\left[a^3(t)\rho(t)c^2\right] = 0 \Longrightarrow \frac{\dot{\rho}}{\rho} = -3\frac{\dot{a}}{a}, \tag{14}$$

from which follows

$$\rho_\mathrm{m}(t) = \rho_0 a^{-3}. \tag{15}$$

Here, ρ_0 is the density at present day. As one can see, the density changes as the volume changes. In case of relativistic matter the adiabatic equation becomes

$$\frac{\mathrm{d}}{\mathrm{d}t}\left[a^3(t)\rho(t)c^2\right] + \frac{\rho(t)c^2}{3}\frac{\mathrm{d}a^3(t)}{\mathrm{d}t} = 0 \Longrightarrow \frac{\dot{\rho}}{\rho} = -4\frac{\dot{a}}{a}, \tag{16}$$

resulting in

$$\rho_\mathrm{r}(t) = \rho_0 a^{-4}. \tag{17}$$

Relativistic matter is, additionally to the volume effect, also affected by the redshift effect resulting in the additional factor a^{-1} compared to ρ_m.

We can also include the cosmological constant in this picture of perfect fluids, with a density of $\rho_\Lambda = \Lambda c^2/(8\pi G)$. With the assumption $\dot{\rho_\Lambda} = 0$ the adiabatic equation (Eq. (11)) suggests $\rho_\Lambda + p_\Lambda/c^2 = 0$, or written as equation of state parameter,

$$w_\Lambda = p_\Lambda/(\rho_\Lambda c^2) = -1. \tag{18}$$

This is a fluid with a negative pressure, a property, which is suggested by the observation of an accelerating universe. Whether the equation of state parameter is really minus one is still under research. Current results from Planck collaboration (Planck Collaboration et al., 2013a) yield $w = -1.13^{+0.13}_{-0.10}$, which is consistent with a cosmological constant. Depending on the value of the equation of state parameter, we call this fluid either dark energy ($w \neq -1$) or cosmological constant ($w = -1$).

We can define a critical density such as

$$\begin{aligned} \rho_\mathrm{cr} &:= \frac{3H^2(t)}{8\pi G}, \\ \rho_\mathrm{cr0} &:= \frac{3H_0^2}{8\pi G}. \end{aligned} \tag{19}$$

For a sphere filled with matter of that density the gravitational potential is equal to its specific kinetic energy. If the density is exceeding this value, will result in a collapse of the sphere, whereas a lower density will let the sphere expanding. Applying this picture to the whole universe, it would determine the density at which the universe would either expand, collapse or approach a constant size.

Including dark energy this assumption does not hold anymore, but it is useful to express the energy densities of the different kind of matter in terms of the critical density.

$$\Omega(t) := \frac{\rho(t)}{\rho_\mathrm{cr}}, \quad \Omega_0 := \frac{\rho(t_0)}{\rho_\mathrm{cr0}} \tag{20}$$

Using this we get for the different energy densities

$$\Omega_\mathrm{r}(t) := \frac{\rho_\mathrm{r}(t)}{\rho_\mathrm{cr}}, \Omega_\mathrm{m}(t) := \frac{\rho_\mathrm{m}(t)}{\rho_\mathrm{cr}}, \Omega_\Lambda(t) := \frac{\Lambda}{3H^2(t)}. \tag{21}$$

Inserting this together with their scale dependencies from Eq. (15) and Eq. (17) into Friedmann's equation we get

$$H^2(a) = H_0^2 \left[\Omega_{r0} a^{-4} + \Omega_{m0}^{-3} + \Omega_{\Lambda 0} - \frac{Kc^2}{a^2 H_0^2} \right]. \tag{22}$$

In the special case of the present state where we have $a = 1$, the Hubble parameter becomes the Hubble constant $H^2(a = 1) = H_0^2$ and we can solve this equation for the K dependent term to get the curvature parameter.

$$\Omega_K := \frac{-Kc^2}{H_0^2} = 1 - \Omega_{r0} - \Omega_{m0} - \Omega_{\Lambda 0} \tag{23}$$

Putting this back to the Friedmann's equation we get the practical parameter expression of the Friedmann's equation

$$H^2(a) = H_0^2 \left[\Omega_{r0} a^{-4} + \Omega_{m0}^{-3} + \Omega_{\Lambda 0} + \Omega_K a^{-2} \right]. \tag{24}$$

And the normalized Hubble parameter

$$E(a) := \frac{H(a)}{H_0} = \sqrt{\Omega_{r0} a^{-4} + \Omega_{m0}^{-3} + \Omega_{\Lambda 0} + \Omega_K a^{-2}}. \tag{25}$$

Due to the scale dependency, the importance of each parameter on the acceleration of the universe changes when the scale of the universe changes. For $a \to 0$ the radiation term plays the dominant role, followed by a matter dominated phase and ending for $a \to \infty$ in a universe dominated by the cosmological constant or dark energy. The curvature term is usually set to zero since observations suggest a flat universe within sub percent range, $100\Omega_K = 0.1^{+0.62}_{-0.65}$ (95% confidence limits) from Planck collaboration (Planck Collaboration et al., 2013a).

2.5 AGE AND EXPANSION RATE OF THE UNIVERSE

Since the Hubble parameter connects expansion rate with size of the Universe ($H = \dot{a}/a$), we can calculate the age of the universe by assuming time starts at $a = 0$ via

$$\frac{da}{dt} = H_0 a E(a) \Rightarrow H_0 t = \int_0^a \frac{da'}{a' E(a')}. \tag{26}$$

During the radiation dominated phase, one can approximate the normalized Hubble parameter as $E(a) = \sqrt{\Omega_{r0}} a^{-2}$ and we obtain

$$H_0 t = \frac{a^2}{2\sqrt{\Omega_{r0}}} \Leftrightarrow a = \sqrt{2 H_0 t \sqrt{\Omega_{r0}}}. \tag{27}$$

The universe scales in this phase like $a \propto \sqrt{t}$. Due to the a^{-4} dependency the radiation dominated phase is believed to end some hundred years after the Big Bang. Compared to the overall age of the universe of several billion years, the duration of this phase is negligible.

In the matter dominated phase one can assume $E(a) = \sqrt{\Omega_{m0} a^{-3}}$. The integral of Eq (26) results in

$$H_0 t = \frac{2a^{3/2}}{3\sqrt{\Omega_{m0}}} \Leftrightarrow a = \left[\frac{3}{2} H_0 t \sqrt{\Omega_{m0}} \right]^{2/3}. \tag{28}$$

As one can easily see in this case, the universe evolves as $a \propto t^{2/3}$.

For the late Universe, the cosmological constant will play the dominating role. In that case we have $E(a) = \sqrt{\Omega_\Lambda}$ and from it follows,

$$H_0 t = \frac{\ln a}{\sqrt{\Omega_\Lambda}} \Rightarrow a \propto \exp\left[\sqrt{\Omega_\Lambda} H_0 t\right]. \tag{29}$$

In this phase the universe expands exponentially.

As we know how the scale radius behaves during the different phases, we want to calculate the age of the Universe. We neglect the radiation term and assume a flat universe. Equation (26) then implies

$$H_0 t = \int_0^a \frac{\sqrt{a'}\mathrm{d}a'}{\sqrt{\Omega_{\mathrm{m}0} + \Omega_\Lambda a'^3}}. \tag{30}$$

This integral can be solved by substituting $x := a^{3/2}$, which results in

$$H_0 t = \frac{2}{3\sqrt{\Omega_\Lambda}} arc\sinh\left[\sqrt{\frac{\Omega_\Lambda}{\Omega_{\mathrm{m}0}}} a^{3/2}\right]. \tag{31}$$

Inserting the recent results from Planck (Planck Collaboration et al., 2013a) of $\Omega_\Lambda = 0.685$, $\Omega_{\mathrm{m}0} = 0.315$ and $a = 1$, we get

$$t_0 \approx \frac{0.951}{H_0} \approx 13.8\mathrm{Gyrs}. \tag{32}$$

2.6 REDSHIFT AND ANGULAR DIAMETER DISTANCE

The measurement of the redshifts of galaxies were one of the key observations of modern cosmology. At its observation it was interpreted as Doppler shift resulting from peculiar motion of the galaxies, away from the observer.

We now interpret this observation in the framework of the theoretic model introduced in this chapter. In Section 2.2 we showed that spatial hyper-surfaces can shrink or expand based on a scale function $a(t)$. In the sections afterwards, we got an understanding how the scale radius behaves for different components of energy in the universe.

We now want to calculate the redshift of a co-moving source, emitting light at a time t_e, reaching a co-moving observer at $\chi = 0$ at time t_o. For light is the line element of the FLRW metric (Equation (7)) $\mathrm{d}s = 0$. We therefore get

$$c|\mathrm{d}t| = a(t)\mathrm{d}\chi. \tag{33}$$

Because both, observer and light emitting source, are co-moving, their coordinate distance χ_{eo} stay constant

$$\chi_{eo} = \int_{t_e}^{t_o} \mathrm{d}\chi = \int_{t_e}^{t_o} \frac{c\mathrm{d}t}{a(t)}. \tag{34}$$

Therefore the coordinate distance with respect to the emission time is zero:

$$\frac{\mathrm{d}\chi_{eo}}{\mathrm{d}t_e} = \frac{c\mathrm{d}t_e}{a(t_0)\mathrm{d}t_o} - \frac{c}{a(t_e)} = 0 \Rightarrow \frac{\mathrm{d}t_o}{\mathrm{d}t_e} = \frac{a(t_o)}{a(t_e)}. \tag{35}$$

The time intervals $\mathrm{d}t$ can be interpreted as the time interval between two maxima of a light wave $\mathrm{d}t = \lambda/c$ and we get the formula for the cosmic redshift

$$\frac{\lambda_o}{\lambda_e} = 1 + \frac{\lambda_o - \lambda_e}{\lambda_e} = \frac{a(t_o)}{a(t_e)}. \tag{36}$$

Inserting for t_o the present time, we get $a(t_o) = 1$. The connection between scale radius and redshift becomes

$$z = a^{-1}(t_e) - 1 \Leftrightarrow a(t_e) = (1+z)^{-1}. \tag{37}$$

The observed cosmological redshift is therefore the result of the expansion of the universe and not the result of peculiar motion. At the first glance, this interpretation of redshift does not appear much different to the first one. Due to GR, any particle with a non vanishing rest mass can never exceed the speed of light, but the space itself does not have that restriction. This results in a finite co-moving horizon within sources are causally connected, which can not only expand but also shrink.

Another distance measure is the angular diameter distance. It is defined as ratio of diameter over angular size of a source $D_A(z) = D/\vartheta$. It is connected to the scale radius as

$$D_A(z) = a(z) f_K(\chi). \tag{38}$$

For weak lensing, which will be one of the major topics of this thesis, the angular diameter distance between two sources is needed. For $z_1 < z_2$ we get,

$$D_A(z_1, z_2) = a(z_2) f_k(\chi(z_2) - \chi(z_1)). \tag{39}$$

2.7 STRUCTURE FORMATION

In the past sections we learned how a homogeneous and isotropic universe behaves over the vast time since the Big Bang. Fortunately the universe is not completely homogeneous, because this would mean that the universe would have no structure.

In order to build the observed structures such as stars, galaxies or clusters of galaxies, small perturbations of the density are needed, which then grow due to gravitational collapse. These perturbations of the density field are believed to be caused by quantum mechanical fluctuations, which were magnified in size during a phase of rapid expansion ,called inflation, which as happened within the first 10^{-32} s after the Big Bang.

These perturbations are still small for baryonic matter at $z \approx 1100$, where the differences between the strongest anisotropies can be measured to be of the oder of 10^{-5}, estimated from the cosmic microwave background. At that this point another kind of matter, which we call cold dark matter (CDM) plays an important role. As already mentioned in the introduction, the rotation curves of galaxies as well as the masses of galaxy clusters suggest that a great amount of mass in these objects have to be invisible. While investigating the density perturbations from the CMB and modeling the structure formation, which we will discuss in the following sections, it could be shown that the observed density perturbations of baryons are not high enough to create the observed structures. Due to the strong radiation field during the early phase of the universe, baryonic matter could not collapse due to radiation pressure. If we now assume that dark matter does not interact with electromagnetic fields, it does not feel the radiation pressure and can collapse earlier. The baryonic matter then follows the perturbations raised by dark matter.

This is another piece of evidence for dark matter, and its non baryonic nature. The prefix cold means, that it has a significant amount of rest mass compared to its kinetic energy. An example of hot dark matter would be neutrinos, which have a very small rest mass. Their influence on structure formation would be counteracting the structure formation. Cold dark matter makes about $\sim 80\%$ of the matter density. The amount of neutrinos is only $\sim 0.4\%$ and its influence on structure formation is small.

2.7.1 *The growth of perturbations*

It is assumed that quantum fluctuations have induced inhomogeneities in the density field. These perturbations can be well described by a Gaussian random density field $\rho(t, \vec{x})$ in co-moving coordinates. Note that there are models of inflation, which can modify the original distribution away from Gaussianity, but current observations do not show strong deviations from a Gaussian random field. We therefore stay simple, and define the density contrast $\delta(t, \vec{x})$ as

$$\delta(t, \vec{x}) = \frac{\rho(t, \vec{x}) - \bar{\rho}(t)}{\bar{\rho}(t)}, \tag{40}$$

where $\bar{\rho}(t)$ is the mean density. The density contrast is expressed as relative overdensity with respect to the mean density at time t and therefore dimensionless.

For a first approximation and since the majority of matter is in the form of dark matter, we neglect the pressure terms in the following theoretic model. We also focus on scales smaller than the horizon R_{H}, allowing us to use Newtonian approximations. Following from the picture of a self-gravitating fluid, the motion of this fluid can be derived via the following three equations: The continuity equation,

$$\frac{\partial \delta(t, \vec{x})}{\partial t} + \frac{1}{a(t)} \vec{\nabla} \cdot \left([1 + \delta(t, \vec{x})] \, \vec{v}(t, \vec{x}) \right) = 0 \tag{41}$$

states mass conservation. Momentum conservation is formulated with the Euler equation

$$\frac{\partial \vec{v}(t, \vec{x})}{\partial t} + \frac{\dot{a}(t)}{a(t)} \vec{v}(t, \vec{x}) + \frac{1}{a(t)} \left(\vec{v}(t, \vec{x}) \cdot \vec{\nabla} \right) \vec{v}(t, \vec{x}) = -\frac{1}{a(t)} \vec{\nabla} \Phi(t, \vec{x}). \tag{42}$$

Due to restrictions to sub-horizon scales, we can use the Poisson equitations as follows

$$\vec{\nabla}^2 \Phi(t, \vec{x}) = \frac{3 H_0^2 \Omega_{\mathrm{m}}}{2 a(t)} \delta(t, \vec{x}). \tag{43}$$

In this equations $\vec{v}(t, \vec{x})$ is the peculiar velocity, which vanishes for co-moving observers. $\Phi(t, \vec{x})$ is the (newtonian) gravitational potential, which is expressed in co-moving coordinates and the $\vec{\nabla}$ operator is defined with respect to co-moving coordinates.

For small overdensities and peculiar velocities, one can find a solution by replacing the continuity equation and the Euler equation by the linearized equations

$$\begin{aligned} &\frac{\partial \delta(t, \vec{x})}{\partial t} + \frac{1}{a(t)} \vec{\nabla} \cdot \vec{v}(t, \vec{x}) = 0 \text{ and} \\ &\frac{\partial \vec{v}(t, \vec{x})}{\partial t} + \frac{\dot{a}(t)}{a(t)} \vec{v}(t, \vec{x}) = -\frac{1}{a(t)} \vec{\nabla} \Phi(t, \vec{x}). \end{aligned} \tag{44}$$

Rearranging and differentiating of the three equations then yields

$$\frac{\partial^2 \delta(t, \vec{x})}{\partial t^2} + \frac{2 \dot{a}(t)}{a(t)} \frac{\partial \delta(t, \vec{x})}{\partial t} - \frac{3 H_0^2 \Omega_m}{2 a^3(t)} \delta(t, \vec{x}) = 0. \tag{45}$$

The dependency on $\vec{x}$ is only implicit. We can therefore solve the differential equation via a separation approach of

$$\delta(t, \vec{x}) = D_-(t) \Delta_-(\vec{x}) + D_+(t) \Delta_+(\vec{x}). \tag{46}$$

Since we are only interested in solutions, which grow with time, we can ignore the first term $D_-(t)$ and focus on the second term $D_+(t)$. The growth factor $D_+(t)$ can be described as

$$D_+(a) \propto \frac{H(t)}{H_0} \int_0^a \frac{1}{(\Omega_r a'^{-2} + \Omega_m a'^{-1} + \Omega_\Lambda a'^2)^{3/2}} da'. \tag{47}$$

Here we already assumed a flat universe. Additionally assuming a negligible Ω_r this equation reduces only to a dependency on the matter and dark energy density.

$$\delta(t, \vec{x}) = D_+(t)\delta(t = 0, \vec{x}) \tag{48}$$

The density perturbations can be fully characterized by the power spectrum, defined as

$$\langle \tilde{\delta}(t, \vec{k}) \tilde{\delta}^*(t, \vec{k}') \rangle = 8\pi^3 \delta_D^{(3)}(\vec{k} - \vec{k}') P(t, k), \tag{49}$$

where $\delta_D^{(3)}$ is the three-dimensional Dirac delta distribution and $\tilde{\delta}$ is the Fourier transform of the matter density contrast,

$$\tilde{\delta}(t, \vec{k}) = \int \delta(t, \vec{k}) e^{-ix \cdot k} d^3x. \tag{50}$$

Here, we introduced the comoving wavenumber k as Fourier variable. Since the density perturbations have to satisfy the cosmological assumptions of homogeneity and isotropy the power spectrum $P(t, k)$ depends only on the modulus of $\vec{k}$.

The growth of structure can now expressed as a change in the power spectrum as

$$P(t, k) = D_+^2(t) P_0(k), \tag{51}$$

where $P_0(k)$ is the power spectrum at $t = 0$. Single-field inflation models predict scale-invariant primordial power spectra of $P \propto k^{n_s}$, where the spectral index n_s is assumed to be slightly below one. The deviation from unity is expected from cosmic inflation models. Recent results by the Planck collaboration (Planck Collaboration et al., 2013a) quotes a value of $n_s = 0.9603 \pm 0.0073$.

More realistic models account for the dependency on the size of the perturbations with respect to the horizon scale plays, as well as the matter component. As already mentioned, dark matter started to collapse earlier than baryonic matter, since it does not feel radiation pressure. This again affects the scale length which can be causally affect the growth. Finally this model only holds for small perturbations up to the order of $\delta(t, k) = 1$, with ongoing growth of the perturbations, structure formation gets increasingly nonlinear. For an intermediate range one could apply the Zel'dovich approximation, which treats the problem in a kinematic way. This approximation also breaks down at some point and numerical simulations can not be avoided anymore.

Figure 3 shows the result of the Millennium Simulation (Springel et al., 2005), a simulation using dark matter as the only matter component. It shows the dark matter distribution of a thin slice within the simulation to illustrate the structure formation from $z = 18.3$ (~ 0.2 Gys after the Big Bang) till today. One can see how the inhomogeneities grow, resulting in large under dense bubbles called voids, strongly overdense regions associated with galaxy clusters, which are connected by overdense bands called filaments. The structures, which we see here in the simulation, are very similar to those of the introducing image of this Figure 2 from the SDSS survey. Note that in the SDSS image the distance is given in redshift, which also produces artifacts at the position of galaxy clusters due to the peculiar motion of the galaxies within the clusters potential.

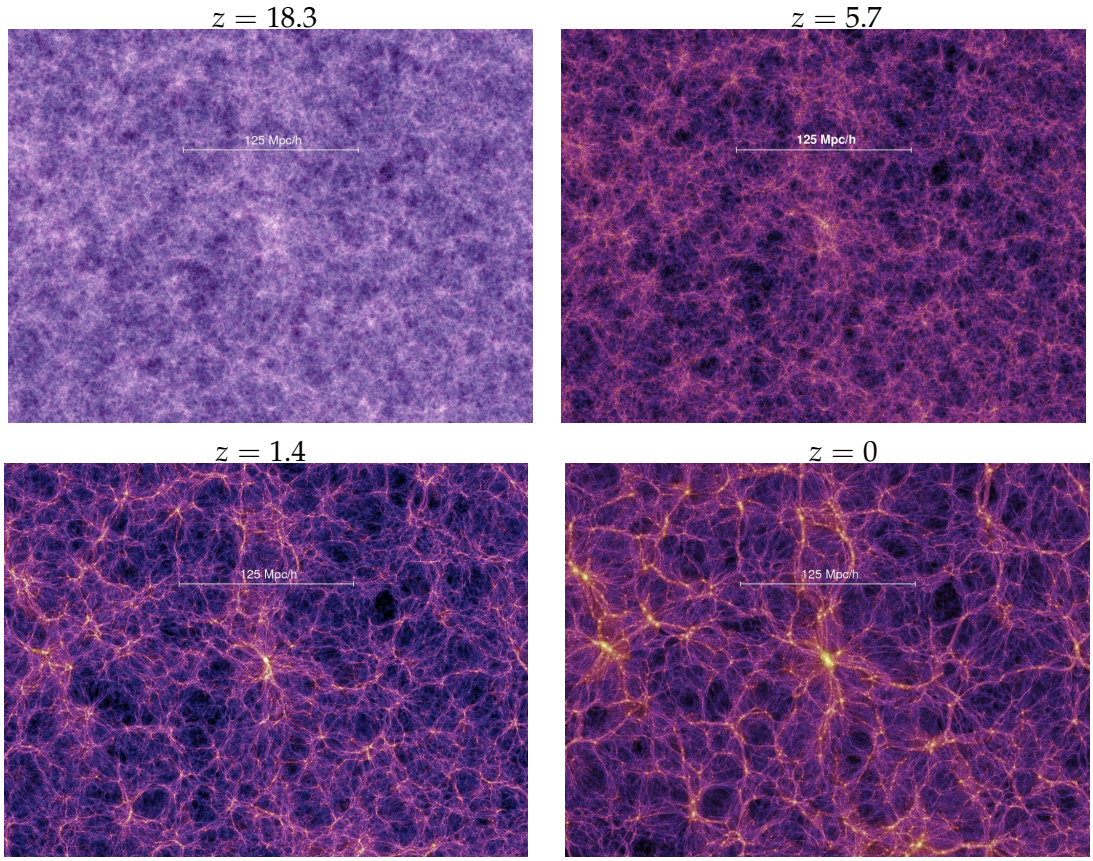

Figure 3: Dark matter distribution at different redshifts in the Millennium Simulation (Springel et al., 2005)

2.7.2 *Spherical Collapse Model*

To gain a better understanding of the collapse of overdensities, one can use the so-called spherical collapse model. Lets assume a sphere, which has a slightly higher density than the mean δ_c. Lets further assume a matter dominated Einstein-de Sitter universe with $\Omega_m = 1$ and $\Omega_\Lambda = 0$. We then can describe the evolution of the sphere as a sub-universe with a matter density larger than the critical density. Since the matter density is super critical, this sub-universe will first expand to a certain maximal radius r_{max} and then start to collapse.

We have shown that the Friedmann equation of closed matter dominated universe has the form

$$\frac{1}{a(t)}\frac{da}{dt} = H_0\sqrt{\Omega_{m,0}a^{-3} + (1-\Omega_{m,0})a^{-2}}. \tag{52}$$

For such a sub-universe, we can find simple functional forms for radius r and time t, if we express the evolution of the scale factor in terms of the development angle θ,

$$\theta = H_0\eta\sqrt{(\Omega_{m,0}-1)}, \tag{53}$$

as

$$r(\theta) = A(1-\cos\theta) \tag{54}$$

and

$$t(\theta) = B(\theta - \sin\theta). \tag{55}$$

Here A and B are defined as

$$A = \frac{\Omega_{\mathrm{m},0}}{2(\Omega_{\mathrm{m},0}-1)};\ B = \frac{1}{H_0}\frac{\Omega_{\mathrm{m},0}}{2(\Omega_{\mathrm{m},0}-1)^{3/2}}. \tag{56}$$

The development angle is a scaled version of the *conformal time* $\eta(t)$, which is given as

$$\eta(t) = \int_0^t \frac{1}{a(t)}\mathrm{d}t \tag{57}$$

As one can see, the radius and therefore the size of the sphere has a periodic solution. For our problem only solutions within one period make sense.

The maximum radius of the sphere before its collapse is reached at $\theta = \pi$. This gives us

$$r_{\max} = r(\pi) = \frac{\Omega_{\mathrm{m},0}}{(\Omega_{\mathrm{m},0}-1)}. \tag{58}$$

And is reached at the time

$$t_{\max} = \pi B = \frac{\pi}{H_0}\frac{\Omega_{\mathrm{m},0}}{2(\Omega_{\mathrm{m},0}-1)^{3/2}}. \tag{59}$$

At that time the sphere has an overdensity of

$$\frac{\rho}{\rho_0} = \Omega_{\mathrm{m},0}\left(\frac{a}{r_{\max}}\right)^3 \approx 5.55. \tag{60}$$

Here $a = (\frac{2}{3}H_0 t)^{2/3}$ is the scale factor of the background Einstein-de Sitter universe. This value relates to an overdensity of $\delta_c = 1.06$ in linear approximation.

Following this model, the sphere would collapse to a single point at $\theta = 2\pi$. Realistic halos are in general not perfectly spherical symmetric objects, as well as the baryonic content of the halo exhibits effects of radiation pressure. A real overdensity therefore does not collapse to a singularity. One can assume that the overdensity reaches a point where it is virialized. Based on the virial theorem ($E_{\mathrm{kin}} = -\frac{1}{2}E_{\mathrm{pot}}$) it is possible to give some dimensions of these structures. Assuming that all energy was stored in form of potential energy at $r_{\max}$ we get

$$E = E_{\mathrm{pot}} = -\frac{3GM^2}{5r_{\max}}, \tag{61}$$

where G is the gravitational constant and M the enclosed mass within the sphere. The virial radius is simply $r_{\mathrm{vir}} = \frac{1}{2}r_{\max}$, which is reached at

$$t_{\mathrm{vir}} = t(\theta = 3/2\pi) = \left(\frac{3}{2} + \frac{1}{\pi}\right)t_{\max} \approx 1.81 t_{\max}. \tag{62}$$

During that time the density of the background universe has decreased by a factor

$$\left(\frac{a_{\max}}{a_{\mathrm{vir}}}\right)^3 = \left(\frac{t_{\max}}{t_{\mathrm{vir}}}\right)^2 = \frac{1}{1.81^2}. \tag{63}$$

Since the volume is $1/8$ of that at maximum size the non-linear density is

$$5.55 \times 8 \times 1.81^2 \approx 145. \tag{64}$$

Other authors are using $t_{\mathrm{vir}} = t(\theta + 2\pi)$ instead of $t_{\mathrm{vir}} = t(\theta = 3/2\pi)$, which results in

$$5.55 \times 8 \times 2^2 \approx 178, \tag{65}$$

which corresponds to $\delta_c = 1.686$ in linear approximation. The latter value is important to get theoretical estimates on the halo mass function, discussed in the following subsection.

In this spherical collapse model, we considered a matter dominated universe, expanding this assumptions to a more general case is quite complicated. For a flat universe Bryan and Norman (1998) gave the following approximation for the mean overdensity in a virialized halo

$$\Delta_{\rm vir} = 18\pi^2 + 82(\Omega_{\rm m} - 1) - 39(\Omega_{\rm m} - 1)^2. \tag{66}$$

In the context of cosmology with galaxy clusters, usually radii or cluster sizes are defined with respect to an overdensity. Due to the dependency of $\Delta_{\rm vir}$ on cosmology and the limited capabilities of some methods to measure quantities out to the virial radius, three different characteristic overdensities have been broadly used $\Delta = 200$, $\Delta = 500$ and $\Delta = 2500$.

2.7.3 *The Halo Mass Function*

Based on the linear approximation of structure formation and the spherical collapse model, Press & Schechter (Press and Schechter, 1974) derived an analytical approach to the *halo mass function*. This function models the number density of virialized objects, such as galaxies, galaxy groups and galaxy clusters as a function of mass and redshift. Following Pillepich et al. (2010) the function can be written as

$$\frac{{\rm d}n(M,z)}{{\rm d}M} = f(\sigma(M,z))\frac{\bar{\rho}_{\rm m,0}}{M}\frac{{\rm d}\ln(\sigma^{-1}(M,z))}{{\rm d}M}. \tag{67}$$

Here $\bar{\rho}_{\rm m}$ is the mean matter density today, $\sigma(M,z)$ is the standard deviation of the density field, which can be related to the initial power spectrum as

$$\sigma^2(M,z) = \frac{D_+^2(z)}{2\pi^2}\int_0^\infty k^2 P_0(k)\tilde{W}(k,M){\rm d}k, \tag{68}$$

where $\tilde{W}(k,M)$ is the Fourier transform of a top-head smoothing function with which the density field is filtered to smooth out mass peaks below the considered mass M. By measuring the mass function via counting virialized objects like galaxy clusters, we therefore can constrain the normalizations of the initial power spectrum. As a measure for this normalization, the convention

$$\sigma_8 := \sigma(M_8, z = 0), \tag{69}$$

is used. Here M_8 is the mass within volume, using a smoothing scale of $8h^{-1}$ Mpc.

We use here the reduced Hubble parameter $h = H_0/(100{\rm km/sMpc}^{-1})$. The mass function in Equation (67) contains the function $f(\sigma(M,z))$, which was found by Press and Schechter (1974) to be

$$f_{\rm PS}(\sigma(M,z)) = \sqrt{\frac{2}{\pi}}\frac{\delta_c}{\sigma(M,z)}\exp\left(-\frac{\delta_c^2}{2\sigma^2(M,z)}\right). \tag{70}$$

The spherical collapse model, as well as the linearized models are limited in their validity. For more advanced models of the halo mass function, the function $f(\sigma(M,z))$ is expressed in different forms to perform a better fit to numerical simulations.

Rather recently Tinker et al. (Tinker et al., 2008) proposed the following form for this function as

$$f_{\rm T}(\sigma(M,z)) = A\left[1 + \left(\frac{\sigma(M,z)}{b}\right)^{a_{\rm T}}\right]\exp\left(-\frac{c}{\sigma(M,z)}\right), \tag{71}$$

where A, a_T, b, c are functions of redshift z and overdensity Δ_c and modeled to optimize the fit to the simulations.

The halo mass function does depend on the normalization of the initial power spectrum and via the growth factor, on other cosmological parameters such as Ω_m and Ω_Λ.

Based on this theoretical framework we can use galaxy clusters as one of the most massive class of virialized objects, as tool to measure cosmological parameters. Figure 4 illustrates the dependence of the cluster mass function on cosmological parameters and on redshift.

Going down to smaller sized objects such as galaxy groups, galaxies or star clusters, baryonic matter and therefore pressure caused by various physical interactions play an increasing role. This makes it difficult to use the halo mass function at that mass regime as cosmological tracers. This as well as resolution and volume limitations put limits on the validity of simulation-based mass functions.

2.7.4 *Galaxy Formation*

The structure formation on 'small' scales such as of galaxies or smaller, are difficult to model since baryonic matter becomes an important factor. This might also be the reason why here the most pronounced differences between standard cosmological model and observations are found (Kroupa et al., 2010). It is believed that galaxies form within dark matter halos via accretion of gas as well as by mergers of smaller (proto-)galaxies. It is also believed that structure formation occurs from small to large scales therefore galaxies build first at redshifts $z \sim 10$ whereas clusters of galaxies have formed rather recently at $z < 2$.

Details of galaxy formation and evolution, such as the correlation between galaxy mass and mass of the central black hole, or the influence of the cosmic environment, are not fully understood and its detailed discussion is also beyond the scope of this thesis. The appearance in optical wavelengths will be discussed at a later point in this thesis.

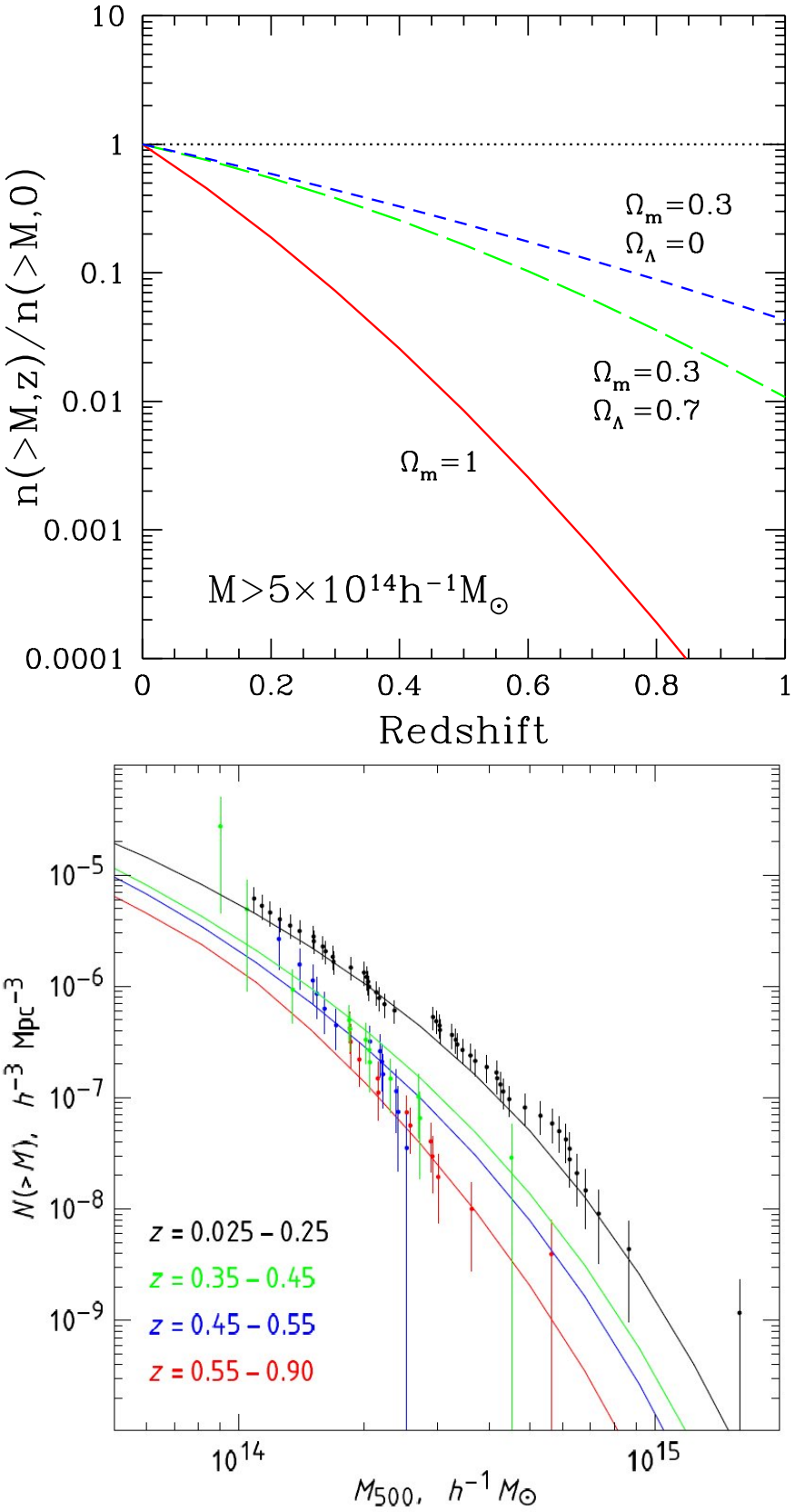

Figure 4: Top: Abundance of massive halos ($M> 5 \times 10^{14} h^{-1} M_\odot$) in dependence of redshift, normalized at $z = 0$, for different cosmological parameters. Figure from Rosati et al. (2002). Bottom: Mass function measured in different redshift bins. Functions are only fitted by varying σ_8, while keeping $h = 0.72$, Ω_m and Ω_Λ fixed. Figure from Vikhlinin et al. (2009).

3

CLUSTERS OF GALAXIES

3.1 CLUSTER OF GALAXIES

"Clusters of galaxies are the largest gravitational bound objects in the universe." This, or similar, is the first sentences of many publications on galaxy cluster since.

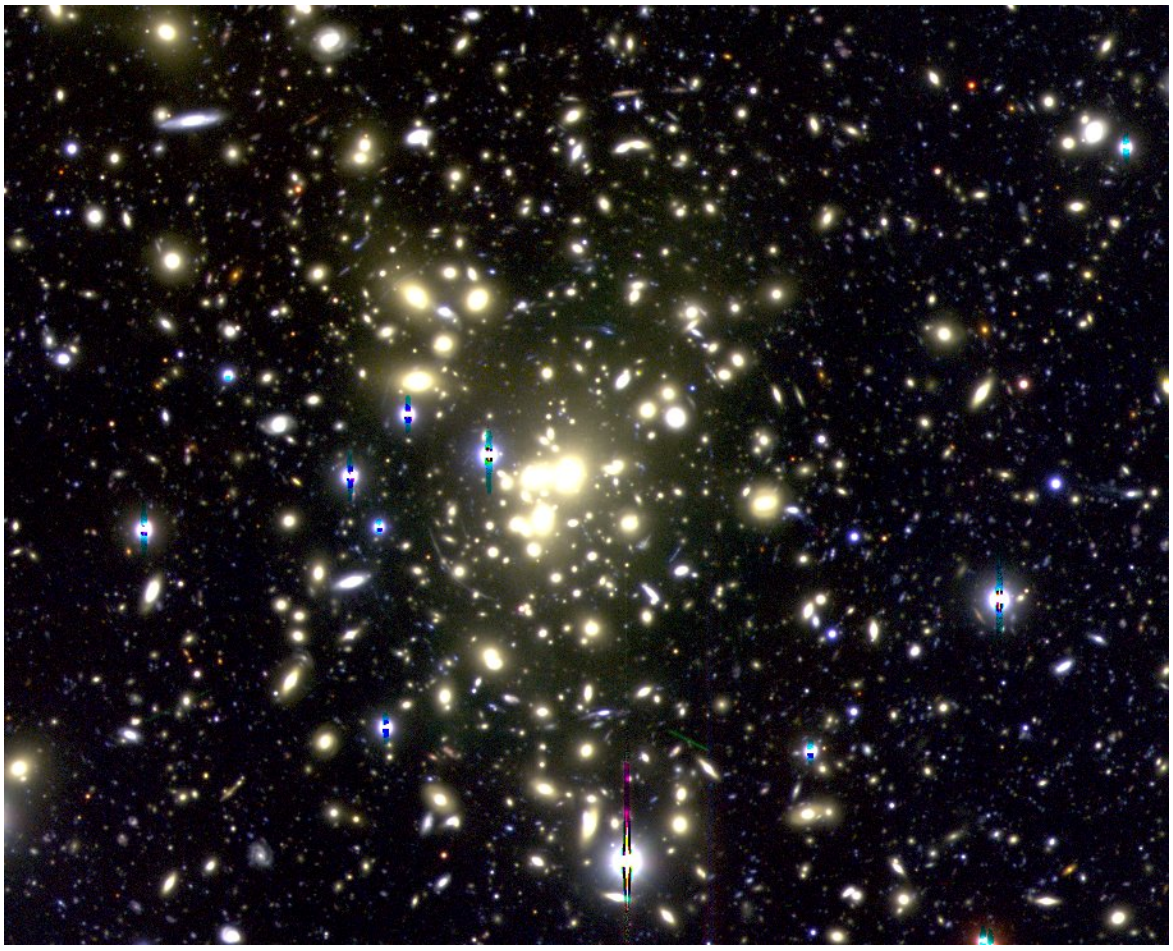

Figure 5: Central region of the galaxy cluster Abell 1689 ($z = 0.18$). Image created from archive Subaru Suprime-cam data.

Clusters of galaxies are, as the name suggests, regions with enhanced number density of galaxies within a given region. Until the beginning of 20th century it was not clear if these objects are superposition of galaxies at different distances or if these galaxies are physically close and gravitational bound to each other. In 1933, Fritz Zwicky measured the velocity dispersion of the Coma cluster and it became clear that these objects built gravitationally bound systems, instantly creating a new question how these objects can be so massive (Zwicky, 1933).

This result was one of the key observations supporting the existence of vast amounts of dark matter in these objects. First large catalogs of galaxy clusters where created George O. Abell in 1958 (Abell, 1958) for the northern hemisphere and Abell et al. (1989) for the southern hemisphere, listing in total 4073 clusters of galaxies.

Based on the standard model, we know that these huge and massive systems were built out of the most pronounced overdensities of the primordial density field. They have masses between 10^{14} $M_\odot$ and some 10^{15} $M_\odot$, of which 80% is in form of dark matter. The remaining mass is mainly ($\sim$ 15%) in the form of hot ($T \approx 10^7 - 10^8$ K) plasma, called *intracluster medium* (ICM), and only a few percent are in form of stars.

Smaller overdensities of galaxies with less than 10^{14} $M_\odot$ are called *galaxy groups*. Due to their smaller mass, it is believed that baryonic physics play a more pronounced role and that therefore the groups differ in some properties from galaxy clusters.

Observations of galaxy clusters in different wavelength regimes are essential for an adequate understanding of these objects, to the level need to use them for constraining cosmological models. The following sections briefly describes the basic appearance and properties of galaxy clusters in different wavelength ranges.

3.1.1 *Optical*

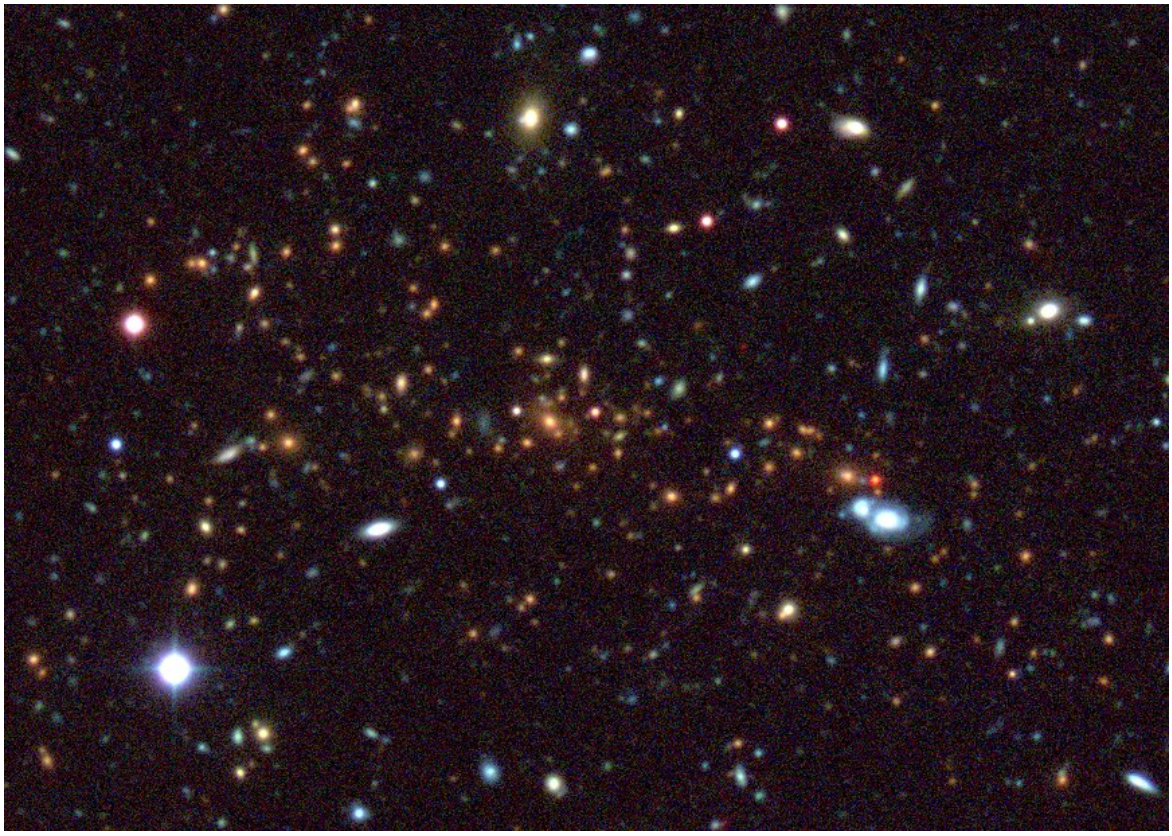

Figure 6: Central region of the galaxy cluster MS1054.4−0321 ($z = 0.83$). The colors of the blue foreground spiral galaxies and the yellow foreground elliptical galaxy differ significantly from overdensity of red elliptical galaxies at the center of this cluster. Image created from observations with WFI at the 2.2m MPG/ESO and archival Subaru Suprime-cam data.

The optical wavelength range extends from the ultraviolet to the near infrared part of the spectrum. Here majority of the emission is coming from stars and active galactic nuclei (AGN). This does not mean that all emission that is observed in clusters comes from the member galaxies. There is also *intracluster* light, which comes from stars not being part of a specific galaxy. The source of these stars might be galaxy mergers or close encounters with other member galaxies, leading to tidal disruptions and a loss of stars. A second mechanism to create stars outside galaxies is ram-pressure stripping, which occurs when

galaxies fall into the central regions with its significant amount of ICM. It is assumed that this can trigger star formation even within the stripped gas (e.g. Sun et al. (2007)).

Ram-pressure stripping of the gas from a galaxy is also assumed to be the reason for another optical feature of galaxy clusters. Observations show that the fraction of red elliptical galaxies increase towards the cluster center and becoming the dominants form of galaxies. These galaxies are in general redder than elliptical galaxies outside clusters. The reason for that is, that the star formation rate of these galaxies is extremely low compared to their size. Young massive stars dominate the bluer part of the galaxy spectrum, but due to their shorter lifetime compared to smaller stars, they die earlier and the remaining stars make the galaxy appear redder than galaxies with ongoing star formation.

These red elliptical galaxies exhibit a tight linear relationship in color-magnitude space. This observed structure in color-magnitude space is called the *red sequence* and is used in optical surveys to find clusters of galaxies and avoid spurious detections based on projection effects (e.g.Gladders and Yee (2000)).

Butcher and Oemler (Butcher and Oemler, 1978) found that at higher redshifts, $z \approx 0.5$, the fraction of blue cluster members is higher than for clusters today. This indicates a higher star formation rate in clusters at higher redshifts. This Butcher-Oemler effect is associated with higher merger rates of galaxy clusters and an incompleted gas depletion. However, observations have also shown fully evolved cluster red sequences at redshifts $z \sim 1.5$ (Snyder et al., 2012).

Another characteristic of most galaxy clusters is the brightest cluster galaxy (BCG), a bright, dominating cD galaxy at the center of the cluster. Those can be used as tracers of the dynamical state of a cluster by measuring their distance to the cluster center that is determined, for example, with X-ray observations. The presence of two dominant galaxies or the absence of a dominant galaxy can also yield important insights into the dynamical state of a cluster.

Beside the study of the evolution of galaxies within clusters, optical observations of the cluster galaxies yield even more information on their host cluster. Observations of their spectra give precise distance measures as well as mass estimates from the velocity dispersion of the cluster galaxies. Additional imaging data can also be used to estimate the mass of a cluster, by using a scaling relation between number of bright cluster members and cluster mass (e.g. Andreon and Bergé (2012)).

Another method uses galaxies behind the cluster and measures the distortion of their images by the gravitational potential of the cluster. This method will be discussed in the following Chapter 4.

3.1.2 *X-rays*

X-ray emission from galaxy clusters was detected soon after X-ray detectors were first used in astronomy. Galaxy clusters are found to be the brightest X-ray sources in the sky. As the resolution of X-ray telescopes increased, the X-ray emission of galaxy clusters could be resolved as diffuse extended sources. The spectrum of this X-ray emission showed that the X-rays are emitted from a hot plasma with temperatures of ten to hundred million Kelvin that is lying in the deep gravitational potential of the cluster. A source of non-thermal emission in clusters are AGN, which are situated within the cluster member galaxies.

The emission of the plasma comes from the scatter of electrons on ions of the plasma, and is called thermal *Bremsstrahlung*, or free-free emission. The bolometric Bremsstrahlung

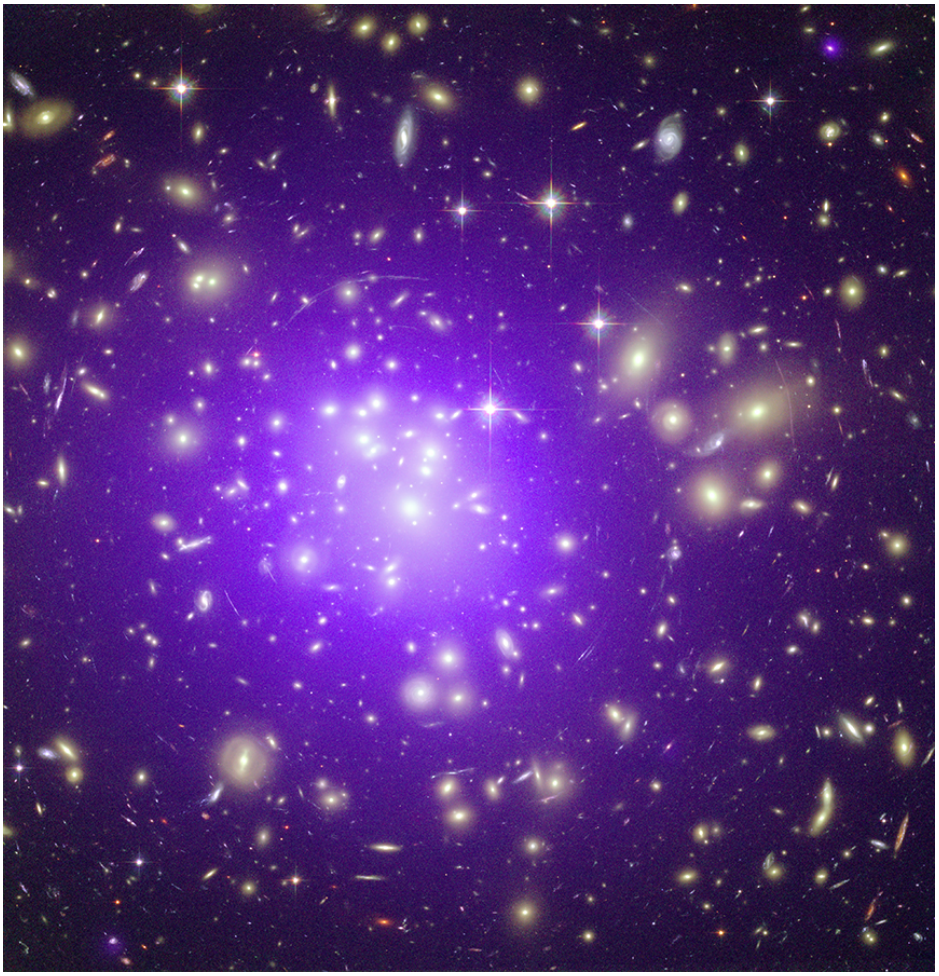

Figure 7: Abell 1689 with X-ray emission highlighted in magenta. Image credit: X-ray: NASA/CXC/MIT/E.-H Peng. Optical: NASA/STSc.

emissivity is proportional to the square of the electron density and the square root of the electron temperature,

$$\eta_{\mathrm{bol}}^{\mathrm{ff}} \propto \sqrt{T_{\mathrm{e}}} n_{\mathrm{e}}^2. \tag{72}$$

The ICM is assumed to be overall neutral and the electron density should therefore follow the gas density of the ICM.

Assuming spherical symmetry, one can fit the surface brightness profile with an underlying density profile of the shape

$$\rho_{\mathrm{fi}}(r) = \rho_0 (r^2/r_{\mathrm{c}}^2 + 1)^{-3\beta/2}, \tag{73}$$

with core radius r_{c}, central density ρ_0 and the ratio of the kinetic energies $\beta = m\sigma_v^2 k_{\mathrm{B}}^{-1} T^{-1}$, where σ_v is the velocity dispersion of the cluster galaxies. This density profile is called a *β-profile* (Cavaliere and Fusco-Femiano, 1978).

When the assumption of hydrostatic equilibrium holds and the elemental composition μ has no positional dependency, one can derive the mass within an radius r as

$$M(r) = \frac{-k_{\mathrm{B}} T(r) r}{\mu m_{\mathrm{p}} G} \left(\frac{\mathrm{d} \ln T}{\mathrm{d} \ln r} + \frac{\mathrm{d} \ln \rho}{\mathrm{d} \ln r} \right). \tag{74}$$

Assuming that the ICM is isothermal and plugging in the β-profile yields

$$M(r) = \frac{3\beta r k_{\mathrm{B}} T}{G m_{\mathrm{p}}} \frac{r^2/r_{\mathrm{c}}^2}{1 + r^2/r_{\mathrm{c}}^2}. \tag{75}$$

This mass estimate can be strongly misleading, because of the assumptions leading to the formula.

The Navarro, Frenk and Wright (Navarro et al., 1996) (NFW) dark-matter profile was found to follow the mass profile of clusters in simulations. Gas in hydrostatic equilibrium within a gravitational potential which arises from a NFW density profile yield density and surface brightness profiles, which are well modeled with a beta profile.

X-ray spectra can be used to determine the temperature of the ICM and the redshift of the cluster. This allows X-rays surveys to reduce the size of the optical follow-up that is needed to constrain cluster redshifts (Lloyd-Davies et al., 2011). However, temperature and redshifts can only be derived for a small fraction of clusters with sufficient amount of detected X-ray photons. The accuracy of the X-ray derived cluster redshifts are only of a level of $10 - 20\%$, which is significantly worse than those of spectroscopic redshifts of cluster galaxies in the optical regime.

For the usage of X-ray observations for precision cosmology, the biases between mass tracers such as hydrostatic mass estimates, temperature or luminosity have to be understood.

3.1.3 *Millimeter-wavelengths (The Sunyaev-Zel'dovich Effect)*

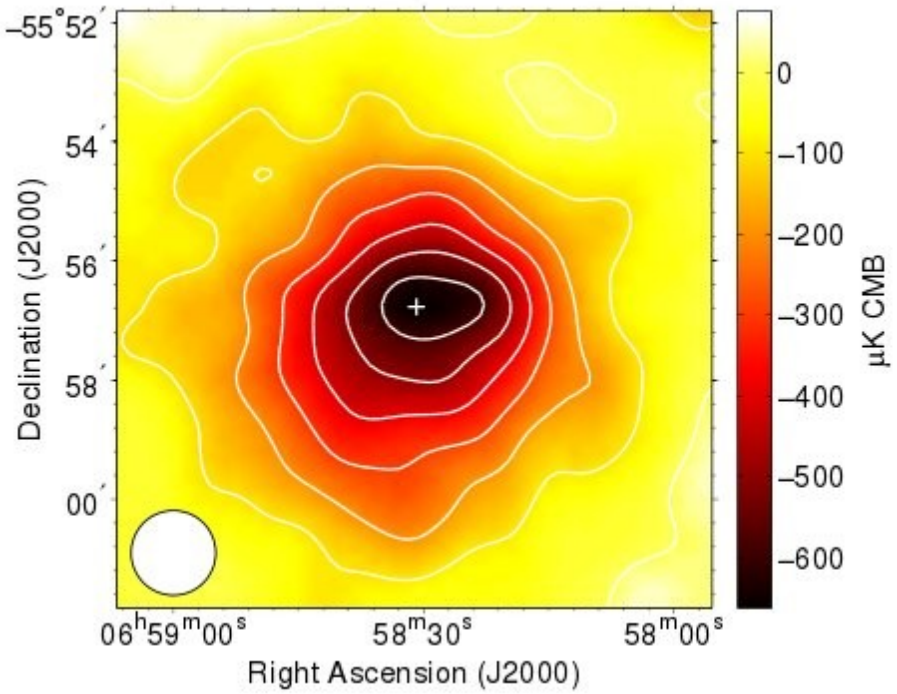

Figure 8: The Bullet cluster as seen via the SZ-Effect from APEX-SZ. Image from Halverson et al. (2009).

Predicted by Rashid Sunyaev and Yakov Zel'dovich in 1970 (Sunyaev and Zel'dovich, 1970) and first measured by (Birkinshaw et al., 1978), the Sunyaev-Zel'dovich (SZ) effect has become one of the most powerful instruments to measure properties of galaxy clusters.

The same hot plasma that is the source of the X-ray emission of galaxy clusters is also source of an effect measurable at wavelength of 0.1 to 10 mm. When photons from the CMB pass through the hot plasma, they Compton-scatter with the electrons of this plasma. Since the electrons are much more energetic than the CMB photons, the electrons lose energy after the scattering, whereas the photons gain energy. Since the number of photons

is conserved, the shape of the CMB spectrum at the position of the cluster is changed by up scattering photons to higher energies (shorter wavelengths). This can be expressed as a temperature change of the CMB via

$$\frac{\Delta T_{\mathrm{SZ}}}{T_{\mathrm{CMB}}} = f(x) \int n_{\mathrm{e}} \sigma_{\mathrm{T}} \frac{k_{\mathrm{B}} T_{\mathrm{e}}}{m_{\mathrm{e}} c^2} \mathrm{d}l = f(x) y. \tag{76}$$

Here n_{e} and T_{e} are the electron density and temperature of the hot plasma in the ICM. T_{CMB} is the temperature of the CMB, σ_{T} the Thomson cross-section, k_{B} the Boltzmann constant, and $m_{\mathrm{e}}c^2$ is the rest mass energy of an electron. The integration is along-the-line of sight, making the observed tSZ signal proportional to the integrated pressure along the line-of-sight. The frequency dependence of the SZ-effect is given by

$$f(x) = \left(x \frac{e^x + 1}{e^x - 1} - 4 \right) (1 + \delta_{\mathrm{SZ}}(x, T_{\mathrm{e}})), \tag{77}$$

where $x = h\nu/(k_{\mathrm{B}} T_{\mathrm{CMB}})$ is the photon energy at frequency ν, divided by the thermal energy and $\delta_{\mathrm{SZ}}(x, T_{\mathrm{e}})$ is a correction for relativistic electrons (Nozawa et al., 2000).

The transition between missing and excess photons occurs at $x = 3.83$, corresponding to $\nu = 217$ GHz. Since the effect depends on T_{CMB} at the redshift of the cluster, the frequency dependency in the cluster rest frame changes with redshift. Due to the cosmic expansion the photons get redshifted after passing the cluster until they reach the observer, which counteracts the frequency dependency on the rest frame and the observable SZ effect gets independent of the cluster redshift.

The Compton parameter y is defined as

$$y = \int \frac{k_{\mathrm{B}} T_{\mathrm{e}}}{m_{\mathrm{e}} c^2} \sigma_{\mathrm{T}} n_{\mathrm{e}} \mathrm{d}l. \tag{78}$$

where σ_{T} is the Thomson cross-section, T_{e} is the electron temperature of the cluster, and m_{e} the electron mass. The integral over l runs along the line of sight and depends only on the electron density n_{e} and the temperature T_{e}.

A measure of the total SZ-effect signal is the integrated Compton-y parameter, Y_{SZ},

$$Y_{\mathrm{SZ}} = \int y \mathrm{d}\Omega. \tag{79}$$

Integrated over the size of the cluster the integrated Compton-y parameter is a measure of the total thermal energy of the cluster. Because of that, this parameter should be a robust mass proxy (Planck Collaboration et al., 2011). Under the assumption of hydrostatic equilibrium, Y_{SZ} is proportional to the following other cluster mass proxies:

$$\begin{aligned} Y_{\mathrm{SZ}} D_{\mathrm{A}}^2 &\propto M_{\mathrm{gas}}^{5/3} f_{\mathrm{gas}}^{-2/3} E(z)^{2/3}, \\ Y_{\mathrm{SZ}} D_{\mathrm{A}}^2 &\propto T_{\mathrm{e}}^{5/2} E(z)^{-1}, \\ Y_{\mathrm{SZ}} D_{\mathrm{A}}^2 &\propto M^{5/3} E(z)^{2/3}, \end{aligned} \tag{80}$$

where $E(z)$ is the normalized Hubble parameter (Eq. (25)) and D_{A} the angular diameter distance. The first two equations are of interest for a comparison between SZ and X-ray observations, whereas the last equation of Equation (80) is of major interest for the comparison with lensing based measurements.

Beside the above mentioned thermal SZ-effect, there exists also the relativistic and the kinetic SZ effect. The kinetic effect arises if a cluster and with it the ICM is moving with respect to the rest frame of the CMB. This effect allows to measure velocities of the ICM along the line of sight. For galaxy clusters this effect is about 20 times smaller than the

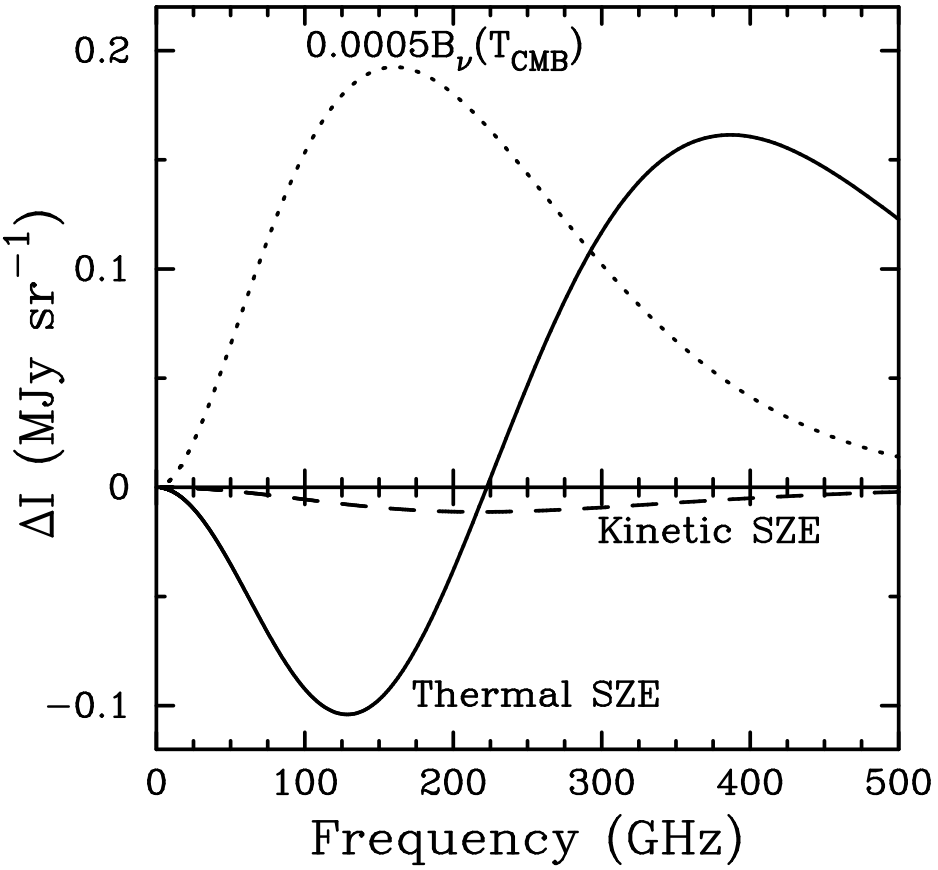

Figure 9: Spectral intensity distortion ΔI of the CMB in dependence of the frequency for a cluster with a temperature $k_B T_e = 10$keV. The kinetic SZ-effect is shown for a peculiar velosity 500km/s. For illustration also the thermal spectrum of the CMB is plotted, scaled by a factor of 0.0005 Figure from Carlstrom et al. (2002).

thermal SZ effect. The first reliable detection of this effect from individual clusters of galaxies was based on galaxy groups with masses of the order $10^{13} M_\odot$ (Hand et al., 2012). Relativistic corrections are important for hot clusters and for the Wien side of the spectrum. It also results in a frequency dependency of the kinetic SZ effect.

3.1.4 *γ-ray*

It is believed that clusters of galaxies can be a source of gamma-ray emission due to dark matter annihilation or decay (Cirelli et al., 2011). Recent results from Hektor et al. (2013) using data from the Fermi Large Area Telescope show evidence of a double-peak-like excess with a significance of 3.6σ at photon energies of 110 GeV and 130 GeV. However, gamma-ray astronomy of galaxy clusters is a young field and most observations yield only upper limits on line emission from clusters of galaxies.

New gamma-ray telescopes such as may be able to detect dark matter annihilation or decay or rule out these effects at higher significance.

3.1.5 *Radio*

Beside the SZ-effect in the mm-wavelength range, clusters of galaxies have also several observable features in the radio regime. The ICM contains highly relativistic particles.

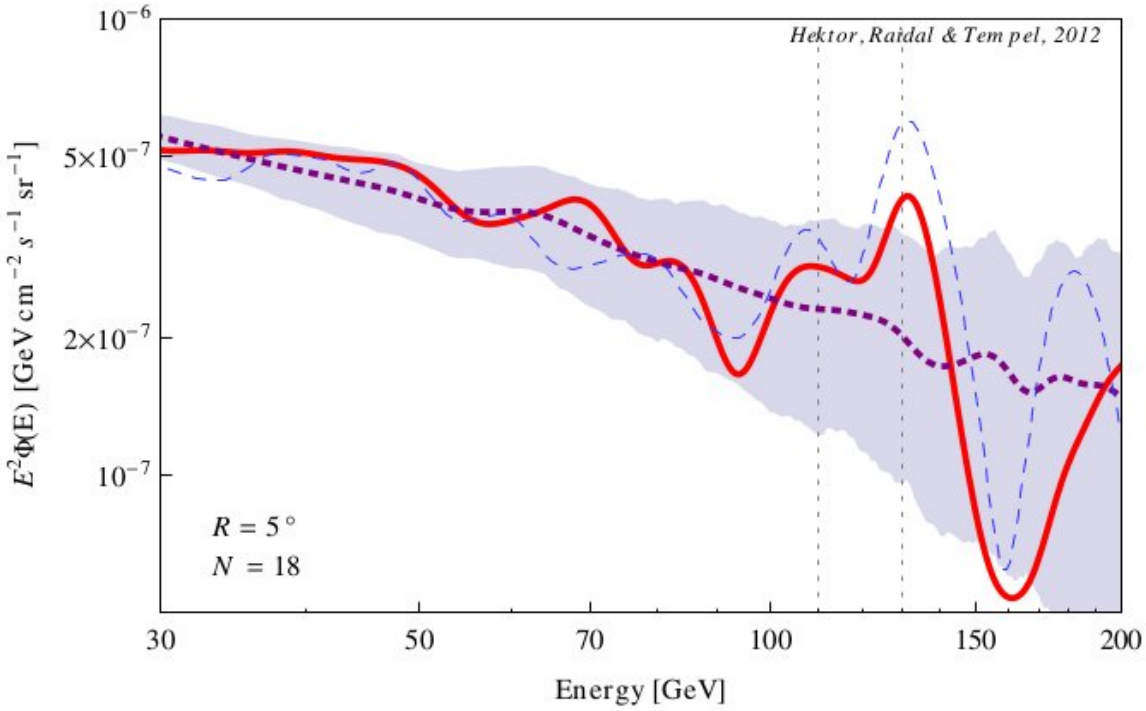

Figure 10: Tentative γ-ray detection of line emission from galaxy clusters from dark matter annihilation. Red: stacked γ-ray spectrum, violet: background spectrum, blue band: 95% confidence range of the background and blue line: spectrum from the galactic center. Image from Hektor et al. (2013)

Together with large-scale magnetic fields in clusters, they build a source of synchrotron emission, which can be measured in radio wavelengths (Feretti and Giovannini, 2008).

One differentiates between four different phenomena, radio halos, radio mini halos, radio relics and radio lobes, where the first three can be associated with the cluster as a whole and the last phenomena with AGN within the cluster.

Radio lobes are powered by the jets of AGNs and therefore are associated to specific galaxies. Radio relics reside at the edge of shock fronts in the ICM that are induced when two clusters merge. They are found in the outskirts of the cluster.

Radio mini halos are found in cool core clusters, which are preferentially relaxed systems. They are smaller than classical radio halos, with sizes of a few hundred kiloparsces and harbor a strong radio galaxy in their center.

Classical radio halos have sizes of the order of 1 Mpc. They are not associated with particular galaxies and their morphology corresponds to that of the ICM. The latter suggest a correlation between cluster mass and powering mechanism of the radio halo (Liang, 2000). Radio halos are mostly found in ongoing cluster mergers and can, as such, help to understand the dynamics the ICM and their hosting clusters.

The exact mechanism of powering the radio halos is not well understood and two different models are in discussion. In the turbulence model, the electrons are re-accelerated by magneto-hydrodynamic turbulences in the ICM, which are caused by the cluster merger (Petrosian, 2001; Brunetti et al., 2001). The second model is called hadronic model and explains the powering mechanism via collisions between cosmic-ray protons with the thermal plasma protons generating relativistic electrons (Dennison, 1980).

Studies using X-rays for cluster selection and mass estimates, with the goal of constraining the mass to radio power scaling relation, are seeing two different populations. While one population seem to follow a correlation between radio power and mass observable, a

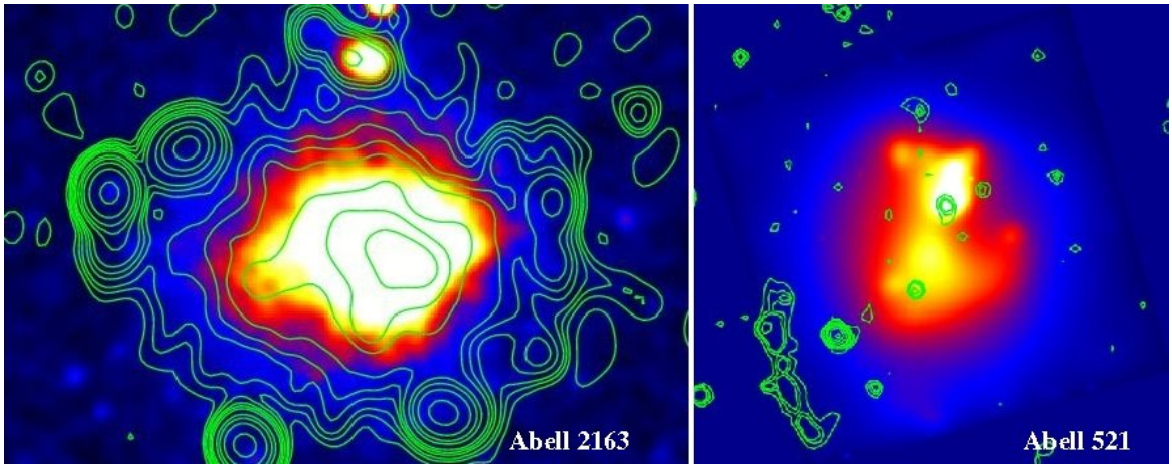

Figure 11: X-ray surface brightness map with radio contours of two galaxy clusters. Image credit: Abell 2163: Feretti et al. (2001), Abell 521 Ferrari et al. (2006)

'radio quiet' population does not show radio halos at all (Brunetti et al., 2007). A reason for that might be the different dynamical time on which the two observables are affected by cluster mergers. Additionally the mass estimate of merging clusters based on X-rays is difficult and likely biased. Measurements using the SZ-effect may be more accurate, since it is less affected by cluster mergers and also the timescale of the observable effects on the merger should be closer to that of radio powering mechanism. Indeed, Basu (2012) and Sommer and Basu (2013) found a robust correlation between radio power and Y_{SZ} with no strong division between two distinct populations. Future work with SZ observations may therefore be able to clarify the correlation between radio halos and mass, as well as the powering mechanism.

3.2 USING CLUSTER OF GALAXIES AS TOOLS IN COSMOLOGY AND ASTROPHYSICS

As shown in the previous section, galaxy clusters can be observed in various wavelengths, probing different physical effects, which are related to different astrophysical questions. I will now present a few aspects in some grater detail, since they will be the targets of investigation at a later point of this thesis.

3.2.1 *The cluster mass function*

In section 2.7.3, we discussed the halo mass function and how it depends on cosmological parameters. The cluster mass function is almost identical to the halo mass function with only small limitations. First of all, due to the definition of galaxy clusters to be of masses greater than $10^{14} M_\odot$, the cluster mass function describes only the high-mass part of the halo mass function. Depending on the definition of a halo, such as being a pure dark matter overdensity or if it also includes baryonic matter, could cause differences between the cluster mass function based on observations of galaxy clusters and the theoretical halo mass function.

However, assuming that in massive clusters baryonic effects do not significantly affect the mass function, and defining the halo mass function such that it includes all sort of matter, the halo mass function and the cluster mass function are identical.

As mentioned in Section 2.7.3, the mass function depends sensitively on the cosmological parameters Ω_m, Ω_Λ and σ_8. Investigating the cluster mass function as a function of

redshift, one can also put constraints on the variability of the cosmological constant, which is usually expressed in the form of the equation of state parameter w.

The cluster mass function is usually compared to the value today, which can result in some counter-intuitive results if one compares the mass function with values at higher z in dependence of the cosmological parameters.

A universe with higher matter density Ω_m builds up structure faster, resulting in a lower number of massive clusters at higher redshifts compared to models with lower Ω_m. Similarly, at fixed matter density but higher Ω_Λ the mass function has to evolve faster to compensate the dilution of the cluster formation from the increased Ω_m. An illustration of these effects can be found in the top panel of Figure 4. The constraining power and degeneracies of different cosmological probes are illustrated in Figure 12.

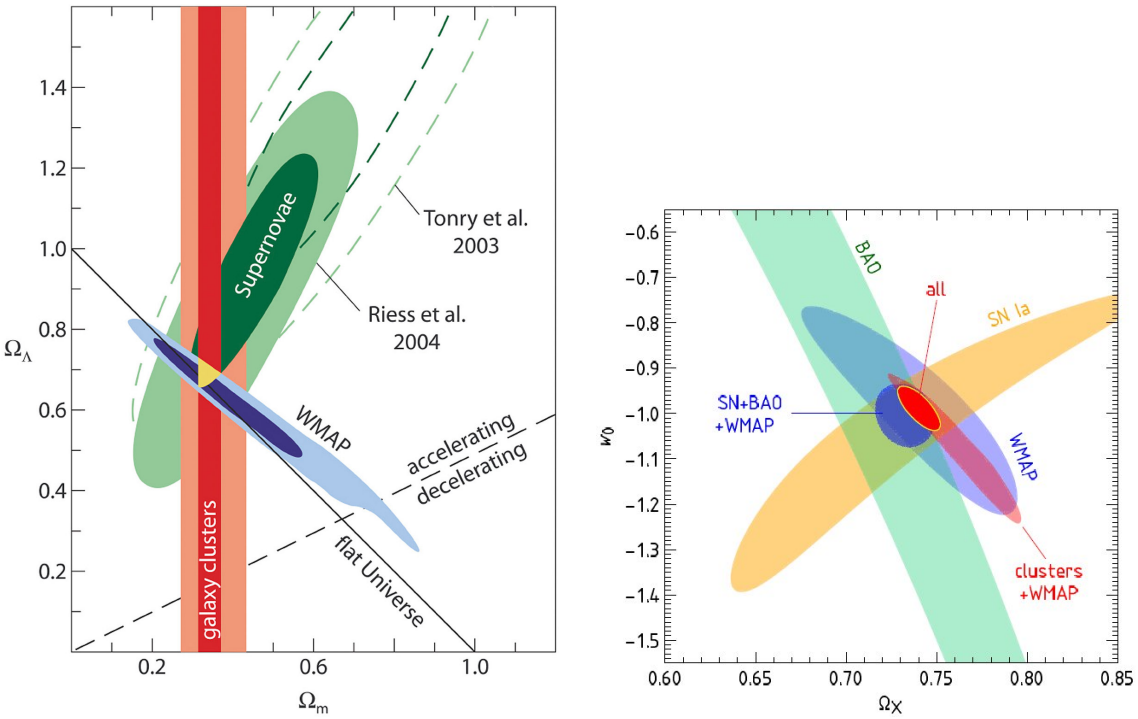

Figure 12: Constraining cosmological parameters: Left: Constraints in the Ω_m-Ω_Λ plane from galaxy clusters (Schuecker et al., 2003), SN 1a (Riess et al., 2004; Tonry et al., 2003) and CMB (Spergel et al., 2003). Image credit: ESO. Right: 1σ constraints in the $\Omega_\Lambda - w_0$ plain: BAOs from Percival et al. (2007), Clusters from Vikhlinin et al. (2009), WMAP from Komatsu et al. (2009) and SN Ia from Davis et al. (2007). Combined contours and image credit Vikhlinin et al. (2009)

A simple way to put limits on cosmological parameters would be to search for the most massive clusters at high redshift. This so called "pink elephants" method simply compares the existence of massive clusters with the probability to exist in a universe with a given cosmology. Beside that only limits on the cosmology can be given, this method has also the problem of working with small numbers. This means that the individual cluster has to be understood sufficiently enough to exclude any false measurement of the cluster mass. Also the cluster mass function at the very high mass end might not be well enough constrained due to the limited volume of cosmological simulations. Additionally, we live in only one accessible realization of the universe with a given set of cosmological parameters. Observations based on only a small number of objects can be hampered by this concrete realization being not representative for this particular observable.

A more robust way to put constrains on cosmological parameters is therefore to measure the mass function over a significant mass range, and its evolution with redshift. For this method, a large number of galaxy clusters over a sufficient large redshift range is needed.

To reach a high number of galaxy clusters at different redshifts with measured masses, one has to find methods to measure the masses in an efficient way. From the last section, we know several properties observed in different wavelengths, which scale with mass. These properties can be used as mass proxies for measuring the cluster mass function. Unfortunately there is not one specific observable that is better than all the others. Each mass proxy has advantages and disadvantages.

For example the temperature decrement caused by the SZ-effect is independent of redshift, which allows one to detect clusters at high redshift, but one also needs additional information such as the redshift to create the mass function. SZ surveys therefore need follow-up observations.

X-ray observations in principle can contain all necessary informations needed for creating the mass function. But X-rays are more affected by the dynamical state of the cluster than SZ observations. Additionally, X-ray observations are affected by redshift for various reasons. One obvious reason is the dependency on the luminosity distance. With a decreasing amount of photons at higher redshifts, it becomes increasingly difficult to constrain all important parameters, such as the redshift for a cluster. This results in the need of follow-up programs to constrain the missing properties.

Optical methods such as richness measurements are more noisy and limited in redshift. Using weak gravitational lensing as described in the following chapter is believed to give reliable, on average unbiased, mass estimates. Similar to X-ray measurements, gravitational lensing becomes increasingly time consuming with increasing cluster redshift, due to the need of background galaxies, which also depends on the luminosity distance. This, together with the dependency of the lensing signal with angular distance ratio between lens and source, limits the redshift range for practicable applications.

The best solution is therefore to combine methods to make optimal use of all methods. In practice this means to use unbiased mass estimators like weak lensing derived masses to calibrate less redshift dependent or time consuming estimators such as X-ray luminosity or Y_{SZ}.

3.2.2 *Scaling relations*

The correlation between mass proxy and cluster mass is expressed in a scaling relation. Investigating scaling relations is essential to make full use of the constraining power of large surveys. Two aspects are of major interest for scaling relations. The first is measuring the scaling as accurate and unbiased as possible. The second aspect is the amount of intrinsic scatter of the observable. A bias in the scaling relation would directly bias the mass function and with that the measured cosmological parameters. Caused by the individual properties of the cluster the mass proxies have a intrinsic scatter around the scaling relation. This results in errors on the mass estimate of individual clusters, which are independent on the accuracy of the measured mass proxy. This again limits accuracy of the derived cluster mass function even if the measured mass proxy is known to high accuracy. Therefore low scatter mass proxies are preferred.

Following the model of structure formation, which we have outlined in Section 2.7, Kaiser (1986) has shown that this leads to a self-similar model of dark matter halos. This means that all clusters should appear to be similar if they are properly rescaled with respect to their mass or size, if non-gravitational effects are neglected. A selection of different scalings, which arise from the self-similar model, can be already found in Equation (80)

and can be easily rearranged to get the relation with mass. Some effects such as the feedback of AGN to the ICM can cause deviations from the self-similar scaling between observables. However, the scaling between different observables are well described by power laws with normalization A and slope parameter B.

Broadly investigated scaling relations are the $M - T_X$ and the $M - L_X$ scaling relations in X-rays (Giodini et al., 2013). Another interesting parameter is the Y_X parameter as a pendant to the Y_{SZ} parameter. Its defined as

$$Y_X = T_X M_{gas}. \tag{81}$$

Simulations by Nagai et al. (2007b) have shown that this mass proxy has a tight correlation with mass, with a scatter lower than T_X and M_{gas} alone.

Scaling relations between SZ-observables, such as Y_{SZ} with mass, came up very recently with the availability of high quality SZ-data from new telescopes, such as the South Pole Telescope (SPT), Atacama Telescope Array (ACT) or in the framework of this work with APEX. Up to now only few publications exist that aim to derive a $Y_{SZ} - M$ scaling relation with a significant number of galaxy clusters, two of them utilize wide field imaging weak lensing masses.

Marrone et al. (2012) used weak lensing measurements based on the Subaru 8.2 m telescope and Y_{SZ} from the Sunyaev-Zel'dovich Array to perform a scaling relation analysis with 18 clusters at redshift $z \simeq 0.2$. A publication by Hoekstra et al. (2012) compare weak lensing derived masses with Y_{SZ} from BIMA (Bonamente et al., 2008) and the Planck Satellite (Planck Collaboration et al., 2011) or 18 and 19 clusters respectively.

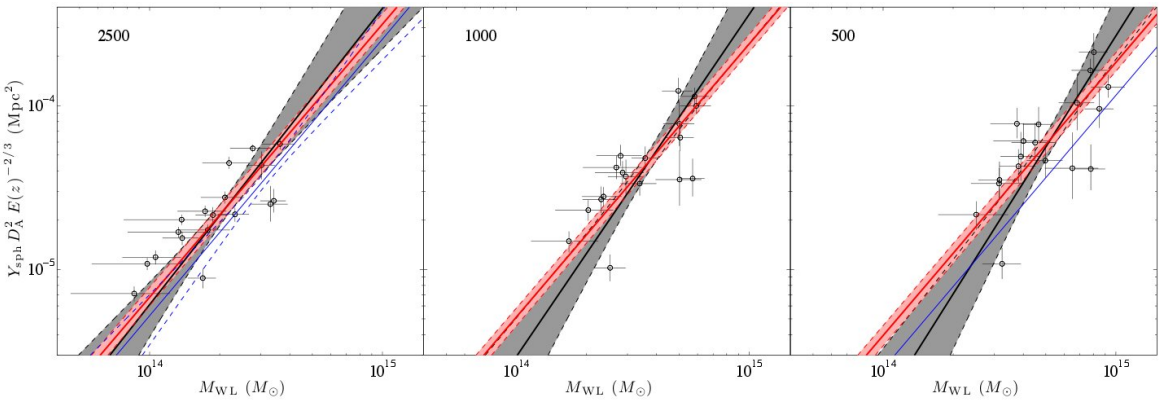

Figure 13: The $M_{WL} - Y$ scaling relation found by Marrone et al. (2012) for three different overdensities (indicated in the upper left corner). The best-fit line with a free slope parameter Bis shown in black, the best-fit relation with a fixed slope expected from self-similarity (B=3/5, see Equation (80)) is shown in red. The 1σ uncertainty regions are shaded and marked with dashed lines. Results from Bonamente et al. (2008) and Andersson et al. (2011) are indicated as thin blue lines in the left and the right plot respectively. Image from Marrone et al. (2012).

Recent results from the Planck Satellite (Planck Collaboration et al., 2013b) have shown that their measurements of σ_8 and Ω_m using SZ cluster measurements are only marginally consistent with the analysis of the primary CMB temperature anisotropies given in Planck Collaboration et al. (2013a). Figure 15 shows the 68% and 95% confidence contours in the $\sigma_8 - \Omega_m$ plane. The blue contours are using X-ray to SZ scaling relations and combining SZ-clusters with observations using baryonic acoustic oscillations (BAO) and big bang nucleosynthesis (BBN). Red shows the result using Planck CMB results. This tension can be solved by either allowing extensions to the standard ΛCDM model, for example certain

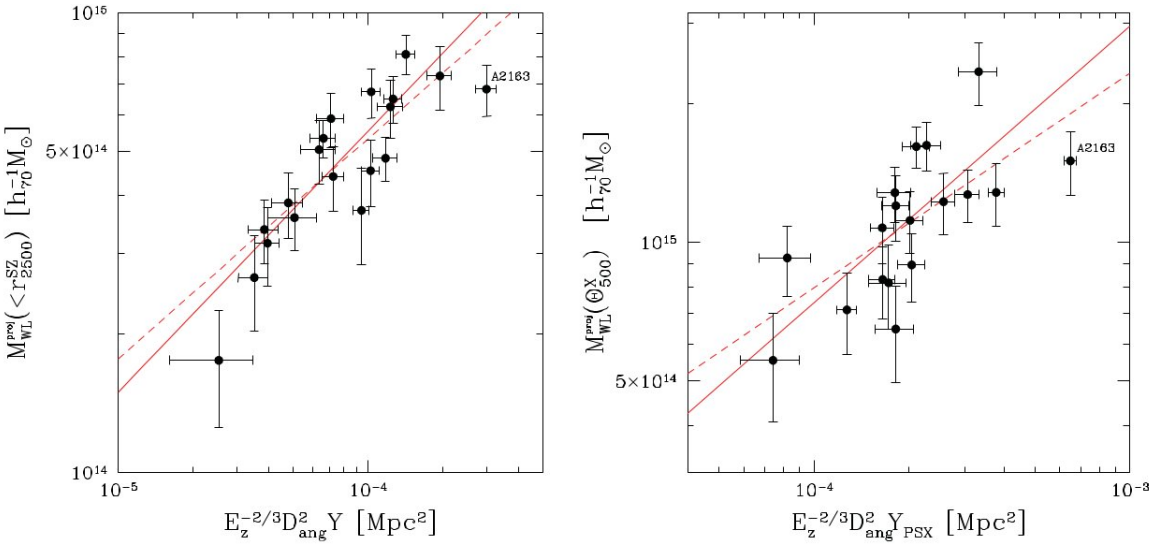

Figure 14: Left plot: The projected weak lensing mass as a function of the SZ signal. The mass is measured within an aperture of radius r^{SZ}_{2500} as determined by (Bonamente et al., 2008), based on a joint analysis of X-ray and SZ data. The solid red line indicates the best-fitting power-law model when the merging cluster A2163 (indicated) is excluded, whereas the dashed line is for the full sample. Right panel: Weak lensing mass within Θ^{X}_{500} as a function of projected Y from Planck Collaboration (Planck Collaboration et al., 2011). Image taken from Hoekstra et al. (2012).

neutrino mass, or allowing the mass bias introduced by deviation from hydrostatic equilibrium to be significantly higher than the expected value. The last point can be constrained by improved scaling relations where this thesis tries to contribute.

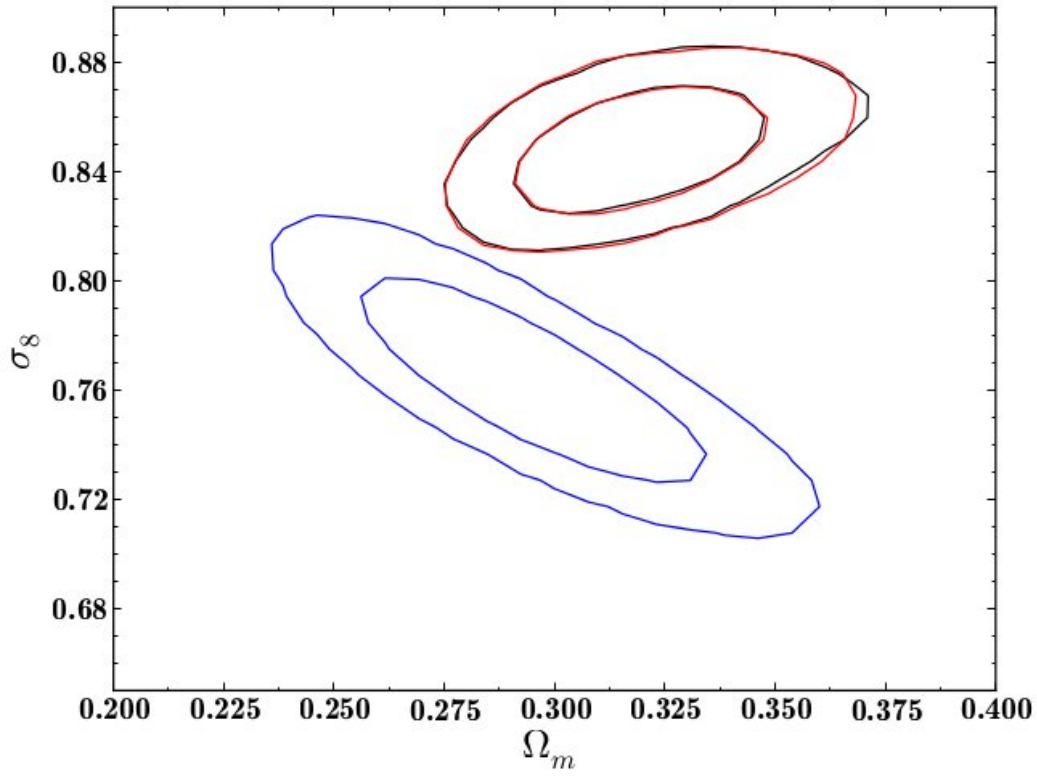

Figure 15: Planck results for Ω_m and σ_8. The likelihood contours for the analysis using CMB only are marked in red, results using SZ + BAO + BBN are marked in blue. The combined Planck CMB + SZ analysis where the mass bias is a free parameter are plotted in black. Image from Planck Collaboration et al. (2013a).

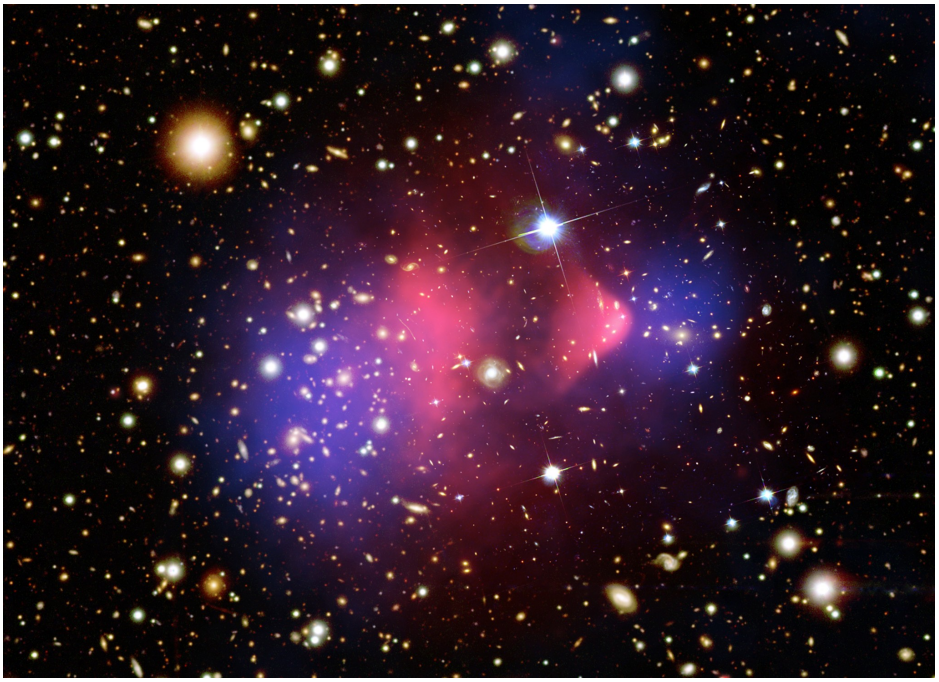

Figure 16: Mass (blue) and gas (pink) distribution of the Bullet Cluster using X-ray for gas and weak lensing for mass distribution. Image from Clowe et al. (2006).

3.2.3 *Gas vs. dark matter distribution*

Merging clusters of galaxies are one of the most energetic processes in the universe. These events are believed to be an important source of heating of the ICM, the energy source for the radio halos and may also influence the galaxy evolution and star formation rate of the member galaxies.

One of the most fundamental insights they give is related to the existence of dark matter and its self interaction cross-section. If two clusters merge with a small impact parameter, they fly basically through each other unless virialization takes place and the merger system builds one virialized object. During this encounter the different constituents of the cluster feel different amounts of pressure. Where dark matter and galaxies feel almost no pressure, except of the gas inside the galaxies, the hot plasma of the ICM feel significant amount of pressure. As a result the gas and the dark matter become separated from each other. If the initial conditions of the merger can be constrained in sufficient way, one can estimate the probability that dark matter particles scatter with each other.

The number of clusters on which this method can be applied is limited since the merger has to be observed at a time after the first encounter but before the gas can stream back to the dark matter dominated potential. Additionally the merger has to be seen roughly in the plane of the sky to allow the parameters of the merger to be sufficiently well constrained. For these reasons the number of known clusters with gas offsets compared to the DM distribution is small, on the order of 10. Three prominent systems where those studies where applied, are also part of the cluster sample presented in this thesis, the Bullet Cluster, A2744 and A520. The Bullet cluster was used to put the tightest constrains on dark matter self-interaction cross-section (Clowe et al., 2006). In thesis I will present two additional candidates, which might have the potential to be of similar importance to the already studied ones.

4

GRAVITATIONAL LENSING

From GR, we interpret that the energy-momentum tensor of matter affects space-time and that light rays, which are following null geodesics $ds^2 = 0$, do not necessarily follow straight lines in 3-space. Or in other words, gravitational fields bend light rays.

The idea that light is bend by gravitational forces is not special to GR. Also in classical Newtonian physics, the deflection of light can be calculated, if one assumes that light consists of massive particles. The deflection angle calculated in GR differs from the classical value by a factor of two. The measured deflections of stars close to the Sun, observed during the ellipse 1919 by Eddington, impressively supported the theory of GR.

There is a huge number of different techniques and applications, which uses the deflection of light by gravitational potentials. The focus of this thesis lies on weak gravitational lensing caused by galaxy clusters, therefore other aspects of gravitational lensing may remain unmentioned or are only briefly discussed. We refer the interested reader to Schneider (2006c,b), where this section is also based on, for a more complete overview in gravitation lensing.

4.1 DEFLECTION OF POINT SOURCES

Depending on the mass distribution, which creates the deflecting potential, as well as the position and shape of the lensed object can make the accurate treatment of the problem extremely difficult. It is therefore useful to start with a simple model, which assumes weak gravitational fields, such that $\Phi/c^2 \ll 1$ holds. Additionally we assume, that the extension of the deflecting potential in line of sight is small compared to the distance to the observer, as well as to the lensed source. This allows us to use the *thin lens* approximation, where the deflection is assumed to happen in a plane perpendicular to the line of sight, at the distance of the lens.

The geometry of the problem is shown in Figure 17. As distance measure we use here the angular diameter distance as defined in Eq. (38) reflecting the situation that we work with cosmological distances. For lensing on stars, such as the sun, other distance measures have to be used.

We use here the angular diameter distance D_s for the distance between observer and deflected source, D_d the distance from observer to the deflecting potential and D_ds is the distance from the deflector to the source as calculated with Equation (39).

The true, or unlensed position, of the source is $\boldsymbol{\beta} = \boldsymbol{\eta}/D_\mathrm{s}$, where the deflected or observed position is at $\boldsymbol{\theta} = \boldsymbol{\xi}/D_\mathrm{s}$. Here the positions $\boldsymbol{\beta}$ and $\boldsymbol{\theta}$ are in celestial coordinates with respect to the line of side axis, and $\boldsymbol{\eta}$ and $\boldsymbol{\xi}$ are vectors in the source and the deflector plane respectively.

The difference between observed and true position can be expressed in form of the *deflection angle*, $\hat{\boldsymbol{\alpha}}(D_\mathrm{d}\boldsymbol{\theta})$. In the limit of a small deflection angle we get

$$\boldsymbol{\beta} = \boldsymbol{\theta} - \frac{D_\mathrm{ds}}{D_\mathrm{s}}\hat{\boldsymbol{\alpha}}(D_\mathrm{d}\boldsymbol{\theta}), \tag{82}$$

or expressed using the *scaled deflection angle* $\boldsymbol{\alpha}(\boldsymbol{\theta}) := \frac{D_\mathrm{ds}}{D_\mathrm{s}}\hat{\boldsymbol{\alpha}}(D_\mathrm{d}\boldsymbol{\theta})$

$$\boldsymbol{\beta} = \boldsymbol{\theta} - \boldsymbol{\alpha}(\boldsymbol{\theta}). \tag{83}$$

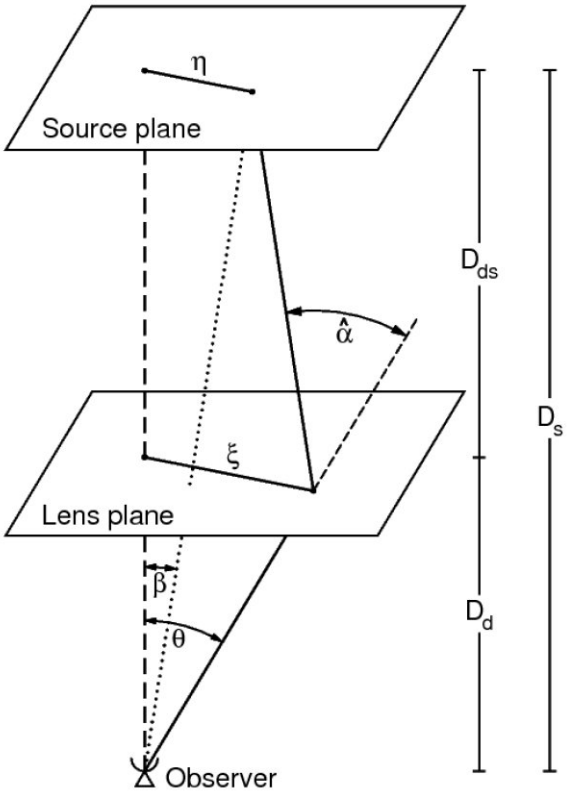

Figure 17: Sketch of the geometry in the thin lens scenario. The light source with distance $\boldsymbol{\eta}$ from the optical axis and D_s from the observer gets deflected by a potential at distance D_d at impact parameter $\boldsymbol{\xi}$ by the angle $\hat{\boldsymbol{\alpha}}$ and appears at position $\boldsymbol{\theta}$) while the true position is $\boldsymbol{\beta}$. Figure from Schneider (2006b).

This equation, connecting true and observed postion via the deflection angle, is called *lens equation* and is of central importance in lensing theory. The deflection angle contains the scaling with D_{ds}/D_s, which is a central factor that has to be derived in lensing measurements.

We assume a mass distribution $\rho(\boldsymbol{\xi}, z)$ expressed as a function of the two dimensional vector $\boldsymbol{\xi}$ in the lens plane and the position z, perpendicular to the lens plane. Based on the thin lens approximation, where we assume that the deflection happens only in the lens plane, we can express the deflecting potential via the *surface mass density* $\Sigma(\boldsymbol{\xi}) = \int \rho(\boldsymbol{\xi}, z)\mathrm{d}z$. The deflection angle can than be expressed as

$$\hat{\boldsymbol{\alpha}}(\boldsymbol{\xi}) = \frac{4G}{c^2} \int \Sigma(\boldsymbol{\xi}') \frac{\boldsymbol{\xi} - \boldsymbol{\xi}'}{|\boldsymbol{\xi} - \boldsymbol{\xi}'|^2} \mathrm{d}\boldsymbol{\xi}'. \tag{84}$$

Outside a spherical symmetric mass distribution such as a star or a point mass with a mass M and an impact parameter $r = |\boldsymbol{\xi}|$ the deflection angle simplifies to

$$\hat{\alpha} = \frac{4GM}{c^2 r}, \tag{85}$$

or expressed in Schwarzschild radii ($R_S = 2GM/c^2$) it gets the well known form

$$\hat{\alpha} = \frac{2R_S}{r}. \tag{86}$$

Keep in mind that this formula was derived for weak gravitational fields and does not hold for impact parameters close to the Schwarzschild radius. A typical regime where this equation is valid, is the light deflection close to stellar objects, like the observations made by Eddington in 1919 or for microlensing effects (Wambsganss, 2006).

If a source is lying close to the optical axis and if the potential is steep enough the lensing effect produces multiple images of the source. A deeper investigation of Equation (83)

(Schneider, 2006c) showed that in first order approximation multiple images can be created if the surface mass density exceeds a critical value of

$$\Sigma_{\rm cr} := \left[\frac{4\pi G}{c^2}\frac{D_{\rm d}D_{\rm ds}}{D_{\rm s}}\right]^{-1}. \tag{87}$$

We can now express the surface mass density in terms of the critical surface mass density

$$\kappa(\boldsymbol{\theta}) := \frac{\Sigma(D_{\rm d}\boldsymbol{\theta})}{\Sigma_{\rm cr}}. \tag{88}$$

This dimensionless parameter is called *convergence*, and allows to distinguish between the two regimes of multiple images $\kappa(\boldsymbol{\theta}) > 1$ and the regime where only one solution of Eq.(83) exist. The first regime is usually referred as *strong lensing* regime where else for $\kappa(\boldsymbol{\theta}) \ll 1$ is referred as weak lensing regime. We will discuss these regimes and the transition between both regimes in the following section.

For a axis symmetric mass distribution, we can define a characteristic radius where the mean surface mass density equals the critical surface mass density

$$\theta_{\rm E} = \left(\frac{4GM(\theta < \theta_{\rm E})}{c^2}\frac{D_{\rm ds}}{D_{\rm d}D_{\rm s}}\right)^{1/2}. \tag{89}$$

This radius is called *Einstein radius*. A source placed on the optical axis at distance $D_{\rm s}$ would result in an ring image with a radius of $\theta_{\rm E}$.

Beside of using the two dimensional surface mass density, we can consequently define the two dimensional *lensing potential*, $\psi(\boldsymbol{\theta})$, as analogue to the three dimensional gravitational potential $\Phi(\boldsymbol{\xi}, z)$. In terms of the normalized surface density κ we get

$$\psi(\boldsymbol{\theta} = \frac{1}{\pi}\int \kappa(\boldsymbol{\theta'}) \ln|\boldsymbol{\theta} - \boldsymbol{\theta'}| {\rm d}\boldsymbol{\theta'}. \tag{90}$$

The analogs of the Newton's second law and the Poisson equation are connected to the normalized deflection angle and the convergence as

$$\begin{aligned} \nabla\psi(\boldsymbol{\theta}) &= \hat{\boldsymbol{\alpha}}(\boldsymbol{\theta}), \\ \nabla^2\psi(\boldsymbol{\theta}) &= 2\kappa(\boldsymbol{\theta}). \end{aligned} \tag{91}$$

4.2 EXTENDED SOURCES AND GRAVITATIONAL SHEAR

So far we have only considered effects visible for point sources. In the case of extended sources additional effects become visible. Focusing on the weak lensing regime, one can assume that the lensing potential ψ does not change significantly over the typical size of an source image. Thus we can use the first-order result of the Taylor Expansion of Eq.(83), giving the linearized lens equation

$$\boldsymbol{\beta} - \boldsymbol{\beta_0} = \mathcal{A}(\boldsymbol{\theta_0}) \cdot (\boldsymbol{\theta} - \boldsymbol{\theta_0}). \tag{92}$$

The lens mapping can be expressed via the Jacobian matrix $\mathcal{A}(\boldsymbol{\theta})$, which is defined as

$$\mathcal{A}(\boldsymbol{\theta}) = \frac{\partial\boldsymbol{\beta}}{\partial\boldsymbol{\theta}} = \left(\delta_{ij} - \frac{\partial^2\psi(\boldsymbol{\theta})}{\partial\theta_i.\partial\theta_j}\right). \tag{93}$$

The trace of the Jacobian is

$${\rm tr}\mathcal{A} = 2 - \Delta\psi = 2(1 - \kappa). \tag{94}$$

Subtracting the trace $\mathrm{tr}\mathcal{A}$ from $\mathcal{A}$ gives the trace free shear matrix

$$\Gamma_{ij} := \mathcal{A} - \frac{\delta_{ij}}{2}\mathrm{tr}\mathcal{A} = \kappa\delta_{ij} - \psi_{,ij}, \tag{95}$$

where the common notation $\psi_{,ij:} = \frac{\partial^2\psi(\boldsymbol{\theta})}{\partial\theta_i\partial\theta_j}$ is used. Using the substitution $\gamma_1 = (\psi_{,11} - \psi_{,22})/2$ and $\gamma_2 = \psi_{,12}$, we get the following shape of the shear matrix of

$$\Gamma = -\begin{pmatrix} \gamma_1 & \gamma_2 \\ \gamma_2 & -\gamma_1 \end{pmatrix}. \tag{96}$$

Using $\kappa = (\psi_{,11} + \psi_{,22})/2$ we can rewrite the Jacobian matrix expressed in convergence and shear

$$\mathcal{A} = \begin{pmatrix} 1 - \kappa - \gamma_1 & -\gamma_2 \\ -\gamma_2 & 1 - \kappa + \gamma_1 \end{pmatrix}. \tag{97}$$

This showed, that we can decompose the Jacobian into an isotropic part, describing an isotropic stretching of the source and in an anisotropic part describing the distortion of the image. The distributions γ_1 and γ_2 can be interpreted as the real and the imaginary part of complex shear

$$\gamma := \gamma_1 + \mathrm{i}\gamma_2 = |\gamma|\mathrm{e}^{2\mathrm{i}\phi}. \tag{98}$$

As mentioned in the introduction of this chapter, lensing describes the deflection of photons, as such it does not change the energy or the total number of photons emitted by the source[1]. Additionally surface brightness of a source is conserved under the lens equation Eq.(83). Assuming the bolometric surface brightness $I = S/\mathrm{d}\omega$ the lens mapping according to Eq.(92) gives

$$I(\boldsymbol{\theta}) = I^{(\mathrm{u})}[\boldsymbol{\beta}(\boldsymbol{\theta})] = I^{(\mathrm{u})}[\boldsymbol{\beta}_0 + \mathcal{A}(\boldsymbol{\theta}_0)\cdot(\boldsymbol{\theta} - \boldsymbol{\theta}_0)], \tag{99}$$

where the superscript (u) denotes the "unlensed" quantity as it would be observed under the absence of the lens. The result is an enlarged image due to the convergence and distortion that transforms a circular extended source into elliptical lensed image. To investigate this deeper, we rewrite the Jacobian matrix using the *reduced complex shear* $g(\boldsymbol{\theta}) = \gamma(\boldsymbol{\theta})/(1 - \kappa(\boldsymbol{\theta})$ to

$$\mathcal{A}(\boldsymbol{\theta}) = (1 - \kappa(\boldsymbol{\theta}))\begin{pmatrix} 1 - g_1(\boldsymbol{\theta}) & -g_2(\boldsymbol{\theta}) \\ -g_2(\boldsymbol{\theta}) & 1 + g_1(\boldsymbol{\theta}) \end{pmatrix}. \tag{100}$$

In weak lensing regime we can calculate the magnification μ of the source via the determinant of the Jacobian matrix as follows

$$\mu = \frac{1}{\det\mathcal{A}} = \frac{1}{(1-\kappa)^2 - |\gamma|^2}. \tag{101}$$

The lens mapping results in an change of the size of the image of a factor $1/[(1-\kappa)(1-|g|)]$ in one direction and $1/[(1-\kappa)(1+|g|)]$ in the perpendicular direction in the image plane. This results in an axis ratio assuming a circular unlensed image of $r = (1-|g|)/(1+|g|)$. As will be shown in the next section, the semi-major axis will be aligned tangential for

1 The thin lens approximation exclude the case of an observer within the deflecting potential. Else photons would appear gravitational blue shifted.

spherical symmetric mass distribution. The magnification of the source together with the conserved surface brightness, results in an increase of the total flux by a factor μ compared to the unlensed image.

Between the weak lensing and strong lensing regime, there exist an transition range where lens properties κ and γ change significantly over the size of the lensed image. Here the next higher order Taylor Expansion of the lens equation Eq.(83) becomes important. This regime is called *gravitational flexion* and the distorted image becomes arc like shaped.

4.3 MASS MEASUREMENT VIA WEAK GRAVITATIONAL LENSING

In the previous section we discussed the effects on a source image, caused by a deflecting gravitational potential. In this section we move on and define observables, identify limitations and describe methods to measure the mass of galaxy clusters.

First, we have to clarify what type of source we can use as source, if we want to probe the potential of a galaxy cluster. Since galaxy clusters are at cosmological distances, we need sources that are observable at larger distances. In principle we can split these sources in extended and point-like sources. Observable sources at that distances, which can be treated as point-like sources are AGNs, supernovae and gamma-ray bursts. Examples for extended sources are galaxies and the CMB. Beside the fact that the listed point sources are not as abundant as normal galaxies, for typical observation times, point sources can only offer the magnification effect as an observable. Extended sources additionally offer the distortion of the image as observable. This, and the ease to obtain sufficient high number densities of sources, make galaxies the major type of source for lensing observations.

However, galaxies are not a perfect source for weak lensing. Galaxies differ in shape, size and color. Additionally they are not uniformly distributed in the sky, but built structures such as clusters, filaments and voids. Also the distribution itself is different for different galaxy types, resulting in a different abundance of spiral galaxies in galaxy clusters compared to filaments.

Since the unlensed properties of each single galaxy such as size, shape or brightness is unknown one has to use an ensemble of galaxies, where its mean properties are known. Examples of such observables are the mean ellipticity, mean size, mean brightness or mean source density. The error on the observable is not only driven by the quality of measurements for the single galaxies, but is also driven by the intrinsic scatter of the observable. Schneider et al. (2000) has shown that using the ellipticity of sources offer the highest signal to noise for similar deep observations.

Beside the possibility to use several observables at the same data (Umetsu et al., 2011), most publications on lensing use only shape measurements. This might be related to expected signal to noise difference between the different methods, but could also be partially the result of the well tested and implemented methods for shape measurements compared to the other methods.

In this thesis the focus is also on the shape measurement method but a potential use of magnification related methods will be also discussed at a later point.

4.3.1 *Shape estimator and reduced shear*

Galaxies can have various shapes and are in general not simple spheres. To measure their shapes, simple elliptical models will fail to describe the shape in a sufficient way. This problem gets even worse if one thinks about small, noisy and pixelized images of galaxies, which will build the majority of the available background galaxies.

One possibility to solve this problem is to describe the light distribution of a galaxy by its brightness moments. The first two moments of a brightness distribution $I(\boldsymbol{\theta})$ are defined as such

$$\begin{aligned} I_{(1)} :&= \bar{\boldsymbol{\theta}} = \frac{\int \boldsymbol{\theta}\, W(I(\boldsymbol{\theta}))\, I(\boldsymbol{\theta})\, \mathrm{d}^2\boldsymbol{\theta}}{\int W(I(\boldsymbol{\theta}))\, I(\boldsymbol{\theta})\, \mathrm{d}^2\boldsymbol{\theta}}, \\ I_{(2)} :&= Q = Q_{ij} = \frac{\int (\theta_i - \bar{\theta}_i)(\theta_j - \bar{\theta}_j)\, W(I(\boldsymbol{\theta}))\, I(\boldsymbol{\theta})\, \mathrm{d}^2\boldsymbol{\theta}}{\int W(I(\boldsymbol{\theta}))\, I(\boldsymbol{\theta})\, \mathrm{d}^2\boldsymbol{\theta}}. \end{aligned} \tag{102}$$

Here $W(I(\boldsymbol{\theta}))$ is a weight function and $I_{(1)}$ defines the galaxy image center $\bar{\boldsymbol{\theta}} = (\bar{\theta}_1, \bar{\theta}_2)$. The second brightness moment is a rank 2 tensor with $i, j \in 1, 2$.

Using the second brightness moments allows us to define ellipticity estimators. Currently there are two definitions widely used in weak lensing, the first one ϵ is preferentially used in theory while the second one χ is more used in practical implementations. Both are defined via the minor to major axis ratio $r = b/a$ and the angle φ of the semi-major axis, and are defined as polars such as

$$\begin{aligned} \epsilon &= \frac{1-r}{1+r} \exp(2i\varphi), \\ \chi &= \frac{1-r^2}{1+r^2} \exp(2i\varphi). \end{aligned} \tag{103}$$

Expressed with the second order brightness moments we get

$$\begin{aligned} \epsilon :&= \frac{Q_{11} - Q_{22} + 2iQ_{12}}{Q_{11} + Q_{22} + 2\sqrt{Q_{11}Q_{22} - Q_{12}^2}}, \\ \chi :&= \frac{Q_{11} - Q_{22} + 2iQ_{12}}{Q_{11} + Q_{22}}. \end{aligned} \tag{104}$$

As one can see, both definitions are quite similar and are also resulting in similar behavior with respect to φ, but with different normalizations.

The second order brightness moments transform under the lens mapping as $Q^{(\mathrm{u})} = \mathcal{A}Q\mathcal{A}$. For the reduced shear this yields the following equations:

$$\epsilon = \begin{cases} \frac{\epsilon^{(\mathrm{u})} + g}{1 + g^* \epsilon^{(\mathrm{u})}} & |g| \leq 1 \\ \\ \frac{1 + g\epsilon^{(\mathrm{u})*}}{\epsilon^{(\mathrm{u})*} + g^*} & |g| > 1 \end{cases} \tag{105}$$

and

$$\chi = \frac{\chi^{(\mathrm{u})} + 2g + g^2 \chi^{(\mathrm{u})*}}{1 + |g|^2 + 2\mathcal{R}e(g\chi^{(\mathrm{u})*})} \tag{106}$$

Here the index (u) denotes the unlensed property of the source. For weak lensing only the case $|g| \leq 1$ is relevant, while $|g| > 1$ gets important in the strong lensing regime. Due to the assumption that the intrinsic ellipticities of a sample of galaxies are randomly distributed, the expectation values of χ and ϵ are vanishing

$$\mathcal{E}\left(\chi^{(\mathrm{u})}\right) = \mathcal{E}\left(\epsilon^{(\mathrm{u})}\right) = \mathbf{0}. \tag{107}$$

Seitz and Schneider (1997) could show, that inserting this assumption into Eq.(105) results in the simple relation between expectation value and shear

$$\mathcal{E}(\epsilon) = \begin{cases} g & |g| \leq 1 \\ 1/g^* & |g| > 1 \end{cases}. \tag{108}$$

The noise of the observable can be estimated from the dispersion of the intrinsic ellipticities

$$\sigma_\epsilon = \sqrt{\frac{1}{2N}\sum_{i=1}^{N}(\epsilon_{1,i}^2 + \epsilon_{2,i}^2)}. \tag{109}$$

where ϵ_1 and ϵ_2 are the two components of the polar ϵ. For χ the analog of Eq.(108) is more complex, which is the reason why ϵ is preferred in theory. The code that is used for the shape measurements in this thesis uses χ, which is partially related to the older roots of this code as well as it does not need a case distinction that would be needed for ϵ.

The intrinsic scatter in ellipticity is usually an order of magnitude higher than the lensing induced shear. This is the major reason why a large number of galaxies have to be measured to estimate the shear signal from galaxy shapes. Additionally to that, the shape measurement itself has inaccuracies, which increase the needed number of galaxies for shear measurements. The assumption that the ellipticities of galaxies are randomly oriented can locally be violated as shown in Joachimi and Schneider (2009). In case of massive structures such as clusters, this effect is sub-dominant for the overall mass estimate, since the background sources that are used to derive the cluster mass are distributed over a large area, which suppresses the influence of intrinsic alignment.

In contrast to that, convergence maps use galaxies within a certain characteristic angular distance, which is typically smaller than that used to interfere the total cluster mass. Therefore the convergence map can locally be affected by intrinsic alignment.

4.3.2 *Tangential Shear and Aperture Mass*

For an axial symmetric lensing potential, the deflection of a source image has also to be axial symmetric. Therefore the lens equation (Eq.(83)) reduces to the one dimensional form $\beta = \theta - \alpha(\theta) = \theta[1 - \bar{\kappa}(\theta)]$, where $\bar{\kappa}(\theta)$ is the mean convergence within a distance θ from the center. Using the Jacobian matrix, we can find the following connection between shear and convergence

$$\gamma(\boldsymbol{\theta}) = [\kappa(\theta) - \bar{\kappa}(\theta)]e^{2i\tilde{\varphi}}. \tag{110}$$

Here $\tilde{\varphi}$ is the phase angle of the complex representation of $\boldsymbol{\theta}$ as $\theta e^{i\tilde{\varphi}}$.

One can find, that for sources that are lying on the θ_1 axis are sheared along the perpendicular (θ_2) axis, by solving the Eigenvalue problem of the Jacobian matrix for the sub-critical regime. Due to the rotation symmetry one can conclude that sources get elongated along the tangential direction.

We can now decompose the shear into a tangential and a cross component with respect to the phase angle φ in a polar coordinate system

$$\gamma_+ = -\mathcal{R}e(\gamma\, \mathrm{e}^{-2i\varphi}), \qquad \gamma_\times = -Im(\gamma\, \mathrm{e}^{-2i\varphi}). \tag{111}$$

The minus ensures that the source get stretched tangentially for $\gamma_+ > 0$ and radially for $\gamma_+ < 0$. Since shear is a polar, the cross component has to vanish $\gamma_\times = 0$. The cross shear correspond to a rotation of 45 degrees or $\pi/4$ with respect to the tangential direction.

In the case of an axially symmetric lensing potential, we therefore observe a tangential shear pattern but a vanishing cross component. The same behavior is also valid for the actual observable, the reduced shear g, which can be decomposed in the same way into tangential and cross components. Also the ellipticity estimators χ and ϵ are defined as polars and can be decomposed in the same way.

For more general lens potentials Equation (110) gets only slightly modified (Bartelmann, 1995) and turns to

$$\langle \gamma_+ \rangle = \bar{\kappa} - \langle \kappa \rangle. \tag{112}$$

Here $\langle \gamma_+ \rangle$ and $\langle \kappa \rangle$ are the averages along a circle of radius θ and $\bar{\kappa}$ is the average within the circle.

This shows that using the tangential shear is still useful for more general potentials and motivates the *aperture mass* (Schneider, 1996), a filtered estimate of the shear around a central point $\boldsymbol{\theta}_c$. The aperture mass is defined as

$$M_{ap}(\boldsymbol{\theta}_c) = \int_0^{\theta_{ap}} \kappa(\boldsymbol{\theta}) U(|\boldsymbol{\theta} - \boldsymbol{\theta}_c|)\, d\boldsymbol{\theta} = \int_0^{\theta_{ap}} \gamma_+(\boldsymbol{\theta} - \boldsymbol{\theta}_c) Q(|\boldsymbol{\theta} - \boldsymbol{\theta}_c|)\, d\boldsymbol{\theta}. \tag{113}$$

The filter functions $U(\theta)$ and $Q(\theta)$ have to satisfy the following conditions

$$\begin{aligned} 0 &= \int_0^{\theta} \theta' U(\theta') d\theta' \,, \\ Q(\theta) &= \frac{2}{\theta^2} \int_0^{\theta} \theta' U(\theta') d\theta' - U(\theta). \end{aligned} \tag{114}$$

It can be used to obtain a lower bound of the mass within a an aperture θ_{ap} (Kaiser et al., 1995).

The aperture mass can be converted to the aperture mass signal-to-noise or S-statistic. This is a useful tool to evaluate the detection significance or, as used in this thesis, as a diagnostic tool for the optimization of the detection. The S-statistic is a discretized version of the aperture mass divided by the noise, and is defined as

$$S_{\vec{\theta}_{ap}}(\theta_c) = \frac{\sqrt{2}}{\sigma_\epsilon} \frac{\sum_i \epsilon_{+,i}\, Q_i(|\boldsymbol{\theta}_i - \boldsymbol{\theta}_c|)}{\sqrt{\sum_i Q_i^2(|\boldsymbol{\theta}_i - \boldsymbol{\theta}_c|)}}. \tag{115}$$

The sum in the equation above runs over all galaxies i with tangential ellipticity $\epsilon_{+,i}$ at position $\boldsymbol{\theta}_i$ within the aperture θ_{ap}.

As we learned in the sections before, the amount of the image deformation does not only depend on the deflecting potential but also on the geometry of the lens configuration and especially on the angular diameter distance ratio D_{ds}/D_s. Therefore the expected lensing signal from gravitational potential imprinted in an ensemble of galaxies depends on the mean distance ratio $\langle D_{ds}/D_s \rangle$.

4.3.3 *Convergence Map and Finite-Field Inversion*

From measuring the S-statistic or the aperture mass at a certain postion $\boldsymbol{\theta}_c$ to making a map by measuring the quantity at a grid is a short step. Such S-statistics maps are used in this thesis to investigate the lensing signal.

To produce convergence maps, we use the Seitz and Schneider finite-field inversion (Seitz and Schneider, 1996), which is based on the Kaiser and Squires (Kaiser and Squires, 1993) inversion. Kaiser and Squires found that the shear field of an arbitrary matter distribution, which is described as

$$\gamma(\boldsymbol{\theta}) = \frac{1}{\pi} \int_{\mathbb{R}^2} \mathcal{D}(\boldsymbol{\theta} - \boldsymbol{\theta}') \kappa(\boldsymbol{\theta}')\, d^2\boldsymbol{\theta}' \,, \quad \mathcal{D}(\boldsymbol{\theta}) = -\frac{1}{(\theta_1 - i\theta_2)^2}, \tag{116}$$

can be inverted using Fourier transforms to yield,

$$\kappa(\boldsymbol{\theta}) = \kappa_0 + \frac{1}{\pi} \int_{\mathbb{R}} \mathcal{R}e[\mathcal{D}^*(\boldsymbol{\theta} - \boldsymbol{\theta}')\, \gamma(\boldsymbol{\theta}')] d\boldsymbol{\theta}' \,. \tag{117}$$

Under the restriction of the strict weak lensing limit $\kappa \ll 1$, such that $g \approx \gamma$ holds, the observed reduced shear can be used to reconstruct the mass distribution. The direct convolution suffers from the assumption of a infinitely well sampled and infinite large field, which is certainly not the case for realistic observations. It also shows that the convergence can only be recovered up to an constant κ_0. This is the so-called *mass-sheet* degeneracy, which leaves the reduced shear unchanged under the transformation

$$(1-\kappa) \to \lambda(1-\kappa), \quad \gamma \to \lambda\gamma. \tag{118}$$

This problem can be solved by including an additional observable probing κ or γ in a different way, such as magnification observables.

There are several methods to overcome the problems that arise by the direct inversion. The method used here is based on finite-field inversion and express the problem in terms of $K(\boldsymbol{\theta}) = \ln[1-\kappa(\boldsymbol{\theta})]$ as a von Neumann problem of the finite data field $\mathcal{U}$, which is defined by the condition of its value on the boundary $\partial\mathcal{U}$

$$\nabla^2 K = \nabla \mathbf{u}_\mathrm{g}\,, \quad \text{with} \quad \mathbf{n}\cdot\nabla K|_{\partial\mathcal{U}} = \mathbf{n}\cdot\mathbf{u}_\mathrm{g}, \tag{119}$$

where $\mathbf{n}$ is a normal vector and $\mathbf{u}_\mathrm{g} = \nabla K$ is,

$$\mathbf{u}_\mathrm{g} = -\frac{1}{1-g_1^2-g_2^2}\begin{pmatrix} 1-g_1 & -g_2 \\ -g_2 & 1+g_1 \end{pmatrix}\begin{pmatrix} g_{1,1}+g_{2,2} \\ g_{2,1}-g_{1,2} \end{pmatrix}\,. \tag{120}$$

While it is in principle possible to measure the mass of galaxy clusters based on convergence maps, this method is used in this thesis only to map the general matter distribution.

This has several reasons, the distortions due to telescope optics and therefore their corrections are larger at the edge of the observed field, which can affect the mass reconstruction. The used implementation of the finite-field inversion is sensitive to holes in the data field. It also restricts on weak lensing limit $\kappa < 1$ that is partially violated in our fields because of observations of massive clusters. The used code does not include individual distance estimates of the observed galaxies, which leave additional information unused. This can partially be accounted by linearly rescaling g with $D_\mathrm{ds}/D_\mathrm{s}$ with respect to a reference distance ratio. Unfortunately this holds only for small values g and results in an systematical error with increasing convergence.

4.3.4 *NFW Model and Profile fitting*

Dark matter N-body simulations of structure formation have shown that dark matter halos follow well a density profile of,

$$\rho_\mathrm{NFW} = \frac{\delta_\mathrm{c}\rho_\mathrm{c}}{x(1+x)^2} \quad \text{with } x = \frac{r}{r_\mathrm{s}}\,, \tag{121}$$

out to the virial radius (Navarro et al., 1996).

The mass of a halo with this profile is then

$$M(x) = 4\pi\delta_\mathrm{c}\rho_\mathrm{c}r_\mathrm{s}^3\int_0^x \frac{x'}{(1+x')^2}\mathrm{d}x' = 4\pi\delta_\mathrm{c}\rho_\mathrm{c}r_\mathrm{s}^3\left[\ln(1+x) - \frac{x}{1+x}\right]. \tag{122}$$

As one can see, this mass diverge for $x \to \infty$, which implies that the mass has to be measured within a characteristic radius. In Section 2.7.2, we discussed the spherical collapse model and found that dark matter halos can be characterized by a radius r_Δ, at which the mean density within this radius is Δ times the critical density ρ_c.

The scale radius r_s can be express in terms of the characteristic radius r_Δ and its corresponding concentration parameter c_Δ as

$$r_s = \frac{r_\Delta}{c_\Delta}. \tag{123}$$

We define the characteristic mass

$$M_\Delta = \Delta\rho_c \frac{4\pi}{3} r_\Delta^3. \tag{124}$$

Inserting Equation (123) in Eq.(122) and comparing with Eq.(124) shows, that the characteristic overdensity δ_c can then be expressed in terms of c_Δ as

$$\delta_c = \frac{\Delta}{3} \frac{c_\Delta^3}{\ln(1+c_\Delta) - c_\Delta/(1+c_\Delta)}. \tag{125}$$

The NFW profile depends essentially on only one parameter (e.g. the mass), but is usually fitted by the two parameters r_Δ and c_Δ.

The potential that arises from a NFW density profile can be projected to the lens plane to obtain the lensing potential $\psi(\boldsymbol{\theta})$, from which convergence and shear can be calculated.

Bartelmann(Bartelmann, 1996) has shown that the convergence of such a lensing potential can be written in terms of the dimensionless radial distance $x = D_d\theta/r_s$ as

$$\kappa_{NFW}(x) = \frac{2r_\Delta\delta_c\rho_c}{c_\Delta\Sigma_{cr}} \begin{cases} \frac{1}{x^2-1}\left[1 - \frac{2}{\sqrt{1-x^2}}\operatorname{arctanh}\left(\sqrt{\frac{1-x}{1+x}}\right)\right] & (x<1) \\ \frac{1}{3} & (x=1) \\ \frac{1}{x^2-1}\left[1 - \frac{2}{\sqrt{1-x^2}}\arctan\left(\sqrt{\frac{x-1}{1+x}}\right)\right] & (x>1) \end{cases}. \tag{126}$$

The shear can be derived from Eq. (110) using the convergence or directly from the lensing potential. Wright and Brainerd (2000) have shown that the shear can be described as

$$\gamma_{NFW}(x) = \frac{r_\Delta\delta_c\rho_c}{c_\Delta\Sigma_{cr}} \begin{cases} \left[\frac{4(3x^2-2)}{x^2(x^2-1)\sqrt{1-x^2}}\operatorname{arctanh}\left(\sqrt{\frac{1-x}{1+x}}\right) + \frac{4}{x^2}\ln\left(\frac{x}{2}\right) + \frac{2}{1-x^2}\right] & (x<1) \\ \left[\frac{10}{3} - 4\ln 2\right] & (x=1) \\ \left[\frac{4(3x^2-2)}{x^2(x^2-1)\sqrt{x^2-1}}\arctan\left(\sqrt{\frac{x-1}{1+x}}\right) + \frac{4}{x^2}\ln\left(\frac{x}{2}\right) + \frac{2}{1-x^2}\right] & (x>1) \end{cases}. \tag{127}$$

The reduced shear is then

$$g_{NFW}(x) = \frac{\gamma_{NFW}(x)}{1 - \kappa_{NFW}(x)}. \tag{128}$$

We are following a similar approach as described in Israel et al. (2010b) and derive the best fitting profile parameters r_{200} and c_{200} by minimizing the merit function

$$\chi^2 = \sum_{i=1}^{N} \frac{|g_i(\theta_i, \Sigma_{crit,i}; r_{200}, c_{NFW}) - \tilde{\varepsilon}_{t,i}(\theta_i)|^2}{\tilde{\sigma}_i^2 \left(1 - |g_i(\theta_i, \Sigma_{cr,i}; r_{200}, c_{NFW})|^2\right)^2}, \tag{129}$$

which is calculated on a regular grid in the r_{200}-c_{200} plane. Here $g_i(\theta_i, \Sigma_{crit,i}; r_{200}, c_{NFW})$ is the tangential reduced shear predicted by the NFW model with r_{200},c_{200} at position θ_i for a critical surface mass density $\Sigma_{cr,i}$. Here r_{200} corresponds to the radius within the enclosed mass density equals 200 times the critical density $\rho_c(z_d)$ at cluster redshift z_d. The modified tangential ellipticity $\tilde{\varepsilon}_{t,i}$ is the measured tangential ellipticity multiplied by

a global calibration factor $f_0 = 1.08$. The error $\tilde{\sigma}_i$ scales as $\tilde{\sigma}_i = f_0 \sigma_\varepsilon / \sqrt{2}$ where σ_ε is the dispersion of the measured ellipticities. Note that the sum in Eq. (129) is taken over all background galaxies, we therefore not apply a radial binning of the reduced shear.

In contrast to the original merit function used in Israel et al. (2010b), we are not assuming a source sheet with common Σ_{crit}. Instead, we use individual $\Sigma_{\text{crit},i}(\beta_i)$, based on the estimated angular diameter distance ratio $\beta_i = D_{\text{ds}}(z_{\text{d}}, z_i)/D_{\text{s}}(z_i)$ for each galaxy i.

This allows to avoid biases at higher reduced shear, where $g \approx \gamma$ and therefore $g \propto D_{\text{ds}}/D_{\text{s}}$ gets inaccurate. The profile fit stays limited to the weak lensing regime, because it still requires that the potential does not change significantly over the size of the source.

The mass is finally estimated by identifying the smallest χ^2 in the r_{200}-c_{200} plane and calculated via Equation (124).

Clusters of galaxies are usually not spherical symmetric but we use a large sample of clusters where the average profile can be assumed to be spherical symmetric. Note that this assumption only holds if the cluster selection does not depend on the orientation of the cluster.

Part III

THE APEX-SZ WEAK LENSING PROJECT

The following part of the thesis describes the scientific project, the data acquisition and reduction, and the analysis methods used to obtain the final results. The first chapter describes the cluster sample and the observing strategy. The following chapter the data reduction and the shear measurement pipeline. The last chapter in this part describes the background selection method based on the photometric properties in three optical broadband filters.

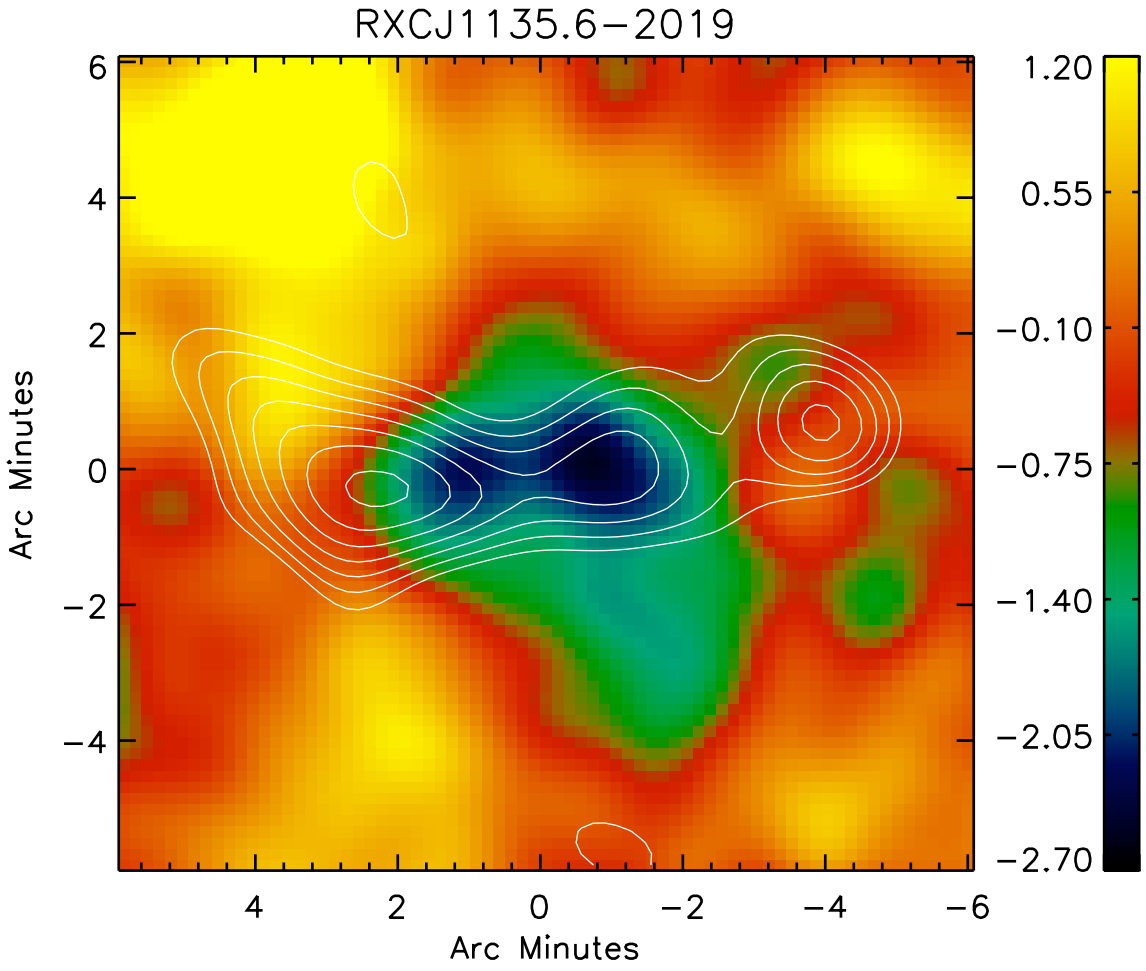

Figure 18: RXCJ1135: SZ-map from APEX-SZ with weak lensing convergence contours using WFI. The separation between the two cores is about 1.35 Mpc.

5

THE APEX-SZ WEAK LENSING FOLLOW-UP PROJECT

5.1 APEX AND APEX-SZ

Figure 19: The 12m APEX telescope at Llano Chajnantor, Chile.

APEX is acronym for Atacama Pathfinder EXperiment and is a 12 m submillimeter telescope designed for wavelengths between 0.2 mm and 2.0 mm. The telescope is located 5100 m above sea level, at Llano Chajnantor, Chile. Designed as a pathfinder experiment for the Atacama Large Millimeter Array (ALMA) telescope array, the APEX telescope is a modified prototype of the ALMA telescopes.

The Atacama Pathfinder EXperiment Sunyaev-Zel'dovich (APEX-SZ) instrument was a millimeter wavelength (150 GHz) cryogenic receiver for the APEX telescope. It was designed to observe galaxy clusters through the temperature decrement that arises from the Sunyaev-Zel'dovich Effect at this frequency. Consisting of 280 superconduction transition-edge sensor (TES) bolometers and a frequency-domain-multiplexed readout system it played a key role in the introduction of these technologies in astronomy.

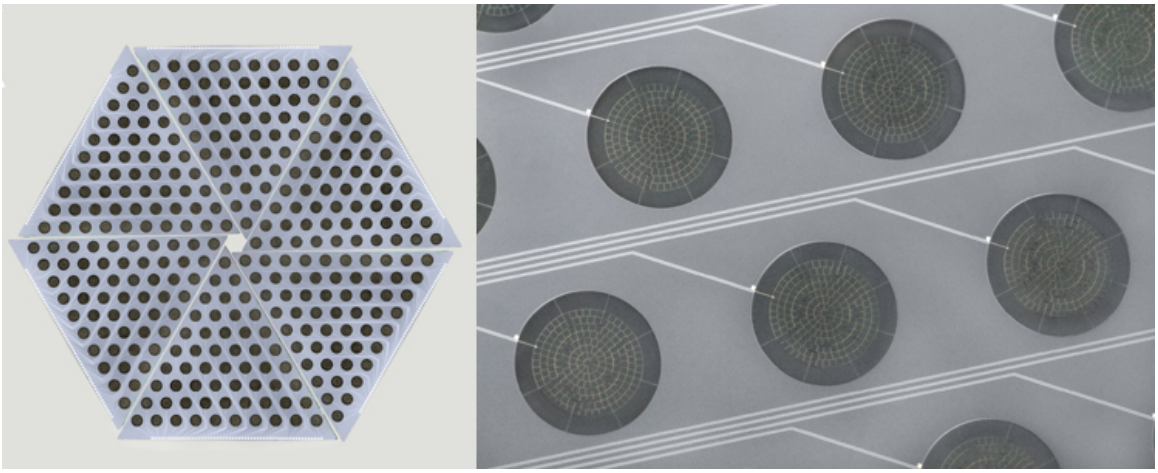

Figure 20: The APEX-SZ bolometer array (left). Zoom to the spider-web bolometers (right).

At 150 GHz, the Full Width at Half Maximum (FWHM) of the telescope optics is about 58 arcsecond and the instruments Field of View (FoV) is about 22 arcminutes. This allows to image the full SZE signal even for clusters at low redshift ($z \sim 0.1$).

5.1.1 *The APEX-SZ cluster sample*

The observation strategy with APEX-SZ was mainly focused on targeted observation of galaxy clusters. Almost 780 hours of observation time was spend on galaxy clusters, resulting in ~ 42 cluster detections. The cluster observation include the X-ray selected REFLEX-DXL sample (Zhang et al., 2004), as well as an even larger complete X-ray sample, extracted from the REFLEX-2 catalog (Boehringer et al., 2013) including the DXL sample that consists of 29 clusters. The selection in the $L_X - z$ plane can is shown in Figure 21.

A list of all clusters observed with APEX-SZ can be found in Table 1, showing the redshift, the total time spent on a cluster and an indication whether the cluster is considered as detected. The last entry additionally highlights detections that are only marginal significant. Comparing the non-detected with the detected clusters one can see, that the mean redshift is higher and the mean observation time is lower for the non detections. This explains partially why these clusters are not detected, but the detectability of a particular cluster also depends on its intrinsic properties and the observing conditions. Any unexplainable non-detection would be a source of concern and would have to be investigated.

None of our non detections rise serious concerns regarding this point, but the cluster RXCJ2011.3-5725 should be discussed in greater detail. Dedicated efforts were made to detect this cluster, as it is part of the X-ray selected sample. The total exposure time of 22.5 h should be enough for a detection, but half of it was observed under bad weather conditions, leaving this cluster a $\sim 2.5\sigma$ non detection. Data from the Chrandra X-ray satellite are too shallow to put constraints on cluster properties. Due to bad weather conditions and the presence of a bright star close to the cluster center have also prohibited to obtain lensing informations on this cluster. All this together makes it difficult to judge if this cluster should be detected or not.

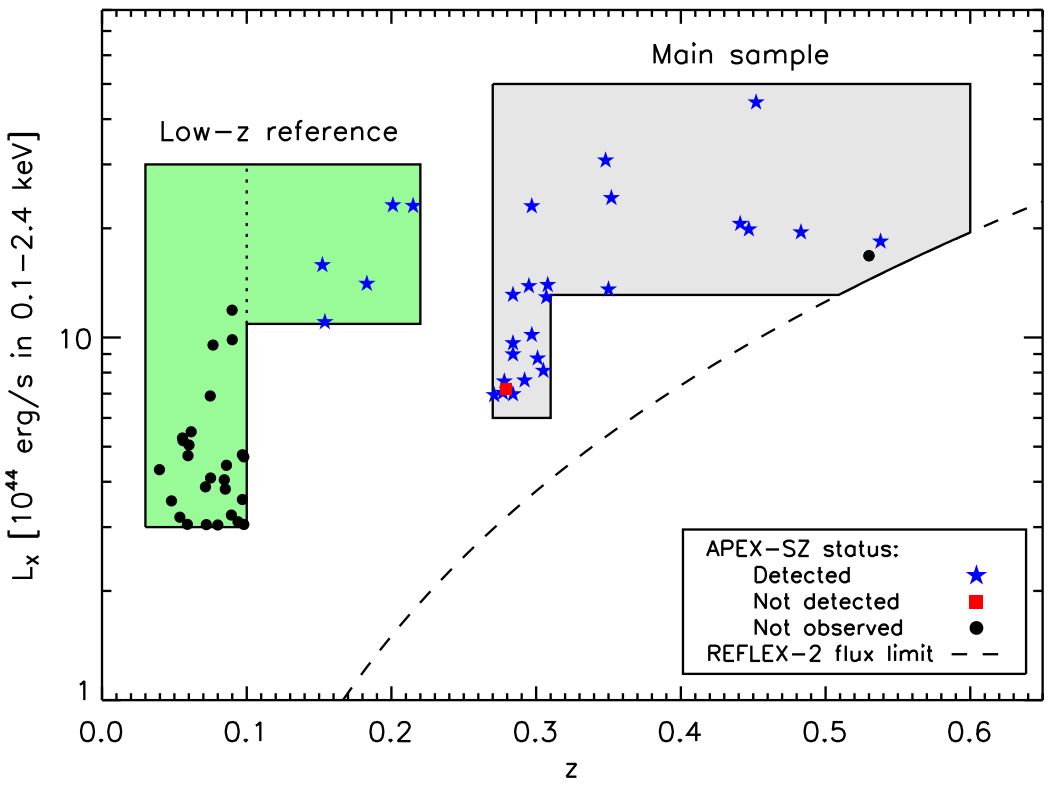

Figure 21: X-ray selection. Left box: low-redshift sample. Right box: Extended DXL sample. Image credit: F. Pacaud

Table 1: Cluster of galaxies observed with APEX-SZ at 150 GHz, sorted by right ascension and divided between detections and non-detections. Beside cluster names, the table shows the position (R.A., Dec.), the redshift (z), the time spent on the target in hours (time) and a classifier stating the detection status (detection). The detection status is dived in yes, no and marginal judged on the SZ maps kindly provided by M. Nord. Clusters marked with ($\star$) are part of the extended DXL sample.

Cluster	R.A.	Dec.	z	Time [h]	Detection	Ref.
A2744*	00:14:18.8	-30:23:00	0.307	22.2	yes	1
RXCJ0019.0 − 2026*	00:19:07.8	-20:27:21	0.277	8.5	yes	2
A2813*	00:43:24.4	-20:37:17	0.292	8.7	yes	3
A209	01:31:52.6	-13:36:37	0.206	8.9	marginal	2
XLSSC006	02:21:45.1	-03:46:19	0.429	43.3	yes	4
RXCJ0232.2 − 4420*	02:32:18.7	-44:20:41	0.284	8.7	yes	5
RXCJ0245.4 − 5302*	02:45:27.7	-53:02:10	0.302	13.1	yes	6
A383	02:48:03.6	-03:32:09	0.187	15.3	marginal	7
RXCJ0437.1 + 0043*	04:37:09.8	00:43:37	0.284	9.9	yes	8
MS0451.6 − 0305*	04:54:11.4	-03:00:52	0.539	8.3	yes	9
A520	04:54:19.0	02:56:49	0.199	21.8	yes	10
RXCJ0516.6 − 5430*	05:16:38.0	-54:30:51	0.295	26	yes	11

Continued on next page

Table 1 – continued from previous page

Cluster	R.A.	Dec.	z	Time [h]	Detection	Ref.
RXCJ0528.9 − 3927⋆	05:28:52.5	-39:28:16	0.284	20.7	yes	5
RXCJ0532.9 − 3701⋆	05:32:55.9	-37:01:35	0.275	22.2	yes	3
A3404	06:45:29.3	-54:13:08	0.167	14.1	yes	5
Bullet⋆	06:58:31.1	-55:56:49	0.297	11.5	yes	12
A907	09:58:21.1	-11:03:22	0.153	27	yes	13
RXCJ1023.6 + 0411	10:23:39.6	04:11:10	0.280	15.4	yes	14
MS1054.4 − 0321	10:56:58.0	-03:37:37	0.831	13.7	yes	15
MACSJ1115.8 + 0129⋆	11:15:52.1	01:29:53	0.348	17.5	yes	11
A1300⋆	11:32:00.7	-19:53:34	0.308	20.7	yes	10
RXCJ1135.6 − 2019⋆	11:35:36.8	-20:19:42	0.305	17	yes	16
RXCJ1206.2 − 0848⋆	12:06:12.2	-08:48:22	0.441	14.8	yes	11
XMMUJ1230.3 + 1339	12:30:16.9	13:39:04	0.980	23.7	marginal	17
MACSJ1311.0 − 0311	13:11:00.0	-03:11:00	0.494	25.6	yes	18
A1689⋆	13:11:29.5	-01:20:17	0.183	17.9	yes	10
RXJ1347 − 1145⋆	13:47:30.6	-11:45:12	0.451	10.2	yes	19
MACSJ1359.2 − 1929	13:59:10.3	-19:29:24	0.447	9.6	marginal	20
A1835	14:01:02.0	02:51:32	0.253	12.5	yes	10
RXJ1504⋆	15:04:07.7	-02:48:18	0.215	10.4	yes	21
A2163⋆	16:15:45.8	-06:08:55	0.203	12.7	yes	10
A2204⋆	16:32:45.7	05:34:43	0.152	20.3	yes	22
RXCJ2014.8 − 2430⋆	20:14:49.7	-24:30:30	0.160	10.1	marginal	23
RXCJ2151.0 − 0736⋆	21:51:01.2	-07:36:03	0.284	8.1	yes	16
A2390	21:53:34.6	17:40:11	0.228	5	marginal	10
MACSJ2214.9 − 1359⋆	22:14:59.0	-13:59:41	0.483	7.6	yes	24
XMMXCS*J*2215.9 − 1738	22:15:58.5	-17:38:03	1.450	11.8	yes	25
XMMUJ2235.3 − 2557	22:35:20.6	-25:57:42	1.390	37.1	marginal	26
MACSJ2243.3 − 0935⋆	22:43:20.8	-09:35:18	0.447	7.1	yes	27
RXCJ2248.7 − 4431⋆	22:48:54.3	-44:31:07	0.348	6.8	yes	11
A2537⋆	23:08:23.2	-02:11:31	0.297	15.5	yes	28
RXCJ2337.6 + 0016⋆	23:37:39.7	00:17:37	0.278	9.3	yes	14
Mean:			0.38	15.5		
Not detected:						
ZwCl0024 + 1652	00:26:35.6	17:09:44	0.39	1.4	no	29
RXCJ0956.4 − 1004	09:56:26.4	-10:04:12	0.17	10.7	no	30
XMMCJ0959	09:59:40.8	02:31:11	0.73	8.1	no	31
2XMM J122929.1 + 015131	12:29:29.2	01:51:26	0.98	3.4	no	32
RDCS1252.9 − 2927	12:52:54.4	-29:27:17	1.24	33.4	no	33
MACSJ1931.8 − 2635⋆	19:31:48.0	-26:35:00	0.35	9.4	no	18

Continued on next page

Table 1 – continued from previous page

Cluster	R.A.	Dec.	z	Time [h]	Detection	Ref.
RXCJ2011.3 − 5725*	20:11:23.1	-57:25:39	0.28	22.5	no	11
MACSJ2046.0 − 3430	20:46:00.5	-34:30:17	0.42	12.9	no	20
ACO S 1077	22:58:52.3	-34:46:55	0.31	16.6	no	34
RCSJ2319.9 + 0038	23:19:53.2	00:38:12	0.89	9.8	no	35
Mean:			0.58	12.82		

References:

(1) Boschin (2002)
(2) Struble and Rood (1987)
(3) Zhang et al. (2004)
(4) Andreon et al. (2004)
(5) de Grandi et al. (1999)
(6) Edge et al. (1994)
(7) Fetisova et al. (1993)
(8) Ebeling et al. (2000)
(9) Jørgensen and Chiboucas (2013)
(10)Struble and Rood (1999)
(11)Böhringer et al. (2004)
(12)Tucker et al. (1998)
(13) Ebeling et al. (1996)
(14) Böhringer et al. (2000)
(15) Tran et al. (2007)
(16) Boehringer et al. (2013)
(17) Fassbender et al. (2011)
(18) Allen et al. (2008)
(19) Schindler et al. (1995)
(20) Allen et al. (2008)
(21) Böhringer et al. (2005)
(22) Pimbblet et al. (2006)
(23) Böhringer et al. (2007)
(24) Bonamente et al. (2006)
(25) Hilton et al. (2007)
(26) Mullis et al. (2005)
(27) Ebeling et al. (2010a)
(28) Cruddace et al. (2002)
(29) Novicki et al. (2002)
(30) Taylor et al. (2004)
(31) Finoguenov et al. (2007)
(32) Dawson et al. (2009)
(33) Rosati et al. (2004)
(34) Abell et al. (1989)
(35) Gilbank et al. (2008)

5.2 MOTIVATION OF A WEAK LENSING FOLLOW-UP

In Chapter 2 we learned that clusters of galaxies can be used as a tool to constrain cosmological parameters. The following Chapter 3 showed that galaxy clusters offer observables in several wavelengths, which can be used for cosmology, as well as investigating baryonic physics, the properties of dark matter or the evolution of galaxies. Hence, multi-wavelength data for a sample of clusters of galaxies offer much more information than single wavelength data.

For this obvious reasons an optical follow-up of SZE observations of the APEX-SZ instrument was started in October 2009. The observations where conduced on the 2.2m ESO/MPG telescope at La Silla observatory in Chile, which in combination with archival data, resulted in a complete follow-up of all APEX-SZ detections with $z < 0.9$.

The sample consists of about 40 galaxy clusters, for which also X-ray data from the XMM-Newton or the Chandra satellite are available. This offers the chance to perform a homogeneous analysis in all wavelengths ranges, which helps to control systematics.

The information, stored in the full data set, allows to investigate various scientific topics related to galaxy clusters and other astronomical objects in the observed fields. Since the investigation of all fields in greater depth is not possible in a framework a single PhD work, we have to limit the investigation to some particular scientific topics.

This thesis therefore focuses on a systematic method of measuring weak lensing masses and using these masses for constraining the scaling relation between lensing mass and integrated Compton Y parameter measured by APEX-SZ. Additionally a few interesting galaxy clusters are investigated in greater detail, showing possible applications and results of the methods developed in the context of the major project.

5.3 THE WEAK LENSING PROJECT

The weak lensing project was focused on the complete lensing follow-up of APEX-SZ targets. Due to limitations such as seeing achievable image depth, we considered only clusters at $z < 1$ for the ground-based lensing follow-up. The highest redshifted cluster of this sample is XMMU J1230.3+1339, with $z = 0.98$, classified as a marginal detection in SZ. This cluster was studied with weak lensing techniques by Lerchster et al. (2011) using imaging data from the Large Binocular Telescope (LBT). Since the raw data from this telescope are not public available, a weak lensing analysis would require the acquisition of new imaging data. The low signal-to-noise of the SZ detection and the published results made a successful proposal unlikely. We therefore decided to not propose for additional observations of this target. While classified as a marginal detection based on the SZ map, current measurement results of Y_{SZ} with APEX-SZ, do not show a significant detection of this cluster (Bender et al. 2013,in prep.). This makes MS1054.4−0321 with $z = 0.83$ the cluster with the highest redshift, which is well detected in SZ and for that a lensing analysis is presented in this thesis.

The project started in October 2009 with a first investigation of available archival data as well as with an instructional observing run together with colleges from the *400d* galaxy cluster survey weak lensing program (Burenin et al., 2007) using the Wide Field Imager (WFI) at the 2.2m ESO/MPG (Baade et al., 1999) telescope at La Silla Observatory, Chile. This instrument is already used for weak lensing observations of galaxy clusters for more than a decade (Clowe and Schneider, 2002). The wide field of view of 33 times 34 arcminutes allows one to image even the closest clusters in our sample ($z = 0.1$) out to a distance of 1.75 Mpc from the cluster center.

Due to the small size of 2.2m of the main mirror, the low quantum efficiency in the infrared regime and the typical observation conditions, lensing observations for clusters at redshift higher than $z = 0.5$ should be avoided. However in this thesis we show also results of a cluster at $z = 0.83$ where WFI observations were included.

The search in astronomical archives such as the ESO archive, SMOKA and CFHT science archive have shown, that for a large fraction of our cluster sample archive data exists. Due to the guaranteed time at the 2.2m telescope and the chosen observing strategy, we were able to limit the need of archive data in such a way, that beside data from WFI, only archive data from one additional instrument was need. This additional instrument is *Suprime-Cam* (Miyazaki et al., 2002) at the 8m Subaru telescope in Hawaii, USA.

The photometric selection method developed in this thesis will allow us to combine photometric data from different telescopes, which simplified the task of completing the full cluster sample.

5.4 OBSERVATION STRATEGY

In the community a number of methods exist to obtain, measure and analyze optical data for weak gravitational lensing. As mentioned in Chapter 4, we use the KSB method for shape measurement and a profile fitting method for deriving masses. This leaves us with the point of obtaining data.

There are three common photometric methods to differentiate between unlensed foreground galaxies and lensed background galaxies. The most accurate one uses five or more photometric bands to obtain photometric redshifts for each source. This allows one not only to exclude cluster and foreground galaxies, it also adds the information of the distance of the source, which is important to derive the lensing strength for this galaxy.

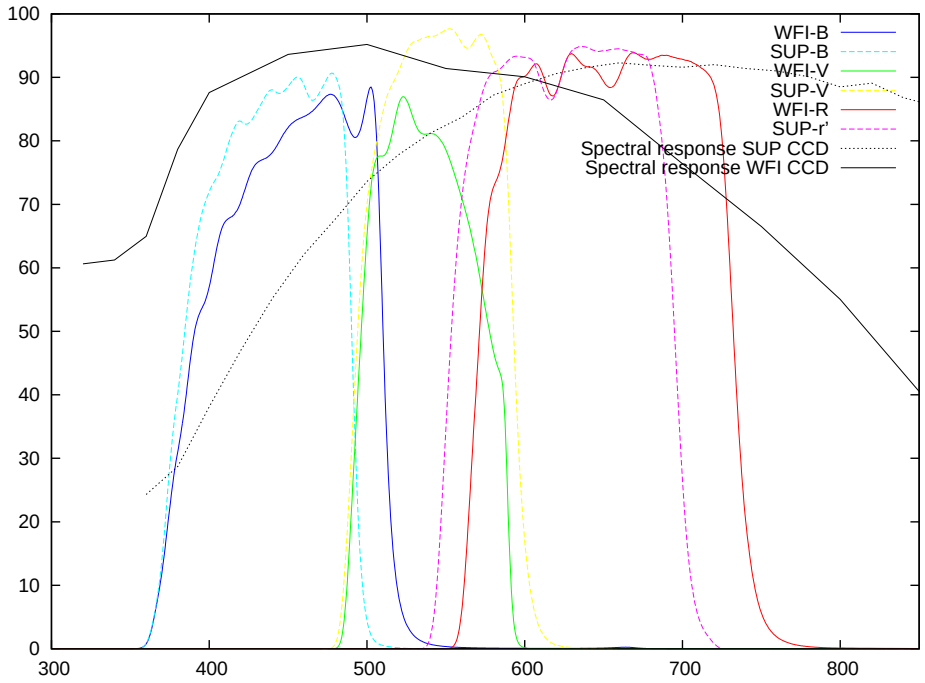

Figure 22: Spectral response curves of WFI and Suprime-Cam CCDs and spectral throughput of three filters of each instrument.

In contrast to this rather time expensive method, the red sequence method needs only two different filter bands. It uses the circumstance that the center of galaxy clusters are dominated by red elliptical galaxies. These galaxies can be easily identified in a color-magnitude diagram, since they follow a tight color magnitude relation with only small change in color with increasing magnitude. This method just excludes galaxies falling on this relation, other cluster members such as blue spirals or foreground galaxies are not identified by this method. This results in a higher contamination fraction compared to other methods. Also due to the lack of individual redshifts for the sources, only general assumptions on the redshift distribution can be made, resulting in an additional source of noise in the mass measurement.

The third method is an intermediate approach using three filter bands. This allows one to identify the red elliptical galaxies, as well as blue cluster members and foreground galaxies, which results in a smaller amount of contamination by cluster and foreground galaxies. The method is extended in this thesis work by individual distance estimates for each source. Hence, this method is a compromise between needed observation time and clean galaxy sample.

Increasing the number of filters per cluster not only results in prohibitive observing times, but it also makes it more difficult to obtain all the required data from the archive. The main argument against the usage of more than three different filters comes from the available instrument. As can been seen in Fig.22 the sensitivity of the CCDs attached to the WFI rises steep shortly before B filter and drops fast after the R filter.

Adding filters to the standard B, V, R filters such as the I band filter, would result in a doubling of the total exposure time needed per clusters. Using less than these three bands do not offer a significant saving of time. The R band is clearly the best suited band for

shape measurements with WFI, the B band offers a better color contrast to the R than the V band, and the total exposure time in V is relatively small compared to the other filters.

We therefore decided to obtain the cluster observations with WFI in three different bands, with total exposure times scaled with redshift. The scheduled exposure times for different redshifts can be found in Table 2. They are similar to those used in the *400d* project and typically yield ~ 10 galaxies per arcmin^2 in the final shear catalog after exclusion of foreground and cluster galaxies.

Table 2: Scheduled exposure times for WFI observations in B, V, R filters and total exposure time for different cluster redshifts

Redshift	**B [s]**	**V [s]**	***R [s]***	**Total [s]**
0.15	7200	3000	9000	19200
0.2	8400	3200	10500	22100
0.3	12000	4500	15000	31500

To resolve a sufficient amount of the small and faint background galaxies, we require a image seeing of better than 1 arcsecond in the R band and better than 1.2 arcseconds for B and V. The higher requirements for the R band are related to usage of this band for the shape measurements. If the seeing is worse it does not only affect the quality of the shape measurement, but it also reduces the number of sources that can be distinguished from stars and can be used for lensing.

5.4.1 *Observations*

The observations were conducted in observing blocks of 5 exposures, with a dithering of about 40 arcseconds between each exposure. The dither pattern is similar to that used by H. Israel (Israel et al., 2010a) in WFI and MEGACAM (McLeod et al., 2000, 2006) observations for the *400d* project. This dither pattern is large, but ensures high homogeneity of the final coadded image. Depending on the filter, in total 15 to 30 individual images were taken for a single passband.

A high number of exposures simplifies the exclusion of single bad exposures without losing to much time. It also allows a better correction of gain differences of the different chips and to achieve better statistics, which enables artifact correction methods such as kappa-sigma clipping. In the lensing band, the big dithering and the high number of images cause a smoother PSF pattern, which then can be modeled easier.

The price for a higher number of exposures is a larger amount of overhead time that is spent on readout and setup of the instrument. This becomes clear with the example of observations of standard fields (Stetson, 2000), which were conducted for absolute calibration in photometric nights. A standard field observation consists of two exposures in each filter, one with 10s and one with 30s. For the three filter observations conducted in this project this yields 2 minutes of total exposure time. The overheads due to telescope setup, CCD readout and filter change results in a total time of this observation of 10 minutes!

With our observational setup, only $10 - 20\%$ of the total time is lost due to overheads.

5.4.2 *Archive Data*

An intense search for archival data was conducted in three major archives, ESO archive, SMOKA archive and CFHT science archive. During the progress of the observations it became clear, that we were able to limit our search to the two instruments already mentioned (WFI and Suprime-Cam). Only few galaxy clusters had also data from other instruments of interest.

Using only two instruments simplifies the investigation of potential biases of mass estimates between the instruments. Including more instruments needs more clusters with observations with two or more instruments in common to check for biases. Also the data processing has to be understood for more instruments resulting in a longer time, needed to process the full cluster sample. Only one exception was made for the particular merging cluster AS0295, where a higher resolution of the mass map was needed to understand the nature of the merger. We therefore used also FORS data (Appenzeller et al., 1998) at the VLT telescope, Paranal, Chile) for the central region of this cluster.

Relying on data from an archive always comes with some risk. The data quality is only known with some inaccuracy and one has to rely on the few quality estimators given for each image in the archive. Two additional estimators, which are not directly obvious, should be mentioned here. At first the ESO and the SMOKA archive offer weather informations for the full night, where these data were taken. Huge changes of parameters like seeing or extinction indicate instable weather conditions likely affecting the data quality. Another, more subtle information, which can be used as quality estimator, is the name of the observer or the PI of the project. Observations on large telescopes are usually conducted in service mode or have back up programs for bad weather conditions. Reading the name of a known lensing expert as PI or observer therefore means that the data have likely lensing quality. In some cases even the title and abstract of the proposed project is listed, clarifying for what these data were meant fore.

To judge if a cluster has a sufficient amount of archive data, we require data, that offer at least the same image depth that is expected from our WFI observations. By comparing the mirror sizes between the 2.2m ESO/MPG and the Subaru telescope, the light collecting area of Subaru is about 14 times larger. By ignoring several smaller effects like different mirror reflectivity prime versus Cassegrain focus or the spectral response of the CCDs, this gives roughly the factor to compare exposure times between the instruments. In most cases the available archival data for Suprime-Cam offer much deeper imaging than the minimum requirements set by the WFI data.

Another requirement is, that at least three different broad band filters are available for the cluster, including one with subarcsecond seeing. If more filters are available, we reduce all of them, and decide later, which combination yields the best contrast between foreground, cluster and background galaxies. In contrast to our WFI observations we do not require a large dither pattern, a large number of exposures or that the R filter is used for lensing. This has the obvious reason that the Suprime-Cam imaging data usually do not have as many exposures per filter because of the shorter total exposure time. Also Suprime-Cam is more sensitive in the redder bands and therefore also offer excellent I band and Z band data suited for lensing measurements.

The criteria, by which a band is finally chosen for the shape measurement will be described at a later point of this thesis. Table 3 shows all detected cluster, together with the filters used for the analysis and the depths and seeing of the lensing band.

Table 3: Optical data of the APEX-SZ sample: Listed are the detected clusters with redshifts from Table 1 and the used filter set for the analysis. The filter used for the shape measurement is markt with ($\star$). Further, the total exposure time (Time) in seconds, the number of coadded exposures (N) and the seeing in arcseconds of the lensing band are listed, as well as the used instrument. In case where WFI and SUP were used in combination, the filter names B, V, R are used for WFI and B_s, V_s, R_s for Suprime-cam.

Cluster	z	Filter	Time [s]	N	Seeing [″]	Instrument
A2744	0.307	$B, V, R^\star$	20997	40	0.87	WFI
RXCJ0019.0 − 2026	0.277	$B, V, R^\star$	14918	30	0.82	WFI
A2813	0.292	$B, V, R^\star$	13497	26	0.89	WFI
A209	0.206	$B, R^\star, Z$	2400	10	0.58	SUP
XLSSC 006	0.429	$V, R_s^\star, Z$	1800	4	0.69	WFI,SUP
RXCJ0232.2 − 4420	0.284	$B, V, R^\star$	13398	25	0.77	WFI
RXCJ0245.4 − 5302	0.302	$B, V, R^\star$	14697	31	0.92	WFI
A383[†]	0.187	$B, V, R_s^\star$	5400	18	0.69	SUP
RXCJ0437.1 + 0043	0.284	$B, V, R^\star$	18097	33	0.82	WFI
MS0451.6 − 0305[‡]	0.539	$B, R_s^\star, Z$	11400	26	0.83	SUP
A520	0.199	$V, R, I^\star$	3000	13	0.57	SUP
RXCJ0516.6 − 5430	0.295	$B, V, R^\star$	14548	25	0.91	WFI
RXCJ0528.9 − 3927	0.284	$B, V, R^\star$	20776	48	0.85	WFI
RXCJ0532.9 − 3701	0.275	$B, V, R^\star$	13998	28	0.73	WFI
A3404	0.167	$B, V, R^\star$	10078	28	0.92	WFI
Bullet	0.297	$B, V, R^\star$	16447	35	0.77	WFI
A907	0.153	$B, V, R_s^\star$	4800	16	0.53	SUP
	0.153	$B, V, R^\star$	8638	24	0.80	WFI
RXCJ1023.6 + 0411[†]	0.280	$B, V, I^\star$	2160	9	0.62	WFI,SUP
MS1054.4 − 0321	0.831	$V, R^\star, Z$	19547	33	0.73	WFI,SUP
MACSJ1115.8 + 0129	0.348	$B, V, R_s^\star$	1200	5	0.63	SUP
	0.350	$B, V, R^\star$	14497	29	0.75	WFI
A1300	0.308	$B, V, R^\star$	16997	34	0.73	WFI
RXCJ1135.6 − 2019	0.305	$B, V, R^\star$	14998	30	0.77	WFI
RXCJ1206.2 − 0848[†]	0.441	$B, V, IC^\star$	1080	3	0.73	SUP
XMMJ1230	0.980					
MACSJ1311.0 − 0311[†]	0.494	$B, V, R_s^\star$	1080	6	0.62	WFI,SUP
A1689	0.183	$B, R_s^\star.I$	7984	29	0.69	SUP
RXJ1347 − 1145	0.451	$V, R, Z^\star$	2700	11	0.54	SUP
	0.451	$B, V, R^\star$	16297	28	0.85	WFI
MACSJ1359.2 − 1929	0.447	$B, V, R^\star$	15032	31	0.84	WFI
A1835[†]	0.253	$B, V, I^\star$	1440	6	0.90	WFI,SUP
RXJ1504	0.215	$B, V_s^\star, R$	2640	11	0.78	WFI,SUP
A2163[†]	0.203	$V, R_s, I^\star$	4500	15	0.68	SUP

Continued on next page

Table 3 – continued from previous page

Cluster	z	Filter	Time	N	Seeing	Instrument
A2204†	0.152	$V, R_s, I^\star$	1680	7	0.67	SUP
RXCJ2014.8 − 2430	0.160	$B, V, R^\star$	14277	27	0.80	WFI
RXCJ2151.0 − 0736	0.284	$B, V, R^\star$	14998	30	0.79	WFI
A2390†	0.228	$B, R_s^\star, Z$	3700	11	0.57	SUP
MACSJ2214.9 − 1359†	0.483	$V, R_s^\star, IC$	1200	5	0.53	SUP
XMMXCSJ2215.9 − 1738	1.450					
XMMUJ2235.3 − 2557	1.390					
MACSJ2243.3 − 0935†	0.447	$B, V^\star, Z$	1080	3	0.75	SUP
RXCJ2248.7 − 4431	0.348	$B, V, R^\star$	32995	55	0.80	WFI
A2537†	0.297	$V, R_s^\star, I$	2400	5	0.69	SUP
RXCJ2337.6 + 0016†	0.278	$B, V, R^\star$	720	3	0.62	SUP

Note:
(†) Data reduction and image co-addition performed by Dr. H. Israel
(‡) Data reduction and image co-addition performed by Dr. M. Schirmer

6

DATA REDUCTION

Optical raw data, as obtained from our observations or from the archive, need to be processed to correct for several artifacts. In this chapter I will describe the data procession from the raw image to the photometry and shape catalog, which will then be used for the lensing analysis. For the standard part of the data reduction, we use the `THELI` (Erben et al., 2005) pipeline. This software package is based on the older *GaBoDS* pipeline created for the data reduction of WFI data for the lensing survey *GaBoDS*. As originally created for WFI the `THELI` is now able to support a huge number of professional instruments including Suprime-Cam.

This makes `THELI` ideally suited for the data reduction of the full cluster sample.

6.1 THELI DATA PROCESSING

The data have to be processed in two different steps. The first step is to reduce data obtained within an observation run and is called "run processing". Here, we correct for effects that are not necessarily constant between different observation runs such as illumination or bias correction. The second step is object related such as photometric and astrometric solutions and is called "set processing" We first describe the data reduction for the WFI sample. The reduction of the Suprime-Cam data is very similar and I discuss only the steps, which differ to the WFI reduction.

Beside science observations, we obtained also calibration observations in each of our observing run. For archival data, we searched for calibration data that were obtained as short as possible after the science observations. If possible we obtained Bias and Dark frames, as well as flatfields and standard star observations.

Since WFI is a very stable instrument even older calibration data would not produce strong effects. Since the first observing run with suitable science data in January 2010 till the last run in February 2012, only one event was noticed, which significantly changed the instrument behavior. In April 23. 2011 the videocard had to be replaced, which changed gains and biases between the chips. Therefore no calibration data before and after this event should be mixed. Since the geometry of the chips themselves were not touched, astrometry and coaddition of data before and after this event is possible.

6.1.1 *Observation run procession*

The data within an observation run were treated commonly, only separated for different filter sets.

- *Overscan correction*: In a first step `THELI` uses the overscan regions to calculate a mean bias that is then subtracted for each frame.
- *Bias correction*: A master bias image is created by taking all bias frames within an observing run, and calculating the median value for each pixel of a chip. This master bias is then subtracted from all science images, as well as for the flatfield and standard observations.

- *Dark frames*: Dark frames are exposures with similar exposure time than typical science observations but obtained with closed shutter. They are treated as bias frames to create a master dark. They can be used in alternative to bias frames to correct for bias and additionally for dark current. Since the Dark current is ignorable for WFI, we use this images just for the detection of bad pixels, which are easier to detect in dark frames than in bias frames.

- *Flatfield correction*: The illumination of the focal plane is not homogeneous, which is the result of the basic limitations of telescope and instrument design but also the result of dust and defects on the mirrors and the filters. For that reason, flatfields have to be obtained for each of the observed filters. The bias corrected flatfields are rescaled to the same statistical mode and then a master flat is created in the same way as master bias and master dark. The bias corrected science images are then divided by the normalized master flatfield. Encoded in the master flat is also the difference in gains between the chips, dividing the science images by the master flat thus also corrects for gain differences.

- *Superflat*: Residual inhomogeneities can be corrected by applying a super flatfield correction. For this, all science images of a given filter of a run are stacked to a median image. To avoid effects caused by the observed sources, the software SExtractor (Bertin and Arnouts, 1996) is used to detect and mask these sources. If images with sufficient large dithering or from different positions of the sky are used, this image contains only a diffuse flat background. The difference from an absolute flat background can be interpreted as the result of an imperfect flatfielding. This superflat can be used in the same way as the normal master flat to correct for this effect.

- *Fringe Correction*: Due to interference of incoming light at different layers of a CCD, a spatial pattern called Fringes is created. This pattern of stray light is constant in time and can be corrected for by subtracting the super flat from the science images. This step is only necessary in the *R* band for WFI, since we do not use redder bands and this effect is not visible for bluer bands. For Suprime-Cam this effect starts to be visible in the *I* band, we therefore apply this correction only for *I* and redder bands for this instrument.

- *Masking*: If only a small number of frames were taken, or the seeing conditions varied strongly, Satellite trails and light deflections have to be masked by hand, using DS9 polygon regions.

- *Flag and Weight Images*: The created masks together with detected bad pixels from the master dark and the illumination from the flatfields are used to create weight and flag images for each single exposure and chip. The weight images thus not only carrying information about pixel defects, but also about the noise, which comes from the inhomogeneous illumination of the chip.

  To apply the superflatting step, one has to ensure that no source of the science images affect the superflat. Bright stars, for example, can create large reflections or halos in the images, which are not or not sufficiently detected by SExtrector, and would show up as a residual in the superflat. Superflats has therefore be checked for such residual effects and if possible such images should be excluded from the data used for the superflat. In some cases it is therefore better to not apply a superflat if its flatness can not be guaranteed.

6.1.2 *Set Processing*

After all images of a cluster have passed the run processing step, they are treated together.

- *Astrometry*: The `THELI` pipeline supports several astrometric reference catalogs. If possible we use the SDSS catalog (Adelman-McCarthy et al., 2008), in regions where it is not available we use the PPMXL catalog (Roeser et al., 2010). For finding an astrometric solution we use the `TERAPIX` software *Scamp* (Bertin, 2006) together with SExtractor that passes the catalogs of detected sources to Scamp. `THELI` recognize the different filter sets and finds a common astrometric solution. The intrinsic astrometric accuracy, assuming a Gaussian distribution has a typical standard deviation of $\sigma = 0.02$ arcsec. This is better than a $1/10$ of a pixel. The external astrometric accuracy with respect to the reference catalog is about 0.2 arcsecond, which is ten times higher than the internal but still below the size of a pixel. A visualization of the scatter of the internal and external astrometry can be seen in Figure 23 and Figure 24.

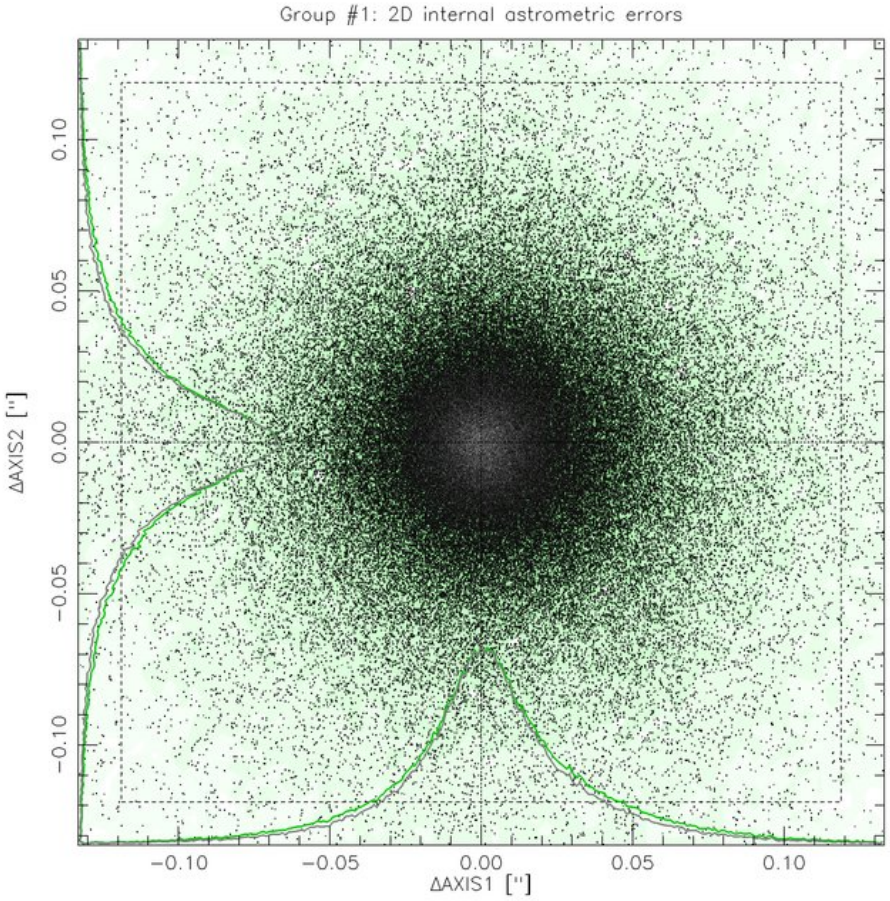

Figure 23: Astrometric residuals between the individual exposures after an astrometric solution was found, for the R band data of the RXC0532 cluster field, observed with WFI. The scatter is typically $\sim 1/10$ of the pixel size.

- *Relative Photometry*: Once an astrometric solution is found, the same sources can be identified in different frames. Assuming the sources or the mean flux of all identified sources is constant for the time of data acquisition, one can calculate the relative photometric zeropoints between all frames. This step is also performed by *Scamp*. The relative zeropoints can also be used as an analytical tool. The zeropoints should stay roughly constant for the observations, if the observations were taken under similar

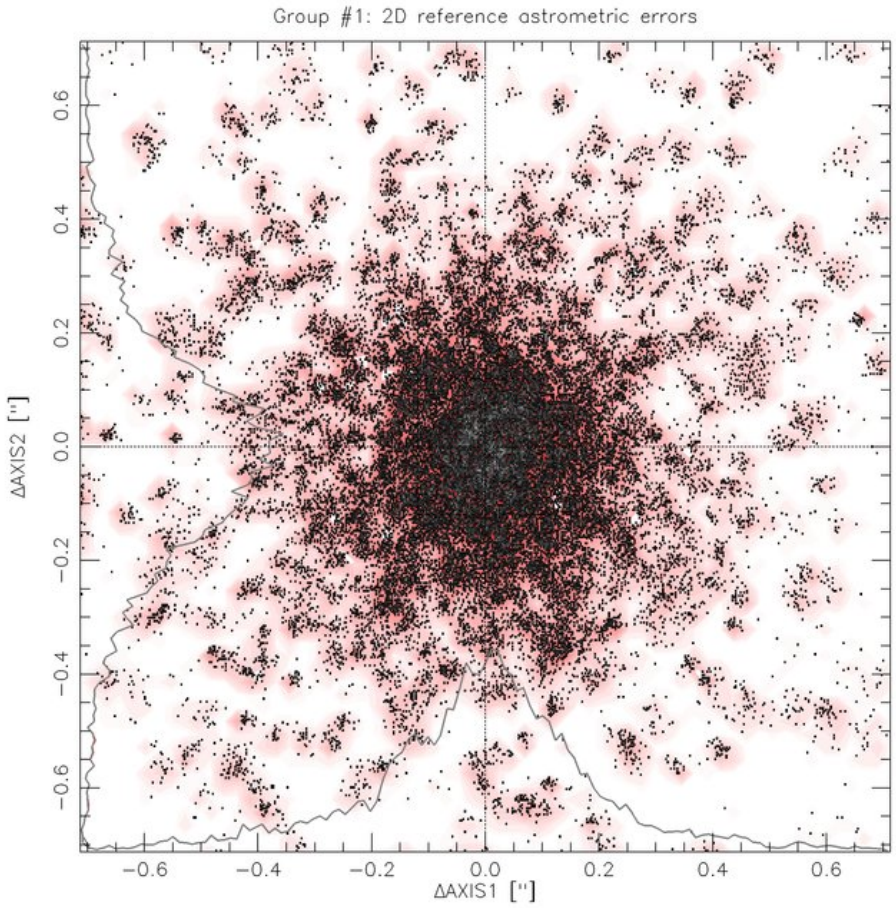

Figure 24: Astrometric residuals with respect to the reference catalog for the R band data of RXC0532.

elevation and photometric conditions. Variations are the results from changes in extinction or observations at different airmasses. Single frames with a strong deviation in relative zeropoint were therefore discarded from the data set.

- *Absolute Photometry*: There are two ways to obtain absolute photometric zeropoints. The direct approach compares fluxes of sources within the science data, with the fluxes listed in a reference catalog. This method therefore requires sources with known fluxes in the observed filter band, lying in the science field. This is barely given for the given cluster fields, because of their location on the southern hemisphere. Due to the deep exposures, sources with a apparent magnitudes of 18 mag or lower, are saturated and therefore not suited for photometric calibration. This forces the usage of fainter sources with higher photometric errors in the reference catalogs and also limits the number of usable reference catalogs. SDSS and PPMXL catalogs offer the needed depth but lack either on photometric accuracy (PPMXL) or do not match the WFI filter set (SDSS). However SDSS matches the Suprime-Cam filter set and were used for absolute calibration if available.

  For most of our observations we used the indirect method. Here standard star fields (Stetson, 2000) were observed during the night to model zeropoint and atmospheric extinction. The connection between observed flux and reference flux is

$$m_{\text{measure}} = m_{\text{ref}} + \alpha c + \gamma a + Z, \tag{130}$$

  here α is the color term, c the color in the reference catalog, γ the extinction a the airmass and Z the photometric zeropoint. The color term accounts for differences

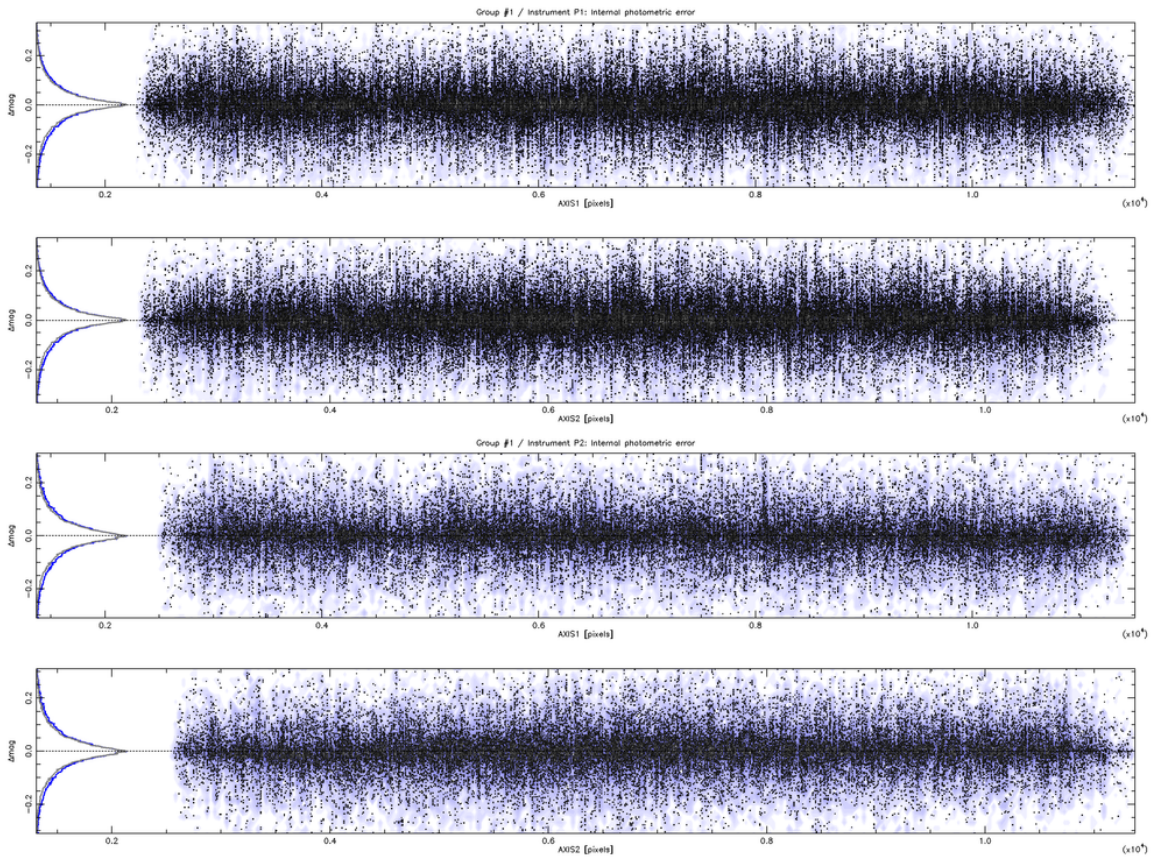

Figure 25: Photometric residuals versus position on the x and on the y pixel coordinates. Upper two plots corresponds to the R band the lower two to V band data for the RXC0532 field.

in the filters and CCD response with respect to the reference filter. At the moment, we are not interested in this, and use it just to improve the quality of the fit. To estimate the zeropoint and the extinction one has to observe at least two standard fields with different airmasses. In general it is recommended to observe three or more fields during the night to check if the night was *photometric*. This means that both parameters have not changed significantly during the night. If this is true than the derived parameters can be applied to the science images to achieve an accurate absolute calibration.

In some cases all science images were taken under non-photometric conditions, for that and to get improved accuracy of measured colors, we perform additional correction steps at a later point of the data analysis.

- *Sky substraction* Before coaddtion the background sky is modeled to get a flat background sky level. This step can account for large reflection nebulae or galactic cirrus, but one has to ensure that the sources of interest are much smaller than the kernel measuring the background level.

- *Coaddition* The final step of the `THELI` data reduction is the weighted coaddition of the science images of a given filter. For that `THELI` uses SWarp (Bertin et al., 2002), which uses the astrometric catalogs created by *Scamp*. It also uses the weight and flag images created during the previous run processing stage to calculate the weighted mean of each pixel. It also removes the large scale distortions of the telescope optics and results in image with constant pixel size.

After coaddition, all three filters are combined to a color image. Here remaining satellite trails and asteroids are showing up very obviously as single colored objects. If this is the case and if the number of frames in this filter is larger than $N = 10$ and the seeing distribution is rather tight, we apply the kappa sigma clipping method implemented as outliers rejection in the THELI pipeline.

The minimum number of images ensures that the standard deviation is sufficiently known. We classify pixels as outliers if in a group of at least 2×2 connected pixels all pixels diverge at least 6 to 7 times the standard deviation from the mean. We exclude outliers and a ring of 1 to 2 pixels around outliers from the coaddition. The exact choice of the parameters depend on the number of frames and their seeing distribution. The restriction on the seeing distribution to be relative tight, together with the rather high deviation from the mean to be classified as outliers, avoids false identifications of the outskirts of sources as outliers.

Using the outliers rejection for excluding satellite trails and reflections may not be as good as hand masking this features, but is much faster. This is an important factor, if one reconsider that a typical WFI data set of a cluster consists of 70 frames with 8 chips each. Masking asteroids is difficult and available code just mask it in the final image. The outliers rejection identify these sources before coaddition and therefore allows the area around such trails to be used for source detection.

The final output of the THELI pipeline is one coadded image per filter and a weight map of the image. An example of that can be seen in Figure 26.

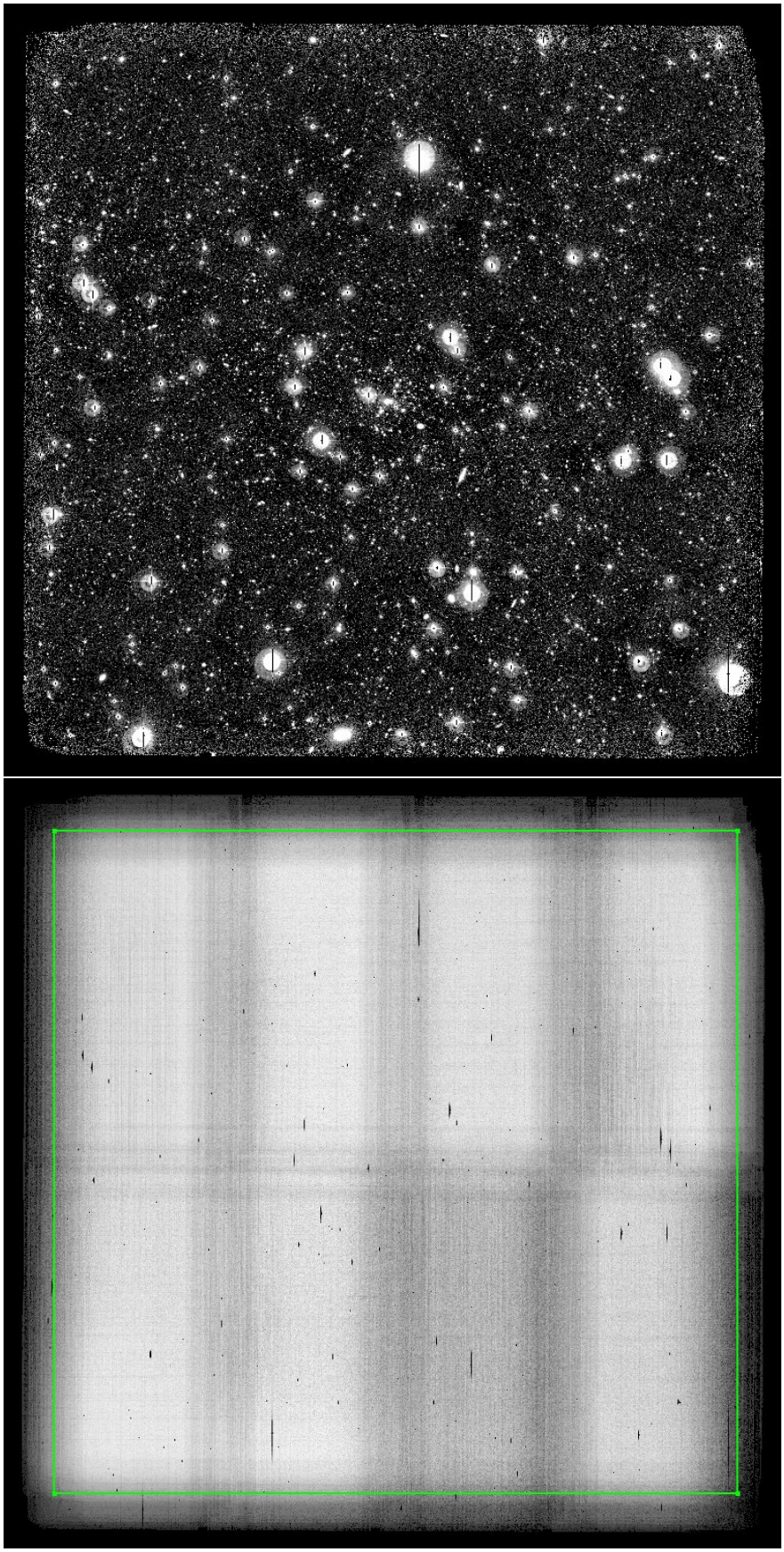

Figure 26: Top: Coadded science image of RXC0532. Left: Corresponding weight image. Green square: Area of the subframe used for further analysis.

6.1.3 *Data reduction for Suprime-Cam*

A large fraction of Suprime-Cam data were reduced by Dr. H. Israel, who used the THELI software to reduce data from MEGACAM at the MMT telescope for his lensing work on eight galaxy clusters from the *4ood* project (Israel et al., 2010b, 2012). The steps of the run processing are basically identical to those applied on WFI data. The main difference is that the instrument underwent several changes from the date of first data release till today, modifying the main configurations. During the first phase till April 2001, only 9 of 10 chips were available. After this, the second phase with 10 available chips started. During this upgrade also chip positions, readout and overscan regions have changed. In August 2008 the chips were exchanged, resulting basically in a new instrument in context of data reduction. Therefore, all the phases have to be treated separately in data reduction and should not be coadded into a single frame.

Due to typically smaller number of frames available per filter, more emphasis was made on masking satellite trails. Also notable is that due to the large collecting area of the telescope and the chosen exposure times stars up to 19 mag are saturated and therefore not usable for astrometric purposes.

Also the source catalog creation for matching with the astrometric reference catalog has to be slightly modified. A large fraction of the detected sources are too faint to be also part of the reference catalog, as well as a huge number of sources in the reference catalog are saturated in the science images. We therefore modify the detection threshold from usually 5-40 σ to higher values to increase the overlap of the two catalogs. Since the WFI data are more homogeneous the standard values are usually left unchanged.

The standard fields are not listed under calibration data in the SMOKA archive, a search for standard fields are therefore very time consuming, since they have to be identified within the science data. We therefore applied only the direct approach for absolute photometric calibration.

6.1.3.1 *Problems with rotated frames*

In some cases the camera was rotated by 90 degrees counter clockwise between exposures. This resulted in mix of frames where north up and where north is associated with the right direction. This should in principle be a situation that can be handled by THELI. Unfortunately in case of Suprime-Cam data, we were not able to find a common astrometric solution for both directions. Since a combined image would likely be affected by a combination of two very different PSF distributions, we decided to proceed with coadded images of unrotated data. The coadded images of only unrotated images still offer a higher or comparable image depth as the average WFI observations.

6.2 SHAPE MEASUREMENT USING THE "TS" KSB PIPELINE

The shape measurement technique used in this thesis is based on the KSB algorithm (Kaiser et al., 1995), including the ideas from Erben et al. (2001). The pipeline is identical to that used in Israel et al. (2010b, 2012) for the lensing analysis of eight high-redshift clusters. It is an adapted version of the "TS" shape measurement pipeline presented in Heymans et al. (2006) and explored in Schrabback et al. (2007) and Hartlap et al. (2009).

6.2.1 *The algorithm*

As already introduced in Section 4.3.1, the measurement of ellipticities of faint galaxy images is not straight forward. The KSB algorithm tries to reconstruct the reduced shear by separating it from the intrinsic ellipticity of a source e^{u} and the PSF effects.

Measuring the second-order brightness moments Q, in principle allows an unbiased estimate of the reduced shear. In real data, galaxies are pixelized and therefore discretized objects. Applying the filter function $W(\vartheta)$, which depends on pixel position, varies the transformation between unlensed and lensed moments $Q^{\mathrm{u}} \rightarrow Q$, since it can not longer be written as a matrix multiplication.

In the weak lensing case of small reduced shear g, and if the PSF anisotropies q are small, the effect can be assumed to be linear. We can now express the problem as

$$e_\beta = e_\beta^{(\mathrm{u})} + \mathcal{P}^{\mathrm{g}}_{\beta\alpha} g_\alpha + \mathcal{P}^{\mathrm{sm}}_{\beta\alpha} q^*_\alpha, \tag{131}$$

which relates the observed ellipticity with the intrinsic ellipticity, the reduced shear and the PSF anisotropies. The Einstein summation conventions has to be applied over the Greek indices. Asterisks show here and in the following equations quantities that were derived from measurements on stellar images. The two 2×2 matrices, $\mathcal{P}^{\mathrm{g}}$ the *pre-seeing polarisability* and $\mathcal{P}^{\mathrm{sm}}$ the *smear polarisability* describe the transformation of the ellipticity under gravitational shear and anisotropic PSF effects.

The KSB algorithm inverts this relation and provides a direct shear estimator ϵ from the measured ellipticities e_β for each galaxy

$$\varepsilon_\alpha = (\mathcal{P}^{\mathrm{g}})^{-1}_{\alpha\beta} e^{\mathrm{ani}}_\beta = (\mathcal{P}^{\mathrm{g}})^{-1}_{\alpha\beta} \left[e_\beta - \mathcal{P}^{\mathrm{sm}}_{\beta\gamma} q^*_\gamma \right]. \tag{132}$$

Here, we used $e^{\mathrm{ani}}_\beta = e_\beta - \mathcal{P}^{\mathrm{sm}}_{\beta\gamma} q^*_\gamma$ for the ellipticity corrected for the PSF anisotropy.

Since stars are too small to be resolved under realistic atmospheric conditions, we can use them to measure the PSF anisotropy that arises from telescope optics, guiding or other effects like wind pressure on the telescope. In general the spectra of stars in the Milky Way and that of redshifted galaxies differ, this can in principle result in different PSF properties for stars and galaxies. We assume that this effect is small within the observed filters and we do not perform shape measurements on stacked images with a mixture of filters.

For stars we can therefore consider $e^{\mathrm{u}*}_\gamma = 0$ and $g = 0$. Using this we can rearrange Eq.(131) resulting in

$$g^*_\gamma = (\mathcal{P}^{\mathrm{sm}*})^{-1}_{\gamma\delta} e^*_\delta. \tag{133}$$

Inserting in Eq.(132), we get the corrected shear estimator as follows

$$\varepsilon_\alpha = (\mathcal{P}^{\mathrm{g}})^{-1}_{\alpha\beta} \left[e_\beta - \mathcal{P}^{\mathrm{sm}}_{\beta\gamma} \left((\mathcal{P}^{\mathrm{sm}*})^{-1}_{\gamma\delta} e^*_\delta \right) \right]. \tag{134}$$

Since the PSF size is not infinitely small, $\mathcal{P}^{\mathrm{g}}$ is composed from the *shear polarisability tensor* $\mathcal{P}^{\mathrm{sh}}$ and the smear polarisability

$$\mathcal{P}^{\mathrm{g}}_{\beta\alpha} = \mathcal{P}^{\mathrm{sh}}_{\beta\alpha} - \mathcal{P}^{\mathrm{sm}}_{\beta\gamma} \left[(\mathcal{P}^{\mathrm{sm}*})^{-1}_{\gamma\delta} \mathcal{P}^{\mathrm{sh}*}_{\delta\alpha} \right]. \tag{135}$$

For a more detailed discussion on the calculation of $\mathcal{P}^{\mathrm{sh}}$ and $\mathcal{P}^{\mathrm{sm}}$ and the KSB method in general, we refer the interested reader to Bartelmann and Schneider (2001).

The used KSB implementation allows to choose between the full matrix inversion, which is mathematical correct but noisy, and the trace approximation that is less noisy but not

strictly mathematical correct. We choose the trace approximation that assumes that the off-diagonal elements are small compared to the diagonal ones. It follows

$$(\mathcal{P}^{\mathrm{sm}*})^{-1}_{\gamma\delta}\mathcal{P}^{\mathrm{sh}*}_{\delta\alpha} \rightarrow \frac{\mathrm{tr}(\mathcal{P}^{\mathrm{sh}*})}{\mathrm{tr}(\mathcal{P}^{\mathrm{sm}*})}\delta_{\gamma\alpha} =: T^*\delta_{\gamma\alpha}\ , \qquad (\mathcal{P}^{\mathrm{g}})^{-1}_{\alpha\beta} \rightarrow \frac{2}{\mathrm{tr}(\mathcal{P}^{\mathrm{g}})}\delta_{\alpha\beta}, \tag{136}$$

where we used the Kronecker delta $\delta_{\alpha\beta}$. Finally we can calculate the shear estimator ε for each galaxy without the need of a matrix inversion

$$\varepsilon_\alpha = \frac{2\delta_{\alpha\beta}}{\mathrm{tr}\left(\mathcal{P}^{\mathrm{sh}}_{\beta\alpha} - T^*\mathcal{P}^{\mathrm{sh}}_{\beta\gamma}\delta_{\gamma\alpha}\right)}\left[e_\beta - \mathcal{P}^{\mathrm{sm}}_{\beta\epsilon}q^*_\epsilon\right]. \tag{137}$$

The anisotropy q^* and T^* are determined by fitting polynomial functions in pixel coordinates to the measurements of stars. While we keep the polynomial order of the fit for T^* fixed to 2, we varied the order of the polynomial fit to q^* between 3 and 5 depending on the ellipticity pattern in the images of the different clusters.

It is observed that the estimated quantities depend on the angular extend of the measured sources (Hoekstra et al., 1998), therefore the shear measurement pipeline performs the fits on q^* and T^* for several Gaussian smoothing scales. The estimate for each galaxy is then performed, by using the values derived from the smoothing scale closest to the galaxy size.

6.2.2 *Limits of shape measurement with KSB*

Since one focus of this thesis is to derive unbiased mass estimates, it is important to know where the limitations of the applied methods are. The performance of the "TS" shear measurement pipeline, was tested within the *Shear Testing Programme* (STEP) programme (Heymans et al., 2006). This test program was focussed on a realistic simulation of cosmic shear surveys using ground-based facilities, which also explains that the largest probed reduced shear was 0.1.

From further investigations in STEP2 (Massey et al., 2007), a shear calibration factor of $f = 1.1$ was found, meaning a systematic underestimation of the shear of 10%. This value was slightly revised by Hartlap et al. (2009), as he examined the shear calibration bias in dependency of signal to noise of the source estimated by the KSB pipeline (Fig.27). He found a deterioration of the shear estimates for sources below $S/N = 7$. Changing the cut in S/N from 4 to 7 STEP2 simulations yield a constant calibration bias of 8%.

The signal to noise dependency of the shear measurement in our data set will be investigated in Section 8.1, using the mass estimates of the full cluster sample. For convergence maps of clusters, we allow the threshold to vary between different fields, with a typical threshold of $S/N \approx 4.5$. Since we are only interested in the overall mass distribution and not a precise absolute calibration, this freedom of lowering the threshold allows a higher resolution of the mass maps for clusters where it is necessary.

So far, no simulations comparable to STEP dedicated to cluster weak lensing were performed. This leaves the range of $g > 0.1$ untested. In Viola et al. (2011), the biases of several KSB methods were investigated up to $g = 0.5$. While mostly focussed on the performance between the different methods, it also give insights about the behavior of our KSB method at higher reduced shear. In the left panel of Fig.28 one can see how the shear bias behaves for galaxy images approximated with a Sersic-model and a S/N of 100. The simulations, used for this plot, do not include PSF effects. On the right panel of the same figure, PSF effects of the size expected in ground based observation are included but applied on noise free images.

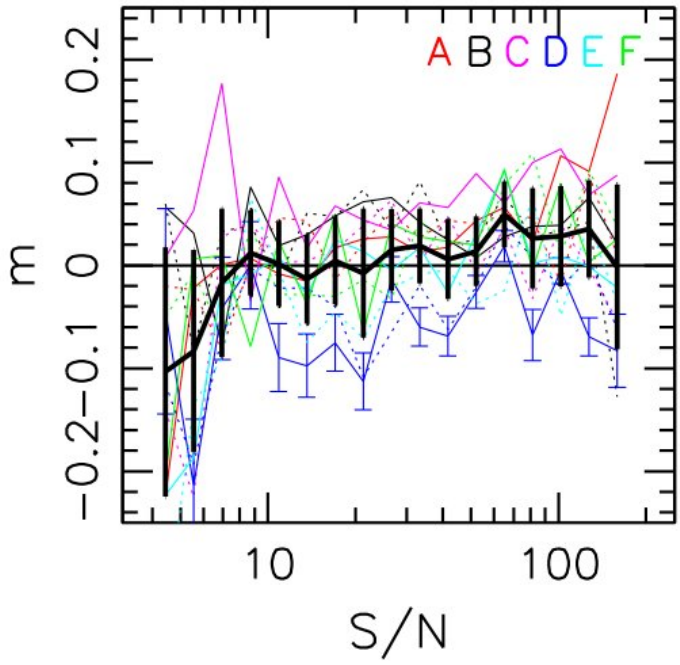

Figure 27: Shear calibration bias for different PSF shapes (A to F) as a function of the S/N of the measured source within the STEP2 simulation (Hartlap et al., 2009). The black line with error bars shows the result with scatter for the PSF type B.

Both plots do not show indications of a strong dependency of the shear bias with reduced shear. While these results are quite promising, the simulations performed in Viola et al. do not incorporate the full complexity of real observations.

Therefore, excluding the central cluster regions with $g > 0.1$ is a possible option to avoid fitting to unprobed regimes in g. However excluding these regions from the profile fit complicates the measurement of the concentration parameter. Some authors such as Applegate et al. (2012) or Hoekstra et al. (2012) use a prior on the concentration parameter to overcome this difficulty. However, using priors can affect your mass estimate as well, and are usually derived from volume limited cosmological simulations. Cosmological simulations as such depend on the used cosmological parameters and can therefore bias the results. The volume limitation results in a small number of very massive clusters, like those in our sample. The mass-concentration relation derived for such massive clusters is therefore relatively noisy compared to smaller mass clusters.

In this thesis we fit the concentration parameter as well as r_{200}. The the reasonably of the derived concentration parameter will be investigated on the full cluster sample and compared with a state of the art mass-concentration relation.

6.2.3 *Preparing data for shape measurement*

Before passing images to the KSB pipeline, we have to prepare the data, to ensure the quality of the shape and the photometric measurements. The first step is to convolve the images to the seeing of the worst image. For that we perform a PSF matching, based on Gaussian PSF models, as it is described in Hildebrandt et al. (2007). The filter width, which is used to convolve the image a to the seeing of the image with the worst seeing b is then

$$\sigma_{\mathrm{fi}} = \sqrt{\sigma_b^2 - \sigma_a^2}, \tag{138}$$

where σ_a and σ_b are the widths of PSF in image a and b assuming a Gaussian PSF.

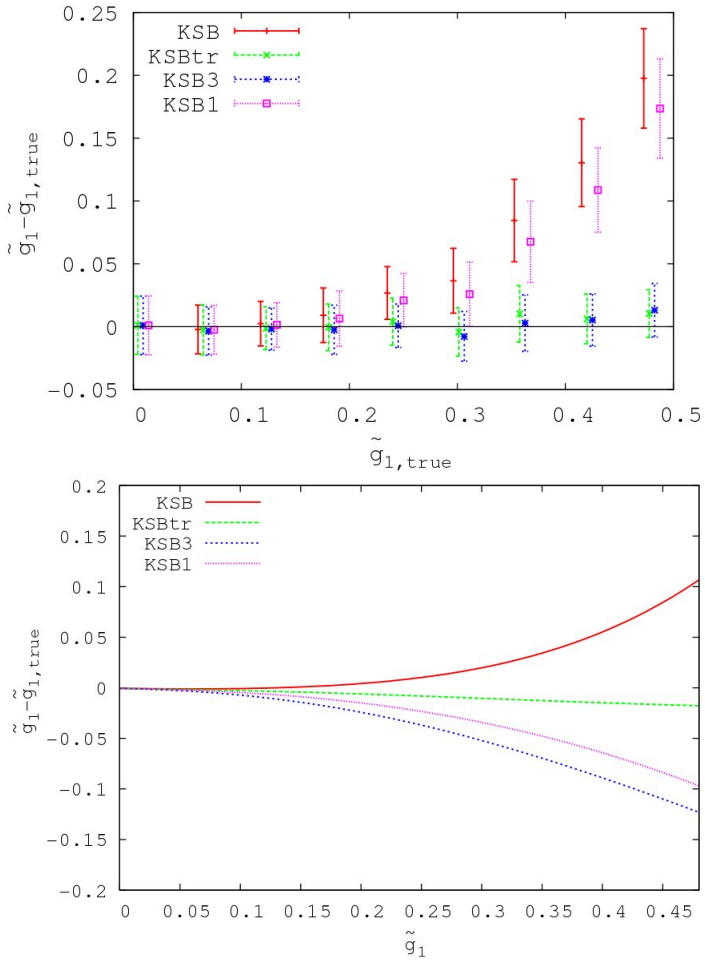

Figure 28: Top: Fig. 2 from Viola et al. (2011), showing the bias in reduced shear of different KSB methods in dependency of the true reduced from simulations including noise. KSBtr is the method closest to our implementation. Bottom: Fig. 10 of the same paper, showing the behavior of the measured reduced shear of a noise free galaxy image under consideration of PSF effects.

The KSB pipeline uses SExtractor in "double image" mode. This needs the input images to have same size, because it performs its measurements in pixel coordinates using one image for detection and the second one for the measurement. We therefore cutting the images in the different filters to the sames size, also excluding the borders with low signal to noise. An example for the cutout region is indicated in Figure 26 as a green box in the weight image.

We also inspect the images for remaining artifacts such as reflections or stellar halos from bright saturated stars. Here, we use also the color composite images, which help to identify artifacts by appearing only single colored. We mask the regions, by using the polygon regions in DS9, and save them in DS9 region files. These files are passed together with the weight image into *Weightwatcher* (Bertin et al., 2002) to create updated weight and flag images.

Depending on the chosen mode for background modeling in SExtractor, less intense masking is required. The standard mode, which we use is "Manual", setting the background value to zero. This results in the detection of stellar halos, and other larger regions with increased background, as single sources, which are then excluded by the KSB pipeline because of their size. Changing the background mode to "AUTO" and choose a sufficient small smoothing kernel allows us to detect sources within reflections, since the reflec-

tions are partially subtracted as background. This mode is of special interest if reflection rings of very bright sources affect a huge area or the central regions of the cluster. The light distribution of reflection rings can be assumed to vary on scales much larger than the typical size the lensed background galaxies. Subtracting a smooth background model therefore can be used obtain measurements on galaxies within these regions. However the light distribution of reflection rings can vary strongly on its borders, resulting in spurious lensing signal. This mode therefore should be only applied in cases where it is of special importance to get a lensing signal at this position and only together with careful masking.

6.2.4 *Running the "TS" KSB pipeline*

The input to the pipeline consists of 4 science images, with corresponding weight and flag images. The first part consist mostly out of SExtrector calls in double images mode. Here, the image from which we want to apply the shape measurement on, is used for source detection while photometry is conducted on the second images. Since the three photometry images are convolved to the worst seeing, while the detection image has usually significantly better seeing, the measured total fluxes of the sources are underestimated. Since the underestimation is the same for all photometry images the flux ratios or "colors" are conserved. We therefore use later the photometry of the shape measurement image, as measure of the brightness of a source.

The obtained SExtrector catalogs are merged to one catalog and then passed to *analysedac*, which is the Erben et al. (2001) implementation of the Core-KSB. Here the object centroid positions are refined and the brightness moments are measured. Sources for which the shape measurement were not successful or that have a half light radius lager than 10 pixels are excluded from the catalog. Within this step also sources with a bright neighbor are excluded since their shape measurement might be affected by the neighbor.

The output of the first part is a filtered catalog with astrometric, photometric and shape informations. After this step, stars have to be identified by its location in the half light radius vs. magnitude space. In Fig.29 one can easily recognize stars because of their constant half light radius. At bright magnitudes the stars get saturated, which means that flux and size can not be estimated reliably. This gets visible in the size-magnitude diagram in a turn of the else constant size-magnitude relation. At faint magnitudes the estimate of flux and size of a source gets increasingly noisy, and get confused with small and faint galaxies. We therefore define a bright and a faint limit $m_{\mathrm{bright}} < R_{\mathrm{source}} < m_{\mathrm{faint}}$, as well as a size range $s_{\mathrm{min}} < r_{\mathrm{h,source}} < s_{\mathrm{max}}$ within we assume to have a clean selection of stars.

It is important to avoid galaxies in this sample, since this could result in a reductions in shear due to false identifications as PSF anisotropy. We considered an additional filtering process using the stellar locus in color-color space, but a conservative choice of m_{faint} turned out to be sufficient.

Passing the selection information to the KSB pipeline, the anisotropy correction is performed using the stars defined in the step before. The final output of the KSB pipeline is the corrected shape catalog together with a set of ascii files, containing the uncorrected, the model and the corrected stellar ellipticities for several Gaussian window scales. The ascii files represent an important diagnostic tool to check the performance of the anisotropy correction.

In principle this analysis can be performed on every single exposure of the lensing band to select only those for coaddition, which show good PSF pattern. However, in context of this project this would mean to run the KSB pipeline on more than 860 exposures plus about 40 times on the coadded images. We therefore decided to apply the KSB pipeline

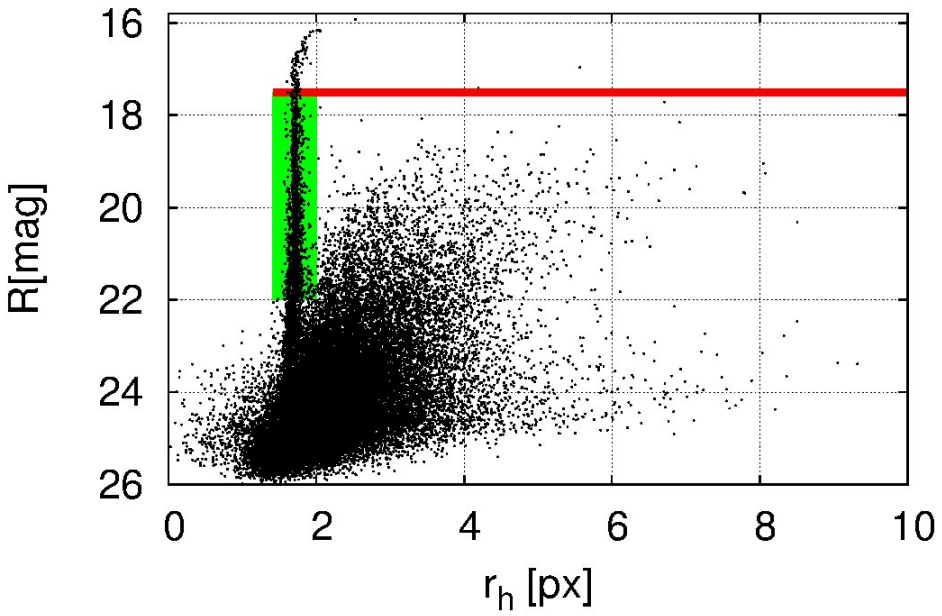

Figure 29: Size-Magnitude-Diagram of RXC0532. Green: Region used to select stars for anisotropy correction. Red: Saturation limit, sources brighter than this value are expected to be saturated and excluded from the analysis.

only to the coadded images. Only if the performance of the PSF correction is not sufficient, we perform a deeper check of the PSF properties of single exposures.

Figures 30 and 31 show the PSF pattern and their correction for RXC0532 and RXC1504 observed with WFI. While for the first cluster a fairly regular PSF pattern is visible, which can be well modeled by a polynomial function, the pattern for the second one is rather chaotic and can not be modeled. Therefore, the coadded image from RXC1504 is rejected. The reason for the bad PSF pattern was found to be caused by the large pointing offset between old archival data and newly obtained data. This problem can be solved by splitting the data into the two pointings, but this would result in a significantly lower number of usable sources. [1] We therefore used data from Suprime-cam for shape measurements and WFI for the photometry.

After PSF correction the mean ellipticity of stars are consistent with zero, with standard deviations of $\sigma \approx 0.008$.

1 The S/N dependency of the shear measurement bias at very low S/N prohibits the combination of two low S/N measurements. Therefore the S/N threshold for the shape measurement can't be lowered in the presence of two data sets to get the same amount of usable galaxies as a combined image.

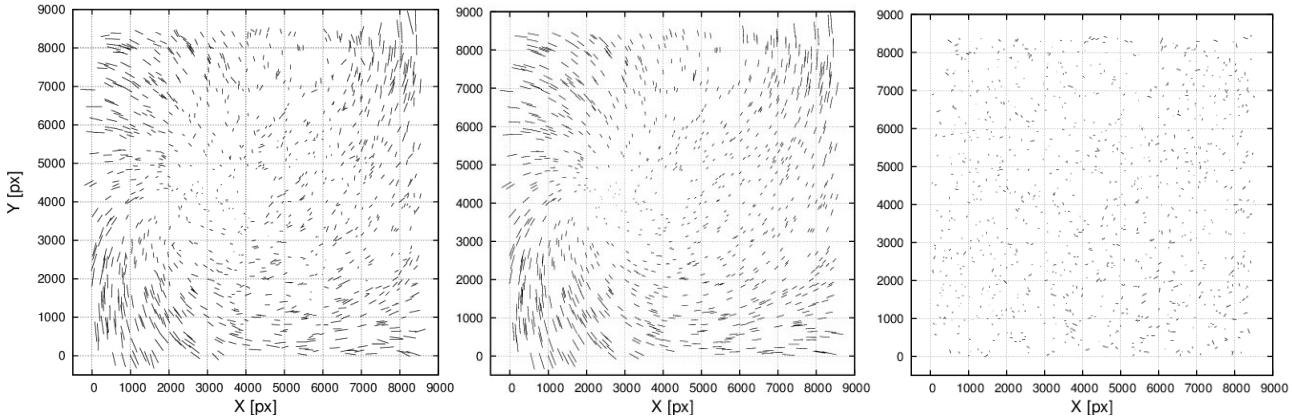

Figure 30: PSF anisotropy of stars in the lensing image for RXC0532. Left: Measured ellipticities of stars at the position in the coadded image. Middle: Best fitting polynomial model. Right: Corrected stellar ellipticities. An ellipticity of $e = 0.1$ corresponds to a line with a length of 1000 pixels.

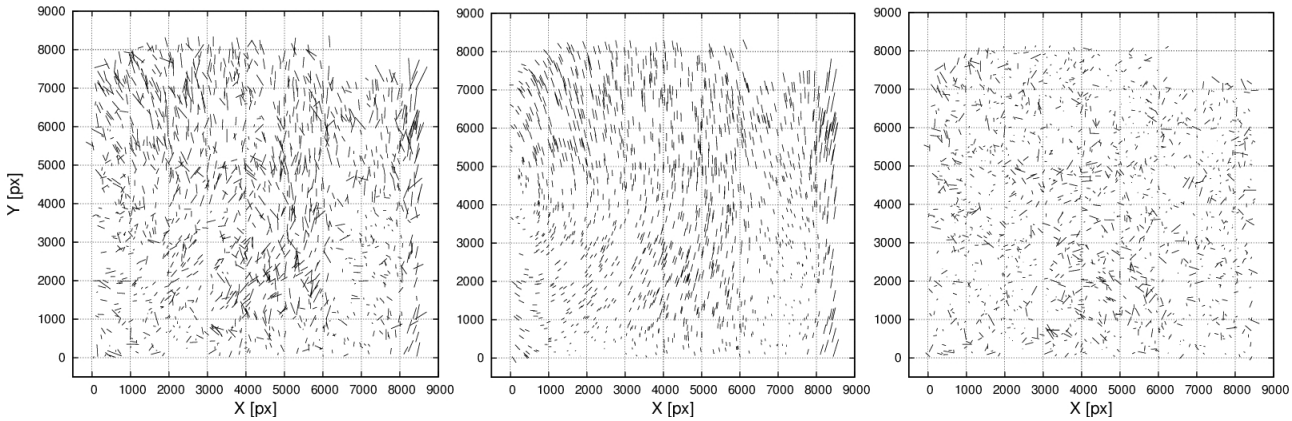

Figure 31: Same as Fig.30 but for RXC1504.

7

BACKGROUND SELECTION AND MEAN LENSING DEPTH

Only galaxies located behind a massive deflector are lensed. While only $\sim$ 3% of the field galaxies lie in the foreground of $z = 0.1$ clusters, this fraction already reaches 30% at $z = 0.5$ for the typical depth of our data. In addition, the cluster galaxies themselves contribute to the contamination of lensing measurements. In the central part of clusters, where the number density of cluster galaxies is high, the fraction of cluster and foreground galaxies diluting the shear signal can become significantly higher than the numbers given above.

To avoid significantly underestimated masses, one has to minimize the amount of foreground and cluster galaxies entering the lensing analysis. Additionally, the remaining contamination and the redshifts of the sources has to be known as good as possible. Photometric measurements play a key role to obtain the necessary informations as we will show in this chapter.

7.1 CURRENTLY USED BACKGROUND SELECTIONS

To put the method that is described in this chapter into the right context, we shortly review currently used methods to select background galaxies based on observations in three broadband filters.

Most background selection methods are using polygonal regions in color-color space to exclude foreground and cluster galaxies from the background sample. Additionally they apply faint and bright magnitude cuts to exclude foreground galaxies or to limit the selection to a certain magnitude. The major difference between the different authors is the size, shape and justification why the polygons are chosen as they are.

In a set of publication describing the "Weighting the Giants"(WTG) project (von der Linden et al., 2012; Kelly et al., 2012; Applegate et al., 2012), which aims to accurately measure the masses of 51 clusters with weak lensing, uses a red sequence technique to exclude cluster galaxies from the background galaxy sample. The method usually applied in the color-magnitude diagram (CMD), based on 2 filter observations, is here simultaneously applied in a second CMD using a third filter. The left panel of Figure 32 illustrates the background selection for the cluster MACSJ0417.5-1154 of their sample. Sources lying between the blue lines in color-magnitude space in both filter combinations are assumed to be part of the red sequence of the cluster and are excluded from the background catalog. An additional magnitude cut is applied, leaving only sources brighter than this cut in the lensing analysis.

In High et al. (2012) the selection polygon is chosen, based on the distribution of CFHTLS-deep photo-z galaxies in the color-color space with $z < z_{\rm d} + 0.05$. For different redshift bins and color combinations, the selection polygon has to be manually modified. An example of the selection for a cluster at $z_d = 0.383$ is shown in Figure 33

Another approach was made in Medezinski et al. (2010), who investigated the density distribution of galaxies in the color-color plane. Additionally, the mean distance of the galaxies with respect to the cluster center is evaluated on a grid in the color-color plane. While the first identifies regions with a relevant number of galaxies the second map shows the location of cluster galaxies in the color-color plane. An example of such maps are shown in Figure 34.

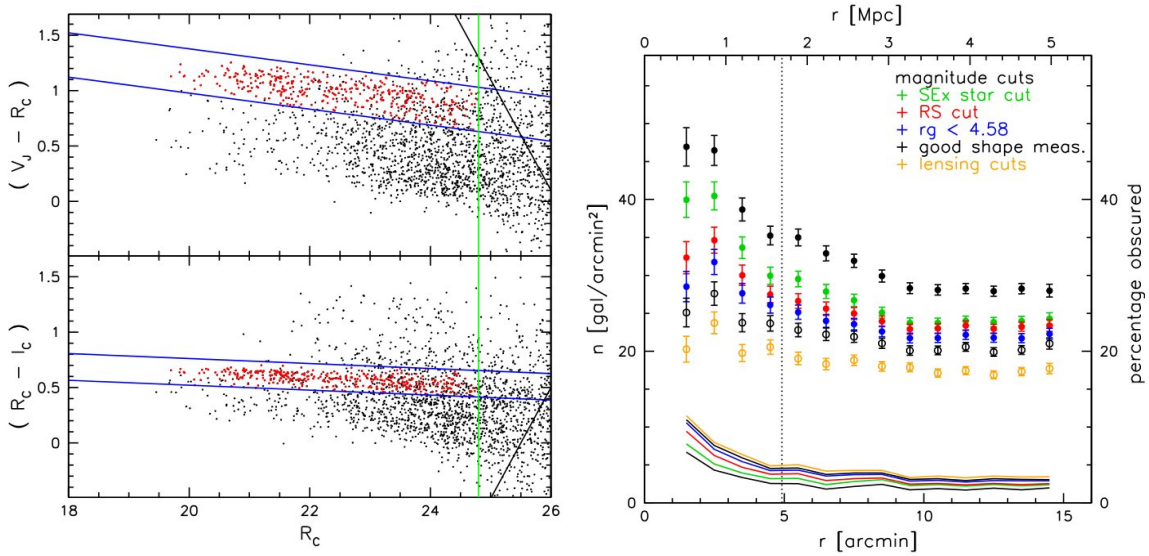

Figure 32: Left: Background selection used for three filter data in the WTG project. Sources falling with the blue lines of both color-magnitude diagrams are excluded from the background sample, as well as sources fainter than the magnitude cut illustrated by a green line. Right: Number density of galaxies with respect to cluster centric distance for various source catalogs of the MACSJ0417.5-1154 field. The lines at the bottom of the figure indicate for each number density profile the fraction of pixels obscured by masks or bright objects excluded from the sample. Both figures taken from Applegate et al. (2012).

For the regions identified in both distributions, redshift distributions based on photo-z catalogs are obtained, as well as the radial dependency of the number density and reduced shear are investigated. Based on that, those regions are identified as foreground, cluster and background populations. An example of this selection can be seen in Figure 35 for the cluster A370.

All three methods are able to identify and exclude late-type galaxies at cluster redshift from their catalogs. Only the last two methods also exclude bluer cluster galaxies and foreground galaxies. The background galaxy sample of both methods do not show a significant increase of the number density of galaxies towards the cluster center. This indicates that those background samples are rather clean of cluster galaxies. Only the profiles by Applegate et al. (2012) show an increase of the number density towards the cluster center, making an additional contamination correction necessary.

For all methods a reference catalog is needed, on which the same photometric cuts have to be applied. From this reference catalog the mean lensing depth $\langle\beta\rangle$ is measured, to relate the observed shear to the cluster mass. This mean lensing depth of the reference catalog is assumed to be representative for the observed cluster field. It supposes that the reference field is a representative subsample of the true redshift distribution of the sky. This is only true within some uncertainty, defined by the amount of cosmic variance in the fields. For a single cluster field, cosmic variance can significantly affect the redshift distribution even after the exclusion of cluster galaxies. For the full cluster sample of 39 clusters with a quarter degree FoV each, cosmic variance is heavily suppressed (van Waerbeke et al., 2006). Therefore the mean cluster mass is more affected by cosmic variance in the reference field rather than by that of the cluster fields, assuming reference fields such as COSMOS or the CFHTLS-deep fields.

Using the average $\langle\beta\rangle$ instead of the true distance ratio for each individual background galaxy, results in an increase of noise of the measurement.This is conceivable as a projec-

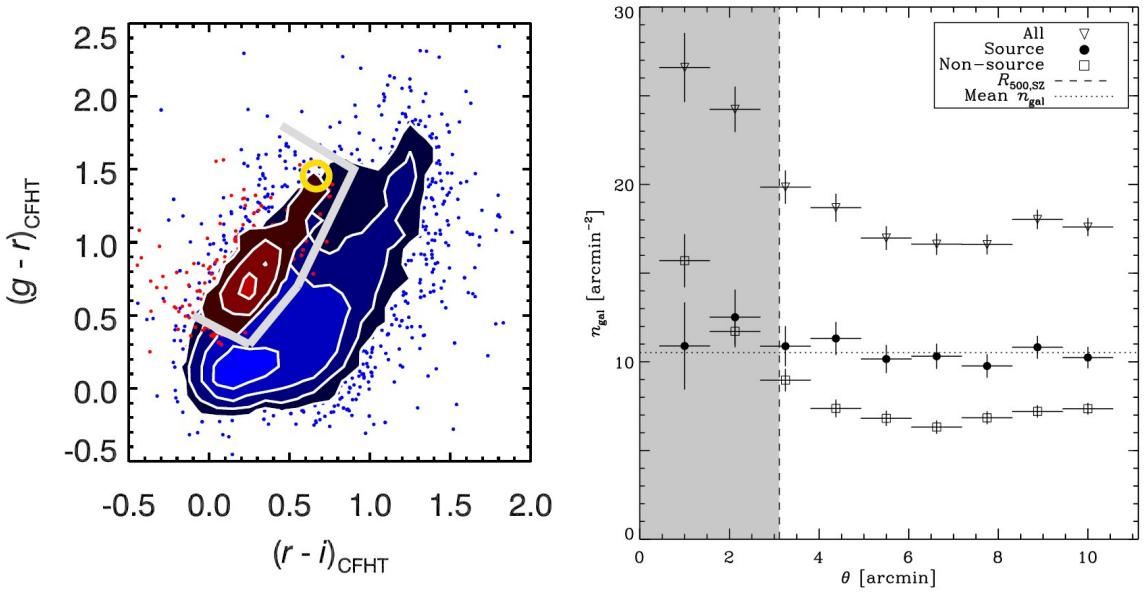

Figure 33: Left: Background selection used by High et al. (2012). Red indicates regions occupied by galaxies with $z < z_d + 0.05$ blue galaxies with higher redshifts in the CFHT-Deep photo-z catalog. Gray lines indicate the selection polygon, the yellow circle the location of red sequence galaxies for a cluster redshift of $z_d = 0.383$. Isodensity contours are given in log scale. Right: Number density of galaxies in the catalog with respect to the cluster centric distance. As source are classified galaxies which are consistent to be background galaxies. Non-sources are those galaxies excluded by the gray selection polygon seen in the left diagram. Images taken from High et al. (2012)

tion of the reduced shear to a common distance ratio without accounting for the dependency of the shear on the distance.

The inclusion of individual distance estimates on a lensing analysis can therefore reduce the scatter in mass estimates caused by cosmic variance. It can also improve the accuracy of the mass estimate by reducing the noise caused by the usage of the mean angular diameter distance ratio.

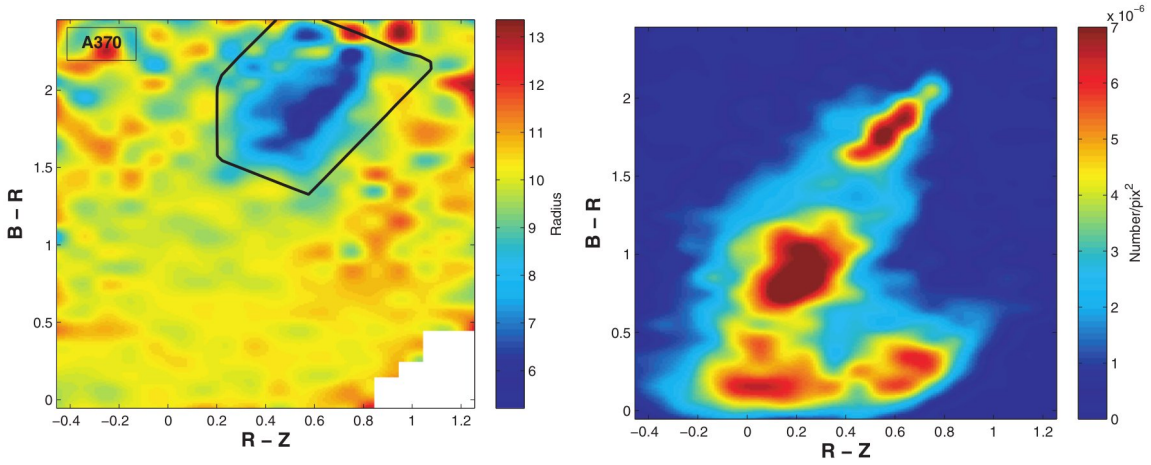

Figure 34: Left: Mean radial distance of galaxies from the center of the cluster A370 in the $R - Z$ vs. $B - R$ plane. Blue colors indicate low distances. The polygon marks the selection in color-color space used to exclude cluster members. Right: Number density of galaxies in the color-color plane of the same cluster field. Image credit Medezinski et al. (2010).

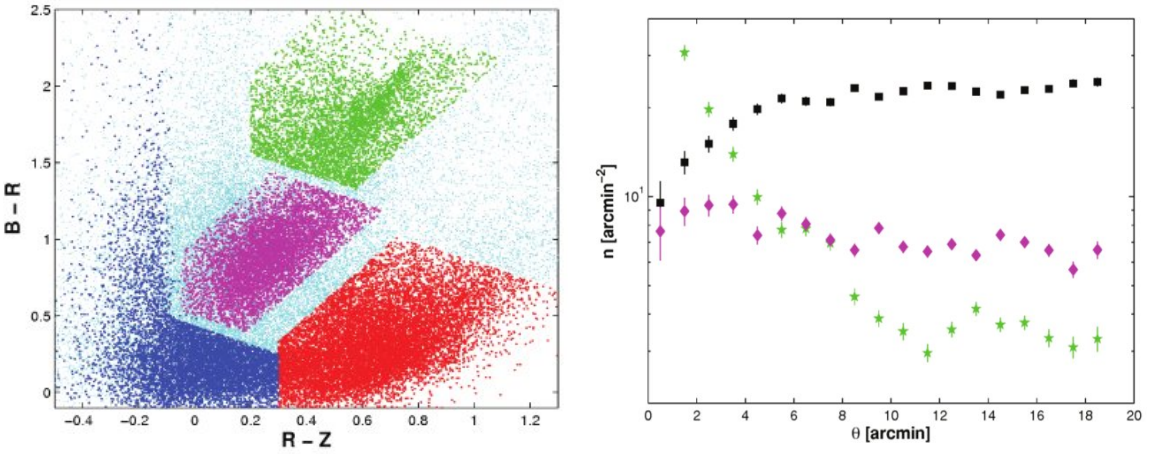

Figure 35: Left: Background selection used by Medezinski et al. (2010) for A370. Individual colored regions are identified by their number density in color-color space and by their mean distance from the cluster in color-color space. Only regions marked in red and blue are used for the lensing analysis. The green region is expected to by occupied by cluster galaxies, the violet region by foreground galaxies. The number density profile of the different samples are plotted in the right plot. Here blue and red catalogs are merged and shown in black. Images taken from Medezinski et al. (2010).

7.2 PHOTOMETRIC CALIBRATION

To account for inaccurate photometric zeropoints of observations not obtained under photometric conditions, and for internal consistency of the observed colors with WFI, we perform an internal color calibration to all WFI observations.

From the previous chapter we know how to select stars in the magnitude-size space. Stars occupy a well defined region of the color-color space known as the stellar locus. This region is mostly created by main sequence stars of the galactic disk of the milky way. All clusters with WFI data were observed in the same B, V and R bands with the same set of chips. Therefore no significant color shift is expected between the stellar loci of different cluster fields caused by instrumental effects. The observed differences between the fields are therefore the result of imperfect absolute calibration, the convolution of the images to the worst seeing and the reddening caused by galactic dust extinction.

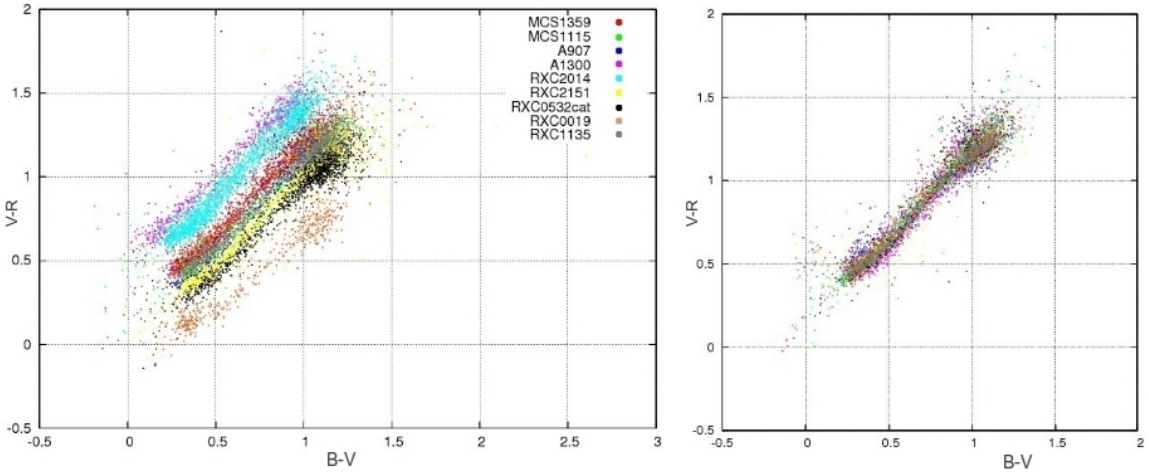

Figure 36: Left: Stellar loci of different cluster fields observed with WFI. Right: Color calibrated stellar loci.

All effects can be described by a shift of the photometric zeropoint, which translates to a shift within the color-color plane. To calibrate the WFI data internally, it is therefore sufficient to calculate the median of the stellar locus to provide the necessary information for the calibration. We additionally measured the median postion of the over densities at the red and the blue end of the stellar locus to gain additional estimates. The shift is then calculated by the mean shift of the three measurements. An example for the calibration is seen in Figure 36.

The following step is the calibration to a photometric reference catalog. This will allow us to relate the measured photometric quantities to those of the reference catalog which contains additional informations such as photometric redshifts. We chose the COSMOS photo-z catalog version 1.4 as reference catalog [1]. This catalog, not yet released to the public, has a limiting magnitude of $R = 26.2$ ($I = 26$) and accurate photometric redshifts based on observations of up to 30 filter bands (Ilbert et al., 2009). It matches the depth of our deep images and has the advantage of including most of the used Suprime-cam filters.

From Equation (130) we know the connection between observed magnitude and reference magnitude in a given filter. This equation can also be used to describe the color transformation between WFI and COSMOS filters. For that, the combined spectral response of

1 Gently provided from Prof. V. Smolcic, priv.

the filter and CCD have to be relatively similar between the two instruments. The magnitude in a given filter can be described as

$$m_{\text{measure}} = m_{\text{ref}} + \alpha c + Z'. \tag{139}$$

Compared to Equation (130), the airmass-dependent term is excluded, since the coadded images are already corrected for that. Despite the fact that our coadded images are already zeropoint corrected, the usage of a different reference filter can introduce a shift in zeropoint. In terms of color we get the general form of

$$m_{\text{measure},1} - m_{\text{measure},2} = m_{\text{ref},1} - m_{\text{ref},2} + \alpha_1 c_1 - \alpha_2 c_2 + Z'_1 + Z'_2, \tag{140}$$

where the suffixes 1 and 2 stand for two different filters. Using $c_{\text{measure}} = m_{\text{measure},1} - m_{\text{measure},2}$ and $c_{\text{ref}} = m_{\text{ref},1} - m_{\text{ref},2}$, we can rewrite this equation to

$$c_{\text{measure}} = c_{\text{ref}} + \alpha_1 c_1 - \alpha_2 c_2 + Z'. \tag{141}$$

Here, we also merged the two zeropoints to one value. In general the colors c_1 and c_2 should be chosen to be close to the used filters, to estimate the spectral slope within the broad band filter. In most cases, we use for our analysis sets of neighboring filters, such as the WFI filters B,V,R. For this reason we can replace c_1 and c_2 with c_{ref}.

Using $\alpha' = \alpha_1 - \alpha_2$ we get the final relation between measured color and reference color as

$$c_{\text{measure}} = (1 + \alpha')c_{\text{ref}} + Z'. \tag{142}$$

If the observed field is also covered by the reference catalog Equation (139) and Equation (142) can be directly estimated. This is not the case for our data. Alternatively, we can use the stellar locus to calculate the color transformations. Similar to the internal calibration of the WFI observations, we identify the prominent features in the stellar locus. This is done in the reference and the measured catalog.

The reference catalog offers two star classifiers to select stars from the catalog. Using both and a R band magnitude limit of 22 mag produces a stellar locus very similar in shape to that observed in WFI. Since we know the selection of stars in the measurement catalogs, we conduct that the qualifiers used for selection in the reference catalog to perform sufficiently well. The similarity in shape also suggest that the filters used in both instruments are rather similar.

Once prominent features are identified, the *stretching terms* α' for each of the two colors are determined by comparing the distances of the prominent features in the reference and the measured locus. The stretching terms can be calculated as

$$\begin{aligned} \Delta c_{\text{ref},1} &= \frac{c_{\text{measure},1}}{1 + \alpha'_1} \\ \Delta c_{\text{ref},2} &= \frac{c_{\text{measure},2}}{1 + \alpha'_2}, \end{aligned} \tag{143}$$

where $\Delta c_{\text{ref},1}$ and $\Delta c_{\text{ref},2}$ are the differences between the two features in color 1 and 2 in the reference catalog, and $c_{\text{measured},1}$ and $c_{\text{measured},2}$ the corresponding differences in the observed stellar locus. After the stretching terms are found, the shifting terms Z'_1 and Z'_2 are determined in the same way as in the internal calibration.

Figure 37 shows the internally calibrated stellar locus of WFI observations, the stellar locus from COSMOS and the calibrated stellar locus from WFI. The calibrated stellar locus agrees well with the reference catalog. The width of the stellar locus from COSMOS is

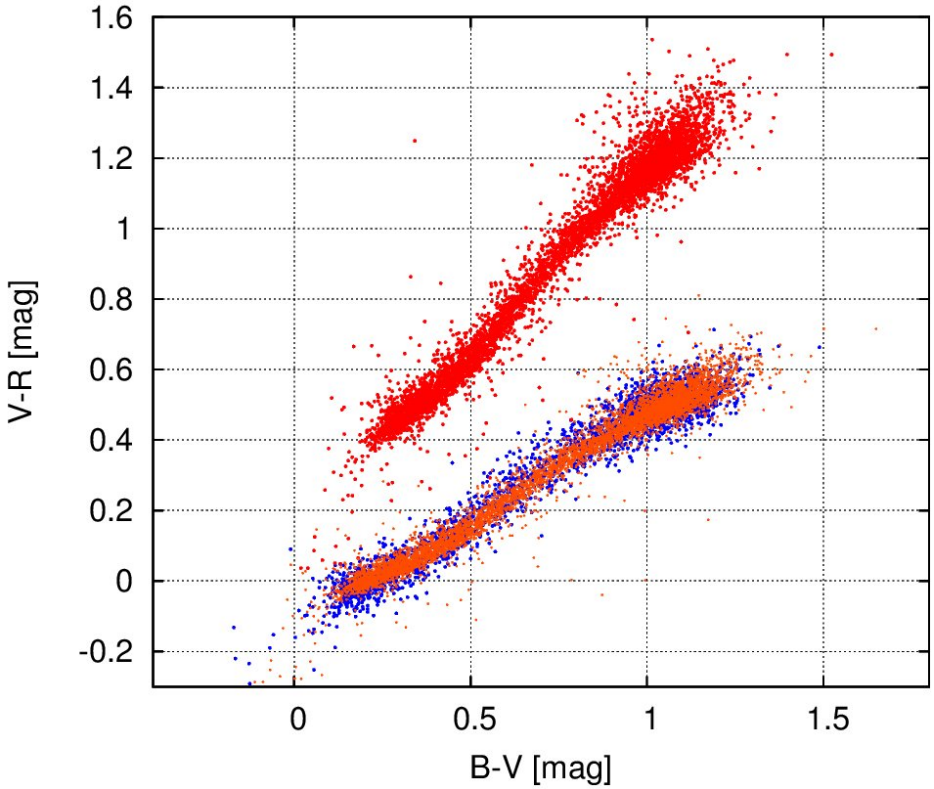

Figure 37: Color calibration between WFI B,V,R and COSMOS B,V,r filters. Red: Combined stellar locus from Figure 36. Blue: Stellar locus from COSMOS. Orange: Calibrated stellar locus from WFI.

slightly higher than that from WFI. This can be caused by small offsets in the zeropoints within the mosaic image used to derive the photometry of the COSMOS catalog. It can also be the result of the color transformation or larger photometric errors. The letter case rather unlikely since the COSMOS data are in general deeper than our WFI observations.

In case of Suprime-cam data, the color calibration to COSMOS is easier, since most of the Suprime-cam filters used are included in the COSMOS catalog. Because of that, stretching terms have only be derived for those colors in which the filters differ from COSMOS. The shifting terms have to be derived for each field, since color changes due to galactic extinction as well as small offsets in zeropoints occur in each cluster field differently.

In High et al. (2009) a similar method is shown using the stellar locus to calibrate data to the SDSS catalog. In this paper it could be shown that this method also allows us to account for galactic extinction if the stellar locus of the reference frame is corrected for that. This is the case for the COSMOS catalog, which allows us to skip the correction for galactic extinction.

7.3 THE COLOR-COLOR-DIAGRAM OF THE COSMOS CATALOG

The use of reference catalogs relies crucially on the assumption that galaxies sharing similar photometric properties have a similar probability distribution in redshift. Depending on the type and amount of available photometric informations, this probability distribution can be broader or tighter, single or multi peaked.

To investigate the probability distribution in color-color or color-color-magnitude space, one has to rely on the accuracy of the redshifts used to obtain the distribution. One option is to use a catalog with spectroscopic redshifts (Brunner et al., 1999). However, spectro-

scopic redshifts for sources as faint as those observed in our data set are difficult to obtain. To the knowledge of the author, no spectroscopic catalog exists which reaches limiting magnitudes of $I = 26$ and covers a suitable area in color-color space to compare our photometric measurements with.

As an alternative to spectroscopic redshifts one can also use a photometric redshift catalog as reference. Photometric redshifts (photo-z) are obtained by fitting spectral energy distributions to photometric measurements. The typical output of a photo-z code is also a redshift probability distribution, but in published photo-z catalogs only point estimators are given. Because of that, using a photo-z catalog as reference catalog can be significantly affected by the usage of point estimators. Since the quality of the point estimator strongly depends on the used filter sets, we use the COSMOS photo-z catalog which uses 30 filters over a large frequency range. This catalog has a high accuracy in redshift space and a lower number of outliers compared to other photo-z catalogs (Ilbert et al., 2009).

In Figure 38, we plotted B-V and V-R colors of galaxies from the COSMOS catalog for the two magnitude bins $R < 22$ and $22 < R < 24$. Color coded are different redshift bins, as stated in the figure. Circles mark regions for which the redshift distribution is shown in Figure 39. Investigating the distribution of galaxies of a single redshift bin, we see that they are arranged in elongated stripes in the cc-diagram. These stripes reflect the diversity of galaxy types starting at the blue corner (low B-V and V-R values) with strongly star forming galaxies and ending at the red side with elliptical galaxies with no significant star formation.

In the color-color diagram for bright galaxies one can easily recognize regions just occupied by one redshift bin, indicating that the redshift distribution has to have a width of less than $\Delta z = 0.15$. Also regions with several overlapping redshift bins are visible indicating a broad redshift distribution at this position. Comparing the color-color distributions of two magnitude bins, one can see magnitude dependent effects. At the blue corner, around region 1, a highly occupied region with galaxy redshifts higher $z = 0.9$, which is almost empty at brighter magnitudes. The opposite is visible for Region 3 which has a higher number density at bright magnitudes than in the $22 < R < 24$ brightness bin.

Taking a closer look at the six regions for which we have plotted the redshift distribution, we can indeed see very tight redshift distributions as well as broad ones. In these histograms we additionally show the redshift distribution for faint galaxies with $24 < R < 26$. We refrain from plotting the color-color diagram from this magnitude bin, since the larger photometric errors, broader redshift distributions and larger redshift range would result in a rather non informative diagram.

Investigating Region 1, one can see that this region is basically empty of bright galaxies but becomes the densest region with increasing redshift. This region shows a broad redshift distribution ranging from $z = 0.5$ to $z = 2.5$. At higher magnitudes the increasing photometric errors also result into a contribution of low redshift galaxies from the neighboring region. Region 2 is occupied by star forming galaxies of redshifts $z < 0.5$ as well as ellipticals with low star formation with $z < 0.1$. At faint magnitude also a population of high redshift galaxies with $z \approx 3$ is visible, showing that the chosen filter combination is not able to distinguish between the low and the high redshift population. Regions 3, 4 and 5 are occupied by galaxies with very low star formation rate. In the bright and the medium brightness bin, one can see very tight redshift distributions. The area marked by these three regions is where we expect the red sequence galaxies of cluster galaxies in a redshift range $0.15 < z < 0.8$. This is almost the full redshift range of our cluster sample. The projection of the red sequence from color-magnitude space to color-color space results in a region with increased number density. Finally Region 6 show a broad redshift distribution in the range of $0.4 < z < 1.5$ with only smaller changes with magnitude.

In general one observes a broadening of the redshift distributions when going to fainter magnitudes. This is partially related to the increasing photometric errors of the catalog, but is also a result of a true broadening caused by the increasing number of galaxies at higher redshifts becoming visible at faint magnitudes.

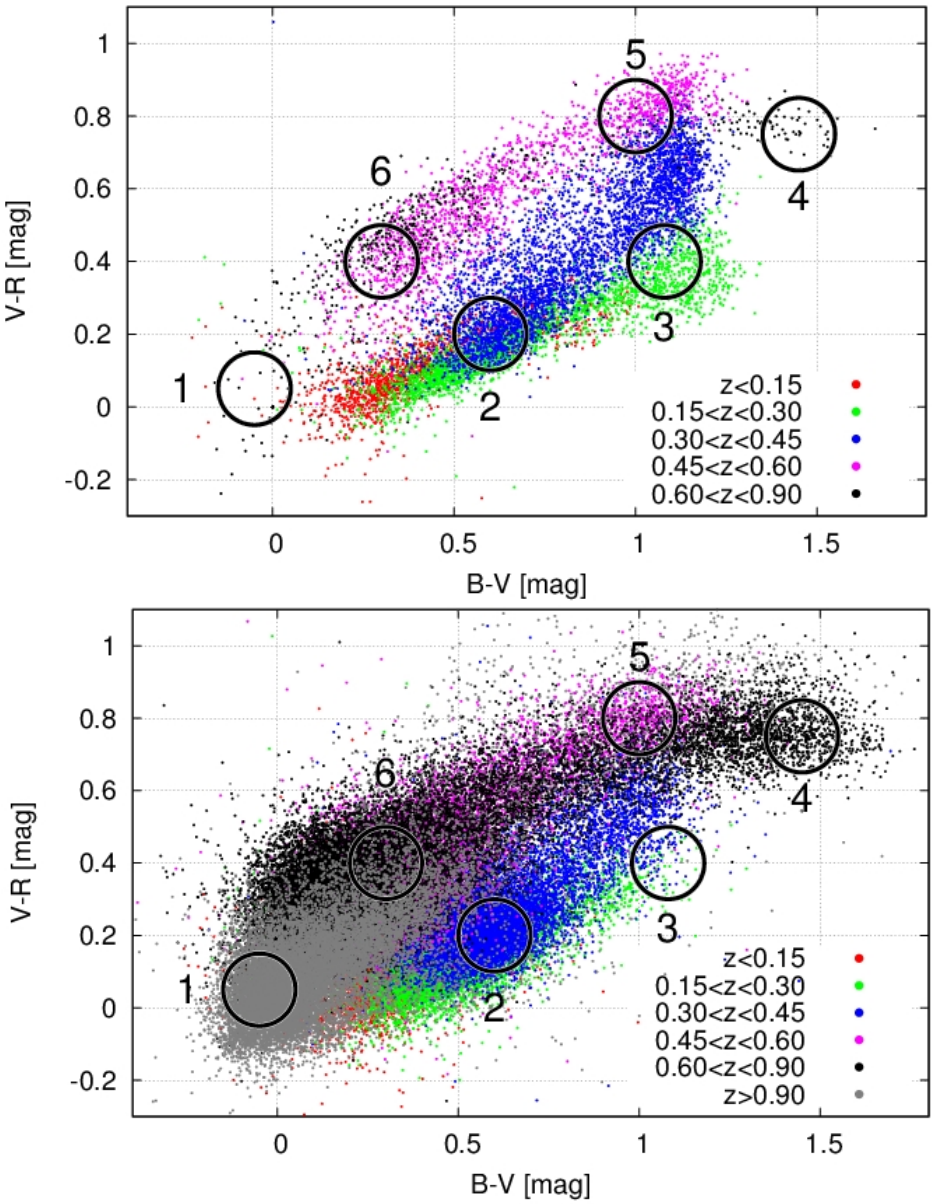

Figure 38: Distribution of COSMOS photo-z galaxies in color-color space. Top: Galaxies brighter than $R = 22$. Bottom: Galaxies between $R = 22$ and $R = 24$. Color coded are different redshift slices. Circles mark different regions for which redshift distributions are shown in fig 39

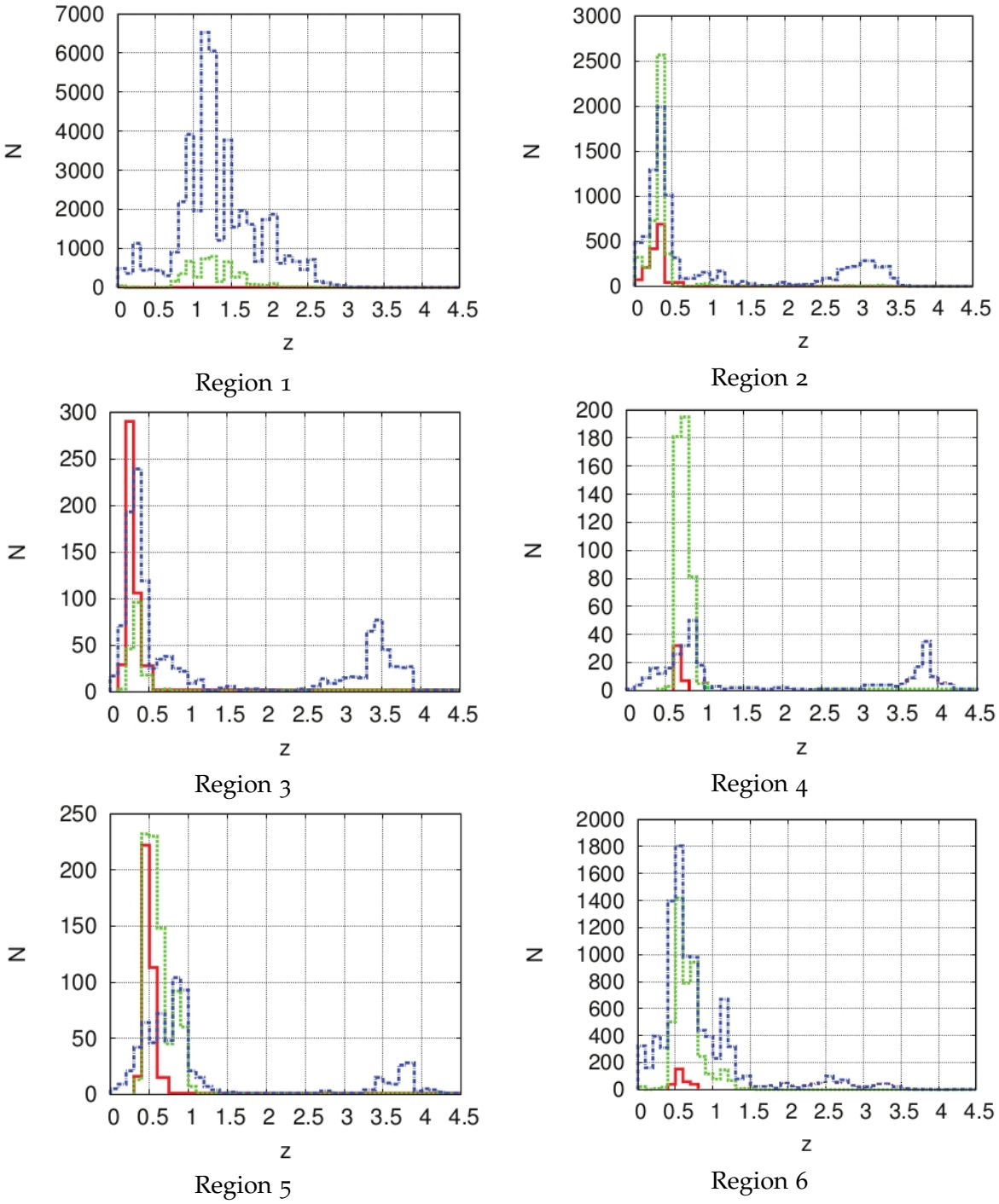

Figure 39: Redshift distribution of galaxies falling into the cc-regions marked in Fig. 38. Red: galaxies brighter than $R = 22$, green: galaxies with $22 < R < 24$, blue: galaxies with $24 < R < 26$

7.4 ESTIMATING CLUSTER REDSHIFTS AS AN ANALYTICAL TOOL

In Section 7.2, we showed that we are able to cross-calibrate the colors of stars in our observations with those in the COSMOS catalog. To check the quality of the color calibration for the galaxies in the catalog, we follow a similar approach as used in High et al. (2009). Those authors tested their implementation of a stellar locus regression by investigating the difference between photometric and spectroscopic redshift cluster redshifts. The spectroscopic redshifts are given for a huge fraction of our cluster detections so that we can estimate the error in color calibration Δc by measuring the scatter in redshift Δz between observed red shift based on colors and the redshift from spectroscopic measurements for those clusters.

Differing from High et al. (2009), we do not fit red sequence models in color-magnitude space for different color combinations, to obtain photometric cluster redshifts.

Instead of that, we search for red sequence galaxies in color-color space. The projection of the red sequence into the cc-plane results in a local overdensity of red galaxies. The color-color plot in the left panel of Figure 40 shows the same galaxies as Figure 38 but highlights galaxies classified as E and SO in the photo-z catalog in red. The right panel shows the mean position of these galaxies as a function of their redshift for the filter combination B, V, R (right track) and for V, R, Z left track. The expected position of the overdensity by red cluster galaxies would therefore fall on these tracks. The panels show that, at low redshifts, the track for the filters B, V, R cross a region with a high amount of star forming galaxies at higher redshifts. For this filter combination, the estimation of the position of the red cluster galaxies might be affected which would lead to additional errors on the photometric redshift.

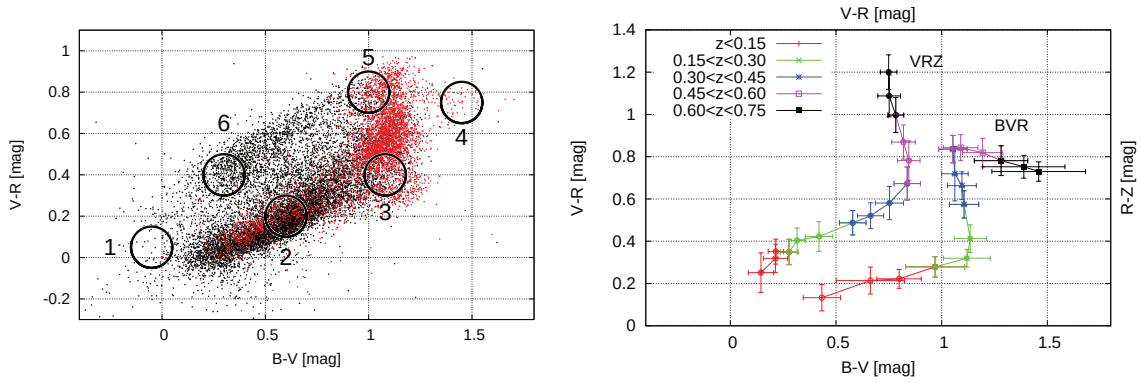

Figure 40: Left: CC-diagram of COSMOS galaxies with R<22 mag. Galaxies classified as E or So are highlighted in red. Right: Binned mean position of elliptical galaxies in color-color space. The color code is similar to Figure 38 the binning is $\Delta z = 0.05$. The right curve belongs to the filter combination B,V,R with corresponding axis labels on the bottom and left. The left curve shows same but for the combination V,R,Z. The corresponding axis labels are on the top and on the right side.

An example can be seen in Fig.41 for MACS1115. The overdensity is clearly visible for this cluster in the left panel, over plotting galaxies from the COSMOS catalog with redshifts similar to the cluster redshift, one can see a very good agreement.

The cluster redshift is derived in an iterative procedure. First, we create a number density map on a regular grid in the cc-plane with galaxies brighter than $R = 23.5$ and within a cluster centric distance of 5 arcmin. The latter criterion ensures that other structures in the observed field do not affect the measurement by creating additional overdensities in the color-color plane. In the presence of massive clusters or absence of other structures

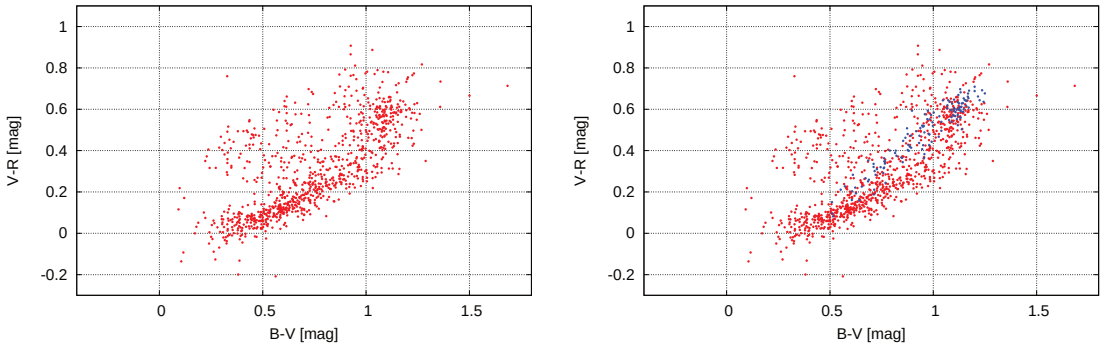

Figure 41: Left: CC-diagram of MACS1115 for galaxies with R<21 mag. Right Similar to the left plot but showing COSMOS galaxies with $0.34 < z < 0.355$ in blue, the cluster redshift is $z = 0.3475$.

this criterion does not affect the measurement. We restrict the number density map to $B - V > 0.8$ to ease the search for the cluster created overdensity.

As overdensity region, we define all pixels around the density peak, which have a pixel value of at least 80 % of the peak value. We use the same grid in color-color space to create a redshift map by using all galaxies in the COSMOS catalog with $R < 23.5$. To obtain an estimate of the cluster redshift, we select all grid cells in the redshift map which lie within the overdensity region found in the density map. The cluster redshift is then derived as the weighted arithmetic mean of the redshift values, where the weights are given by the density measured in the corresponding cc-position in the density map.

After the initial redshift estimate, we refine the magnitude range of the galaxy selection to account for the magnitude dependency of the red sequence. We create new density and redshift maps using only galaxies with $R_{\max} - 1.75 < R < R_{\max}$ where $R_{\max}$ is given by

$$\mathrm{R_{max}} = 21.06 - 5 \times \log_{10}\left(\frac{\mathrm{D}_L(0.3045)}{\mathrm{D}_L(z_d)}\right), \tag{144}$$

where $\mathrm{D}_L(z_d)$ is the luminosity distance based on the cluster redshift derived in the step before. $\mathrm{D}_L(0.3045)$ is the luminosity distance of the cluster we used for calibrating the selection range. We use the refined density map to measure a new redshift estimate for the cluster. This step of refining the magnitude selection and measuring the cluster redshift is repeated iteratively unless the redshift estimate converges to fix value.

We find a root mean square between our color-z and spectroscopic-z of $\sigma = 0.0039$ and a mean difference of $\delta z = 0.001$ for a test sample of 11 clusters. Table 4 shows spectroscopic redshifts and redshifts obtained by our color-color method.

In case of MS1054 a first redshift estimate failed. The investigation of the color-color diagram has revealed a second cluster within the field. Figure 42 shows the cc-diagram for a 6 arcmin aperture centered on MS1054. Since the two overdensities at $V - R \approx 0.8$ and $R - Z \approx 1.3$ and $R - Z \approx 2.0$ are rather shallow, we also show a cc-diagram from another position in the field with same aperture. The second cluster at lower redshift could be identified as STACS J1057.2−0340 with spectroscopic redshift of $z = 0.548$ based on three cluster members. After shrinking the aperture to 3 arcminutes the redshift of MS1054 could be correctly derived.

Based on the left panel of Fig. 40 one can estimate the color dependency on the redshift estimate to be $\delta c \approx \delta z / 0.42$ mag for the given cluster sample. Following from that, the observed scatter in the derived redshift suggest an uncertainty in color of $\sigma_c = 0.009$ mag.

Table 4: Photometric redshifts of clusters: Spectroscopic (z_{spec}) and color-color based photometric redshifts (z_{cc}) for a selection of 12 clusters.

Cluster	z_{spec}	z_{cc}	Filters
MACSJ1359.2−1929	0.447	0.4474	B, V, R
MACSJ1115.8+0129	0.3475	0.3462	V, R, Z
RXJ1504.1−0248	0.2153	0.2094	B, V, R
RXCJ2151.0−0736	0.2841	0.2864	B, V, R
RXCJ2248.7−4431	0.3475	0.3421	B, V, R
RXCJ0019.0−2026	0.2773	0.2792	B, V, R
RXCJ0245.4−5302	0.3018	0.297	B, V, R
RXCJ0532.9−3701	0.2747	0.2734	B, V, R
RXJ1347−1145	0.4510	0.4541	B, V, R
RXJ1347−1145	0.4510	0.4477	V, R, Z
MS1054.4−0321	0.8307	0.837	V, R, Z
Bullet	0.2965	0.291	B, V, R

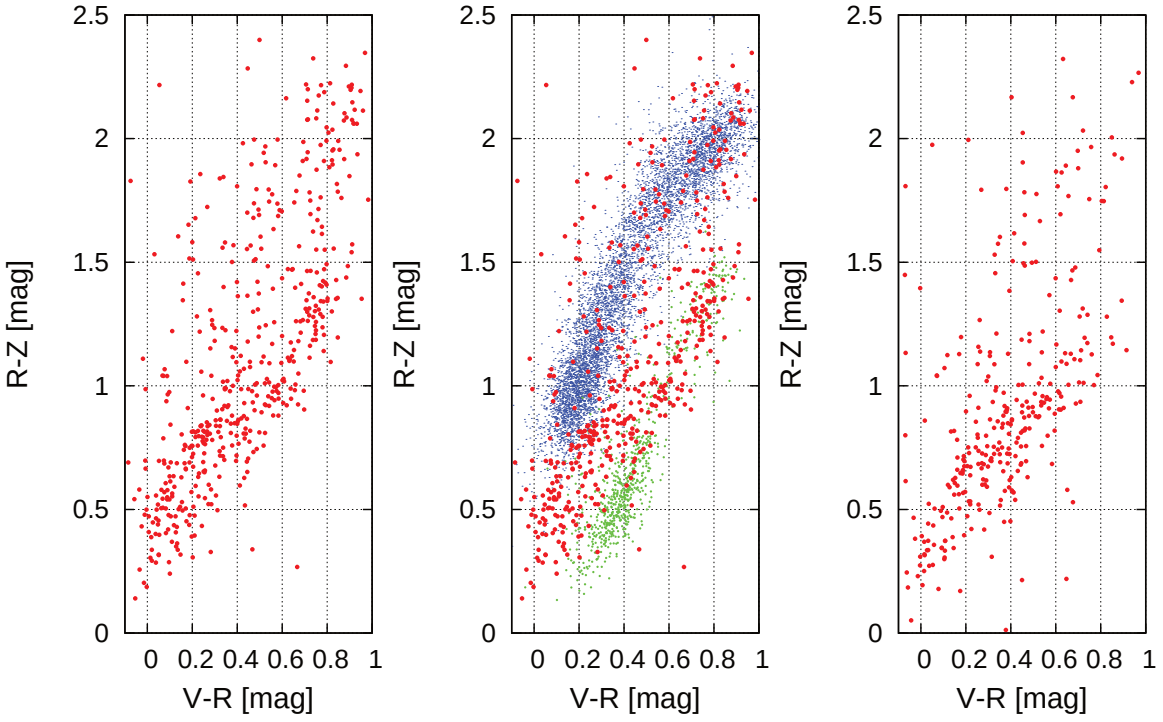

Figure 42: Left: CC-diagram of galaxies with R<23 mag within an aperture of 6 arcmin around MS1054. Middle: Same diagram as left one, but including COSMOS galaxies with $0.78 < z < 0.88$ in blue and galaxies with $0.555 < z < 0.57$ in green. Right: CC-diagram of another position in the MS1054 field with 6 arcmin aperture but not containing a cluster.

Since most of the clusters used to derive this estimate are around $z = 0.3$ and uses the B, V, R filter combination, we preferentially probe the color calibration in $V - R$ direction. To account for that we multiply σ_c by a factor $\sqrt{2}$ and get an accuracy for our color calibration of $\sigma_{cc} \approx 0.013$.

Note that the observed scatter in cluster redshifts is about a factor four smaller than that seen by High et al. (2009) in his test. If this small scatter gets confirmed with larger cluster samples, this would mark a significant increase in accuracy for photometry based cluster redshifts. As a result this would allow to avoid additional spectroscopic follow-up programs for cluster search projects.

7.5 BACKGROUND SELECTION BASED ON COSMOS

The redshift distribution of galaxies in the COSMOS catalog strongly depends on the position in color-color-magnitude space (ccm space). We can use the redshift distributions from COSMOS as redshift probability distributions for our color calibrated cluster data.

To convert the photo-z information in color-color-magnitude space into an background selection, we choose two selection parameters, the angular diameter distance ratio, β_g, and the purity estimator, p_g which estimates probability of a source of being a background galaxy.

Shear and convergence scale linearly with β_g through their scaling with the critical surface mass density, Σ_{crit}. Following from that, the reduced shear g scales strictly monotonic with β_g. Using β_g as selection criterion enables us to exclude regions which carry no or only low signal, as typical for regions dominated by foreground and cluster galaxies.

The purity estimator can help to brake the degeneracy between regions with high galaxy redshifts and high cluster and foreground contamination and regions with smaller galaxy redshifts and low contamination. As the presence of the cluster alters significantly the redshift distribution at low redshifts compared to the distribution in the COSMOS field, the purity estimator can only put a lower limit to the contamination.

To calculate β_g and p_g for each galaxy g in our lensing catalog, we apply the following scheme to each source. We define an elliptical cylinder in ccm space centered on the position of the galaxy in ccm-space. The elliptical base is defined by σ_{c1} and σ_{c2}, which are the measurement errors of the two colors measured for this galaxy. The height of the cylinder is defined by the error of the relative magnitude in the lensing band.

We use this cylinder to select galaxies in the ccm-space of the photo-z catalog. To ensure sufficient statistics, we require at least 50 selected galaxies. If not enough galaxies are selected, we increase the cylinder by 10% in each direction until the minimum number of sources or a maximum size is reached. In the latter case we treat the measurement as outlier and set $\beta_g = 0$. The angular diameter distance, β_g, is then calculated as the weighted mean $\beta(z_d, z_k)$ of the selected galaxies in the photo-z catalog

$$\beta_g = \frac{\sum_{k=1}^{N} w(\Delta c_{1,k}, \Delta c_{2,k}) \beta(z_d, z_k)}{\sum_{k=1}^{N} w(\Delta c_{1,k}, \Delta c_{2,k})}. \tag{145}$$

As weight function, $w(\Delta c_{1,k}, \Delta c_{2,k})$, we use a 2 dimensional Gaussian function with standard deviations σ_{c1} and σ_{c2}. The two parameters $\Delta c_{1,k}$ and $\Delta c_{2,k}$ are the differences in color of the photo-z galaxy k with respect to the lensing catalog galaxy l,

$$\Delta c_{1,k} = c_{1,k} - c_{1,l}, \ \Delta c_{2,k} = c_{2,k} - c_{2,l}. \tag{146}$$

We restrict our weighting to the color-color plane since the magnitude dependency within the cylinder is weak compared the color dependency. We also tested a full 3D weighting but with no significant improvement so that we chose the simpler treatment.

In the same way as β_g we can calculate p_g by replacing $\beta(z_k)$ with the Heaviside step function $\Theta(z_k - z_d)$, where z_d is the redshift of the cluster. This yields

$$p_g = \frac{\sum_{k=1}^{N} w(\Delta c_{1,k}, \Delta c_{2,k})\Theta(z_k - z_d)}{\cdot} \sum_{k=1}^{N} w(\Delta c_{1,k}, \Delta c_{2,k}) \tag{147}$$

A first selection can be made by investigating behavior of the signal to noise of the lensing detection as measured in S-statistics (Equation (115)) maps. We use the Schirmer et al. (2007) filter function for creating S-statistics maps and investigating the behavior of the signal to noise in dependence of the exclusion of galaxies with low β_g. We can find a cut value $\beta_{\mathrm{cut,max}}$, which maximizes the S/N at the position of the cluster. This value marks the point from which on the noise increase by the loss of background galaxies becomes dominant against the gain in signal caused by a cleaner catalog.

The S/N estimator is affected by noise due to the finite number of galaxies, the usage of $\beta_{\mathrm{cut,max}}$ for selection therefore likely bias the mass high. Because of that, we interpret $\beta_{\mathrm{cut,max}}$ as the smallest meaningful cut value which can be applied. To find the final cut parameters for the clusters, we will investigate the dependency of the mass estimate on β_{cut} starting from $\beta_{\mathrm{cut,max}}$ on the full cluster sample.

In Figure 43, we show the dependency of the peak S/N on the number of remaining galaxies in the lensing catalog for two clusters, A907 ($z = 0.153$) and RXC0532 (z=0.274). The red curve is obtained by varying β_{cut} and keeping only galaxies with $\beta_g > \beta_{\mathrm{cut}}$. For comparison we show also the S/N behavior for a selection which excludes bright sources leaving only galaxies with $R_g > R_{\mathrm{cut}}$ in the lensing catalog. Compared to multi-color selections, which are using a rather arbitrary selections, the magnitude selection is beside photometric redshift methods the only one which depends on only one parameter, allowing a direct comparison with our selection method.

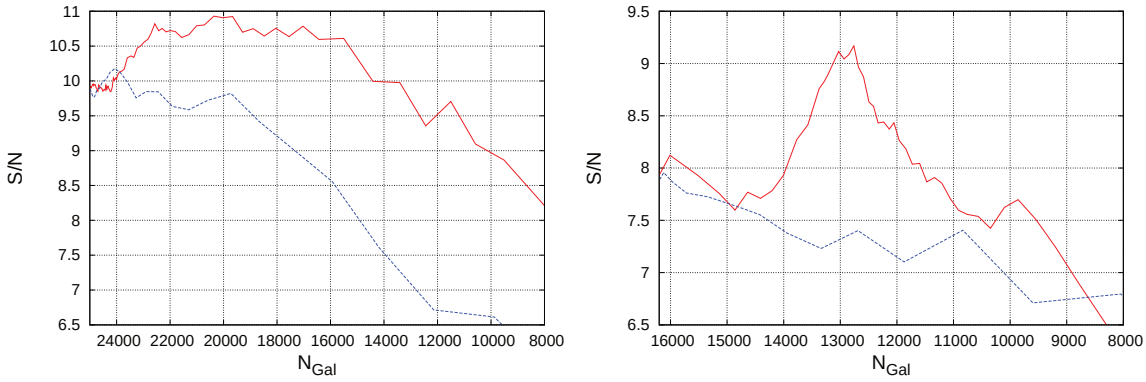

Figure 43: Peak S/N vs remaining background galaxies using β_g for selection (red) and magnitude cut (blue) for A907 (left) and RXC0532 (right).

In Figure 44 we show the color-color diagram for RXC0532 at $z = 0.275$, for the same two magnitude ranges as used in Figure 38. Blue dots show sources with $\beta_g < \beta_{\mathrm{cut,max}}$ which are expected to comprise mostly foreground and cluster galaxies. Plotted in red are galaxies expected to be background galaxies. The comparison with the COSMOS field shows that we exclude galaxies with $z < 0.4$. For the bright magnitude bin, it also shows an overdensity of galaxies at the position of Region 3 in the color-color diagram of COSMOS. This is the overdensity created by red sequence galaxies of the cluster. Comparing the color-color diagrams for the fainter galaxies, we see less galaxies in Region 4 and 5, indicating the absence of massive structures with $0.5 < z < 0.9$ in our field. Comparing the two magnitude ranges we see again the increase of the source density at Region 1 and a decrease in Region 3.

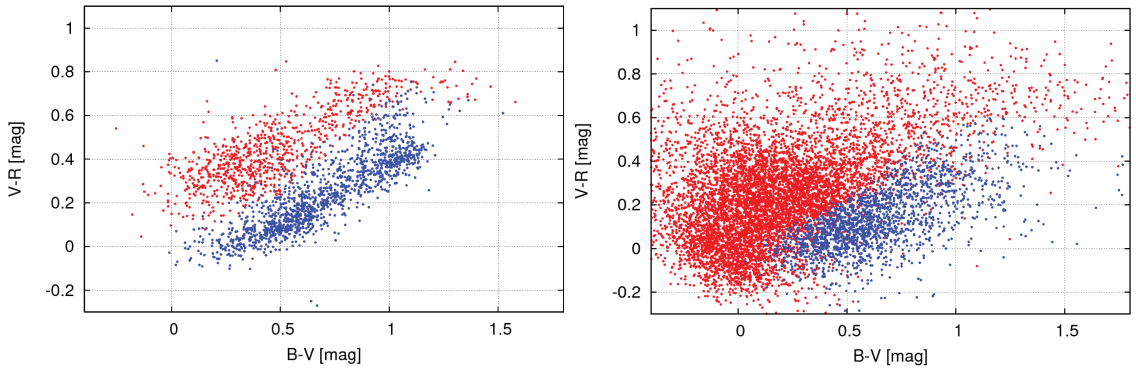

Figure 44: Left panel: Galaxies in the RXCJ0532 field brighter than $R = 22$ mag and $\beta_g > \beta_{\mathrm{cut,max}}$ shown in red and $\beta_g < \beta_{\mathrm{cut,max}}$ in blue. Right panel: Same plot, but for the magnitude range $22 < R < 24$ mag

Finally we illustrate the selection in color-color-magnitude space in Figure 45. Watching from the blue to the red and from the red to the blue corner one can see the smooth magnitude dependency of the selection. At higher magnitudes bluer galaxies tend to be included in the background catalog. This is caused by larger photometric errors which results in the scattering of higher redshift sources in to the color-color space previously dominated by cluster and foreground galaxies. Also visible is the red sequence of galaxies, as large number of bright galaxies with almost similar color.

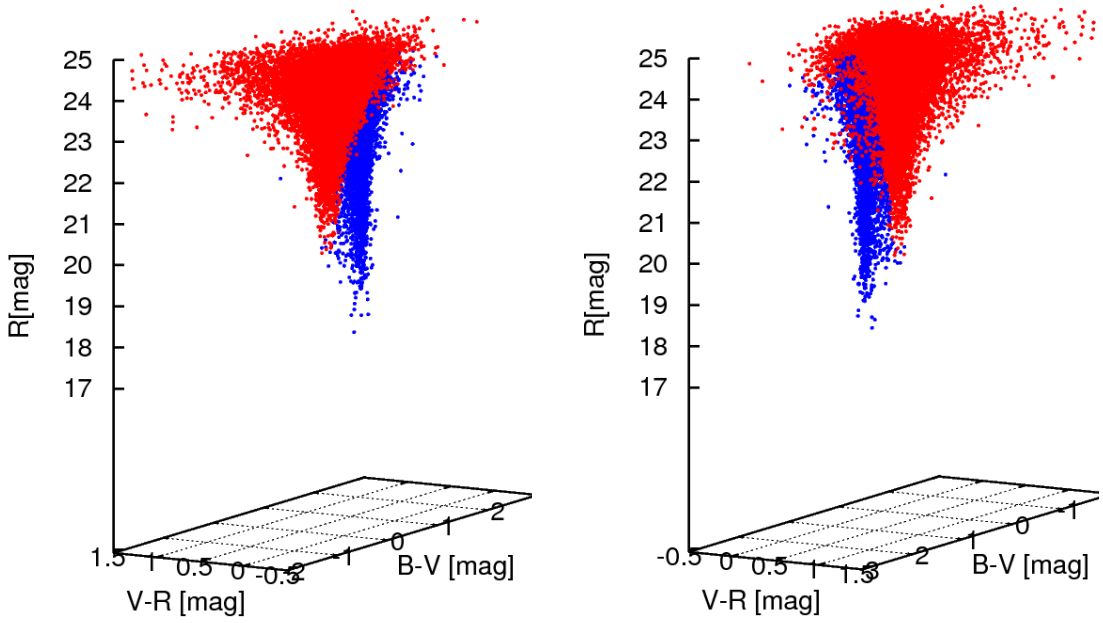

Figure 45: 3D illustration of the background selection of RXC0532. Left: As seen from the blue to the red corner. Right: Seen from the red to the blue corner. The color code is the same as in Figure 44.

7.6 LIMITS OF THE BACKGROUND SELECTION

Various factors limit the potential of the presented three-filter background selection. We separate them into three major branches: limitations caused by the number and type of available filters, limitations based on the characteristics of the reference catalog and limitations based on the implementation of the method.

7.6.1 *Limitations caused by number and type of filters*

The method presented in this thesis uses only three filters but can in principle be extended to larger number of filters. This would then become more similar to other empirical redshifts method such as Brunner et al. (1999) or Lima et al. (2008), but directly using probability distributions in β rather than in redshift and a high precision photo-z catalog. Reducing to two filters would result in a significant loss of constraining power regarding the redshift distributions and would not allow to exclude blue cluster members from the background sample. Also the used filter bands have a crucial influence on the performance of the background selection. Discussing all possible combinations is beyond the scope of this thesis.

In general it is assumed that bluer bands help to constrain the redshifts at lower redshift, while redder bands help to constrain the redshifts at higher redshift. This is not strictly true and can already be seen in the B, V, R color diagrams from COSMOS. Here the B filter only helps to discriminate between the high redshift galaxies around Region 1 and low redshift galaxies from Region 2 to 3. The discrimination of galaxy redshifts up to $z \approx 0.6$ is possible due to the $V - R$ color. For all of our clusters we have either B or V band observations to ensure sufficient resolution at low redshifts and at least one redder band for lensing shape measurements and constraining higher redshifts. The used filter sets are sufficient in their constraining ability for clusters up to $z = 0.9$, depending on the used filter combination. At higher cluster redshifts redder filter combinations are suggested to constrain the redshifts for galaxies occupying Region 1 in the B, V, R color-color diagram.

7.6.2 *Limitations caused by the reference catalog*

The method assumes that the reference catalogue provides a fair sampling of the full color-color-magnitude space which can be occupied by galaxies. If a region in ccm-space is not populated by the reference catalog, but occupied by galaxies in the observed cluster field, an estimate of β_g may not be possible or the result is likely biased.

The COSMOS field extend over a size of two square degrees, the volume probed at low redshift is therefore small and does not include clusters or massive groups below $z = 0.15$. This results in a lack of galaxies, sampling the region of the red sequence for clusters at this redshift or below. Since the galaxies closest to the expected position in ccm-space of the red sequence for clusters at $z < 0.15$ have only marginally higher redshifts, the bias is small. Hence, the signal optimization of the background selection will also exclude these galaxies, but $\beta_{\mathrm{cut,max}}$ might slightly shift to higher values. Due to the exclusion of these galaxies from the background sample, the mass estimate will not be affected. For higher redshifts the ccm-space of red sequence galaxies is sufficiently covered. The limiting magnitude of $R \approx 26.2$ marks the end of the unbiased sampling of the ccm-space, deeper imaging data can not be calibrated with this reference catalog.

Another factor which limits the performance of the background selection is cosmic variance. The method relies on the assumption that the redshift distribution of the reference

catalog represents the mean distribution of the sky. The scatter introduced by cosmic variance on the mean redshift of a COSMOS sized field can be estimated to be of the order of 3%, following the outcomes from van Waerbeke et al. (2006). The translation of this into the distribution of β for different cluster redshifts is not clear, since the scatter induced by cosmic variance is different at different cluster redshifts.

Cosmic variance can influence the background selection in three ways. First it leaves regions in color-color-magnitude space unsampled as discussed before. Second, some regions in ccm-space are under or over populated by galaxies. As example, if the reference catalog was chosen to preferentially include or exclude massive structures, this would affect the number of sources in Regions 3 to 5 in Figure 38. The third effect is that it modifies the redshift distributions at ccm-regions with broad or multiply peaked redshift distributions.

Our background selection estimates β_g for each galaxy, therefore it automatically accounts for differences in source densities in ccm-space as long as the redshift distribution in the specific ccm-regions are not altered. Assuming that holes in the sampling of the ccm-space only exist for very low redshifts, which are excluded from the background sample, our method is only affected by the third effect which modifies the redshift distribution.

To estimate how big the scatter in mean angular diameter distance ratio, $\langle\beta\rangle$, induced by cosmic variance might be, and how far the background selection can reduce the scatter, we explored the behavior of this quantity in 9 individual COSMOS subfields of $30' \times 30'$. The size matches the typical field size of our observations. We apply our background selection on these fields assuming three different cluster redshifts ($z = 0.18$, $z = 0.275$, $z = 0.45$). We are using $\beta_{\mathrm{cut,max}}$ parameters found to be typical for clusters at that redshifts in our sample. After application of the background selection, we measure the mean lensing depth $\langle\beta_{\mathrm{mes}}\rangle_i$ based on our method and the mean lensing depth $\langle\beta_{\mathrm{true}}\rangle_i$ obtained by using the original COSMOS photo-z redshifts of each galaxy for each individual field i.

The upper plot of Figure 46 shows the mean of the ratio $\langle\beta_{\mathrm{mes}}\rangle_i / \langle\beta_{\mathrm{true}}\rangle_i$ over all subfields as a function of the R band magnitude limit. The error bars show the standard deviation of mean ratios. The plot indicates that we are able to recover the true lensing depth at subpercent level for cluster observations exceeding limiting magnitudes of 24.5 and moderate cluster redshifts.

The plot in the middle of the same figure illustrates the scatter of the true mean lensing depth between the subfields, induced by cosmic variance in dependence of the magnitude cut. The plot shows the measured standard deviation, σ_{true}, of the $\langle\beta_{\mathrm{true}}\rangle_i$ distribution, normalized with mean value, $\langle\langle\beta_{\mathrm{true}}\rangle_i\rangle$, as a function of the limiting magnitude.

The scatter introduced by cosmic variance is only $1-3\%$ for the typical depth of our observations but depends strongly on cluster redshift and magnitude limit. Due to the case that the different fields are subfields from one single field, the individual redshift distributions are partially correlated. Therefore the derived values in top and the middle plot of Figure 46 are likely underestimating the true scatter between uncorrelated fields. However, the middle plot can be interpreted as a lower limit of the scatter in $\langle\beta_{\mathrm{mes}}\rangle$ induced by cosmic variance.

The last panel in Figure 46 shows ratio of the standard deviation of the differences $d_i = \langle\beta_{\mathrm{mes}}\rangle_i - \langle\beta_{\mathrm{true}}\rangle_i$, here called σ_{mes}, and the true scatter between the subfields σ_{true}. A perfect recovery of the mean lensing depth would result in a ratio $\sigma_{\mathrm{mes}}/\sigma_{\mathrm{true}} = 0$. Ratios larger or equal unity are expected, if the method does not account for effects from cosmic variance or if the measurement error on $\langle\beta_{\mathrm{mes}}\rangle$ is larger than the scatter induced by cosmic variance.

The plot at the bottom of Figure 46 shows ratios of 0.6 to 0.8 over a huge range of magnitude limits. This shows that the scatter between the fields can be reduced by $20-40\%$

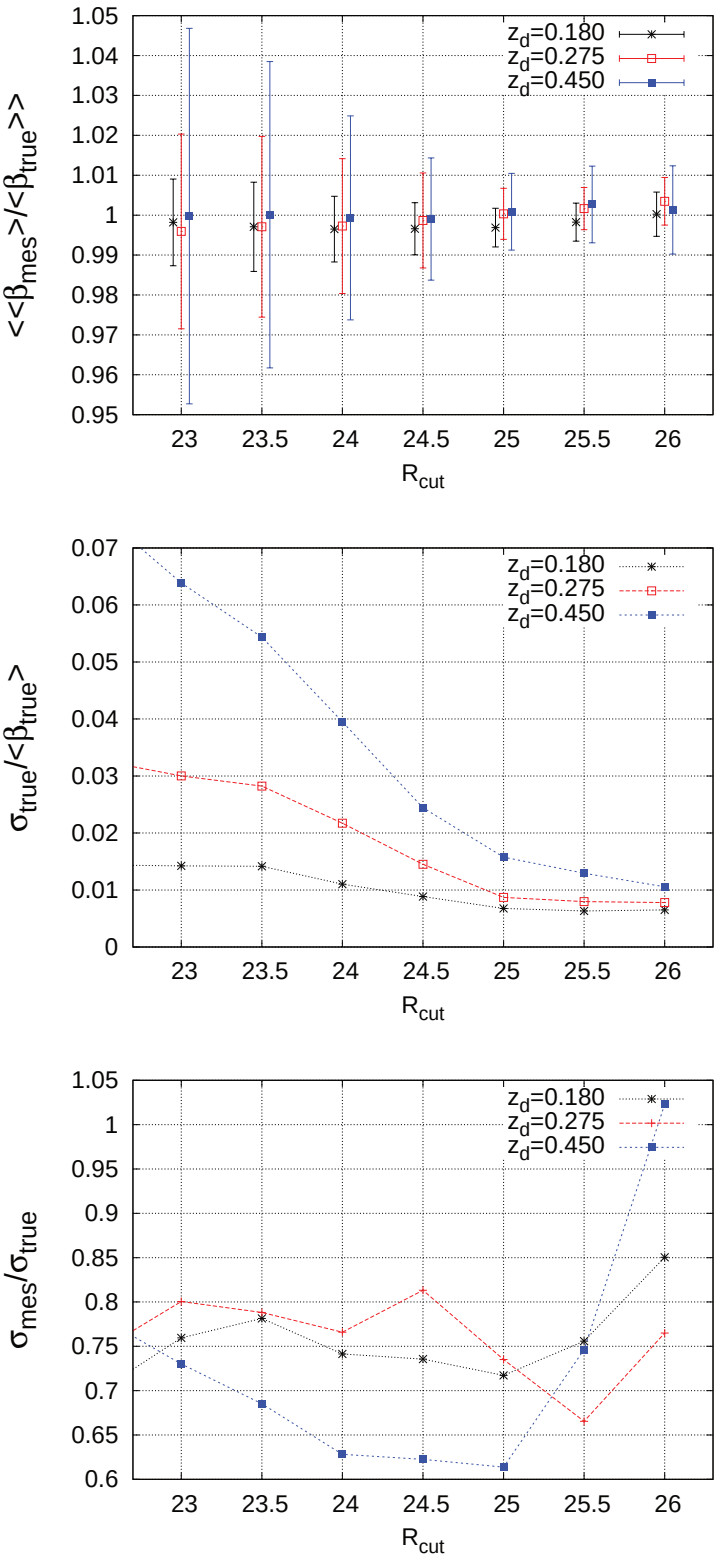

Figure 46: Top: Mean ratio of $\langle\beta_{\mathrm{mes},i}\rangle / \langle\beta_{\mathrm{true},i}\rangle$ against R band magnitude limit. Middle: Scatter of the true mean lensing depth over the mean of the mean lensing depth. Bottom: Ratio of the scatter of $\langle\beta_{\mathrm{mes},i}\rangle - \langle\beta_{\mathrm{true},i}\rangle$ over the true scatter of $\langle\beta_{\mathrm{true},i}\rangle$ as a function of the R band magnitude cut.

with respect to the scatter introduced by cosmic variance. At high limiting magnitudes, the

effects caused by cosmic variance becomes similar small as the scatter introduced by the variance of the redshift distributions in the individual ccm regions.

The outcome of the middle and the lower plot of Figure 46 have two implications. First we can put a lower limit of the scatter induced by cosmic variance depending on image depth and cluster distance. The second implication is, that the cosmic variance induced change of the redshift probability distribution is dominant against the induced change of the density distribution in ccm-space. The reduction of the cosmic variance induced scatter, as seen in Panel c), does not only indicate that we can reduce the scatter in our cluster fields, it also indicates that we can partially account for the cosmic variance in our reference catalog as well.

The bottom plot shows also that our method is more effective to reduce the scatter for clusters at higher redshift. This may appear counterintuitive: the higher the redshift of the cluster, the higher the redshifts of background galaxies behind it, which implies a reduced impact of cosmic variance. For the typical selection parameters for a cluster at $z = 0.45$ and limiting magnitude of $R_{\rm cut} = 25$, we get a remaining contamination of $\sim 15\%$, while for clusters at $z = 0.3$ we typically find about $\sim 4\%$ contamination. The better estimate of the foreground contamination is therefore the reason why higher redshift clusters benefit more from the background selection method.

For these simulations, we used the original colors given in the COSMOS catalog, to obtain the best possible match between $\langle\beta_{\rm mes}\rangle_i$ and $\langle\beta_{\rm true}\rangle_i$. To check if it affects the result, we created 20 additional realizations of 3 different subfields, by varying the colors within their measurement errors. This mimics 20 observations of the same field with similar depth, for three out of the nine sub-fields. The scatter we find in $\langle\beta_{\rm mes}\rangle$ between the 20 different realizations is about one order of magnitude smaller than the observed scatter between the different fields. The mean of the different realizations is consistent with the value obtained using the exact colors. This means that the results shown in Figure 46 are not affected by choice of using the exact colors given in the reference catalog.

7.6.3 *Implementation based limitations*

The implementation of a method is in most cases a compromise between accuracy and computational time. Also time available to spend on coding and optimization play a role on the performance of a method.

As an example, our code creates a lookup table of $\beta(z)$ for redshifts between 0 and 10 separated by steps $\Delta z = 0.0005$. This table is then used to obtain β for each galaxy in our reference catalog. This simple step strongly reduces the computing time compared to individual calculation of all ≈ 780000 galaxies in the cosmos catalog, but is paid by the discretization of the redshift space.

The resolution in redshift is chosen to be far smaller than the typical accuracy of photometric redshifts and should therefore not affect the accuracy of the final result. A similar approach for the color-color-magnitude space is not applicable due to the fact that a three-dimensional grid with grid size similar to the photometric errors would have at least ten times more pixels as galaxies in our lensing catalog.

The individual treatment of the galaxies in the reference catalog as well as that of the lensing catalog put limitations on the catalog sizes, if a maximum computing time is given. For a typical amount of 20000 galaxies in the lensing catalog, the code needs about 30 minutes to obtain β_g for all galaxies. In comparison, the simulations of the previous subsection contain about 100000 galaxies, because of the absence of shape measurement related filtering and the higher depth of the COSMOS data compared to the mean depth of our observations. These fields take already two hours computing time. While the computing

time scales roughly linear to the amount of lensing sources, this is possibly not the case for the size of the reference catalog. The usage of larger galaxy samples especially in the reference catalog may result in a huge non-linear increase of the computing time. There current implementation is therefore limited to reference catalogs which do not significantly exceed the number of sources in the COSMOS field.

Another step to keep the implementation fast is the usage of the point estimator β_g (Eq.(145)) for each galaxy. This replaces the probability distribution in β by its mean $\bar{\beta}$. The expectation value of g for a broad distribution in β is

$$\langle g \rangle = \langle \frac{\beta\gamma'}{1-\beta\kappa'} \rangle \neq \langle \frac{\bar{\beta}\gamma'}{1-\bar{\beta}\kappa'} \rangle, \tag{148}$$

where $\gamma' = \gamma/\beta$ and $\kappa' = \kappa/\beta$. The inequality becomes stronger at higher convergence. In principle our method would allow to obtain the probability distributions of β for each source, but would need additional computing time to express the distribution either in a parametrized or in a histogram form. We have shown that the redshift distribution at low redshift is tight, actually this is mostly true for higher redshift galaxies too, thanks to the flat behavior of β at these redshifts, as seen in Figure 47.

Since we restrict our profile fits to the weak lensing regime, the convergence can be assumed to be small. This further minimizes the error caused by the usage a point estimator.

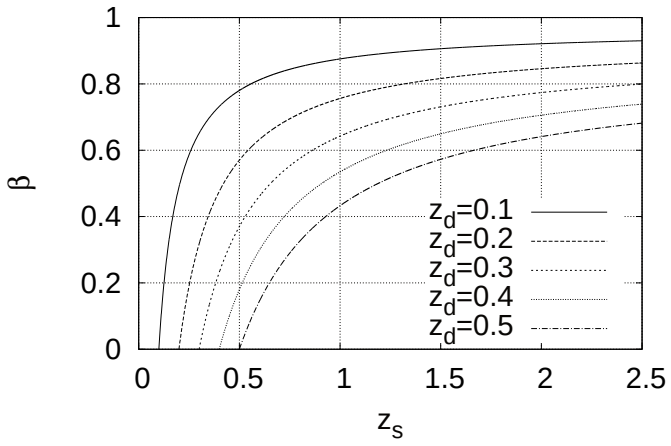

Figure 47: Angular diameter distance ratio β over source redshift for different cluster redshifts, for the standard ΛCDM model.

To evaluate if the point estimator produces a significant bias, we performed another set of simulations. We created 10 mock observations by randomly selecting 100,000 galaxies from the cosmos catalog for each field. The random selection avoid effects caused by cosmic variance which are visible in the previous simulations. We randomly distribute these galaxies in a $30' \times 30'$ field and assign a reduced tangential shear corresponding to a NFW density profile with $r_{200} = 1.98$ Mpc and $c = 7.0$. We further assigned a very small scatter of $\sigma_\varepsilon = 0.01$ to the ellipticities, to apply the mass measurement code without modifications.The same lens is simulated for the two different redshifts $z = 0.18$ and $z = 0.45$.

Figure 48 shows the mass ratio between measured and true mass in dependence of the limiting magnitude, for two different lens redshifts. Each bin shows the average and standard deviation obtained from 10 simulated observations. We show the result obtained with the simple point estimator and with an additional correction as described in Seitz and Schneider (1997). The obtained mass estimate is consistent with no bias at all magnitudes. However, a slight tendency to overestimate the mass by $\approx 0.4\%$ is indicated. Given the

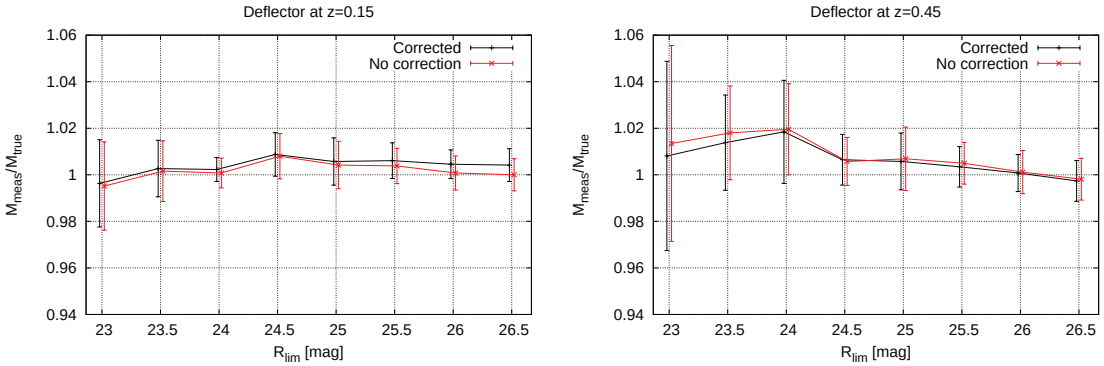

Figure 48: Mass ratio $M_{\text{meas}}/M_{\text{true}}$ over faint magnitude limit of galaxies included in the shear catalog, for a NFW lens at $z = 0.15$ left and the same lens at $z = 0.45$. Black: Results based on our standard point estimator. Red: Additionally applying correction for broad redshift distributions in Seitz and Schneider (1997).

typical statistical error on mass, of about 25and the limited size of our sample, we conclude that the effect of point estimator is insignificant. The difference between the uncorrected and corrected point estimator is also insignificant, indicating that indeed the width of the β distributions are in general small.

7.7 CONTAMINATION BY CLUSTER AND FOREGROUND GALAXIES

The background selection we developed here, as well as other commonly used methods, do not result in a background sample which is completely free of foreground or cluster galaxies. This is not necessary if one assumes that the ellipticities of foreground and cluster galaxies are randomly distributed. The effect of a potential alignment between the cluster galaxies is currently under investigation, yielding contradicting results depending on the cluster redshift (Pereira and Kuhn, 2005; Hung and Ebeling, 2012). If the assumption holds, contamination do not add a positive or negative signal to the shear signal, but reduce it by the fraction of contamination.

For mass estimates of large cluster samples, one can assume that foreground galaxies are randomly distributed and not spatially correlated with the cluster position. In classical three filter methods as described in Section 7.1, the foreground contamination is already accounted in the calculation of the mean lensing depth. This comes from the definition that β is zero for sources at cluster redshift or lower. The mean lensing depth therefore gets diluted in the same way as the shear gets diluted. The same is true for our method, but with the advantage that our method can also account for a varying amount of foreground contamination due to the individual treatment of the galaxies as seen in Fig.46.

The contamination by cluster galaxies is in general more difficult to account for, since the amount of contamination depends on the total amount of cluster galaxies which scales with the cluster mass. Also its correlation with cluster distance results in position dependent effect. Contamination by cluster galaxies would therefore also modify the shape of the shear profile. Our background selection excludes blue as well as red cluster members to a large fraction, minimizing this effect. In a similar way as for cosmic variance our method also partially accounts for the increased amount of cluster contamination. Remaining cluster galaxies are likely close to but outside of the main color-color region of cluster galaxies. Those regions have usually only marginally higher redshifts than the cluster and a higher contamination fraction than other regions in ccm-space. Following from that, remaining

cluster galaxies would have a small β_g and therefore affect the mass estimate less than in other three filter methods which assume $\beta_g = \langle\beta\rangle$ for all galaxies[2].

A frequently used method to trace contamination by cluster galaxies is the number density of sources as a function of the radial distance to the cluster center. The usual assumption is that a clean sample would have a flat number density profile and contamination by cluster galaxies would show up by an increase of the number density towards the cluster center. The interpretation of these plots is in reality more difficult, since there are several effects counteracting.

The magnification effect can create a similar or a counteracting number density profile, depending on the brightness and size distribution of the background galaxy sample. Additionally to that, effects such as the obscuration by cluster and foreground galaxies, holes in the dataset created by bright sources, changes in the depth of the field and small scale clustering galaxies complicate a correct estimate of the contamination. Finally one has also to account for a next neighbor filtering in the lensing catalog, which excludes close source pairs from the catalog to avoid incorrect shape measurements. Since the total number density of sources and therefore the probability of close pairs increase towards the cluster center, this filter has a radial dependency. This effect is difficult to model, therefore some authors like Applegate et al. (2012) use an other source catalog for their contamination estimate than the final lensing catalog. However, close pairs not only affect their individual shear measurements but also their photometry, resulting in the probability that the lensing catalog might be cleaner than other catalogs.

The number density plots of the lensing catalogs seen in Figure 49 are accounting for most of the measurement effects except of the next neighbor filtering and small scale clustering. For RXC 1504 we had additionally to account for the different image depths caused by the overlapping and non-overlapping regions of the two different pointings.

A usual method to correct for cluster contamination is the fit of a contamination profile to the radially binned number density. Under the assumption that a clean background sample is flat, the fitted profile would directly yield an estimate of the contamination fraction. As visible in Figure 49, in our case all plots show a depletion towards the cluster center[3]. Since we can not completely disentangle the effects of magnification and next neighbor filtering we do not claim to detect a magnification signal in these clusters. The depletion shows that the classical method assuming a flat clean background can not be applied. The usage of number density plots for contamination correction therefore needs the right modeling of the magnification bias signal, as well as the next neighbor filtering. To the knowledge of the author this was not done by any author using this correction method.

Given its link to cluster galaxy contamination and its possible use as a mass estimator through the magnification bias, it is tempting to investigate the observed depletion in greater detail. However, the typical mean values of the purity estimator are ranging from 0.86 ($z = 0.45$) to 0.98 ($z = 0.15$) including foreground contamination, and the uncertainties of such number densities profiles do neither promise to give greater insights into cluster contamination, nor strong constrains in mass estimates based on magnification.

An alternative approach to number density profile is to investigate the shear profile of two subsets of the background sample. Since we assume that due to the smooth variation of the redshifts in the cc-plane, the low redshift regions are more contaminated than the high redshift ones, we can split the background sample at its median β. To compare both

2 Lensing methods using weights based on detection S/N or related estimators are more affected by contamination because of the higher mean brightness of cluster galaxies compared to the full background sample. Contaminating cluster galaxies therefore tend to have a higher weight as the average background galaxy.

3 This depletion is also visible in pre-KSB catalogs but less prominent.

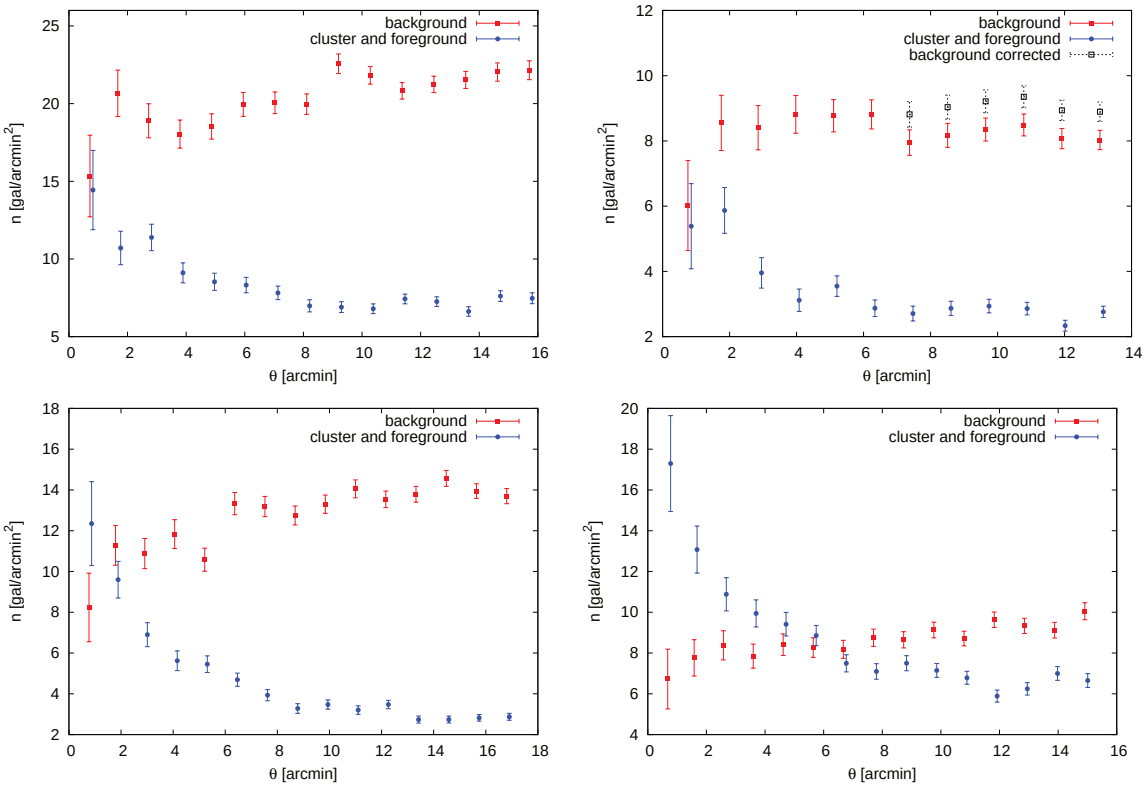

Figure 49: Binned galaxy number density. Top left: A907 ($z = 0.15$). Top right: RXC1504 ($z = 0.22$). Bottom left: RXC0532 ($z = 0.27$). Bottom right: RXC1347 ($z = 0.45$). Blue circles: sources excluded from the lensing catalog, red squares: galaxies included in the lensing catalog, black squares: corrected for variation in image depth due to two different pointings in RXC1504

profiles, one has to rescale the shear to a common β. This is done using the weak lensing approximation $g \approx \gamma$, which results a linear scaling between angular diameter distance and reduced shear $g \propto \beta$. The advantage of the method is that it is independent on the next neighbor filtering, small-scale clustering and other effects which affect number density plots. The disadvantage is that splitting the background sample in two, results in two very noisy profiles. This limits the conclusions we can draw from this method.

Figure 50 shows the shear plots for the same four example clusters as shown in Fig.49. As the contamination should increase towards the cluster center the difference between both subsamples should be most pronounced in the central bins. For all clusters we do not see a significantly higher reduced shear for the high redshift subsample than that of the low redshift one. Following from that, we do not see evidence of significant contamination by cluster galaxies.

While this method is mostly indicative for our mostly shallow data with about $n \approx 10$ background galaxies per square arc minute, deeper lensing data such as space-based data sets might be able to use this method for modeling remaining cluster contamination.

For our cluster sample we conclude, that the remaining contamination of cluster galaxies is small and preferentially classified as sources only slightly above the cluster redshift, which result in a down-weighting of these sources in the mass estimate. the affect of the foreground contamination is statistically accounted for in the calculation of β_i. Additionally, our background method accounts, at least partially for variance in the foreground contamination. We therefore do not apply additional corrections on our mass profile fits.

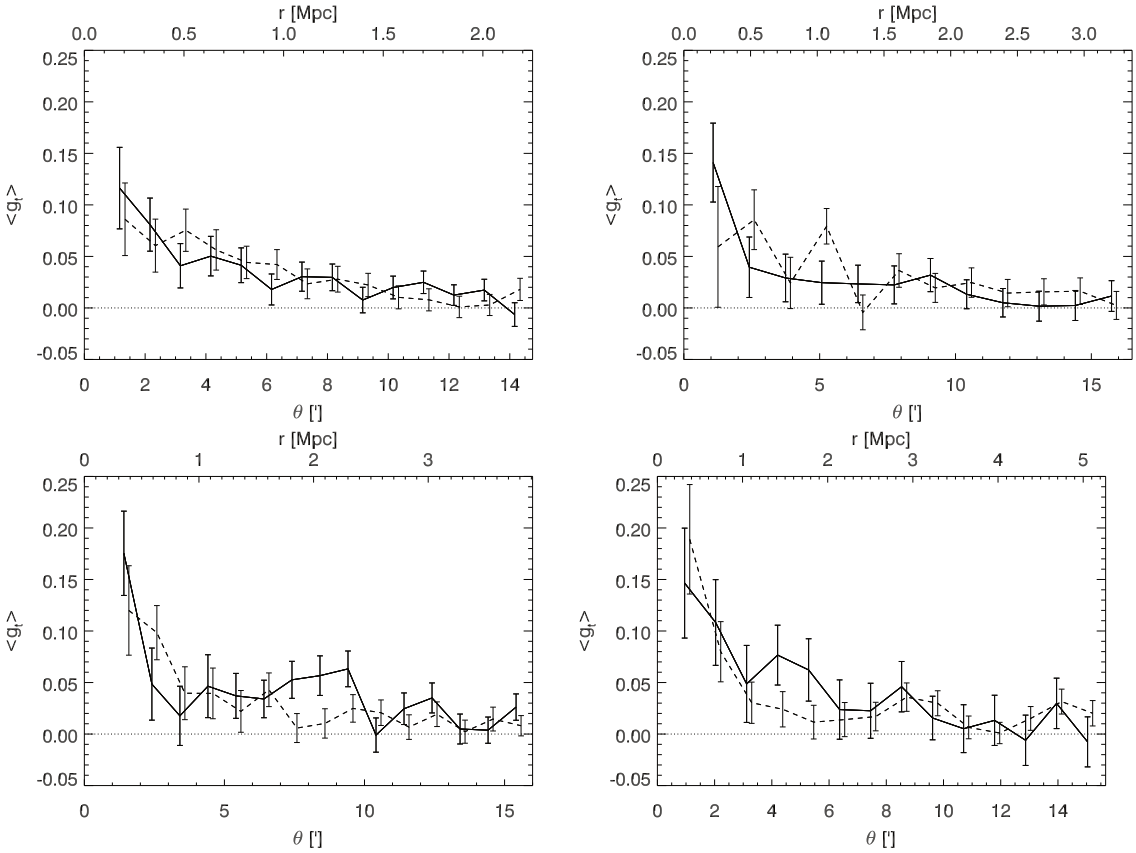

Figure 50: Binned tangential shear in dependency from the cluster centric distance: Top left: A907 ($z = 0.15$). Top right: RXC1504 ($z = 0.22$). Bottom left: RXC0532 ($z = 0.27$). Bottom right: RXC1347 ($z = 0.45$). The continuous line represents the low redshift subsample, the dashed line the high redshift background subsample. Profiles are scaled to the same lensing depth.

7.8 CONTAMINATION BY STARS

The estimate of the half-light radius becomes increasingly noisy for faint sources. Together with the seeing conditions, this limits the ability to distinguish between stars and galaxies, for faint and small galaxies. We follow a similar approach as described in Israel et al. (2010b) and include sources with half light radii $s_{\rm ana} < r_{\rm h} < s_{\rm max}$ and $R > 23.5$. The lower boundary is $s_{\rm ana} \approx 0.95 s_{\rm max}$, which corresponds typically to the mean seeing of the images (see Figure 29).

The magnitude limit of $R = 23.5$ is about one magnitude fainter than that typically used in Israel et al. (2012). This is compensated by the inclusion of sources within the same half-light radius range as described before but with $m_{\rm bright} < R < 23.5$, which do not have more than 10 stars within one sigma distance in color-color space. For that we choose the stellar locus from COSMOS used before for the color calibration, as a reference locus. This criteria excludes all main sequence stars, as well as small galaxies consistent in color with the stellar locus. The majority of the galaxies in that brightness and size range are occupying the Regions 1 and 6 described in Section 7.3, making this additional color selection quite efficient in distinguishing between stars and galaxies.

The limitation to $R_{\rm source} = 23.5$ for this kind of selection has two reasons. The increasing photometric errors to fainter magnitudes result in an exclusion of an increasingly large area in color-color space, reaching regions like Region 1, which are densely populated by

galaxies. While this limitation depends on the typical depth of our images, this limit is further supported by the following consideration.

The absolute magnitudes of main sequence stars depends on their mass and due to the lower mass limit of stars for fusing Helium in their center, a lower limit of about $M_V \approx 17$ mag can be assumed for their absolute magnitudes (Henry, 2004). Assuming a typical $V - R$ color of 1.2 mag for the low mass stars, the limit of $R_{source} = 23.5$ exclude all main sequence stars within a distance of about 350 pc from the sun.

The number density of stars perpendicular to the galactic plane can be described by a sum exponential profiles, describing a thin and a thick disk component and a halo component (Jurić et al., 2008). Using a simplified model with only one exponential function, Jurić et al. (2008) found a scale height of $h \approx 270$ pc. Assuming this simplified model we exclude about 60% of all stars down to 45°galactic latitude. Note that we used here the faint limit of the main sequence stars, the average brightness is likely higher resulting in a even higher fraction of stars, which fall within the $R_{source} = 23.5$ limit.

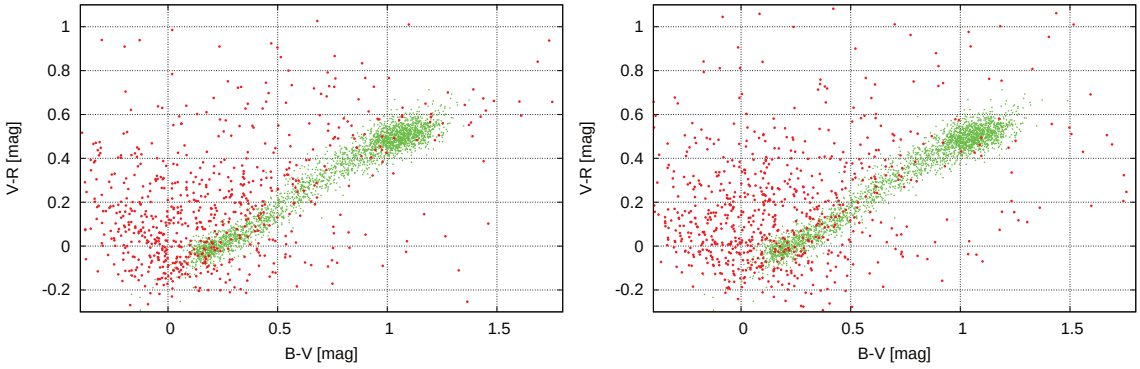

Figure 51: Left: Color-color diagram for sources with $23.5 < R_{source} < 24.5$ and 1.7 px $< r_h <$ 1.82 px in the field of RXC0532 in red. The stellar locus of stars in the COSMOS field with $R < 22$ are plotted in green. Right: The similar to the left plot but for 2.0 px $< r_h <$ 2.1 px.

In the left plot of Figure 51, we show sources with $23.5 < R_{source} < 24.5$ and 1.7px $< r_h <$ 1.82px for RXC0532. From the size-magnitude diagram for this cluster field in Figure 29, we know that this is the size range expected to be contaminated by stars. In right plot of the same figure, we show sources of the same cluster field with source sizes of 2.0px $< r_h <$ 2.1px, which is close but clearly outside the size region of stars. Highlighted in green is the stellar locus for this filter combination. One can see that both color-color diagrams are very similar. Sources at the position of the stellar locus exist in both diagrams, but no significant enhancement of sources at the position of stellar locus is visible in the left plot. We therefore conclude that the large majority of main sequence stars are brighter than $R_{source} = 23.5$. Other galactic objects such as brown or white dwarfs remain in the catalog since they are not following the main sequence.

Part IV

RESULTS AND CONCLUSIONS

The following chapters present the results of the weak lensing analysis. The derived cluster masses and concentration parameters are compared with the literature and the scaling relation between mass and Y_{SZ} is investigated. Multi-wavelength data are used for a deeper investigation of five galaxy clusters. The final chapter presents the summary and the conclusions of this thesis.

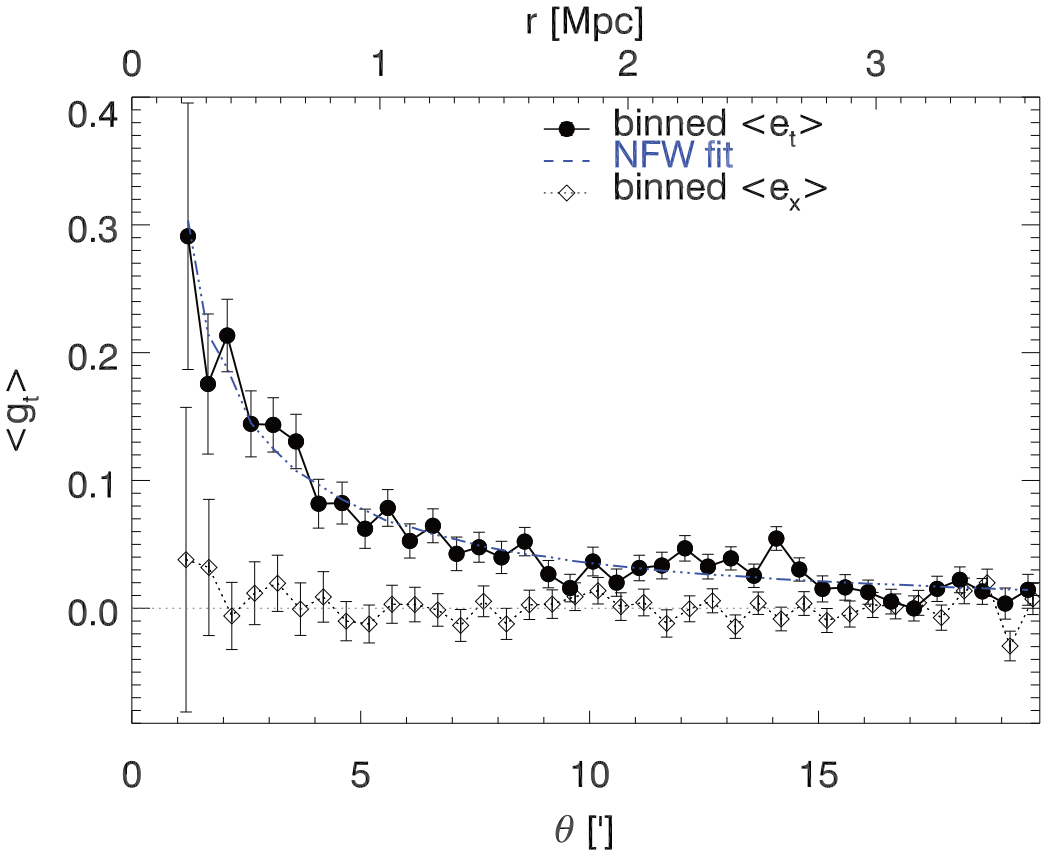

Figure 52: Azimuthally averaged tangential ellipticities of A1689 and fitted shear profile as a function of cluster centric distance.

8

RESULTS BASED ON THE FULL CLUSTER SAMPLE

This chapter presents mass estimates of the weak lensing follow-up project. We also use the weak lensing masses to derive a scaling relation between mass and Y_{SZ} measured with APEX-SZ.

8.1 GLOBAL PARAMETERS FOR NFW PROFILE FIT

In Chapter 4 we described the theoretical basis of our mass measurements, while in Chapter 6 and 7 the practical part related to the shear measurement. The mass is estimated by calculating the merit function Equation (129) on a regular grid to find the best fitting NFW density profile to the observed shear catalog. The step size of the grid is typically $\Delta r_{200} = 0.01$ Mpc and $\Delta c_{200} = 0.05$, which is about ten times smaller than the typical error on those parameters.

We learned from Chapter 6, that the "TS" shear measurement pipeline was only tested to values of $g = 0.1$. However, we saw also, that simulations showed a good recovery of the reduced shear up to $g = 0.5$ by KSB implementations using the trace assumption. We account for some of the limitations of the KSB method, by using only sources in the profile fit that have $\min(\mathrm{tr}\mathcal{P}^g) > 0.1$ and a maximum ellipticity of $\max(|\epsilon|) = 0.8$. These values are identical to those used in Israel et al. (2010b, 2012), whose results are based on the same shear measurement pipeline. Additional to that, we limit the inner radial distance, to which we fit our shear profile. We chose the inner limit for each cluster individually, depending on the observed strength of the shear profile. We do not fit to regions with averaged reduced shear larger than $g = 0.3$, to avoid to fit too far into untested shear regimes. Reducing the limit to lower values would not allow us to keep the concentration parameter as a free parameter in the fit. The typical inner border of the fitting range is $\theta_{\mathrm{in}} = 45$ arcsec, which corresponds to 200 kpc at the typical distance of our clusters.

The outer border of the fitting range depends on the shear profile and on the field of view of the instrument. In contrast to some authors such as Okabe et al. (2009), we do not fit the shear profile out to the maximal possible distance in the given images. The image distortions caused by the telescope and instrument optics are usually largest at the edges of the image. The corrections that have to be applied to the shape measurement are therefore also the largest at this position. We limit the maximum fitting radius to 900 arcsec for Suprime-Cam and 1000 arcsec for WFI, which usually excludes the image corners. For clusters at higher redshifts or lower mass, we shrink this radius to a distance where the shear signal is consistent with zero. This minimize the influence of other structure within or close to the cluster field.

The NFW profile was intended to describe the mass distribution within the virial radius. Fitting the NFW profile much further out than the virial radius can result in a bias of the mass estimate (Becker and Kravtsov, 2011; Oguri and Hamana, 2011). To account for this effect some authors (Applegate et al., 2012) are limiting the profile fit to a fixed physical distance such as 3 Mpc. The same authors investigated the size of this effect by performing mass measurements to 3 Mpc and to 5 Mpc. They found that the mass derived from the fit out to 5 Mpc, is marginally lower by a factor of $0.987^{+0.012}_{-0.010}$. We adapt the fitting range for each cluster individually, the typical fitting range is about 4.1 Mpc, which lies between

both radii. We therefore do not expect a significant bias due to fitting the NFW profile to that radius.

For the center for the profile fit, we chose, if possible, the postion of the BCG. In a few cases, especially for extreme mergers such as A520, A2744 or RXC1135, the center had to be chosen individually because of their complex morphology. Using other center definitions such as the location of the shear or S-statistic peak could bias the mass estimate. X-ray based center estimates are not available for all clusters and in case of dissociative mergers, like those in our sample, would also produce a bias.

An example of the confidence level in the $r_{200} - c_{200}$ plane and a shear profile for RXC0532 can be found in Figure 53. Another radial shear profile of a cluster is shown as introduction of this part in Figure 52.

8.1.1 *Signal to noise dependent shear bias*

In Chapter 6, we discussed a possible dependency of shear the measurement bias on the signal-to-noise of the source detection, for low signal-to-noise detections. We now want to investigate this effect to find a minimum signal-to-noise threshold, from which on we can assume to have a constant shear measurement bias. For that, we measure the mass of all clusters for different signal-to-noise thresholds. Figure 54 shows the result of this test. In the left panel of this figure, we show the normalized scale radius for all clusters. The thick line in black shows the median of all clusters and the error bar represents the standard deviation for each threshold. The dependency on signal to noise becomes clearer in the bottom panel, where we only show the dependency of the median. Here, we also plot the error on the mean, showing a significant trend of underestimating the scale radius at low S/N, similar to that seen in Hartlap et al. (2009).

The default value used in Israel et al. (2010b, 2012) of 4.5 tends to underestimate the scale radius by about 1 percent. Starting at a S/N of 5.0 we do not see any significant dependency on the signal to noise threshold. We choose a S/N threshold of 5.5 for a conservative model.

8.1.2 *Selection induced bias*

In Section 7.5, we showed how to find the signal-to-noise optimized selection parameter $\beta_{\mathrm{cut,max}}$. We argued that this value likely results in a overestimation of the shear signal, resulting in a mass bias. We chose the same method as before to investigate this effect. We used the S/N threshold of conservative model and calculate the mass of all clusters in dependency of the cut value β_{cut}. For that, we compute the redshift $z_{\mathrm{cut,max}}$ that corresponds to the signal to noise optimized cut for each cluster. We then vary the selection by adding Δz to $z_{\mathrm{cut,max}}$ and calculate the corresponding $\beta_{\mathrm{cut}}(z_{\mathrm{cut,max}} + \Delta z)$. This allows us to express the selection in terms of Δz instead of the less intuitive form of β, or a normalized version of it. In the top panel of Figure 55, we show the dependency of the normalized scale radius on Δz for all clusters and its median dependency. Similar to the test of the signal-to-noise dependent bias, we show the bottom panel of Figure 55 the median and its error in a zoomed plot. As expected, one can see an indication of overestimating the scale radius by 1% at the signal to noise optimized cut value $\Delta z = 0$. Before and after that value, the scale radius is consistent with each other. We are able to recover the mass, even if we significantly vary the selection. This shows that our method correctly accounts for redshift effects and that remaining contamination do not significantly affect the mass measurement.

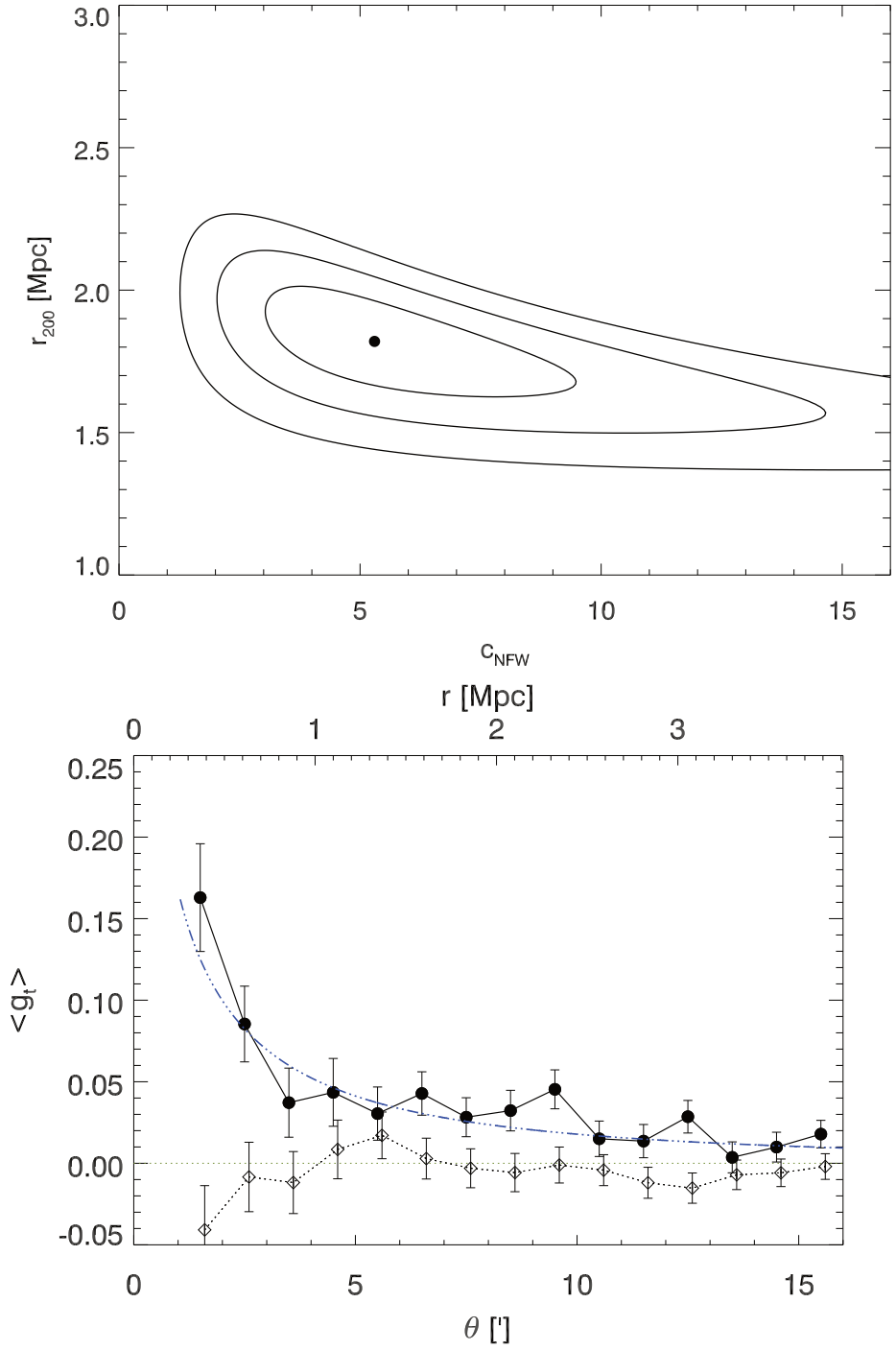

Figure 53: Top: Best fit NFW parameters with 1σ, 2σ and 3σ confidence contours in the $r_{200} - c_{200}$ plane for RXC0532. Bottom: Azimuthally averaged ellipticities as function of the cluster centric distance of RXC0532. The radial distance from the cluster center is given in arcminutes as well as in Mpc. The best fitting reduced shear profile is shown in blue. Filled circles show the tangential, the open diamonds the cross component of the ellipticity.

For our conservative model settings, we chose $\Delta z = 0.04$ to account for the selection induced bias. Since the usage of $\beta_{\text{cut,max}}$ overestimates the mass by the same fraction as the choice of a S/N threshold of S/N= 4.5 results in an underestimate, both effects are canceling out each other. This combination yields a higher number of galaxies in the background sample with no mass bias on average. We use this combination of parameters for a S/N optimized model.

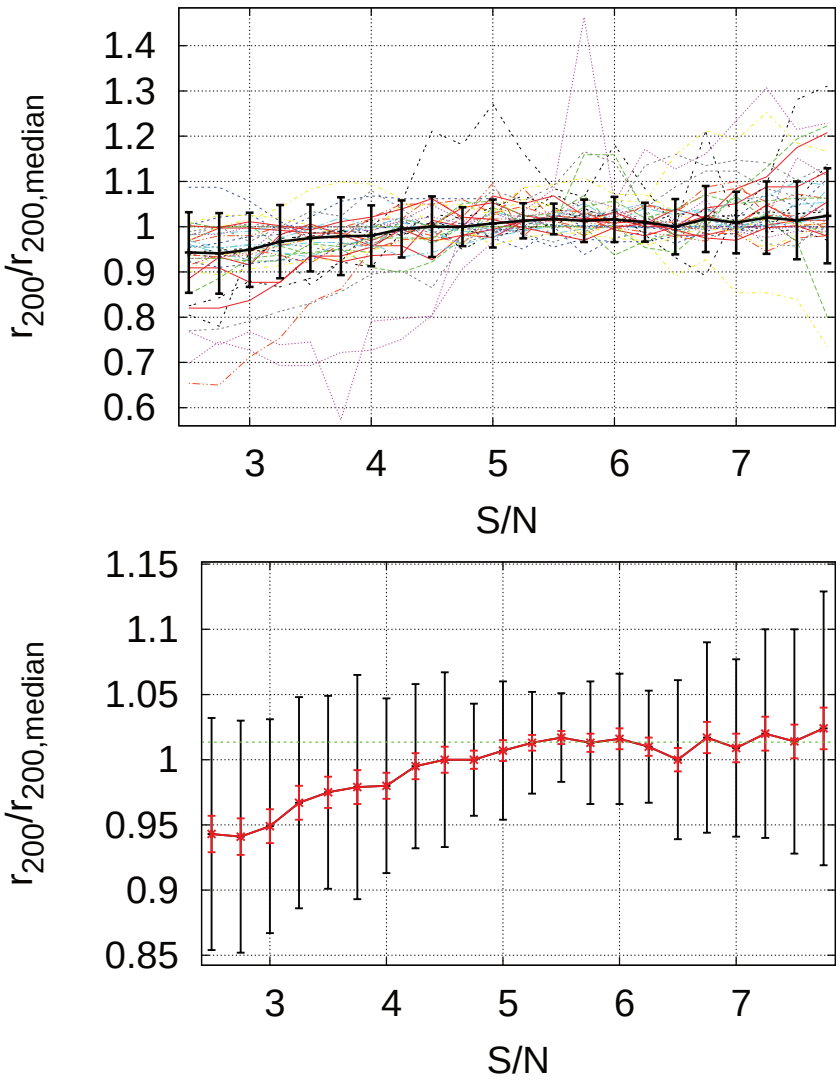

Figure 54: Top: Normalized scale radius vs. signal to noise threshold. Thin lines are results for individual clusters, thick black line shows the median and the standard deviation at this bin. Bottom: Similar to the left plot but only showing median. The standard deviation within each bin is given as black error bars the error on the mean as red error bars. The green line shows a constant fit to values $S/N > 5.5$.

The observed trend, seen in Figure 54, could in principle be modeled, to lower the used S/N threshold. However, the increased scatter at lower thresholds does not offer great improvements on the mass estimates. A summary of all global parameters for both models can be found in Table 5.

8.2 CLUSTER MASSES OF THE FULL SAMPLE

We show in Table 6 the best fit results for the S/N optimized parameter set. The best fit results for the overdensity $\Delta = 500$ and those of the conservative selection are listed in Table 12. The mean difference in M_{200} between conservative and S/N optimized selection is $0.006 \pm 0.02\%$ and therefore not significant.

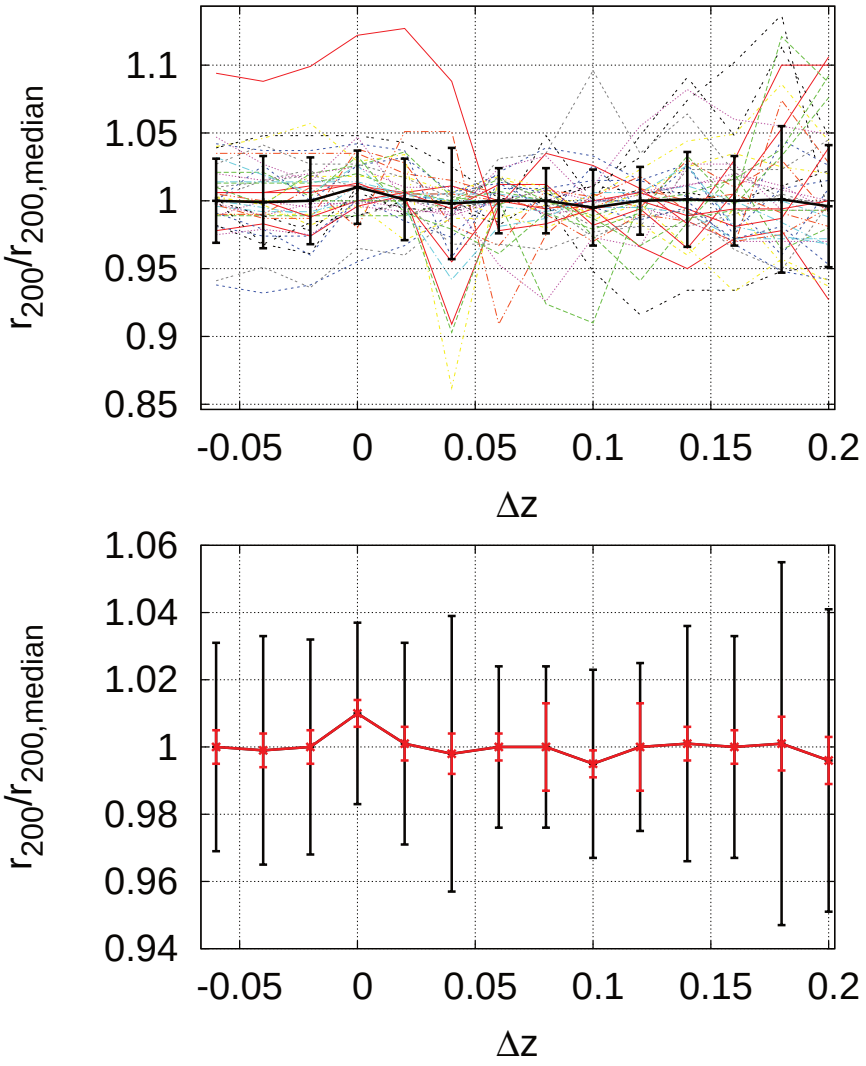

Figure 55: Top: Normalized scale radius vs. Δz. Thin lines are results for individual clusters, thick black line shows the median and the standard deviation at this bin. Bottom: The median showed in the left plot with the error on the mean in red and the standard deviation within each bin as black error bars.

Table 5: Global and average parameters of the full cluster sample.

Parameter	**Conservative**	**S/N optimized**
$\max(\lvert\epsilon\rvert)$	0.8	0.8
min(S/N)	5.5	4.5
Δz	0.04	0.0
$\min(\mathrm{tr}\mathcal{P}^g)$	0.1	0.1
center	BCG	BCG
f_0	1.08	1.08
$\langle\theta_{\mathrm{in}}\rangle$	0.2 Mpc	0.2 Mpc
$\langle\theta_{\mathrm{out}}\rangle$	4.1 Mpc	4.1 Mpc
$\theta_{\mathrm{out,max}}$	$900'', 1000''$	$900'', 1000''$

Table 6: Cluster masses and catalog properties: Weak lensing results of the best fit NFW halo parameter ($r_{200}, c_{200}, M_{200}$) for the S/N optimized selection. Also shown is the signal to noise optimizing cut value ($\beta_{\mathrm{cut,max}}$), the mean lensing depth ($<\beta>$), the mean purity ($<p>$), the minimal half-light radius of background sources (s_{ana}), maximum half-light radius for star/galaxy separation (s_{max}) and the number density of background galaxies. The radial fitting range of the profile fit is given in arcminutes (θ_{in},bθ_{out}) and in Mpc (D_{min},bD_{max}). The S/N of the cluster peak found in the S-statistic is given in the last column. For the clusters A907, MACSJ1115 and RXCJ1347, the WFI based masses are listed in the first line, the SUP based masses are listed in the following line without reciting the cluster name.

Cluster	r_{200} [Mpc]	c_{200}	M_{200} [$10^{14}\mathrm{M}_\odot$]	$\beta_{\mathrm{cut,max}}$	$<\beta>$	$<p>$	s_{ana} [px]	s_{max} [px]	$\bar{n}$ [arcmin^{-2}]	θ_{in} [$\prime\prime$]	θ_{out} [$\prime\prime$]	D_{min} [Mpc]	D_{max} [Mpc]	S/N
A2744	$2.12^{+0.13}_{-0.13}$	$3.95^{+2.55}_{-1.35}$	$14.8^{+2.9}_{-2.6}$	0.29	0.532	0.931	2.10	2.24	13.1	120	1000	0.54	4.92	9.2
RXCJ0019.0−2026	$2.04^{+0.14}_{-0.14}$	$3.05^{+1.2}_{-0.75}$	$12.9^{+2.8}_{-2.5}$	0.26	0.526	0.97	1.82	1.92	11.2	30	1000	0.13	4.24	10.0
A2813	$1.90^{+0.19}_{-0.19}$	$2.3^{+1.5}_{-0.9}$	$10.5^{+3.5}_{-2.9}$	0.25	0.524	0.929	2.06	2.18	11.2	40	900	0.18	3.94	8.7
A209	$2.08^{+0.12}_{-0.1}$	$2.15^{+0.65}_{-0.55}$	$12.6^{+2.3}_{-1.7}$	0.55	0.754	0.997	1.28	1.36	18.8	90	1000	0.30	3.38	13.7
XLSSC 006	$1.50^{+0.16}_{-0.15}$	$4.45^{+2.85}_{-1.85}$	$6.1^{+2.2}_{-1.6}$	0.29	0.464	0.896	1.74	1.84	11.4	30	850	0.17	4.76	6.8
RXCJ0232.2−4420	$1.58^{+0.18}_{-0.2}$	$15.5^{+32.4}_{-7.8}$	$6.0^{+2.3}_{-2.0}$	0.32	0.522	0.995	1.91	1.99	7.1	50	900	0.21	3.40	6.7
RXCJ0245.4−5302	$1.48^{+0.2}_{-0.22}$	$9.35^{+13.95}_{-4.5}$	$5.0^{+2.3}_{-1.9}$	0.15	0.474	0.913	2.18	2.22	5.9	15	1000	0.07	4.48	7.6
A383	$1.57^{+0.13}_{-0.13}$	$7.85^{+3.45}_{-2.25}$	$5.3^{+1.4}_{-1.2}$	0.57	0.711	0.981	1.96	1.96	15.0	40	900	0.13	2.85	9.2
RXCJ0437.1+0043	$1.94^{+0.26}_{-0.24}$	$2.15^{+1.8}_{-1.05}$	$11.1^{+5.1}_{-3.6}$	0.27	0.507	0.961	1.83	1.89	7.0	10	900	0.04	3.86	6.6
MS0451.6−0305	$1.52^{+0.16}_{-0.16}$	$9.95^{+37.95}_{-3.75}$	$7.3^{+2.5}_{-2.1}$	0.30	0.37	0.837	2.38	2.45	9.2	30	900	0.19	5.77	5.3
A520	$2.13^{+0.27}_{-0.24}$	$0.9^{+0.7}_{-0.5}$	$14.7^{+6.3}_{-4.4}$	0.35	0.689	0.971	1.54	1.63	16.4	5	900	0.02	2.99	10.0
RXCJ0516.6−5430	$2.40^{+0.44}_{-0.26}$	$0.5^{+0.45}_{-0.45}$	$21.3^{+14.0}_{-6.2}$	0.23	0.497	0.976	2.04	2.07	8.3	60	1000	0.26	4.85	6.7
RXCJ0528.9−3927	$1.92^{+0.24}_{-0.22}$	$0.95^{+0.85}_{-0.6}$	$10.8^{+4.6}_{-3.3}$	0.52	0.619	0.977	1.91	2.00	6.0	20	1000	0.09	4.29	6.2
RXCJ0532.9−3701	$1.80^{+0.13}_{-0.13}$	$5.3^{+2.85}_{-1.65}$	$8.8^{+2.0}_{-1.8}$	0.32	0.561	0.977	1.72	1.78	12.1	45	1000	0.19	4.19	10.6
A3404	$2.10^{+0.23}_{-0.23}$	$4.7^{+2.4}_{-1.5}$	$12.4^{+4.5}_{-3.6}$	0.64	0.713	0.99	2.08	2.24	4.0	60	1000	0.17	2.86	7.1
Bullet	$1.86^{+0.22}_{-0.24}$	$2.45^{+1.8}_{-1.05}$	$9.9^{+3.9}_{-3.4}$	0.25	0.507	0.967	1.83	1.85	6.0	10	1000	0.04	4.84	7.2
A907	$1.78^{+0.82}_{-0.24}$	$2.0^{+1.05}_{-1.95}$	$7.4^{+15.8}_{-2.6}$	0.62	0.73	0.986	1.91	1.91	6.7	30	1000	0.08	2.65	5.1
	$1.81^{+0.15}_{-0.13}$	$3.8^{+1.05}_{-0.9}$	$7.8^{+2.1}_{-1.6}$	0.635	0.783	0.988	1.36	1.36	17.5	60	900	0.16	2.39	10.8

Continued on next page

Cluster	r_{200}	c_{200}	M_{200}	$\beta_{\mathrm{cut,max}}$	$<\beta>$	$<p>$	s_{ana}	s_{max}	$\bar{n}$	θ_{in}	θ_{out}	D_{min}	D_{max}	S/N
RXCJ1023.6+0411	$1.82^{+0.11}_{-0.1}$	$5.45^{+1.2}_{-1.05}$	$9.2^{+1.8}_{-1.4}$	0.42	0.578	0.956	1.38	1.40	16.9	20	900	0.09	3.92	11.4
MS1054.4−0321	$2.03^{+0.36}_{-0.34}$	$7.4^{+40.5}_{-5.85}$	$24.2^{+15.3}_{-10.2}$	0.135	0.176	0.853	1.75	1.80	2.6	100	660	0.76	5.02	5.1
MACSJ1115.8+0129	$1.64^{+0.26}_{-0.32}$	$0.8^{+1.75}_{-0.65}$	$7.3^{+4.0}_{-3.5}$	0.24	0.411	0.911	1.72	1.80	6.6	40	1000	0.20	4.99	4.6
	$1.55^{+0.17}_{-0.19}$	$3.5^{+2.7}_{-1.5}$	$6.1^{+2.2}_{-2.0}$	0.37	0.498	0.969	1.77	1.87	8.1	30	900	0.15	4.49	6.2
A1300	$1.75^{+0.21}_{-0.22}$	$2.45^{+3.9}_{-1.35}$	$8.3^{+3.4}_{-2.8}$	0.28	0.469	0.949	1.79	1.81	8.4	90	1000	0.41	4.51	6.1
RXCJ1135.6−2019	$1.53^{+0.19}_{-0.19}$	$3.05^{+1.95}_{-1.5}$	$5.6^{+2.3}_{-1.8}$	0.24	0.508	0.973	1.81	1.84	12.0	5	1000	0.02	4.50	6.4
RXCJ1206.2−0848	$1.93^{+0.17}_{-0.17}$	$3.65^{+3.75}_{-1.65}$	$13.1^{+3.8}_{-3.2}$	0.26	0.405	0.968	1.97	2.17	7.9	100	900	0.57	5.13	7.0
MACSJ1311.0−0311	$1.49^{+0.16}_{-0.17}$	$3.05^{+2.25}_{-1.35}$	$6.1^{+2.2}_{-1.9}$	0.14	0.42	0.893	1.85	1.85	12.5	5	900	0.03	5.18	5.7
A1689	$2.50^{+0.08}_{-0.08}$	$6.8^{+1.35}_{-0.9}$	$21.3^{+2.1}_{-2.0}$	0.44	0.682	0.956	1.52	1.60	20.3	50	900	0.15	3.69	23.0
RXJ1347−1145	$2.13^{+0.23}_{-0.22}$	$1.85^{+1.35}_{-0.75}$	$17.8^{+6.4}_{-5.0}$	0.15	0.301	0.942	2.00	2.00	6.4	40	1000	0.23	5.77	6.6
	$2.10^{+0.18}_{-0.16}$	$4.1^{+2.55}_{-1.65}$	$17.1^{+4.8}_{-3.6}$	0.16	0.401	0.981	1.66	1.66	5.9	30	1000	0.17	5.77	7.5
MACSJ1359.2−1929	$1.40^{+0.25}_{-0.28}$	$4.1^{+6.9}_{-2.55}$	$5.1^{+3.3}_{-2.5}$	0.195	0.317	0.938	1.86	1.91	7.5	20	900	0.12	5.25	4.0
A1835	$2.22^{+0.16}_{-0.16}$	$4.1^{+1.50}_{-0.9}$	$16.1^{+3.7}_{-3.2}$	0.49	0.618	0.993	2.60	2.60	4.3	60	900	0.24	3.55	10.1
RXJ1504	$1.75^{+0.18}_{-0.17}$	$4.1^{+2.1}_{-1.5}$	$7.6^{+2.6}_{-2.0}$	0.46	0.628	0.958	1.84	1.92	8.0	5	1000	0.02	3.49	7.1
A2163	$2.96^{+0.43}_{-0.36}$	$1.4^{+0.75}_{-0.6}$	$36.1^{+18.1}_{-11.6}$	0.44	0.622	0.998	1.82	1.83	5.8	90	900	0.30	3.00	9.4
A2204	$2.12^{+0.27}_{-0.21}$	$3.05^{+1.05}_{-1.05}$	$12.6^{+5.4}_{-3.4}$	0.5	0.745	0.999	1.82	1.83	5.9	5	1000	0.01	2.64	8.3
RXCJ2014.8−2430	$1.65^{+0.35}_{-0.31}$	$4.85^{+6.75}_{-2.7}$	$5.9^{+4.6}_{-2.7}$	0.65	0.716	0.986	1.91	1.91	3.1	60	1000	0.16	2.61	4.7
RXCJ2151.0−0736	$1.41^{+0.19}_{-0.2}$	$6.2^{+5.7}_{-2.7}$	$4.3^{+2.0}_{-1.6}$	0.34	0.508	0.982	1.76	1.95	7.0	30	1000	0.13	4.35	7.1
A2390	$2.06^{+0.12}_{-0.1}$	$4.85^{+1.2}_{-1.05}$	$12.5^{+2.3}_{-1.7}$	0.4	0.691	0.98	1.60	1.66	14.4	50	1000	0.18	3.65	13.6
MACSJ2214.9−1359	$1.68^{+0.2}_{-0.19}$	$7.55^{+7.35}_{-3.3}$	$9.3^{+3.7}_{-2.8}$	0.12	0.333	0.824	1.38	1.48	6.9	20	660	0.12	4.04	6.7
MACSJ2243.3−0935	$2.07^{+0.22}_{-0.23}$	$3.35^{+6.45}_{-1.8}$	$16.3^{+5.8}_{-4.8}$	0.16	0.371	0.93	1.32	1.58	4.5	120	660	0.69	4.88	6.3
RXCJ2248.7−4431	$2.13^{+0.15}_{-0.14}$	$2.6^{+0.9}_{-0.75}$	$15.8^{+3.6}_{-2.9}$	0.45	0.559	0.929	1.87	1.93	7.4	45	890	0.22	4.38	10.1
A2537	$1.98^{+0.13}_{-0.13}$	$3.8^{+1.65}_{-1.05}$	$12.0^{+2.5}_{-2.2}$	0.31	0.521	0.888	1.54	1.54	15.0	70	1000	0.31	4.42	11.3
RXCJ2337.6+0016	$1.89^{+0.18}_{-0.17}$	$2.0^{+1.2}_{-0.75}$	$10.1^{+3.2}_{-2.5}$	0.19	0.581	0.921	1.80	1.82	8.7	25	900	0.10	3.75	8.2

8.2.1 *Comparison to the literature*

We found three publications, each of them are reporting weak lensing masses of at least five clusters also measured in this work. The largest overlap is with the sample of the Canadian Cluster Comparison Project (CCCP) project (Hoekstra et al., 2012) with 11 clusters. The cluster masses reportet in this publication are based on two filter observations with CFH12k and Megacam at the *Canada France Hawaii Telescope* (CFHT) and were used for the weak lensing versus Y_{SZ} scaling relation showed in Figure 14. In this paper, mass estimates were obtained based on a NFW profile fit, as well as using an aperture mass technique. In Figure 56, we plot masses from Hoekstra et al. (2012) using NFW profile fit, on the left side, and using aperture mass on the right side, against the S/N optimized masses of this work.

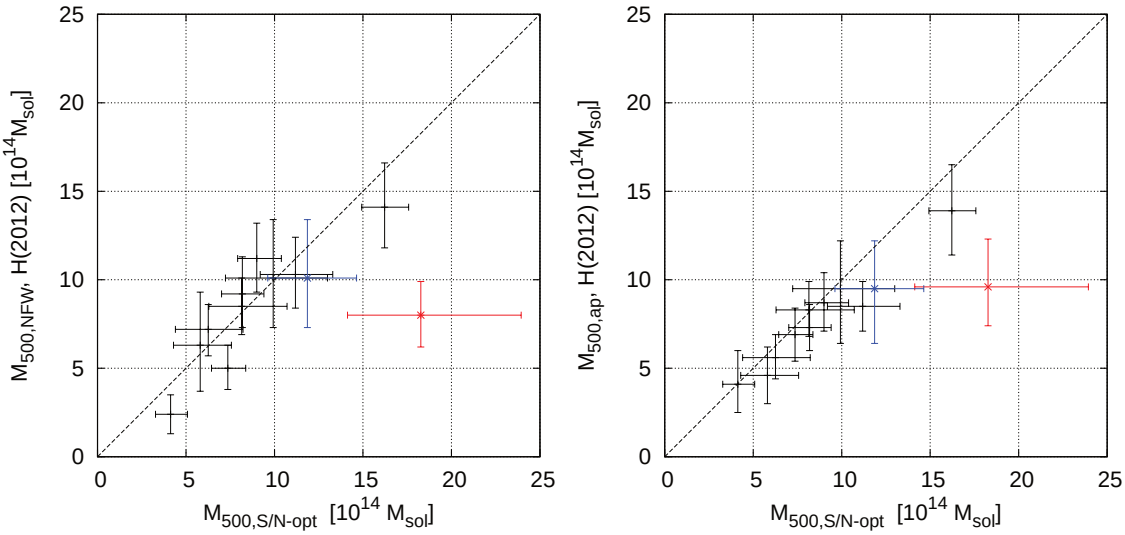

Figure 56: Left: M_{500} based on NFW profile fit in Hoekstra et al. (2012) against M_{500} from this work using the S/N optimized selection. Right: The same as left but using aperture mass given in Hoekstra et al. (2012). Marked in red: A2163. Marked in blue: Suprime-Cam estimate of RXC1347.

The scatter between our results and those of the CCCP project seem to be significantly smaller for the aperture mass method. This might be a result of the usage of a mass-concentration relation for the NFW profile fit instead of leaving the concentration parameter as a free parameter in the work of Hoekstra et al. (2012). The aperture mass method uses a NFW profile fit to values outside the aperture for de-projection issues. This makes the aperture method more comparable with our NFW profile based results.

The cluster marked in red is A2163, which is discussed in Hoekstra et al. (2012) as a potential outlier in the weak lensing vs. SZ scaling relation. Our mass estimate for this cluster is significantly higher, and fits better to the reported scaling relation. RXC1347 is observed in our sample with WFI and Suprime-Cam. The mean ratio between masses derived by Hoekstra et al. (2012) and those derived in this thesis, including both mass estimates of RXC1347 and A2163 is 0.92 ± 0.07 for the NFW mass estimate, and 0.87 ± 0.04 for the aperture mass. The median is 0.97 and 0.89 respectively. Excluding A2163 and the Suprime-Cam based mass estimate of RXC1347 yields 0.97 ± 0.07 and 0.91 ± 0.03. Exchanging the WFI based estimate with the Suprime-Cam estimate of RXC1347 does not significantly change this result.

It should be noted that Hoekstra et al. (2012) finds a mass ratio of the NFW fit based masses to aperture mass of 0.93 ± 0.04, while for the overlapping sample the aperture

mass yields lower masses. This could be a sign that the overlapping subsample is not representative for the full cluster sample of the CCCP project. However, if we assume that the subsample is representative for the full sample, we conclude that we see no significant offset between the masses of the CCCP and ours, but an indication that our estimates are higher by $3-10\%$.

The cluster sample analyzed by Okabe et al. (2009) has five clusters in common with our sample. Two filter Suprime-Cam data were used for weak lensing mass estimates. For comparison with our results, we use the masses obtained with the NFW profile fit to the shear signal. We use partially the same raw data for our mass estimates, but due to the different data reduction and shear measurement pipelines together with the different background selection techniques, we do not expect a significantly higher correlation to our data than for other publications. In the left panel of Figure 57, we plot mass estimates of Okabe et al. (2009) against the signal to noise optimized mass estimates of this work. All but one cluster are below the one to one line. The average ratio is 0.88 and the median is 0.83.

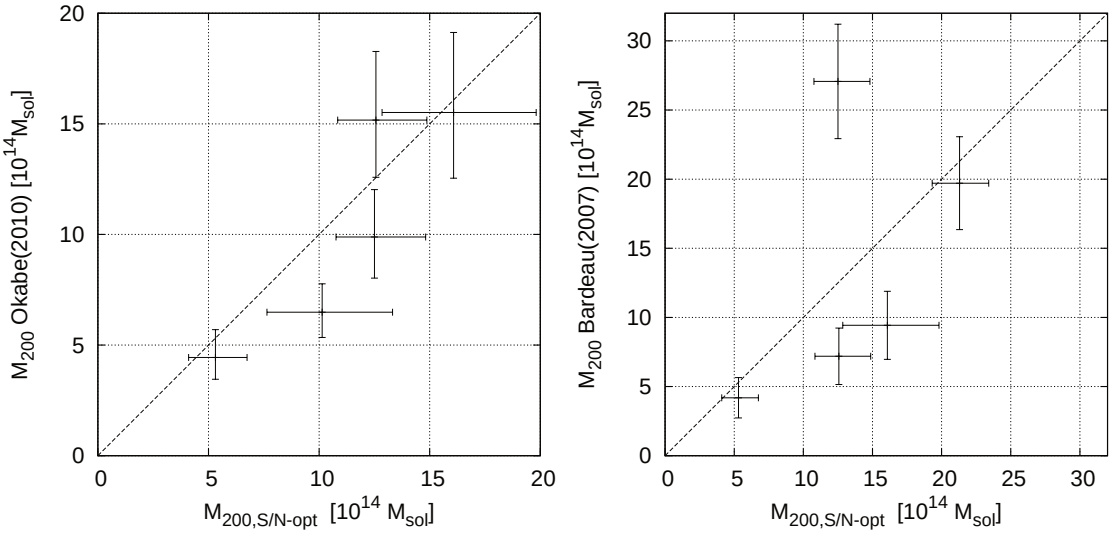

Figure 57: Left: NFW fit based weak lensing masses from Okabe et al. (2009) against S/N optimized estimate of M_{200}. Right: Mass measurements from Bardeau et al. (2007).

The weak lensing analysis by Bardeau et al. (2007) reports the masses of five clusters that are in common with our sample. The mass estimates of these clusters are based on three-band imaging with CFH12k at CFHT. The background selection is based on a red sequence technique, while $\langle\beta\rangle$ is obtained in a color matching approach to a mixed photometric and spectroscopic redshift catalog of the *Hubble Deep Fields* North and South. The comparison between our mass estimates and those of Bardeau et al. (2007) are shown in the right plot of Figure 57. Four out of five clusters have lower masses than ours, but one has a significantly higher mass. This results in an average ratio of 1.01 and a median of 0.79. The outlier in this sample is A1835. This cluster is the only cluster out of eleven in this publication, which was observed in V, R, and I band, all other clusters were observed in B, R and I. This may has caused a wrong background selection or a wrong estimate of $\langle\beta\rangle$. We also note other inconsistencies in this publication. The authors claim symmetric error bars in r_{200} as well as M_{200}. Due to the claimed calculation of M_{200} from r_{200} and the relation $M \propto r_{200}^3$, symmetric errors of one estimate should translate into an asymmetric error in the other parameter.

It is also interesting to note that the quoted estimates of r_{200} do not fit to the masses given in the same table. This could indicate that we do not fully understand the conversion of

the given $M_\odot/h_{70}$ into our units of interest. However, Hoekstra et al. (2012) uses the same units and we do not see any disagreements between overdensity radius and mass. We therefore conclude that the quoted values of r_{200} are either derived independently from the given mass estimates or that another definition of the units are used as in Hoekstra et al. (2012), which we could not trace back.

The clusters A209, A383, A2390 and A1835 are included in all three publication. Figure 58 shows the direct comparison of all three publications of this clusters[1].

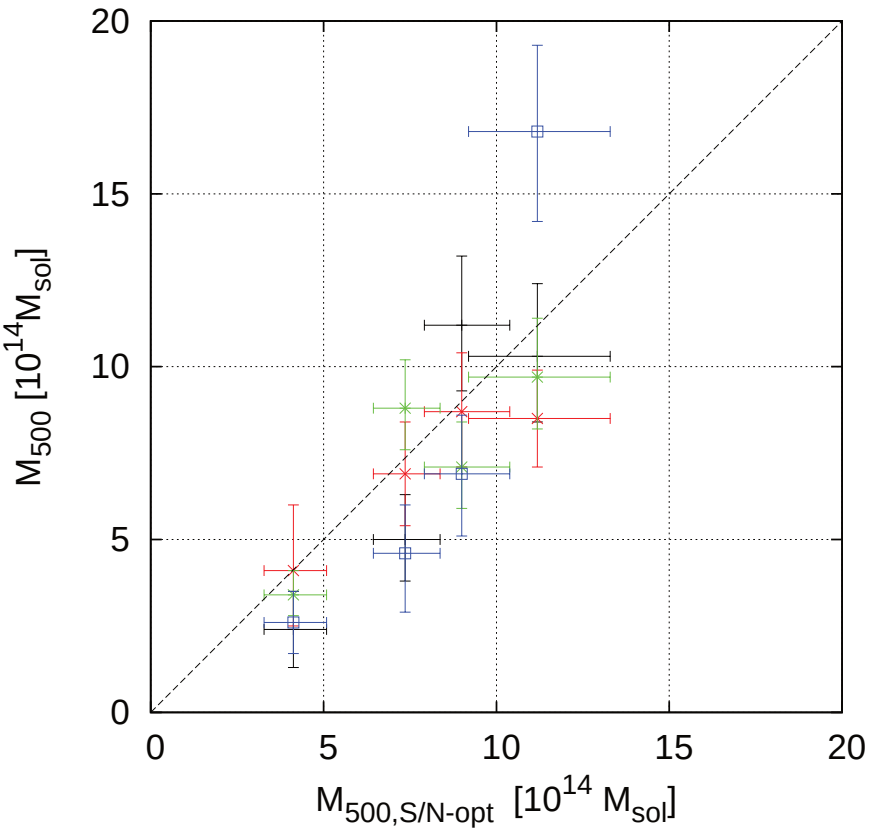

Figure 58: Mass estimate of four clusters included in all three publications against S/N optimized mass estimates. Black: Hoekstra et al. (2012) NFW based mass estimates. Red: De-projected aperture mass from the same author. Green: Mass estimates from Okabe et al. (2009). Blue: Estimates from Bardeau et al. (2007).

In the direct comparison one can see that the estimates by Bardeau et al. (2007) are the lowest for the three lower mass systems but the highest for the most massive one. Our mass estimates are in excellent agreement with three out of four mass estimates by Hoekstra et al. (2012) using the aperture mass.

Another sample with 11 clusters in common is that of the *Weighting The Giants* project (WTG). The project goals are similar to those of this work, of obtaining unbiased mass estimates for scaling relations. Unfortunately the available preprint version of the paper does not include the mass estimates. A refereed journal article is not available yet[2], but in their paper, the authors compare their mass estimate with other authors. The authors find an average ratio between 14 clusters from Okabe et al. (2009) and their mass estimates of 0.77 and a median of 0.72. The ratio between seven clusters in common with Bardeau et al. (2007) yield a mean of 0.84 and a median of 0.72. The authors of WTG also find a

1 For computation of M_{500} out of M_{200} from Bardeau et al., we assumed the given concentration parameter corresponds to the value at M_{200}.

2 Status: 27. August 2013

difference between lower mass systems and the two most massive clusters in common. The ratios reported by WTG are similar or even lower than ours, indicating that the masses of those authors to be similar or slightly higher than the measurements in this thesis. A final comparison is planned as soon as the masses are available.

Summarizing the comparison between various publications, we see that our masses are consistent with those of Hoekstra et al. (2012), with only a slight trend of obtaining higher masses as those authors. We found smaller scatter but higher mean difference for the aperture mass estimates. The mass estimates of Okabe et al. (2009) and Bardeau et al. (2007) are lower by $10-20\%$. A similar behavior was also reported by the WTG project (Applegate et al., 2012), in their comparison with those authors. This indirectly indicates that the masses of the WTG project yield similar or slightly higher masses than those reported in this work.

8.3 MASS-CONCENTRATION RELATION

The concentration is found to be related to the mean density when the cluster has formed (Navarro et al., 1996; Bullock et al., 2001). Assuming the model of the hierarchical structure formation, more massive systems form later than less massive ones. Both together results in the mass-concentration relation, studied by various authors (Bullock et al., 2001; Duffy et al., 2008; Bhattacharya et al., 2013). The dependency of the mass-concentration relation on structure formation was used by Ettori et al. (2010, 2011), to put constraints on Ω_m and σ_8. For that, X-ray observations of 44 clusters of galaxies were used.

In our weak lensing analysis, we fit the concentration c_{200} as well as r_{200} for all clusters in our sample. Weak lensing in general, and the low number densities of background galaxies for most of our clusters, do not allow to put tight constraints on the derived concentration parameters.

The scatter and bias of weak lensing derived masses and concentrations was investigated by Bahé et al. (2012), which used about 30000 galaxy cluster halos with $M_{200} > 10^{14} M_\odot$ at $z \approx 0.2$ from the Millenium Simulation (Springel et al., 2005). The analysis of simulated weak lensing data are very similar to our method, using a χ^2-minimization to the tangential shear profile to galaxies within a cluster centric distance of 0.5 to 15 arcminutes. One outcome of this publication is, that the median concentration derived from weak lensing NFW fits are underestimating the true concentration by $\sim 7\%$ and the mass by $\sim 5\%$, which is almost mass independent, except for clusters within the highest mass interval. For the highest mass clusters ($M_{200} > 10^{14.8} M_\odot$) no significant mass bias is seen, but the concentration is still underestimated by a similar amount as seen for clusters with lower masses.

The median mass of our sample is $\langle M_{200} \rangle \approx 10^{15}$ and about three quarters of our sample have masses ($M_{200} > 10^{14.8}$), making the highest mass range in Bahé et al. (2012) the most relevant for our discussion. In addition to that our median redshift of $\langle z \rangle = 0.288$, implying that even more of our clusters would fall into the highest mass range at $z = 0.2$. This indicates that the majority of our clusters are lying in the mass range with the lowest bias in mass.

Beside this promising result, we want to stress that at the highest mas range, the number of clusters in the Millenium Simulation becomes small compared to lower mass bins. The results of Bahé et al. (2012) for the highest mass bin are based on lensing measurements of 57 cluster, each of them observed in 50 randomly selected viewing angles. The next lower mass bin uses 285 clusters, observed in 5 different directions. However, we do not assume that the results of the highest mass bin are significantly affected by the lower number of clusters.

Based on that, we expect only a small negative bias of about 7% for our estimates of the concentration parameter.

This estimate does not include effects such as underestimation of the contamination by cluster galaxies or potential changes in the shear calibration bias for higher shear values. Underestimation of the cluster contamination will bias the concentration low, while a change of the shear calibration bias at higher shear can bias the concentration in both directions. A potential effect that could bias the concentration high in our sample, is the combination of targeted observations and magnification effect. Most of our observations are centered on the cluster position, resulting in the highest image depth at central postion at the cluster center[3]. The magnification effect of the gravitational lens also results in the detection of faint sources that would not been detected without the lens. Both effects result in a systematic change of the redshift distribution towards higher redshifts. The ignorance of these effects would result in a systematic underestimation of the mean lensing depth at the cluster center, which results in the aforementioned overestimation of the concentration parameter.

The limit of the profile fit to $g < 0.3$, the incorporation of individual redshift estimates and the exclusion of a large fraction of cluster galaxies by our background selection, should minimize those effects on the contamination parameter.

We use the mass-concentration relation reported in Bhattacharya et al. (2013) for comparison with our measurement. The mass-concentration relation from these authors is based on large volume dark matter simulations with a co-moving box sizes of up to 2000 Mpc/h and 2048^3 pixels and cosmological parameters close to those derived from the WMAP7 (Jarosik et al., 2011) data set. The volume probed in this simulation is about 125 times larger than that used in Duffy et al. (2008) for deriving their scaling relation or 64 times larger than the Millenium Simulation used in Bahé et al. (2012). This increased volume improves significantly the statistics at the high mass end of the scaling relation that is probed by our sample.

The mass-concentration relation found in Bhattacharya et al. (2013) is expressed via the relation between concentration parameter and the *peak hight parameter* ν. The peak hight parameter is defined as $\nu = \delta_c(z)/\sigma(M,z)$, where δ_c is the density threshold in linear theory (see Section 2.7.1 and Section 2.7.2) and $\sigma(M,z)$ specifies the variance of the matter fluctuations over the scale $\propto M^{1/3}$ at redshift z.

The best fitting $\nu - c$ relation is

$$c_{200,B13}(\nu) = D(z)^{0.54} \times 5.9\nu^{-0.41}, \tag{149}$$

for all systems and

$$c_{200,B13}(\nu) = D(z)^{0.53} \times 6.6\nu^{-0.35}, \tag{150}$$

for relaxed systems. Here $D(z)$ is the linear growth factor for a flat ΛCDM universe. The distribution of the concentrations in the simulations can be described by a Gaussian with variance of $\sigma_c = 0.33c$. The $\nu - c$ relation can be converted to a $M - c$ relation by using the connection between ν and the cluster mass given by

$$\nu(M,z) \approx \frac{1}{D(z)} \left[1.12 \left(\frac{M}{5 \times 10^{13} M_\odot/h}\right) + 0.53\right]. \tag{151}$$

The difference between the scaling relation using all clusters and that of using only relaxed systems is about 4% at median redshift and mass of our sample. We therefore do not expect

3 Note that flatfielding only results in comparability of the fluxes of sources over the image position. The image depth or S/N still follows the spatial distribution seen in the flatfield or weight images, with its highest values at the central region of the image.

to see significant differences between relaxed and disturbed systems with the given errors from our weak lensing measurements.

In Figure 59 we show the ratio between our c_{200} measurements and the value obtained with the mass-concentration relation over the cluster mass M_{200}. We do not show the error bars in mass and cut the error bars in y direction at $c_{200}/c_{\mathrm{BHHV2013}} = 8$ for visualization purposes. The y error bars do only include the error from the measured c_{200} and ignores other uncertainties such as the scatter of the m-c relation or the error of the mass estimate. Even when using this rather optimistic error bars, most of the values are consistent with unity. The lowest values are coming from merging systems such as A2163 (also the most massive cluster), A520 and RXC0516, where a single NFW profile is a bad description of the mass distribution.

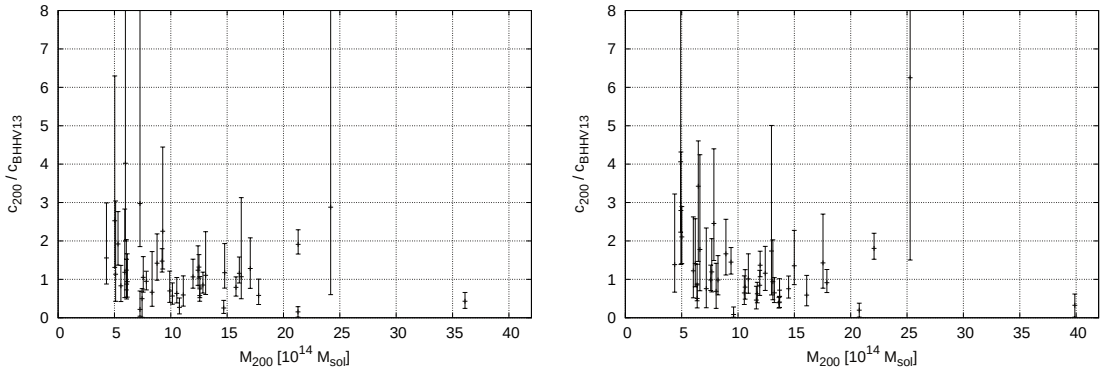

Figure 59: Left: Ratio between measured concentration and concentration derived from the Bhattacharya et al. (2013) m-c relation for the S/N optimized background selection. Right: The same, but using the result of the conservative background selection. Error bars only reflect the error of the measured c_{200}.

In Figure 60 we show a binned version of the m-c relation. For that, we divided the cluster sample in eight mass bins each including five clusters. For each mass bin we calculated the median ratio of $c_{200}/c_{\mathrm{BHHV2013}}$, the standard deviation of this ratio and the median mass. The error bars in x direction show the minimum and the maximum cluster mass included in this bin. We do not aim to derive weighted averages, since the necessary knowledge about the scatter in x and y direction including projection effects, intrinsic scatter in c or the error of the scaling relation and their correlation are difficult to obtain and is also beyond the scope of this test.

We can see on average a very good agreement between our concentrations and those from the m-c relation. The indication of a slight increase towards lower mass clusters is also seen in the lensing based results of Oguri et al. (2012) and X-ray based results of Ettori et al. (2010, 2011), which were discussed in Bhattacharya et al. (2013).

However, this effect is not significant and can be the result of the increased scatter in the measurement of the concentration parameter at lower masses, also seen in Bahé et al. (2012). Since the concentration parameter has to be grater than zero in our fit, the distribution of concentrations becomes increasingly asymmetric if the amount of scatter increases. This affects the estimate of the true scaling relation, if not accounted for.

Finally we calculated the mean, the error on the mean (assuming a normal distribution) and the median concentration ratio of the full cluster sample. We find a mean of 1.17, a median of 1.06 and an error of 0.12, for the S/N optimized results. In case of the conservative selection, we find a mean ratio of 1.3, a median ratio of 0.98 and the an error of 0.17. The large difference between mean and median obviously comes from the asymmetric scatter and the equal weight of each measurement, independent on the size of the measurement

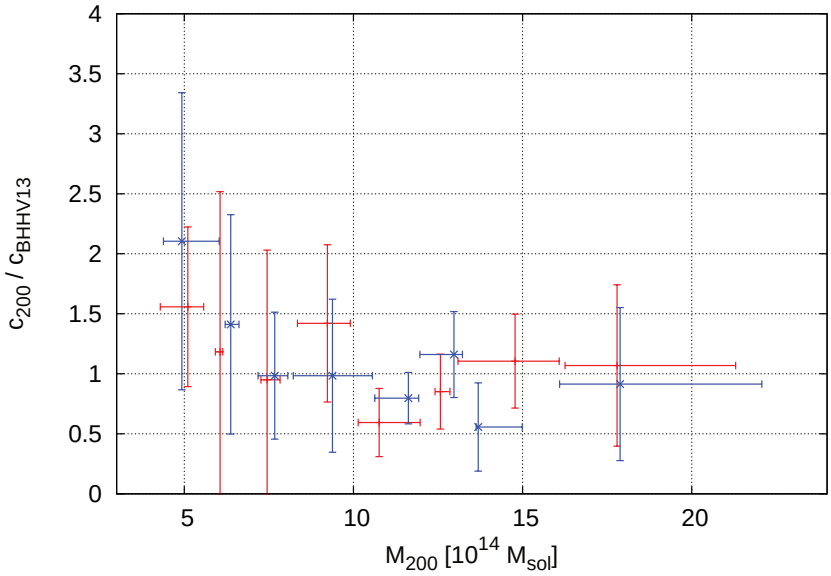

Figure 60: Binned ratio between measured concentration and concentration derived from the discussed scaling relation. Each bin shows the median concentration ratio and mass of 5 clusters. The error in mass represents the bin width and the error in concentration the standard deviation of the concentration ratio within the bin. Red shows the results from the S/N optimized selection, blue those of the conservative selection.

error. Using the median as a more robust measure of the mean distribution, we see very good agreement between the m-c relation reported in Bhattacharya et al. (2013) and our measurement.

We do not find evidence of an underestimation of the concentration parameter, but the results are consistent with the underestimation of 7% predicted by Bahé et al. (2012). This test let us conclude, that we are able to reasonably recover the concentration parameter in our measurement without applying a prior to this parameter.

8.4 THE $Y_{SZ} - M_{WL}$ SCALING RELATION

We present here the $Y_{SZ} - M_{WL}$ scaling relation for 29 clusters from the APEX-SZ instrument as well as for 17 clusters of galaxies from the Planck satellite.

8.4.1 *APEX-SZ Data*

The weak lensing follow-up of APEX-SZ detections was conducted to obtain masses estimates for the investigation of the scaling relation between mass and integrated Compton Y parameter. The observations were performed in a circular drift scan pattern, which concentrate the effective integration time in a region around the cluster and limits the overhead time due to telescope turn-arounds, compared to a raster like scan pattern. The telescope conducts circular scans, centered on a fix position in altitude and azimuth position, while the source is drifting through the FOV due to earths rotation. After 11 to 20 circles, the telescope slews to track the source and starts a new set of circular scans. The radius of the circles was chosen based on the expected angular size of the cluster signal, and ranges between $6'$ to $12'$. The typical time for one circle is 4 to 7 seconds. This scan pattern results in sky coverage of about $45' \times 60'$ per cluster, but with a high position dependency in effective integration time.

The data reduction of SZ observations is a complex topic of its own, and differs from instrument to instrument. In case of APEX-SZ, two independent data reduction and analysis pipelines were implemented. The SZ-maps shown in this thesis, are from Dr. Martin Nord[4], who implemented a data reduction pipeline based on the software packed BOA[5]. An overview of the data reduction steps of this pipeline can be found in Nord et al. (2009), for a detailed description, we refer to the thesis work by M. Nord (Nord, 2009). Maps based on this reduction pipeline were used to judge whether a cluster is detected or not (see Table 1).

A second data reduction and analysis pipeline is based on the software package Matlab[6] and was used in Halverson et al. (2009) for the data reduction and analysis of the Bullet Cluster observations. A detailed description of the Matlab based pipeline can be found in the thesis work of Dr. Amy Bender (Bender, 2011)

We briefly list here the major effects that have to be accounted for to obtain the SZ signal of a galaxy cluster. Periodic effects are induced by the circular scan pattern, resulting in a varying amount of ground signal picked up by the telescope and thermal fluctuations caused by vibrations of the telescope. Other time dependent effects are coming from the change of the airmass for a given target and the variation of the atmospheric opacity due to changes in the humidity. Various instrumental effects such as the changes in gain due to changing amounts of incident optical power to the receiver or differences in the optical time constant of the bolometers have to be corrected as well. Finally the influence of other astrophysical signals such as the primary CMB and point sources has to be modeled.

The SZ signal is analyzed by fitting a parametrized model to the data. The analysis of the full cluster sample and the validation of the obtained spherical integrated $Y_{SZ}(r)$ is still in progress. So far, we have preliminary results for 29 cluster detections, using the output of the Matlab based reduction pipeline (Bender et al. 2013,in prep).

The measurements of $Y_{SZ}(r)$ listed in Table 7 are based on the best fit results of two parametrized models. The SZ profile that arises from electrons following the β-density profile (Equation (73)) can be derived via Equation (76) to be in the form of

$$\Delta T_{SZ} = \Delta T_0 \left(1 + \frac{\Theta^2}{\Theta_c^2}\right)^{(1-3\beta)/2} . \tag{152}$$

Here ΔT_0 is the central temperature decrement and Θ_c is the angular core radius. The exponent β[7] and Θ_c exhibit significant degeneracy in our APEX-SZ maps, we therefore fix the power law slope to $\beta = 0.86$, which is the best-fit value found in Plagge et al. (2010). The results based on this profile are labeled $Y_{SZ,\beta}$ in Table 7.

The second model is a generalized version of the NFW profile (GNFW), suggested by Nagai et al. (2007a), which can be expressed in terms of the intra cluster medium pressure as

$$P_e = \frac{P_0}{(r/r_p)^c \left[1 + (r/r_p)^a\right]^{(b-c)/a}}. \tag{153}$$

In this equation, P_0 is the normalization of the pressure profile, r_p the scale radius and a, b, c are the slope parameters of the profile. The slope parameters are fixed to the best-fit results of $a = 0.9$, $b = 5$ and $c = 0.4$ found in Nagai et al. (2007a), reducing the free

4 AIfA, University of Bonn
5 http://www.eso.org/sci/libraries/SPIE2012/8452-65.pdf
6 http://www.mathworks.de/products/matlab/
7 Note that in this context β corresponds to the power law slope parameter and not to the angular diameter distance ratio used in the lensing related parts of this work.

parameters to P_0 and r_p. Using the ideal gas law, $P_e = n_e k_B T_e$, we can express Equation (76) in terms of the pressure as

$$\frac{\Delta T_{SZ}}{T_{CMB}} = f(x) \int \frac{\sigma_T}{m_e c^2} P_e dl. \tag{154}$$

A MCMC likelihood analysis is used to find the best fitting model parameters for the data field of $10' \times 10'$ size, centered on the cluster. The radius of the sphere, for which Y_{SZ} is derived, is determined by using the X-ray based $r_{500,X} - T$ relation Vikhlinin et al. (2006).

The choice of this radius is motivated by the usage in a $Y_{SZ} - T_X$ scaling relation, for which the listed SZ measurements were originally obtained for. Once the SZ analysis is finalized, the usage of lensing based integration radius is preferred. To improve the comparability of our lensing measurements to the currently available Y_{SZ} measurements, we recalculate our weak lensing masses within $r_{500,X}$.

From Equation (80) we expect that the cluster mass is proportional to the integrated compton-y parameter Y_{SZ} as

$$M \propto E(z)^{-2/3} D_A^2(z) Y_{SZ}^{3/5}, \tag{155}$$

where $E(z)$ is the normalized Hubble parameter and D_A the angular diameter distance at the redshift of the cluster.

The values of Y_{SZ}, listed in the following tables, include this prefactor, to allow direct comparison between clusters with different redshifts.

Table 7: Weak lensing masses and Y_{SZ} within $r_{500,X}$: Listed are the weak lensing masses, based on the S/N optimized as well as the conservative selection, within a sphere of $r_{500,X}$ that was used to derive Y_{SZ}. The listed values of Y_{SZ} are scaled with $E(z)^{-2/3} D_A^2$ to ease the comparison with Figure 62 and Figure 63. We classify the dynamical state (Rel.) in three classes, relaxed (1), elliptical(0.5) and disturbed (0).

Cluster	$M_{S/N}(r_{500,X})$ $[10^{14} M_\odot]$	$M_{cons}(r_{500,X})$ $[10^{14} M_\odot]$	$Y_{SZ,\beta}$ $[10^{-4}\mathrm{Mpc}^2]$	$Y_{SZ,GNFW}$ $[10^{-4}\mathrm{Mpc}^2]$	Rel.	Ref.
A2744	$10.4^{+1.6}_{-1.5}$	$10.8^{+1.7}_{-1.6}$	$2.86^{+2.35}_{-1.11}$	$1.79^{+0.58}_{-0.65}$	0	1
A2813	$6.2^{+1.5}_{-1.4}$	$7.2^{+1.8}_{-1.6}$	$0.41^{+0.33}_{-0.11}$	$0.45^{+0.25}_{-0.23}$	0.5	1
A209	$6.9^{+1.0}_{-0.9}$	$7.2^{+1.1}_{-0.9}$	$1.36^{+1.00}_{-0.53}$	$1.51^{+0.57}_{-0.60}$	1	2
XLSSC 006	$3.9^{+1.0}_{-0.9}$	$4.1^{+1.1}_{-1.0}$	$0.14^{+0.14}_{-0.06}$	$0.15^{+0.09}_{-0.09}$	1	0
RXCJ0232.2−4420	$5.1^{+1.7}_{-1.5}$	$4.3^{+1.8}_{-1.4}$	$1.15^{+0.49}_{-0.36}$	$1.23^{+0.55}_{-0.38}$	1	1
A383	$3.9^{+0.9}_{-0.8}$	$3.8^{+1.2}_{-0.6}$	$0.40^{+0.69}_{-0.47}$	$0.33^{+0.28}_{-0.27}$	1	2
RXCJ0437.1+0043	$5.2^{+1.6}_{-1.5}$	$5.7^{+1.9}_{-1.7}$	$0.90^{+0.64}_{-0.34}$	$0.97^{+0.30}_{-0.29}$	0.5	1
MS0451.6−0305	$5.5^{+1.7}_{-1.4}$	$5.7^{+1.8}_{-1.5}$	$0.59^{+0.51}_{-0.25}$	$0.38^{+0.51}_{-0.25}$	0.5	3
A520	$6.1^{+1.9}_{-1.8}$	$6.7^{+1.3}_{-1.0}$	$1.67^{+0.93}_{-0.60}$	$1.17^{+0.30}_{-0.43}$	0	4
RXCJ0516.6−5430	$6.3^{+2.3}_{-2.8}$	$6.6^{+2.4}_{-2.5}$	$3.48^{+1.08}_{-0.87}$	$1.04^{+0.31}_{-0.30}$	0	0
RXCJ0528.9−3927	$5.1^{+1.8}_{-1.7}$	$5.9^{+2.0}_{-1.7}$	$0.90^{+0.63}_{-0.33}$	$1.01^{+0.35}_{-0.41}$	0	1
RXCJ0532.9−3701	$6.5^{+1.3}_{-1.1}$	$6.7^{+1.4}_{-1.3}$	$1.61^{+0.68}_{-0.43}$	$1.77^{+0.43}_{-0.55}$	1	1
A3404	$8.6^{+2.5}_{-2.2}$	$8.5^{+3.1}_{-2.5}$	$1.04^{+2.81}_{-0.67}$	$1.77^{+0.65}_{-0.77}$	0.5	2
Bullet	$7.8^{+2.4}_{-2.1}$	$8.0^{+2.7}_{-2.4}$	$5.06^{+0.78}_{-0.72}$	$4.67^{+0.45}_{-0.61}$	0	1
A907	$4.3^{+1.1}_{-1.5}$	$3.9^{+1.7}_{-1.3}$	$0.57^{+0.68}_{-0.32}$	$0.83^{+0.34}_{-0.35}$	0.5	2

Continued on next page

Table 7 – continued from previous page

Cluster	$M_{S/N}(r_{500,X})$	$M_{cons}(r_{500,X})$	$Y_{SZ,,\beta}$	$Y_{SZ,GNFW}$	Rel.	Ref.
A907	$5.0^{+1.0}_{-0.8}$	$4.9^{+1.1}_{-1.0}$	$0.57^{+0.68}_{-0.32}$	$0.83^{+0.34}_{-0.35}$	0.5	2
RXCJ1023.6+0411	$6.9^{+1.1}_{-1.0}$	$7.0^{+1.3}_{-1.1}$	$0.84^{+0.30}_{-0.29}$	$0.65^{+0.51}_{-0.27}$	1	5
MS1054.4−0321	$13.7^{+5.7}_{-5.1}$	$16.4^{+7.6}_{-7.3}$	$0.94^{+0.32}_{-0.23}$	$0.79^{+0.23}_{-0.22}$	0	3
MACSJ1115.8+0129	$5.2^{+4.3}_{-3.5}$	$5.4^{+6.1}_{-3.7}$	$0.30^{+0.21}_{-0.08}$	$0.02^{+0.33}_{-0.03}$	1	5
MACSJ1115.8+0130	$5.2^{+1.6}_{-1.6}$	$6.2^{+2.0}_{-1.8}$	$0.30^{+0.21}_{-0.08}$	$0.02^{+0.33}_{-0.03}$	1	5
A1300	$6.4^{+2.1}_{-2.0}$	$5.9^{+2.0}_{-1.7}$	$0.61^{+0.50}_{-0.22}$	$0.36^{+0.81}_{-0.22}$	0.5	1
RXCJ1206.2−0848	$9.6^{+2.4}_{-2.1}$	$9.4^{+2.7}_{-2.6}$	$1.49^{+0.54}_{-0.41}$	$1.41^{+0.68}_{-0.56}$	1	6
A1689	$13.8^{+1.2}_{-1.1}$	$14.0^{+1.3}_{-1.2}$	$3.66^{+1.31}_{-0.86}$	$4.91^{+0.84}_{-1.36}$	0	2
RXJ1347−1145	$10.4^{+3.2}_{-2.8}$	$9.9^{+3.6}_{-3.2}$	$2.29^{+0.71}_{-0.52}$	$1.95^{+0.81}_{-0.55}$	0.5	5
RXJ1347−1145	$11.7^{+2.7}_{-2.2}$	$12.1^{+2.8}_{-2.8}$	$2.29^{+0.71}_{-0.52}$	$1.95^{+0.81}_{-0.55}$	0.5	5
A1835	$10.2^{+1.9}_{-1.8}$	$10.4^{+2.1}_{-2.1}$	$2.45^{+1.11}_{-0.84}$	$2.34^{+0.59}_{-0.90}$	1	2
RXJ1504	$5.9^{+1.6}_{-1.4}$	$6.3^{+1.9}_{-1.6}$	$1.74^{+1.43}_{-0.78}$	$1.75^{+0.66}_{-0.82}$	1	5
A2163	$17.0^{+5.3}_{-3.9}$	$16.8^{+4.2}_{-5.4}$	$3.12^{+5.27}_{-2.06}$	$3.07^{+1.35}_{-1.49}$	0	4
A2204	$7.9^{+2.5}_{-1.8}$	$7.3^{+2.3}_{-1.8}$	$1.04^{+0.37}_{-0.22}$	$1.34^{+1.07}_{-0.50}$	1	5
RXCJ2014.8−2430	$4.4^{+2.5}_{-1.8}$	$4.7^{+3.0}_{-2.0}$	$0.07^{+1.17}_{-1.29}$	$0.02^{+0.05}_{-0.42}$	1	7
MACS J2214.9−1359	$7.1^{+2.3}_{-1.9}$	$5.5^{+2.5}_{-1.7}$	$2.90^{+0.49}_{-0.65}$	$1.74^{+0.32}_{-0.27}$	1	8
MACS J2243.3−0935	$9.5^{+2.7}_{-2.7}$	$8.9^{+2.9}_{-2.8}$	$3.31^{+0.83}_{-0.71}$	$2.44^{+0.38}_{-0.49}$	0	6
A2537	$7.8^{+1.2}_{-1.1}$	$7.3^{+1.4}_{-1.3}$	$0.76^{+0.53}_{-0.36}$	$0.97^{+0.44}_{-0.44}$	1	1
RXCJ2337.6+0016	$6.3^{+1.4}_{-1.3}$	$6.8^{+1.6}_{-1.4}$	$1.34^{+0.80}_{-0.49}$	$1.16^{+0.48}_{-0.43}$	0	1

References:
(0) This work, based on convergence maps and distribution of cluster members.
(1) Zhang et al. (2006)
(2) Zhang et al. (2008)
(3) Andersson et al. (2009)
(4) Govoni et al. (2004)
(5) Allen et al. (2008)
(6) Ebeling et al. (2010a)
(7) Pratt et al. (2009)
(8) Ebeling et al. (2007)

8.4.2 *Planck Data*

Additional to the results from APEX-SZ, we compare our lensing masses with Y_{SZ} measurements obtained with the Planck satellite and listed in Planck Collaboration et al. (2011). Planck observes in a frequency range from 30 to 857 GHz in nine different bands. The resolution is frequency dependent and ranges from 5′ to 31′. The major advantages of Planck against APEX-SZ are the absence of atmospheric effects and the multi-frequency coverage of the instrument. This allows well calibrated measurements of the CMB as well as that of the SZ effect. The multi-frequency matched filters (Melin et al., 2006) allow to separate the SZ signal from other physical sources. The disadvantage of Planck is the low resolution compared to APEX-SZ. Most clusters of galaxies observed by Planck are not resolved, which makes it necessary to put strong priors on the pressure profile. To obtain a measure of Y_{SZ} at $r_{500,X}$, the universal pressure profile described in Arnaud et al. (2010) is used and its normalization is fitted to the signal within $5 \times r_{500,X}$. This result is then used to calculate Y_{SZ} within a sphere of $r_{500,X}$. The integration radius as well as the center of the profile is determined by X-ray observations of these clusters, using an iterative procedure described in Kravtsov et al. (2006).

Table 8 lists the Y_{SZ} measurements by Planck, as well as our weak lensing masses calculated to the radius for that Y_{SZ} was calculated.

Table 8: Weak lensing masses and Y_{SZ} within $r_{500,X}$: S/B optimized and conservative mass estimates within a spherical radius of $r_{500,X}$, which was used for the measurement of Y_{SZ}. The listed SZ values are scaled with $E(z)^{-2/3}D_A^2$.

Cluster	$M_{S/N}(r_{500,X})$ $(10^{14}M_\odot)$	$M_{cons}(r_{500,X})$ $10^{14}M_\odot)$	$Y_{SZ,Planck}$ $(10^{-4}Mpc^2)$
A2744	$10.1^{+1.6}_{-1.4}$	$10.4^{+1.7}_{-1.5}$	1.57 ± 0.19
A2813	$6.1^{+1.5}_{-1.4}$	$7.0^{+1.8}_{-1.6}$	1.27 ± 0.15
RXCJ0232.2-4420	$5.3^{+1.7}_{-1.6}$	$4.5^{+1.8}_{-1.4}$	0.78 ± 0.12
A520	$6.8^{+2.1}_{-2.0}$	$7.4^{+1.4}_{-1.1}$	0.93 ± 0.13
RXCJ0516.6-5430	$7.5^{+2.7}_{-3.3}$	$7.8^{+2.8}_{-3.0}$	1.17 ± 0.09
RXCJ0528.9-3927	$5.7^{+2.0}_{-1.9}$	$6.5^{+2.2}_{-1.9}$	1.07 ± 0.12
RXCJ0532.9-3701	$6.4^{+1.2}_{-1.1}$	$6.6^{+1.3}_{-1.3}$	0.89 ± 0.12
A3404	$8.4^{+2.5}_{-2.2}$	$8.3^{+3.1}_{-2.5}$	1.03 ± 0.07
Bullet	$8.1^{+2.5}_{-2.2}$	$8.4^{+2.8}_{-2.5}$	2.40 ± 0.13
A1300	$6.2^{+2.0}_{-1.9}$	$5.7^{+2.0}_{-1.7}$	1.17 ± 0.21
RXCJ1206.2-0848	$9.4^{+2.3}_{-2.1}$	$9.2^{+2.6}_{-2.6}$	1.45 ± 0.26
A1689	$13.6^{+1.1}_{-1.1}$	$13.8^{+1.2}_{-1.2}$	1.29 ± 0.14
A2163	$18.9^{+5.9}_{-4.3}$	$18.8^{+4.7}_{-6.1}$	4.26 ± 0.20
A2204	$8.1^{+2.5}_{-1.8}$	$7.4^{+2.4}_{-1.9}$	1.06 ± 0.10
A2390	$9.3^{+1.4}_{-1.1}$	$9.1^{+1.4}_{-1.3}$	1.54 ± 0.12
MACS J2243.3-0935	$10.2^{+2.9}_{-2.9}$	$9.4^{+3.1}_{-2.9}$	1.63 ± 0.20
RXCJ2248.7-4431	$10.7^{+1.9}_{-1.7}$	$10.1^{+2.1}_{-2.0}$	1.96 ± 0.14

8.4.3 *Comparison APEX-SZ vs. Planck*

As a small sanity check, we compare the Y_{SZ} measurements from Planck and APEX-SZ for the 15 clusters that are in common in both samples. For that we plot the we plot the measurements from APEX-SZ using the GNFW model against those from Planck and looking for outliers in the expected one-to-one behavior. For this simple test, we do not aim to correct for different integration radii.

The two highest and the two lowest measurements from APEX-SZ are the most discrepant values from the expected one-to-one relation. While the two highest values in APEX-SZ gives higher values than those from Planck, the two lowest values give lower values as expected from Planck.

Assuming a general relation of $Y_{SZ} \propto M_{WL}$ and that the subsample being representative for the full APEX-SZ sample, we expect that the slope of $Y_{SZ} - M_{WL}$ scaling to be lower for APEX-SZ as that using Planck data.

The region at small Y_{SZ} has much more measurements than the high Y_{SZ} regime. We therefore expect that if the discrepant measurements are outliers only the two high values will have a significant influence on the scaling relation using the full cluster sample.

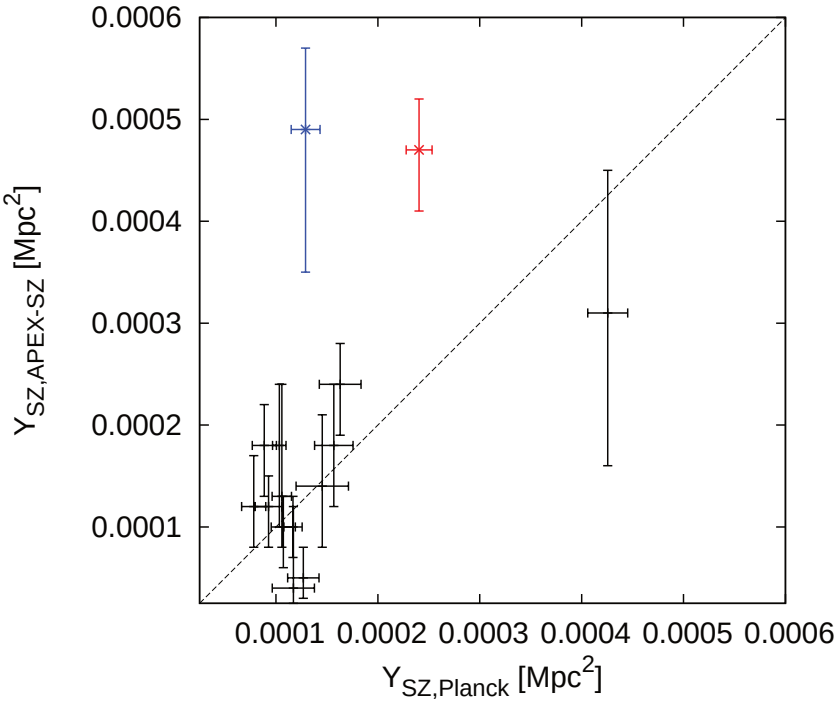

Figure 61: Y_{SZ} measured by APEX-SZ against Y_{SZ} measured by Planck. Marked in red is the measurement of the Bullet cluster, marked in blue the measurement of A1689. The dashed line marks shows a line with a slope equals unity.

We identify the two discrepant clusters as the Bullet cluster and Abell 1689. Both clusters are rather extreme systems. Bullet cluster was already mentioned in this thesis as a example of dissociative merger. Assumptions of hydrostatic equilibrium fail as well as the description of the matter distribution with a single NFW density profile. Additionally the integration radius for the APEX-SZ measurement is taken from the $r_{500} - T_X$ relation, which is a bad choice for merging clusters that are affected by shock heating.

A 1689 is a well studied cluster with high mass and high concentration parameter (Coe et al., 2010; Sereno et al., 2013). A significant amount of substructure is also reported for this system. However, other disrupted systems, such as A520 or A2744 do not show a significant offsets between both instruments.

It is therefore not clear, if these discrepant clusters are real outliers and which of both instruments yield the wrong estimate. In the following analysis of the scaling relation, we will highlight both clusters and give results with both clusters included and excluded from the scaling analysis.

8.4.4 *Regression Analysis*

Deriving the scaling between two observables with significant error bars in both directions and with intrinsic scatter is not trivial. Several methods exist, each treating this problem differently. In the publication by Kelly (2007), several frequently used linear regressions were compared, suggesting that the Gaussian mixture model introduced in this publica-

tion[8] performs best. This fitting method was also used in Marrone et al. (2012) to obtain the best fit parameters of the $Y_{SZ} - M_{WL}$ for 18 clusters of galaxies, observed with the Sunyaev-Zel'dovich Array and Suprime-cam.

From Equation (80) we expect that the scaling between mass and Y_{SZ} to be a power law, which can be described as

$$M_{WL} = M_0 \left(\frac{E(z)^{-2/3} D_A^2(z) Y_{SZ}}{Y_{pvt}} \right)^B , \tag{156}$$

where E(z) is the normalized Hubble parameter (Equation (25)) and D_A the angular diameter distance at cluster redshift z, $Y_{pvt} = 2 \times 10^{-4}\mathrm{Mpc}^2$ the pivot point and M_0 the normalization. From the self-similar model, we expect the power law exponent B to be around 3/5.

To use the original regression method from Kelly (2007), we perform the regression in log-space, where the relation becomes a linear function. For comparison, we also show estimates using the BCES method (Akritas and Bershady, 1996), which was also used in Planck Collaboration et al. (2011).

Another implementation using the Gaussian Mixture model, was created in context of the investigation of the $Y_{SZ} - T_X$ scaling by A. Bender. This version works in linear space, allows the inclusion of non-detections, supports asymmetric error bars and assumes log-normal intrinsic scatter. Unfortunately this Matlab based code uses functions not supported by the older Matlab version available in our institute. We therefore use the methods listed before in this thesis work, but plan the translation of the Matlab based code into IDL for the future work, once the Y_{SZ} results from APEX-SZ are finalized.

8.4.5 *Results using APEX-SZ*

In Table 9, we list the results of our regression analysis on the different samples.

Comparing the results obtained using β-profile with those using GNFW on can see that normalization and slope tends to be smaller for the measurements using a β-profile. A comparison between the masses obtained with the S/N optimized selection and those obtained using the conservative method, yield almost identical results. The interpretation of the results are therefore independent of the details of the used lensing method. A comparison between the two fitting methods show, that BCES tends to give higher values than those from the Gaussian mixture method. However, all measurements agree with each other within their error bars.

Using the full cluster sample, we obtain a normalizations $M_0 = 8.5^{+0.4}_{-0.3} \times 10^{14} M_\odot$ for the β-model and the Gaussian mixture method and $M_0 = 8.7^{+0.6}_{-0.6} \times 10^{14} M_\odot$ for the GNFW-model using the same fitting method. These values are lower than those reported by Hoekstra et al. (2012) who obtained values between $10.4 \pm 0.6 \times 10^{14} M_\odot$ and $11.2 \pm 0.7 \times 10^{14} M_\odot$ using SZ data from Planck. The normalization found by Marrone et al. (2012) using a pivot point of $Y_{pvt} = 1 \times 10^{-5}\mathrm{Mpc}^2$ is 0.37 ± 0.1 in log scale. Using the same pivot value we obtain 0.39 ± 0.1 for the full cluster sample and the GNFW model. This is only slightly higher, and might be caused by the differences between our weak lensing masses and those of Okabe et al. (2009) which where used in this publication.

The slope that we measure, using the β-profile based results, are about $2 - 3\sigma$ lower than the expected value of $B = 0.6$, independent if we exclude the potential outliers or mergers. Hoekstra et al. (2012) and Marrone et al. (2012) also find shallower slopes as expected from self-similarity, if they include all clusters of their sample. Their results of

8 Freely available as IDL code: http://idlastro.gsfc.nasa.gov/ftp/pro/math/linmix_err.pro

$B = 0.44^{+0.12}_{0.11}$ from Marrone et al. (2012) and $B = 0.45 \pm 0.11$ agree well with our results of $B = 0.43 \pm 0.1$ using the Gaussian mixture method and $A = 0.48 \pm 0.13$ using BCES.

Excluding A1689 and the Bullet cluster from the analysis yields a slope and normalization, which is consistent with self similarity and the results of Hoekstra et al. (2012). In general the GNFW based results yield better agreement with literature values and expectation than the β-profile based ones. Since the APEX-SZ values are still preliminary, we do not attempt to interpret the observed differences between both models.

Table 9: Best fit values of the normalization parameter M_0 and slope parameter B for different cluster samples, fitting methods and pressure profiles. The relaxed cluster sample includes all clusters with a dynamical state greater or equal 0.5. The cluster sample described as "w.o. A1689 and Bullet" includes all clusters except the two clusters mentioned. The listed errors do not include systematic effects.

Cluster sample	S/N optimized				Conservative			
	β-profile		GNFW-profile		β-profile		GNFW-profile	
	M_0	B	M_0	B	M_0	B	M_0	B
All								
Kelly	0.93 ± 0.02	0.34 ± 0.08	0.94 ± 0.03	0.43 ± 0.10	0.94 ± 0.03	0.30 ± 0.08	0.94 ± 0.03	0.41 ± 0.09
BCES	0.95 ± 0.04	0.41 ± 0.13	0.98 ± 0.04	0.48 ± 0.13	0.96 ± 0.05	0.41 ± 0.15	0.98 ± 0.05	0.49 ± 0.14
Relaxed								
Kelly	0.96 ± 0.04	0.38 ± 0.09	0.94 ± 0.03	0.47 ± 0.12	0.95 ± 0.04	0.36 ± 0.10	0.96 ± 0.03	0.49 ± 0.10
BCES	0.96 ± 0.05	0.40 ± 0.13	0.97 ± 0.04	0.46 ± 0.12	0.95 ± 0.06	0.36 ± 0.14	1.01 ± 0.05	0.56 ± 0.17
w.o. A1689 and Bullet								
Kelly	0.93 ± 0.03	0.32 ± 0.09	0.97 ± 0.04	0.54 ± 0.18	0.93 ± 0.03	0.28 ± 0.09	0.96 ± 0.05	0.49 ± 0.17
BCES	0.96 ± 0.06	0.44 ± 0.18	1.02 ± 0.07	0.60 ± 0.20	0.97 ± 0.06	0.43 ± 0.20	1.03 ± 0.07	0.61 ± 0.24

Figure 62 show the best fitting scaling relations for $Y_{SZ,\beta}$ and $Y_{SZ,GNF}$ using the signal to noise optimized mass measurements. The bullet cluster, marked in red, is below the scaling relation in both figures, while A1689, marked in blue, fits well into the derived scaling relation. Figure 63 shows the best fit results when A1689 and Bullet cluster are excluded from the fit.

8.4.6 *Results using Planck*

The best fitting parameters of the $Y_{SZ} - M_{WL}$ scaling relation using Planck measurements can be found in Table 10. Similar to the results using APEX-SZ, we do not see significant differences between the conservative and the S/N optimized selections.

Table 10: Best fit values of the normalization parameter M_0 in log scale and slope parameter B using Planck measurements. For further description see Table 9.

	S/N optimized		Conservative	
Cluster sample	M_0	B	M_0	B
All				
Kelly	1.04 ± 0.04	0.62 ± 0.2	1.05 ± 0.04	0.62 ± 0.2
BCES	1.02 ± 0.04	0.59 ± 0.14	1.02 ± 0.04	0.57 ± 0.17
w.o. A1689 and Bullet				
Kelly	1.02 ± 0.03	0.64 ± 0.16	1.02 ± 0.04	0.61 ± 0.16
BCES	0.99 ± 0.04	0.5 ± 0.15	0.99 ± 0.04	0.49 ± 0.19

The slope is in perfect agreement with the self similar predictions, independent of the exclusion of A1689 and the Bullet cluster or not. The normalization converted into linear space is $M_0 = 11 \pm 1 \times 10^{14} M_\odot$ using all clusters, and $M_0 = 10.5^{+1.0}_{-0.9} \times 10^{14} M_\odot$, in very good agreement with the findings of Hoekstra et al. (2012).

In Figure 64 the lensing masses using the S/N optimized selection are plotted against the Y_{SZ} measurements from Planck. Additionally the best fit scaling relation using the Kelly (2007) regression code, together with its one sigma error band is shown in the same figure. The Bullet cluster as well as A1689, marked in red and blue, are the only clusters that are not included in the one sigma error band within their errors. The highest value in mass and Y_{SZ} corresponds to A2163. This cluster was excluded in Hoekstra et al. (2012) as outlier in the scaling relation. The mass estimate in this thesis yield a significantly higher mass for this cluster, which results in a good agreement with the found scaling relation.

8.4.7 *Intrinsic scatter*

As a third parameter of interest in scaling relations is the amount of intrinsic scatter. It describes the minimal scatter between mass and observable that can be reached and is the fundamental limitation on the accuracy of this observable as mass proxy. This scatter in Y_{SZ} at fixed mass was found to be $\sigma_{log(Y|M)} = 0.10 \pm 0.01$ (Planck Collaboration et al., 2011) using X-ray based mass estimates and $\sigma_{log(Y|M)} = 0.12^{+0.07}_{-0.05}$ using lensing. The results for APEX-SZ as well as for the Planck measurements using masses of the S/N optimizes selection method can be found in Table 11. The intrinsic scatter estimated with masses

using the conservative selection is almost identical to that derived from S/N optimized selection, with a largest difference between both of 0.5σ. The table using the conservative selection can be found in Table 13.

Table 11: Intrinsic scatter in Y_{SZ} at fixed mass, $\sigma_{log(Y|M)}$, and intrinsic scatter in mass at fixed Y_{SZ}, $\sigma_{log(M|Y)}$, for APEX-SZ and Planck measurements. Scatter is given in log to the base 10, similar to Hoekstra et al. (2012) and Planck Collaboration et al. (2011)

	APEX-SZ		Planck
Cluster sample	β-profile	GNFW-profile	Arnaud-profile
All			
$\sigma_{log(Y\|M)}$	0.19 ± 0.08	0.13 ± 0.06	0.11 ± 0.04
$\sigma_{log(M\|Y)}$	0.07 ± 0.03	0.06 ± 0.03	0.09 ± 0.03
w.o. A1689 and Bullet			
$\sigma_{log(Y\|M)}$	0.15 ± 0.08	0.09 ± 0.05	0.06 ± 0.04
$\sigma_{log(M\|Y)}$	0.05 ± 0.03	0.06 ± 0.03	0.04 ± 0.03
Relaxed			
$\sigma_{log(Y\|M)}$	0.14 ± 0.08	0.10 ± 0.07	
$\sigma_{log(M\|Y)}$	0.05 ± 0.03	0.06 ± 0.03	

The intrinsic scatter is largest for the APEX-SZ measurements using a β-profile and the smallest using Planck measurements. The scatter for relaxed clusters[9] is similar to that if only A1689 and the Bullet cluster are excluded from the sample. This shows that other disturbed systems in the sample do not significantly affect the amount of intrinsic scatter. This finding is in agreement with Marrone et al. (2012), who found similar amount of intrinsic scatter for relaxed and disrupted systems[10], with a trend to lower intrinsic scatter for disturbed systems.

The intrinsic scatter found in APEX-SZ measurements using the GNFW model agree well with that found by Hoekstra et al. (2012), Marrone et al. (2012) and Planck Collaboration et al. (2011).

Also in agreement with the literature are the results using Planck data with $\sigma_{log(Y|M)} = 0.11 \pm 0.04$ and $\sigma_{log(M|Y)} = 0.09 \pm 0.03$. Excluding the Bullet cluster and A1689 further shrinks the amount of intrinsic scatter to $\sigma_{log(Y|M)} = 0.06 \pm 0.04$ and $\sigma_{log(M|Y)} = 0.04 \pm 0.03$.

8.4.8 *Selection bias*

The scaling relation derived in this thesis work is likely affected by selection biases of Malmquist and Eddington type. These effects can be modeled and corrected for, if a clear selection function is given. This is only the case for the X-ray selected subsample, which is described in Section 5.1.1. However, the current results of the SZ data analysis based on the Matlab pipeline dose not include four clusters of the X-ray selected sample, and classifies three other clusters as non detections. This makes the X-ray selected cluster sample

9 We define the relaxed cluster sample as all clusters with a dynamical state qualifier (Table 7) ≥ 0.5.

10 Note that the intrinsic scatter given in Marrone et al. (2012) is given to the base e, resulting in a factor $\ln(10)$ between those quoted in that paper and our measurements.

incomplete at the current status of the SZ data reduction, and do not allow to correct for selection biases. The quoted values of the scaling relation stay therefore uncorrected for these effects.

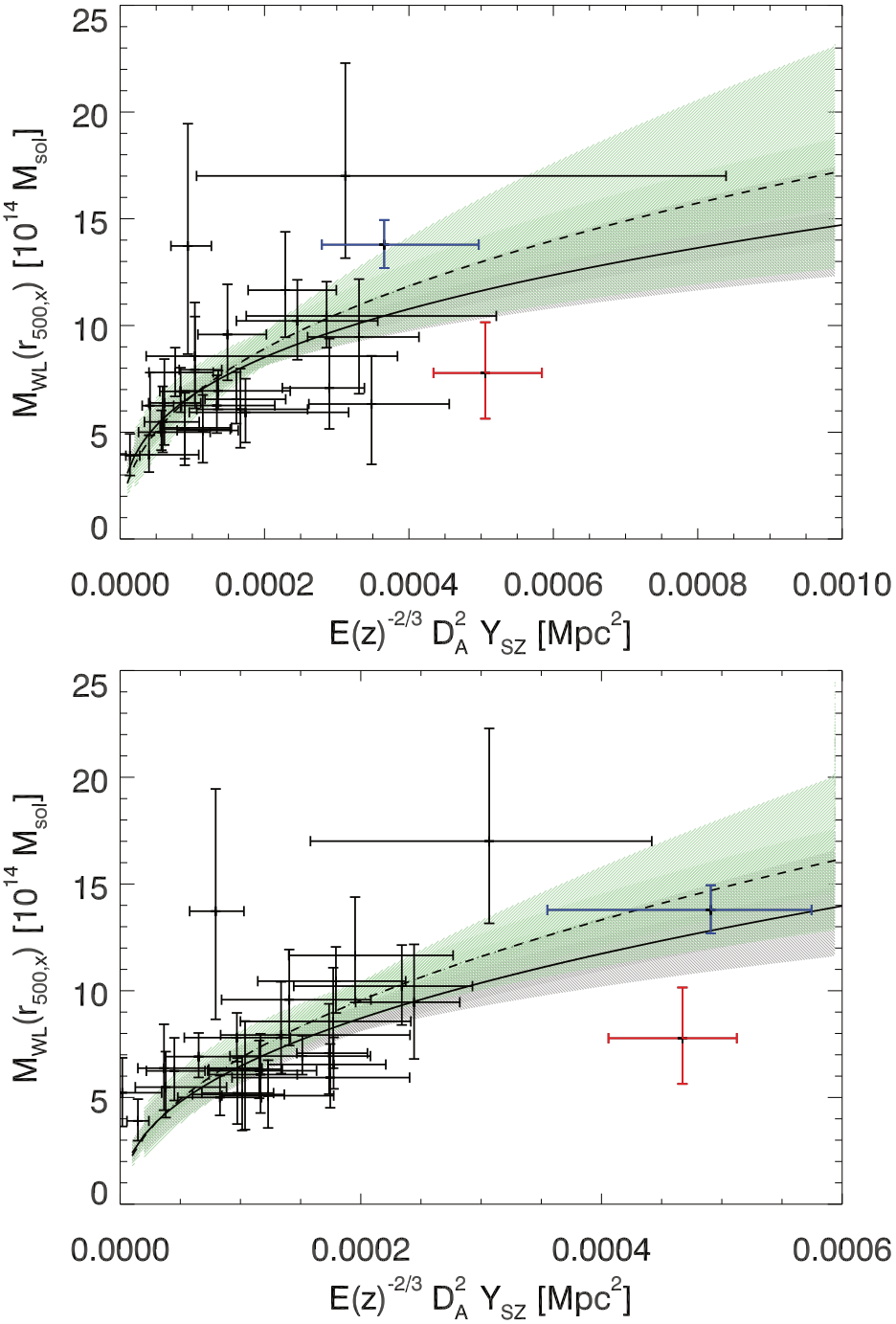

Figure 62: Top: Scaling relation $M_{S/N}$ vs. $Y_{SZ,\beta}$. Bottom: Scaling relation $M_{S/N}$ vs. $Y_{SZ,GNFW}$. Black line: Best fit power law using the regression code by Kelly (2007) with corresponding one sigma range in gray. Dashed line: Best fit power law using BCES, with one sigma error band in green.

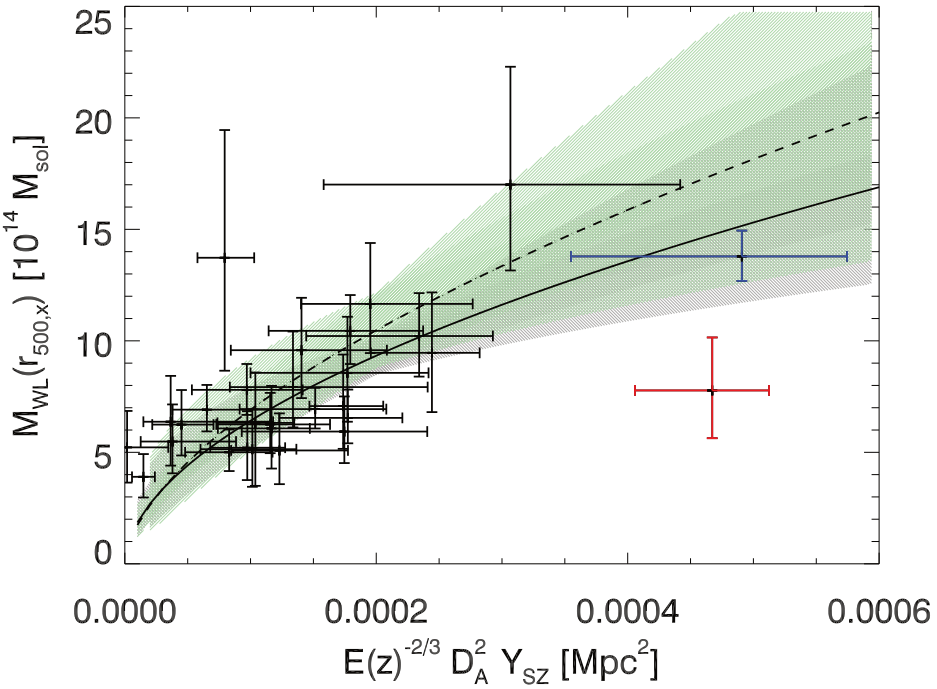

Figure 63: Same as Figure 62 but showing the best fit results excluding A1689 and the Bullet cluster from the fit.

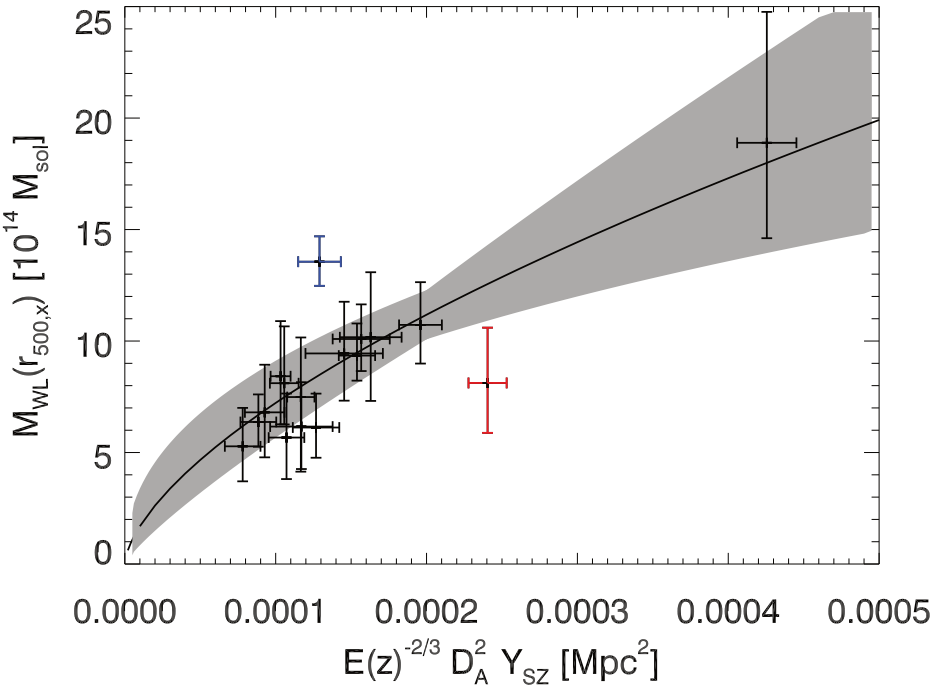

Figure 64: $M_{S/N}(r_{500,X} - Y_{SZ,Planck}$ scaling relation. Black line: Best fit power law using Gaussian Mixture model with 1 sigma error range in gray. Red: Bullet cluster. Blue: A1689.

9 RESULTS ON INDIVIDUAL CLUSTERS

Beside the main project goal of obtaining cluster masses for scaling relations, the data quality and the developed methods also allow deeper analysis of the cluster fields. Especially the multi-wavelength data and the incorporation of redshift information based on galaxy colors allow new insights into the dynamics of galaxy clusters. Dynamically disturbed systems, especially major mergers of galaxy clusters, are interesting to study for several reasons. Due to the deep gravitational potentials they are one of the most energetic processes since the big bang. Cluster mergers can cause shocks in the ICM, visible in X-rays or in sub-mm regime. They are also believed to be the energy source for observed radio features such as radio relics or halos (see Section 3.1.5).

It is well known, that the environment of a galaxy, such as the membership to a massive galaxy cluster, affects the evolution of the galaxy (Section 3.1.1). Less known is the effect of major cluster mergers on galaxy evolution and star formation. At the current state, it is not clear, if cluster mergers trigger star formation (Ferrari et al., 2005; Hwang and Lee, 2009), quench it (Poggianti et al., 2004) or has no immediate effect on it (Chung et al., 2010). The identification and investigation of cluster mergers at different phases of the merging process can shed light on galaxy evolution and star formation rates in dense environments and their characteristic timescales.

Dissociative mergers, in which the ICM and the dark matter got separated, were used to put tight constraints on the dark matter scattering cross-section (Markevitch et al., 2004). A significant fraction of those clusters that became famous for their dynamical properties, such as the Bullet Cluster, A2744 and A520 are part of this sample. These clusters were object of intense studies, incorporating deep, space-based imaging from the Hubble space telescope (HST), which we have not used in this sample. We therefore do not have performed deep investigations on those clusters, since we do not expect new insights from our shallower data. However, we show some results on A520 that may shed some light on the existence or non-existence of a dark core in this cluster.

We performed deeper investigations on clusters that show strong hints of an ongoing merger event and for which the dynamical state was not previously known. We found two candidates of dissociative mergers, which may be of similar importance as the aforementioned famous merging clusters. X-ray observations of RXC0245 indicate a shock front very similar to that seen in the Bullet cluster. The general morphology of the X-ray emission follows the matter distribution obtained with lensing. The second candidate is RXC1135, which shows an elongated double peaked structure in lensing as well as in galaxy distribution. The SZ-map indicates that the majority of the gas lies in the middle between both peaks. The separation between both mass peaks is about 1.35 Mpc, resulting in gas to dark matter offset of about 0.7 Mpc.

A recently accepted joint Chandra / HST proposal, with deep Chandra and HST observations on RXC0245 and a shallow snapshot exposure on RXC1135 will allow us to derive stronger conclusions on both clusters. If they confirm the current interpretation of the cluster dynamics, RXC0245 represent a merger that is in an earlier phase than the Bullet cluster. RXC1135, with its huge offset, may mark a new record in dark matter to gas offset, and would represent a late phase of a cluster merger after its first close encounter.

The following subsections describe the results of the deeper individual analyses.

9.1 A520

A weak lensing analysis by Mahdavi et al. (2007) indicated a mass concentration between the major galaxy over densities, at the position of the main ICM cloud. This lensing feature was also found in Okabe and Umetsu (2008) and recently by Jee et al. (2012). The latter publication uses a mosaic of *Wide Field Planetary Camera* 2 (WFPC2) images from HST in the F814*W* filter. Red cluster galaxies between $22 < \mathrm{F814W} < 24$ where excluded with a red sequence method using additional color information from observations with the Canada-France-Hawaii-Telescope (CFHT). Those authors claim a detection of this mass concentration called "Dark Core" at a 10σ level.

Shortly after the publication of Jee et al. (2012), a publication by Clowe et al. (2012) using the *Advanced Camera for Surveys* (ACS) on the HST in multiple filters was published, stating a non detection of the dark core.

For our lensing analysis we used Suprime-cam data in three filter sets. Due to the known problems of finding a proper astrometric solution for old Suprime-cam data, we created convergence maps to compare them with the high quality space based results. Since the *I* band as well as the *R* band data were obtained under good seeing conditions, with FWHM=0.57 and FWHM=0.70 respectively, we had the chance to use both bands for a lensing analysis. The results of both convergence maps yield an astonishing result. While the *I* band based convergence map follows closely the mass contours found by Clowe et al. (2012), the *R* band based mass map follows well the result by Jee et al. (2012).

In Figure 65, we compare our *I* band convergence contours with the results of Clowe et al. (2012). We are able to recover the same general structure, with the mass peaks 2, 4, 5 and 7. Peak 1 is slightly off, which might be a result of the lower background galaxy density and therefore the lower resolution of our convergence map. We also do not recover a separate peak at position 6, but recover the same elongated structure at postion 4. For comparison we show also the convergence contours for the *R* band in red. The position of the dark core is merked with the number 3.

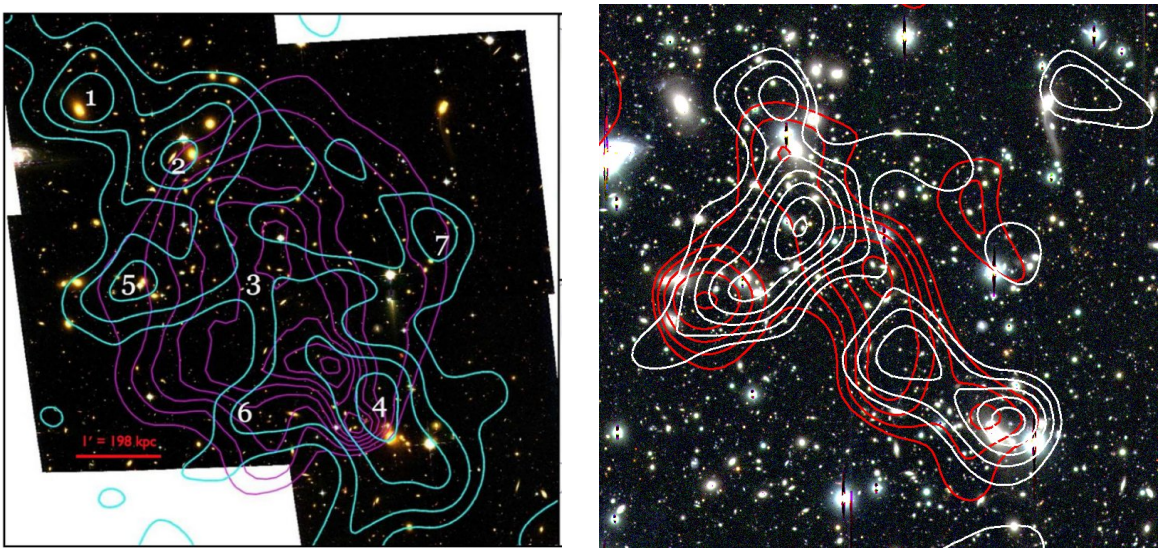

Figure 65: Left: Color composite of A520 with lensing contours (cyan) and X-ray contours from Clowe et al. (2012). Right: Suprime-cam color composite of the same region. White contours show the recovered convergence using the *I* band, red contours are based on the *R* band.

In Figure 66, we show the mass reconstruction by Jee et al. (2012) and the result using the shape measurements of the *R* band. We can identify the same features as before, but

in contrast to the results of the *I* band analysis and the results by Clowe et al. (2012), we get also a peak at postion 3 similar to Jee et al. (2012).

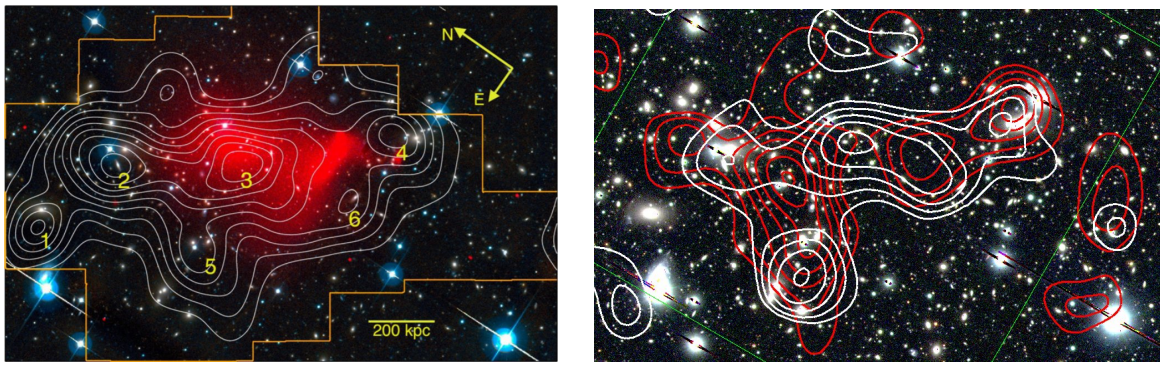

Figure 66: Left: Color composite with X-ray emission highlighted in red and lensing contours (white) of A520, found by Jee et al. (2012). Right: Suprime-cam color composite of the same region, rotated to the same orientation as in Jee et al. White contours now highlight the lensing contours from *R* band and red contours from the *I* band. Green lines show the borders of the ACS field used in Clowe et al.(ref)

The good agreement of the ground based data with those from space, indicate that our measurements for A520 reasonably recover the shear of the sources. Further, the high agreement of the mass map either with the results of Jee et al. (2012) or with Clowe et al. (2012), is a possible key to understand what causes the dark core. A comparison between the shear measurements of sources in both shear catalogs and the investigation of the non-overlapping galaxy samples are planed for the future, but would need the original space-based data to derive final conclusions. If the difference in the convergence maps are caused by a number of galaxies that physically close to each other, the lensing feature, known as dark core, might become a famous example of galaxy alignment.

9.2 RXCJ0245

About 9 ks of X-ray data from XMM-Newton revealed clear bullet like structure for this cluster. As visible in Figure 67 the similarity to the famous Bullet Cluster is astonishingly high. Available shallow 25 ks Chandra data can neither constrain the shock region, but shows very sharp edges of the cold front of the bullet. The apparent opening angle of the cold front of about 30 degrees, as seen in the Chandra image, indicates that the merger should take place almost in the plane of the sky. While the opening angle appears to be smaller than the Bullet cluster, the opening angle of the potential Mach cone visible in the XMM image seems to be larger implying a lower Mach number than in the Bullet cluster. Additional support of the bow shock interpretation comes from a spectroscopic analysis of the X-ray data. The temperature at the bullet region of 7.1 ± 0.7 keV is significantly cooler than the > 9 keV in the surrounding area.

The optical images from WFI reveal a elongated distribution of cluster galaxies, following the apparent merging axis. The two dominating elliptical galaxies are separated by 1.9 arcminutes corresponding to 500 kpc. We found archival data from FORS2 at the VLT in the *R* band, covering the merging region of the cluster. A weak lensing convergence map is created by using WFI and FORS2 data. For the region covered by both instruments, we used the measurements based on FORS2, because of the superior image depth and quality compared to the WFI image. The shape measurements from WFI are used for those regions not covered by FORS2. The background selection is completely based on the colors obtained with WFI to avoid additional color transformations from the FORS2 *R* band to

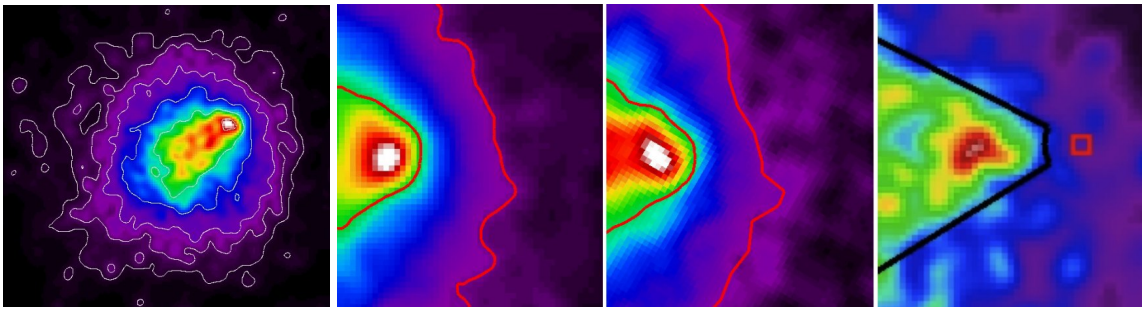

Figure 67: Left: XMM-Netwon [0.5-2.0] keV surface brightnes map of RXC0245. Right: XMM maps of Bullet cluster (left) and RXC0245 (middle) with similar depth. The image of RXC0245 was rotated to the same orientation as that of the Bullet cluster. Smoothing and scale are the same in both images. The red lines indicate the position of the cold and the shock front. The Chandra surface brightness map is seen on the right side. Images from F. Parcaud.

the COSMOS filters. The contours of the resulting convergence map can be found in Figure 68. As one can see, the convergence also underlines the picture of an ongoing cluster merger.

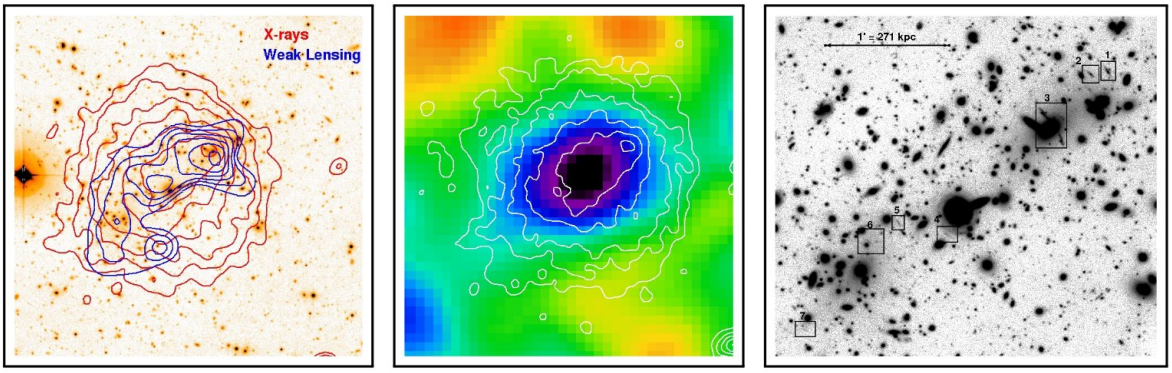

Figure 68: Multi-frequency view of RXC0245. Left: *R* band image from WFI with X-ray surface brightness contours in red and weak lensing convergence contours in blue. Middle: APEX-SZ image with X-ray surface brightness contours in white. Right: FORS2 *R* band image of the core region. Boxes highlight strong lensing arc candidates. Left and middle image from F. Pacaud.

The deeper FORS2 images allowed us to identify several arc candidates indicating high convergence at those regions of the cluster. Because of that, the obtained convergence map using weak lensing can only be of indicative nature, since the most of the interesting regions are actual within the strong lensing regime.

The future HST observations for this cluster will allow us to significantly improve the convergence by combining strong and weak lensing information. This will allow us to resolve the mass distribution to high accuracy and to disentangle the two cluster cores. The observations in three filter bands will then again allow us to use our color selection method to identify lensed background images and possible multiple images of sources.

9.3 RXC1135

RXC1135 was identified as an elongated, two peaked system in the weak lensing convergence map. In Figure 69, we show a *B*, *V*, *R* color composite image of this cluster together with the convergence contours in white. One can see a large elliptical galaxy close to the

eastern (left) peak, while close to the western (right) peak several bright elliptical galaxies are visible. The lensing contours are also extending between the two cluster cores up to the position of peak of the SZ-signal, indicated by red contours. This becomes even clearer in the SZ-map with highlighted lensing contours shown in Figure 18. The spatial correlation between lensing contours and SZ-peak might seduce the reader to over-interpret this convergence feature. One could think about a large amount of gas stored at this position or even interpret it as a hint of a non collision-less dark matter. This feature can also be a result of the limited resolution of the convergence map. Also the SZ-map is relatively noisy and can potentially be affected by point sources. However, the SZ-signal can be interpreted as a strong hint for a gas versus mass offset of this cluster.

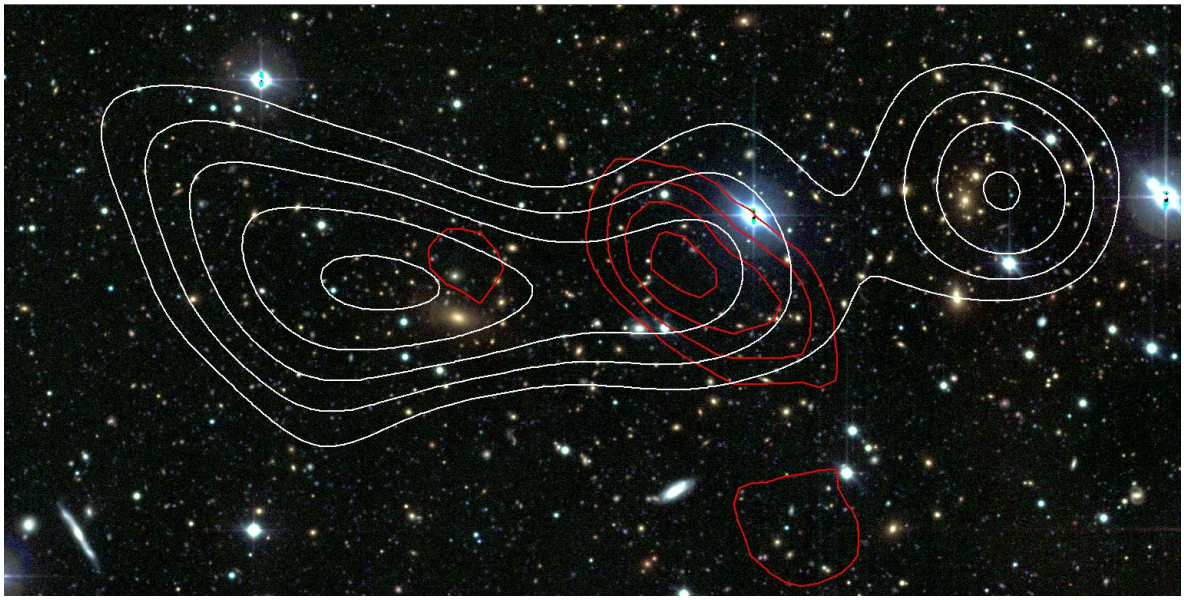

Figure 69: B, V, R color image of RXC1135 with WFI. White contours show the projected mass density, red contours the SZ-signal.

Since galaxies behave in a cluster merger as almost collision-less particles, the distribution of cluster galaxies can be used as tracers of the matter distribution.

The principle used to calculate β_g for each galaxy can be used to calculate the redshift of a source. We included this step into our pipeline that calculates β_g to save time. The galaxy redshift z_g is estimated by using the same reference galaxies as used for calculating β_g, but is simply derived by calculating the median redshift of these reference sources. This gives us the most likely redshift for each source and allows to create number density maps.

For the number density map shown in Figure 70, we used only galaxies with $0.2 < z_g < 04$. Compared to other approaches that are using red sequence techniques to identify cluster galaxies, this method also includes blue cluster members. The distribution of galaxies are consistent with the position of the shear peaks of the cluster. This again highlights the two peaked nature of the cluster merger. Hence, the presence of two peaks indicates that indeed both peaks are likely to be at the same redshift.

To verify this, we used the method described in Section 7.4, to derive cluster redshifts. By using only galaxies within 2 arcmin distance to the individual peaks we found a redshift for the eastern peak of $z_1 = 0.3075$ and for the western peak $z_2 = 0.3034$. Both redshifts agree with each other within the scatter found in Section 7.4 using apertures of 5 arcmin. The obtained redshifts are robust against changes in aperture size to smaller values. Increasing the aperture results in a convergence of both redshift estimates, because of the inclusion of galaxies of the other cluster core into the redshift measurement.

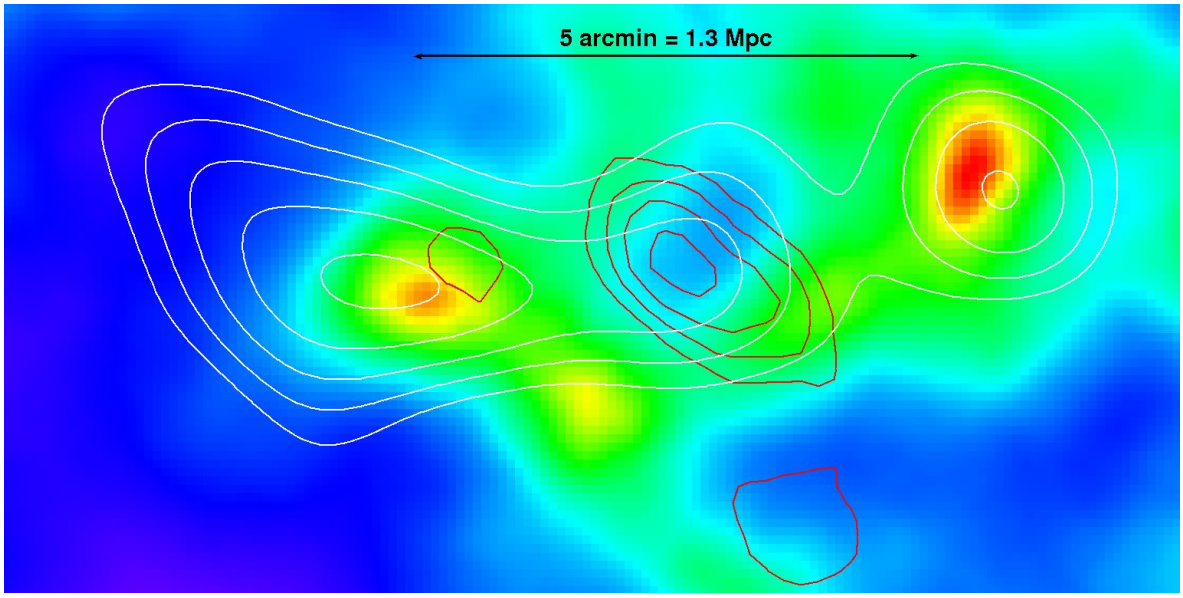

Figure 70: Number density map of cluster galaxies in the field of RXC1135. White and red contours are the same as in Figure 69

The redshift estimates, together with the galaxy distribution, strongly favor the picture of a merging cluster. The future availability of X-ray data from Chandra from our proposal will finally settle the overall gas distribution. If the distribution turns out to be as indicated by the SZ map, the projected distance between cluster cores and gas will be about 670 kpc from each core. The largest currently known projected offset between gas and dark matter is that of DLSCL J0916.2+2951, with 530 kpc (Dawson et al., 2012). This is $\sim$ 20% smaller than that seen in RXC1135.

9.4 MCS1115

Classified as type 1 in the X-ray based morphology system by Ebeling et al. (2010b), MCS1115 is expected to be a relaxed system. In the optical images, huge lensing-induced arcs are visible around the BCG. Also visible is an elongated distribution of elliptical galaxies along the S/E to the N/W axis.

The weak lensing convergence map from WFI as well as that using Suprime-Cam data show the same elongation, as can be seen in Figure 71. Also visible is a group of galaxies at $z \approx 0.15$ on the east of the cluster center, indicated by a single closed red contour from the WFI based convergence map.

Similar to our work on RXC1135, we show number density maps and the lensing contours in Figure 72. Both clearly show an elongated structure from southeast to northwest. For all three positions spectroscopic redshifts of a single elliptical galaxy is available from SDSS. All of them are at a redshift of $z = 0.35 \pm 0.01$, which is identical to that of the main cluster.

Additionally to that, we performed redshift estimates of the sub-clusters using our cluster redshift method. Due to the small separation between all three structures, we used again a small aperture of 2 arcmin radius. Using WFI we obtained redshifts of $z_{\mathrm{SE}} = 0.343$, $z_{\mathrm{cen}} = 0.345$ and $z_{\mathrm{NW}} = 0.332$ for the southeastern, central and the northwestern structure. Using Suprime-Cam data we obtain redshifts of $z_{\mathrm{SE}} = 0.349$, $z_{\mathrm{cen}} = 0.343$ and $z_{\mathrm{NW}} = 0.337$. These measurement underline, that the observed structures are in deed at the same redshift and not the result of a projection effect. The regular shape of the X-ray surface brightness

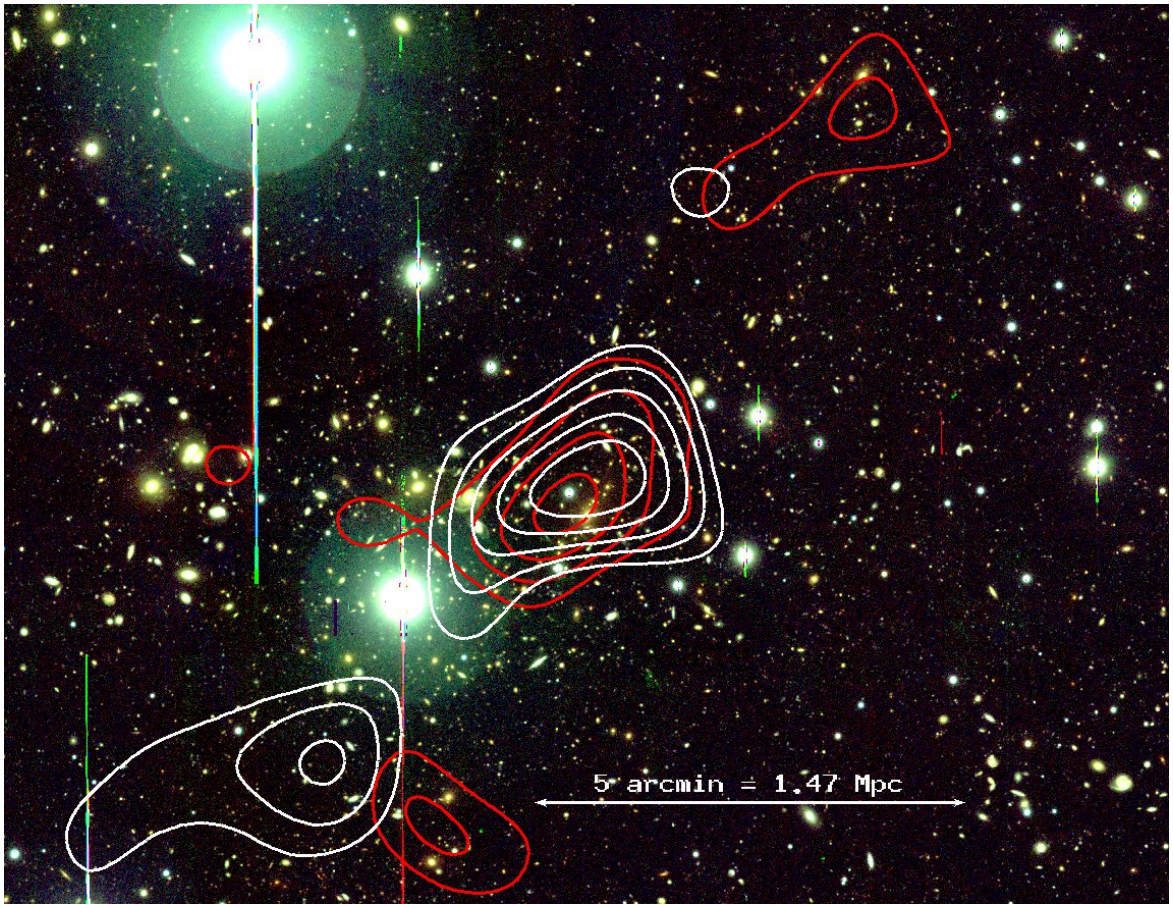

Figure 71: Color image based the Suprim-Cam data set. White contours are weak lensing convergence contours based on Suprime-cam. Red contours are the convergence contours obtained with the WFI data set.

of the cluster center suggests that we see the cluster in a pre-merger state, before the ICM gets significantly disrupted. The high agreement between WFI and SUP in the lensing and number density map, as well as for the cluster redshifts, highlight how goodwe can recover these features regardless which instrument is used.

9.5 RXC0516

Visible in Figure 73 is field of RXC0516, which also appears to be a complex system. At the expected center of the cluster, we find three large elliptical galaxies arranged in a line. The northern galaxy seems to be slightly brighter than the other two, but does not dominate the system. About 1.2 Mpc or 4.5 arcmin western of this constellation, another three elliptical galaxies are visible, similar in size and color to the previous ones. The lensing map shows a two peaked structure corresponding to the two groups of large elliptical galaxies. Additionally it shows an elongation to the southeast and another one at the northwestern part of the cluster. While the southern extension follows the distribution of cluster galaxies, the western extension does not show galaxies at that redshift. Also at higher redshifts, no overdensity of galaxies is found at that position. The X-ray map shows a bright source, close to the western extension. The size of the X-ray source is marginally larger as that of a point source, but the peak emission falls together with a bright point source in the optical image. Because of that, we can not judge if the western elongation is caused by a distant cluster or simply by noise in the shear field.

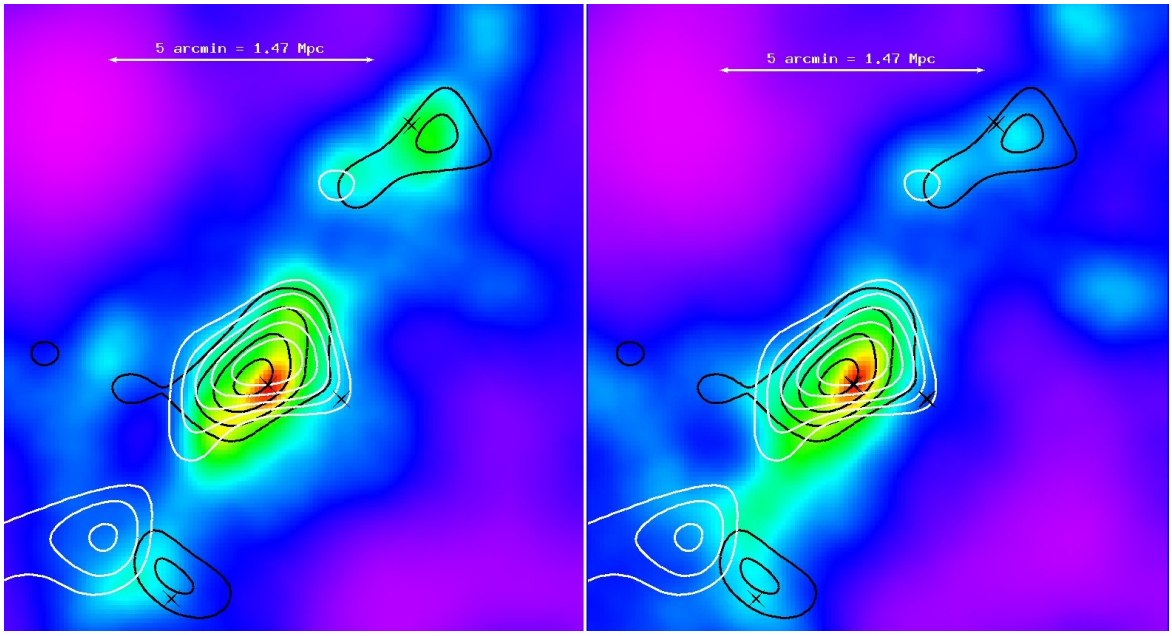

Figure 72: Left: Number density map of galaxies at cluster redshift in the MCS1115 field based on WFI data. Right: same as left but based on Suprime-cam data. White and red contours are weak lensing contours based on Suprime-cam and WFI respectively. Black crosses show the positions of four elliptical galaxies with spectroscopic redshifts similar to the cluster.

The northwestern lensing peak can be associated with the cluster SCSO J0516-542620, with a photometric redshift of $z = 0.38$. The redshift estimate based on our cluster redshift method yields $z = 0.325$- This is significantly lower and closer to the redshift of RXC0516, which is $z = 0.2952$. The southeastern peak falls together with the majority of the X-ray emission and corresponds to RXC0516. Our redshift estimate for this region is $z = 0.2972$ and in very good agreement with the spectroscopic redshift. For the south eastern extension, we measure a redshift of $z = 0.2968$, which is also in a good agreement with the redshift of the main cluster.

The similar redshift and the disrupted X-ray morphology along the north south axis let us conclude that RXC0516 is in a process of merging with the substructure creating the southeastern elongation in the lensing map. Regarding the peak associated with SCSO J0516-542620, the situation is less clear. The lensing and number density peak let us assume that it is of similar mass as RXC0516 but the X-ray emission is significantly lower as for RXC0516. This can be caused by gas stripping due to the merger process or indicate that this system has a lower mass as the weak lensing reconstruction suggest. The redshift for this region indicates that this system is physically close the RXC0516 system, making it likely that it is either in a pre-merging or in a merging state with RXC0516.

Additionally to that complex system, the X-ray surface brightness map shows an other diffuse X-ray source in the south western corner. This cluster is also visible in Figure 74, in our number density map for redshifts of $0.55 < z < 0.75$, and can be identified as SCSO J05158-543906. Unfortunately our cluster redshift method does not converge for the region of interest around this cluster, since the overdensity created in color-color space appears to be affected by remaining galaxies at redshifts of RXC0516. However, the photometric redshift of $z = 0.66$ (Menanteau et al., 2010) for SCSO J05158-543906, is well consistent with the redshifts of the galaxies creating the overdensity in the number density map.

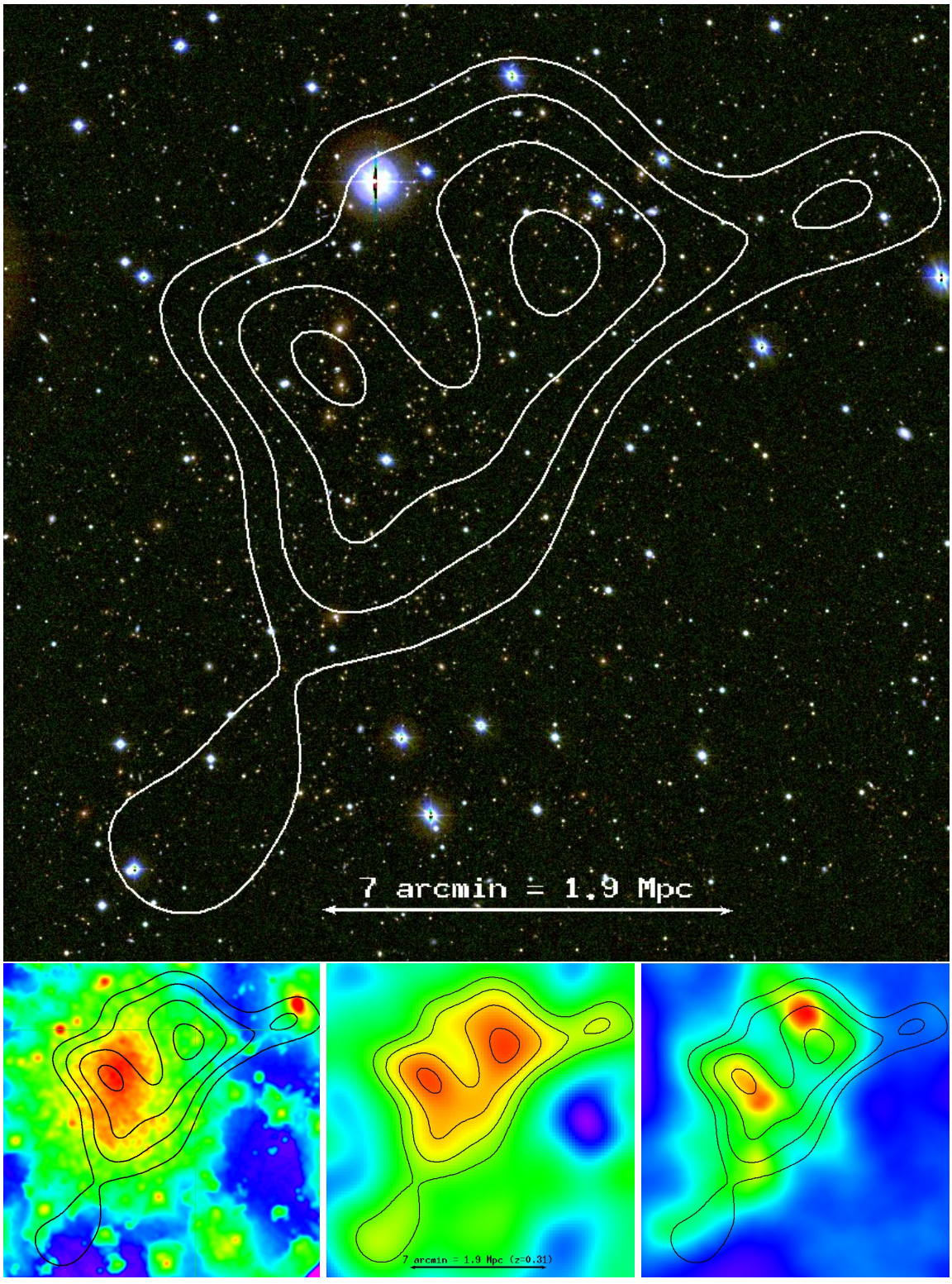

Figure 73: Top: B, V, R color composite of RXC0516, with convergence contours in white. Lower left: X-ray surface brightness map from XMM-Newton in logarithmic scale. Lower middle: Weak lensing convergence map. Lower right: Number density map of galaxies at cluster redshift, with convergence contours.

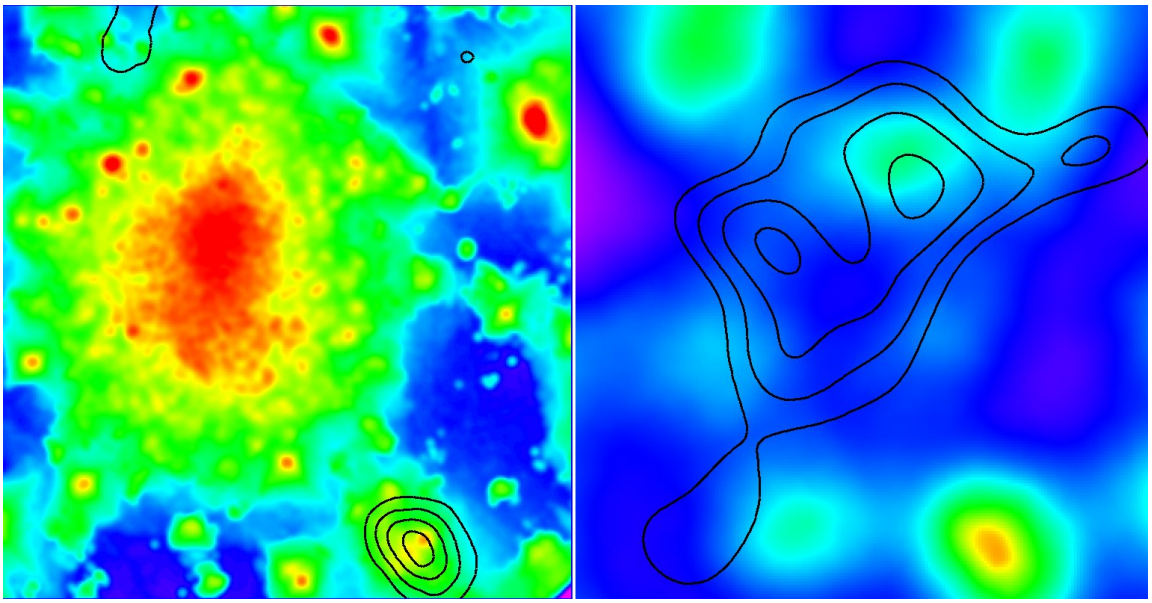

Figure 74: Left: XMM surface brightness map of the RXC0516 field with slightly modified cut levels and size with respect to Figure 73 to improve the visibility of SCSO J05158-543906 (lower,right corner). Contours taken from the map on the right side. Right: Number density map for galaxies in the redshift range of $0.55 < z < 0.75$ with lensing contours similar to Figure 73.

10

SUMMARY AND CONCLUSIONS

10.1 THE FULL CLUSTER SAMPLE

This thesis work describes the weak lensing follow-up analysis of all galaxy clusters at $z < 1$ that were detected via the SZ effect with within the APEX-SZ project.

An observing program of six observation runs, encompassing 44 nights, was conducted with the Wide Field Imager (WFI) at the 2.2m ESO/MPG telescope at La Silla, Chile. Together with archive data from WFI and from Suprime-Cam at the 8m Subaru telescope at Hawaii, this data set allowed the weak lensing analysis for 39 galaxy clusters.

For the weak lensing analysis, a signal optimizing selection of background galaxies was developed, which estimates the angular diameter distance ratio for each individual galaxy. Based on a photometric reference catalog it could be shown that the influence of cosmic variance on the weak lensing analysis can be reduced by up to 40% compared to commonly used background selection methods with the same number of filters.

A new photometric method to derive cluster redshifts was developed. Tests on eleven galaxy clusters with spectroscopic redshifts yield a RMS scatter in redshift of 0.004, about four times smaller than other widely used photometric methods. This new method was also applied to merging systems to constrain the redshifts of the observed substructures.

The derived cluster masses were compared to weak lensing based cluster masses in the literature, yielding good agreement with recent results by Hoekstra et al. (2012). The observed mass-concentration relation was compared to most recent results of large volume dark matter simulations, also yielding very good agreement.

The scaling relation between cluster mass and integrated compton-y parameter, Y_{SZ}, was investigated using measurements of APEX-SZ and the Planck satellite. Using the Y_{SZ} measurements by the Planck satellite, and a power law relation with slope parameter B and normalization M_0, we find $B = 0.62 \pm 0.2$ and $M_0 = 11 \pm 1 \times 10^{14} M_\odot$ as best fit results. These results agree well with recent results from Hoekstra et al. (2012) and with the expectation, $B = 0.6$, from the assumption of self-similar evolution.

The SZ results using APEX-SZ measurements show lower values for the normalization and slope parameters. The best fit parameters, using the Y_{SZ} measurements based on a isothermal β-profile, show the largest discrepancy from theoretical predictions and from the literature. APEX-SZ measurements based on a GNFW-profile yield the best fit parameters, which agree well with results by Marrone et al. (2012) and Hoekstra et al. (2012).

The Y_{SZ} estimates from A1689 and the Bullet cluster differ between APEX-SZ and Planck by 2.5σ and 3.7σ. Excluding both clusters from the scaling relation leads to an increase of the slope to $B = 0.54 \pm 0.18$ and changes the normalization to $M_0 = 9.3^{+0.9}_{-0.8} \times 10^{14} M_\odot$ for the APEX-SZ measurements using the GNFW-profile. This result agrees well with the Planck based results in this work, as well as with the results reported by Hoekstra et al. (2012) after exclusion of A2163. A1689 and the Bullet cluster contribute significantly to the estimated intrinsic scatter between mass and Y_{SZ}. The steeper slope and lower intrinsic scatter seen in the scaling relation of relaxed clusters, compared to the complete sample, is mostly driven by the exclusion of the two potential outliers. The relaxed sample, and the sample without A1689 and the Bullet cluster, yield similar results in normalization, slope and intrinsic scatter.

The intrinsic scatter of Y_{SZ} at fixed mass, $\sigma_{log(Y|M)}$, is 0.19 ± 0.08, 0.13 ± 0.06 and 0.11 ± 0.04 for the β-profile, the GNFW-profile from APEX-SZ and the measurements by Planck respectively. This agrees well with the results by Hoekstra et al. (2012) of $\sigma_{log(Y|M)} = 0.17^{+0.09}_{-0.06}$ for the full sample and $\sigma_{log(Y|M)} = 0.12^{+0.07}_{-0.05}$ without A2163. It also agrees well with the results presented in the Planck early results (Planck Collaboration et al., 2011), which finds $\sigma_{log(Y|M)} = 0.10 \pm 0.01$.

10.1.1 *Future projects using the X-ray selected sample*

Once the data analysis of the APEX-SZ data is finalized, those data in combination with the lensing masses reported in this thesis will be used to place constraints on the $m - Y_{SZ}$ scaling relation, including a correction for selection biases. The recently published cluster catalog by the Planck collaboration includes the complete X-ray selected cluster sample and allows the same scaling analysis as for the APEX-SZ measurements. Such an scaling analysis, including X-ray measurements, is planned for the near future in collaboration with Dr. K. Basu and Dr. F. Pacaud.

10.2 INDIVIDUAL CLUSTERS

Five galaxy clusters were discussed in greater detail. The lensing analysis of A520 using two different filter bands for the shape measurement, lead to convergence maps that may shed light on the existence or non existence of a "dark core" in A520. Based on X-ray data and supported by the weak lensing convergence map, the cluster RXC0245 is identified as a merging system harboring a shock feature similar to the Bullet cluster, but with a smaller apparent distance between both cluster cores.

The weak lensing analysis of RXC1135, in combination with the SZ map from APEX-SZ, indicates a significant offset between the two major density peaks of dark matter and the location of the ICM. The two cluster cores have a physical separation of at least 1.3 Mpc, while the majority of the gas is located in between both cores. The redshifts of the cores are estimated by the new method described in this thesis and agree within the error bars, excluding potential projection effects. Maps showing the number density of cluster members are created for RXC1135, using redshift estimates based on the described background selection. The distribution of cluster galaxies in the RXC1135 field is closely following the weak lensing derived mass distribution, further supporting the picture of an major merger.

Beside these three extreme cases of merging systems, two other merging systems were discussed. MCS1115 shows large amount of structure along the southeast to northwest axis. The redshift of these substructures, estimated from the new photometric method, are consistent with the cluster redshift. The regular shape in SZ and X-rays indicates that this cluster is in a pre-merging state, a time before significant amount of the ICM gets disrupted by tidal forces. The other merging system is RXC0516, which shows a complex morphology in lensing, as well as in X-ray. The galaxy distribution, lensing map and X-ray surface brightness map suggest an ongoing merger in the north/south direction. A second lensing and cluster galaxy density peak is found east of the main cluster peak. It falls within the extended X-ray emission of the main cluster, but does not show a separate X-ray peak. Therefore, the dynamical state of this substructure stays undefined.

10.2.1 *Future work on merging clusters*

In the near future, new X-ray observations with Chandra (Cycle 15, P.I. F. Pacaud), are expected to shed light on the nature of RXC1135 and will hopefully clarify whether this cluster indeed has the larges gas versus dark matter offset observed so far. If confirmed, a larger observing program is planned to investigate the cluster dynamics in greater detail. For RXC0245, deep Chandra observations in combination with deep Hubble Space Telescope data, will allow to perform a detailed analysis of the mass distribution and of the gas properties. This analysis will show whether this cluster is indeed a Bullet-like merging system, seen at an earlier time in merging history as the Bullet cluster.

A uniform analysis of a sample of the most extreme cluster mergers at $z \approx 0.3$ is planned, which can be used to systematically study the merger dynamics and its effect on star formation. A significant fraction of these extreme mergers is included in the presented APEX-SZ sample and builds the basis of a uniform analysis.

10.3 FUTURE APPLICATIONS OF THE DEVELOPED METHODS

The weak lensing methods developed in thesis will also be used in the weak lensing analysis of the 400d project (Israel et al., 2010b). In my future post-doc project, the color method that described in this thesis, will be further extended to include also statistical estimates of the galaxy type, allowing an improved study of the galaxy population and star formation rate. This also allows a combined analysis of lensing convergence maps and maps showing the distribution forming galaxies in the galaxy cluster. This will make it possible to investigate the star formation rate with local mass density.

Optical follow-up observations of SZ or X-ray detected clusters would significantly benefit from the higher accuracy in photometric cluster redshifts provided by the new method presented here, and would reduce the need for spectroscopic follow-up programs. Therefore a publication of this method is planned future if tests on larger cluster samples yield similar results as found in this work.

Part V

APPENDIX

A

TABLES

In this appendix we display tables that are too large or not important enough to be shown in the main part of this thesis.

Table 12: Weak lensing mass estimates for the S/N optimized and conservative background selection, for the overdensities $\Delta = 200$ and $\Delta = 500$. For the clusters A907, MACSJ1115 and RXCJ1347, the WFI based masses are listed listed in the first line, the SUP based masses are listed in the following line without reciting the cluster name.

Cluster	S/N optimized						Conservative					
	r_{200} Mpc	c_{200}	M_{200} $10^{14}\mathrm{M}_\odot$	r_{500} Mpc	c_{500}	M_{500} $10^{14}\mathrm{M}_\odot$	r_{200} Mpc	c_{200}	M_{200} $10^{14}\mathrm{M}_\odot$	r_{500} Mpc	c_{500}	M_{500} $10^{14}\mathrm{M}_\odot$
A2744	$2.12^{+0.13}_{-0.13}$	$3.95^{+2.55}_{-1.35}$	$14.78^{+2.89}_{-2.56}$	$1.38^{+0.07}_{-0.07}$	$2.57^{+1.79}_{-0.94}$	$10.20^{+1.57}_{-1.45}$	$2.13^{+0.14}_{-0.13}$	$4.55^{+3.10}_{-1.65}$	$14.99^{+3.15}_{-2.58}$	$1.40^{+0.07}_{-0.07}$	$2.99^{+2.18}_{-1.15}$	$10.66^{+1.70}_{-1.55}$
RXCJ0019.0-2026	$2.04^{+0.14}_{-0.14}$	$3.05^{+1.20}_{-0.75}$	$12.85^{+2.83}_{-2.47}$	$1.30^{+0.08}_{-0.08}$	$1.95^{+0.84}_{-0.52}$	$8.33^{+1.56}_{-1.36}$	$1.99^{+0.16}_{-0.16}$	$3.05^{+1.40}_{-0.95}$	$11.93^{+3.12}_{-2.65}$	$1.27^{+0.08}_{-0.09}$	$1.95^{+0.98}_{-0.65}$	$7.73^{+1.62}_{-1.53}$
A2813	$1.90^{+0.19}_{-0.19}$	$2.30^{+1.50}_{-0.90}$	$10.53^{+3.48}_{-2.85}$	$1.18^{+0.09}_{-0.09}$	$1.43^{+1.04}_{-0.61}$	$6.30^{+1.56}_{-1.40}$	$2.05^{+0.21}_{-0.20}$	$2.30^{+1.40}_{-0.90}$	$13.22^{+4.49}_{-3.50}$	$1.27^{+0.10}_{-0.10}$	$1.43^{+0.97}_{-0.61}$	$7.91^{+1.99}_{-1.75}$
A209	$2.08^{+0.12}_{-0.10}$	$2.15^{+0.65}_{-0.55}$	$12.57^{+2.30}_{-1.73}$	$1.28^{+0.06}_{-0.06}$	$1.33^{+0.45}_{-0.37}$	$7.36^{+1.01}_{-0.92}$	$2.14^{+0.14}_{-0.12}$	$2.05^{+0.60}_{-0.55}$	$13.69^{+2.87}_{-2.18}$	$1.31^{+0.06}_{-0.06}$	$1.26^{+0.41}_{-0.37}$	$7.90^{+1.18}_{-1.00}$
XLSSC 006	$1.50^{+0.16}_{-0.15}$	$4.45^{+2.85}_{-1.85}$	$6.06^{+2.15}_{-1.64}$	$0.99^{+0.08}_{-0.09}$	$2.92^{+2.01}_{-1.29}$	$4.29^{+1.12}_{-1.02}$	$1.65^{+0.24}_{-0.21}$	$2.40^{+2.55}_{-1.55}$	$8.06^{+4.05}_{-2.70}$	$1.03^{+0.09}_{-0.10}$	$1.50^{+1.78}_{-1.03}$	$4.88^{+1.36}_{-1.24}$
RXCJ0232.2-4420	$1.58^{+0.18}_{-0.20}$	$15.50^{+32.40}_{-7.80}$	$5.97^{+2.28}_{-1.99}$	$1.09^{+0.11}_{-0.12}$	$10.73^{+23.18}_{-5.52}$	$4.96^{+1.62}_{-1.47}$	$1.48^{+0.20}_{-0.20}$	$15.95^{+22.35}_{-7.20}$	$4.91^{+2.27}_{-1.73}$	$1.03^{+0.12}_{-0.12}$	$11.05^{+15.97}_{-5.10}$	$4.08^{+1.67}_{-1.31}$
RXCJ0245.4-5302	$1.48^{+0.20}_{-0.22}$	$9.35^{+13.95}_{-4.50}$	$5.03^{+2.33}_{-1.93}$	$1.01^{+0.12}_{-0.14}$	$6.38^{+9.91}_{-3.17}$	$3.99^{+1.58}_{-1.40}$	$1.47^{+0.22}_{-0.22}$	$10.35^{+5.65}_{-5.20}$	$4.93^{+2.56}_{-1.90}$	$1.01^{+0.13}_{-0.14}$	$7.08^{+4.01}_{-3.67}$	$3.95^{+1.78}_{-1.43}$
A383	$1.57^{+0.13}_{-0.13}$	$7.85^{+3.45}_{-2.25}$	$5.31^{+1.43}_{-1.21}$	$1.06^{+0.08}_{-0.08}$	$5.32^{+2.44}_{-1.59}$	$4.13^{+0.96}_{-0.85}$	$1.54^{+0.17}_{-0.10}$	$8.65^{+3.25}_{-2.85}$	$5.01^{+1.85}_{-0.91}$	$1.05^{+0.10}_{-0.06}$	$5.88^{+2.30}_{-2.01}$	$3.94^{+1.27}_{-0.65}$
RXCJ0437.1+0043	$1.94^{+0.26}_{-0.24}$	$2.15^{+1.80}_{-1.05}$	$11.10^{+5.09}_{-3.63}$	$1.20^{+0.11}_{-0.12}$	$1.33^{+1.25}_{-0.70}$	$6.50^{+2.05}_{-1.81}$	$2.08^{+0.28}_{-0.27}$	$1.95^{+1.65}_{-1.00}$	$13.69^{+6.30}_{-4.67}$	$1.27^{+0.13}_{-0.14}$	$1.19^{+1.14}_{-0.66}$	$7.77^{+2.63}_{-2.26}$
MS0451.6-0305	$1.52^{+0.16}_{-0.16}$	$9.95^{+37.95}_{-3.75}$	$7.27^{+2.55}_{-2.06}$	$1.04^{+0.10}_{-0.10}$	$6.80^{+27.12}_{-2.65}$	$5.80^{+1.76}_{-1.51}$	$1.56^{+0.17}_{-0.17}$	$8.15^{+6.45}_{-3.20}$	$7.86^{+2.86}_{-2.30}$	$1.06^{+0.10}_{-0.11}$	$5.53^{+4.57}_{-2.26}$	$6.13^{+1.95}_{-1.64}$
A520	$2.13^{+0.27}_{-0.24}$	$0.90^{+0.70}_{-0.50}$	$14.69^{+6.33}_{-4.43}$	$1.18^{+0.11}_{-0.13}$	$0.50^{+0.46}_{-0.30}$	$6.26^{+1.96}_{-1.86}$	$2.14^{+0.20}_{-0.15}$	$1.40^{+0.50}_{-0.50}$	$13.63^{+4.19}_{-2.67}$	$1.26^{+0.08}_{-0.07}$	$0.82^{+0.33}_{-0.32}$	$6.90^{+1.31}_{-1.06}$
RXCJ0516.6-5430	$2.40^{+0.44}_{-0.26}$	$0.50^{+0.45}_{-0.45}$	$21.28^{+13.98}_{-6.20}$	$1.23^{+0.13}_{-0.22}$	$0.26^{+0.28}_{-0.23}$	$7.07^{+2.52}_{-3.16}$	$2.38^{+0.44}_{-0.26}$	$0.65^{+0.60}_{-0.60}$	$20.76^{+13.77}_{-6.09}$	$1.26^{+0.14}_{-0.19}$	$0.34^{+0.38}_{-0.32}$	$7.71^{+2.76}_{-2.97}$
RXCJ0528.9-3927	$1.92^{+0.24}_{-0.22}$	$0.95^{+0.85}_{-0.60}$	$10.76^{+4.56}_{-3.29}$	$1.07^{+0.11}_{-0.13}$	$0.53^{+0.56}_{-0.36}$	$4.68^{+1.63}_{-1.54}$	$1.97^{+0.27}_{-0.24}$	$1.60^{+1.25}_{-0.80}$	$11.62^{+5.46}_{-3.75}$	$1.18^{+0.12}_{-0.13}$	$0.96^{+0.85}_{-0.52}$	$6.17^{+2.13}_{-1.78}$
RXCJ0532.9-3701	$1.80^{+0.13}_{-0.13}$	$5.30^{+2.85}_{-1.65}$	$8.78^{+2.04}_{-1.77}$	$1.20^{+0.07}_{-0.07}$	$3.52^{+2.01}_{-1.16}$	$6.42^{+1.25}_{-1.12}$	$1.81^{+0.13}_{-0.14}$	$6.20^{+3.35}_{-2.05}$	$8.92^{+2.06}_{-1.91}$	$1.21^{+0.08}_{-0.08}$	$4.15^{+2.37}_{-1.44}$	$6.70^{+1.35}_{-1.29}$
A3404	$2.10^{+0.23}_{-0.23}$	$4.70^{+2.40}_{-1.50}$	$12.41^{+4.54}_{-3.65}$	$1.38^{+0.12}_{-0.13}$	$3.10^{+1.69}_{-1.05}$	$8.88^{+2.61}_{-2.27}$	$2.10^{+0.29}_{-0.27}$	$4.40^{+2.65}_{-1.70}$	$12.41^{+5.89}_{-4.20}$	$1.38^{+0.15}_{-0.16}$	$2.89^{+1.87}_{-1.18}$	$8.76^{+3.24}_{-2.63}$
Bullet	$1.86^{+0.22}_{-0.24}$	$2.45^{+1.80}_{-1.05}$	$9.91^{+3.95}_{-3.36}$	$1.16^{+0.11}_{-0.12}$	$1.53^{+1.25}_{-0.71}$	$6.04^{+1.84}_{-1.66}$	$1.90^{+0.25}_{-0.25}$	$2.25^{+1.55}_{-1.05}$	$10.56^{+4.74}_{-3.64}$	$1.18^{+0.12}_{-0.13}$	$1.39^{+1.07}_{-0.70}$	$6.27^{+2.12}_{-1.86}$
A907	$1.78^{+0.82}_{-0.24}$	$2.00^{+1.05}_{-1.95}$	$7.45^{+15.76}_{-2.62}$	$1.09^{+0.08}_{-0.14}$	$1.22^{+0.72}_{-1.20}$	$4.26^{+1.05}_{-1.45}$	$1.69^{+0.28}_{-0.23}$	$2.05^{+1.55}_{-1.00}$	$6.37^{+3.72}_{-2.26}$	$1.04^{+0.13}_{-0.13}$	$1.26^{+1.07}_{-0.66}$	$3.68^{+1.57}_{-1.21}$
	$1.81^{+0.15}_{-0.13}$	$3.80^{+1.05}_{-0.90}$	$7.83^{+2.11}_{-1.57}$	$1.18^{+0.08}_{-0.07}$	$2.47^{+0.74}_{-0.63}$	$5.36^{+1.09}_{-0.90}$	$1.79^{+0.15}_{-0.15}$	$3.95^{+1.55}_{-1.10}$	$7.57^{+2.07}_{-1.75}$	$1.17^{+0.08}_{-0.08}$	$2.57^{+1.09}_{-0.77}$	$5.23^{+1.17}_{-1.05}$
RXCJ1023.6+0411	$1.82^{+0.11}_{-0.10}$	$5.45^{+1.20}_{-1.05}$	$9.23^{+1.78}_{-1.44}$	$1.21^{+0.06}_{-0.06}$	$3.62^{+0.85}_{-0.74}$	$6.79^{+1.09}_{-0.96}$	$1.83^{+0.12}_{-0.11}$	$5.35^{+1.40}_{-1.15}$	$9.38^{+1.97}_{-1.59}$	$1.22^{+0.07}_{-0.07}$	$3.55^{+0.99}_{-0.81}$	$6.88^{+1.25}_{-1.05}$
MS1054.4-0321	$2.03^{+0.36}_{-0.34}$	$7.40^{+40.50}_{-5.85}$	$24.19^{+15.28}_{-10.23}$	$1.37^{+0.17}_{-0.20}$	$5.00^{+28.92}_{-4.08}$	$18.64^{+7.78}_{-6.88}$	$2.06^{+0.29}_{-0.37}$	$16.00^{+43.50}_{-12.15}$	$25.28^{+12.25}_{-11.32}$	$1.43^{+0.19}_{-0.26}$	$11.09^{+0.00}_{-8.59}$	$21.04^{+9.82}_{-9.45}$
MACSJ1115.8+0129	$1.64^{+0.26}_{-0.32}$	$0.80^{+1.75}_{-0.65}$	$7.27^{+4.03}_{-3.48}$	$0.89^{+0.20}_{-0.28}$	$0.44^{+1.16}_{-0.37}$	$2.95^{+2.49}_{-1.99}$	$1.80^{+0.36}_{-0.40}$	$0.30^{+0.70}_{-0.25}$	$9.61^{+6.99}_{-5.09}$	$0.86^{+0.25}_{-0.27}$	$0.14^{+0.42}_{-0.12}$	$2.60^{+2.92}_{-1.75}$
	$1.55^{+0.17}_{-0.19}$	$3.50^{+2.70}_{-1.50}$	$6.13^{+2.25}_{-1.99}$	$1.00^{+0.10}_{-0.11}$	$2.26^{+1.90}_{-1.03}$	$4.12^{+1.29}_{-1.25}$	$1.67^{+0.19}_{-0.20}$	$4.35^{+3.15}_{-1.90}$	$7.67^{+2.93}_{-2.44}$	$1.10^{+0.11}_{-0.12}$	$2.85^{+2.22}_{-1.32}$	$5.40^{+1.73}_{-1.58}$
A1300	$1.75^{+0.21}_{-0.22}$	$2.45^{+3.90}_{-1.35}$	$8.34^{+3.38}_{-2.77}$	$1.09^{+0.11}_{-0.13}$	$1.53^{+2.73}_{-0.90}$	$5.09^{+1.64}_{-1.57}$	$1.62^{+0.22}_{-0.22}$	$6.70^{+9.30}_{-4.05}$	$6.62^{+3.08}_{-2.35}$	$1.09^{+0.11}_{-0.12}$	$4.51^{+6.58}_{-2.84}$	$5.03^{+1.71}_{-1.49}$
RXCJ1135.6-2019	$1.53^{+0.19}_{-0.19}$	$3.05^{+1.95}_{-1.50}$	$5.57^{+2.34}_{-1.83}$	$0.98^{+0.09}_{-0.10}$	$1.95^{+1.36}_{-1.02}$	$3.61^{+1.13}_{-0.99}$	$1.60^{+0.21}_{-0.19}$	$3.10^{+1.95}_{-1.50}$	$6.37^{+2.85}_{-2.01}$	$1.02^{+0.10}_{-0.11}$	$1.98^{+1.36}_{-1.03}$	$4.15^{+1.39}_{-1.16}$
RXCJ1206.2-0848	$1.93^{+0.17}_{-0.17}$	$3.65^{+3.75}_{-1.65}$	$13.09^{+3.77}_{-3.16}$	$1.25^{+0.10}_{-0.10}$	$2.36^{+2.64}_{-1.14}$	$8.87^{+2.18}_{-1.99}$	$1.93^{+0.19}_{-0.19}$	$3.10^{+3.60}_{-1.55}$	$13.09^{+4.26}_{-3.50}$	$1.23^{+0.11}_{-0.13}$	$1.98^{+2.53}_{-1.06}$	$8.52^{+2.44}_{-2.38}$

Continued on next page

Continued from previous page												
	r_{200}	c_{200}	M_{200}	r_{500}	c_{500}	M_{500}	r_{200}	c_{200}	M_{200}	r_{500}	c_{500}	M_{500}
MACSJ1311.0-0311	$1.49^{+0.16}_{-0.17}$	$3.05^{+2.25}_{-1.35}$	$6.08^{+2.18}_{-1.85}$	$0.95^{+0.09}_{-0.10}$	$1.95^{+1.57}_{-0.92}$	$3.94^{+1.24}_{-1.15}$	$1.50^{+0.16}_{-0.17}$	$4.90^{+4.05}_{-2.10}$	$6.21^{+2.21}_{-1.88}$	$0.99^{+0.09}_{-0.10}$	$3.24^{+2.86}_{-1.47}$	$4.48^{+1.39}_{-1.24}$
A1689	$2.50^{+0.08}_{-0.08}$	$6.80^{+1.35}_{-0.90}$	$21.30^{+2.11}_{-1.98}$	$1.68^{+0.05}_{-0.05}$	$4.58^{+0.95}_{-0.63}$	$16.22^{+1.36}_{-1.29}$	$2.53^{+0.09}_{-0.09}$	$6.40^{+1.40}_{-1.00}$	$22.07^{+2.44}_{-2.27}$	$1.70^{+0.05}_{-0.05}$	$4.29^{+0.99}_{-0.70}$	$16.66^{+1.50}_{-1.46}$
RXJ1347-1145	$2.13^{+0.23}_{-0.22}$	$1.85^{+1.35}_{-0.75}$	$17.79^{+6.41}_{-4.96}$	$1.29^{+0.12}_{-0.13}$	$1.12^{+0.93}_{-0.50}$	$9.93^{+3.07}_{-2.70}$	$2.06^{+0.25}_{-0.26}$	$1.90^{+1.65}_{-0.90}$	$16.09^{+6.60}_{-5.36}$	$1.25^{+0.14}_{-0.15}$	$1.16^{+1.14}_{-0.59}$	$9.06^{+3.28}_{-2.94}$
	$2.10^{+0.18}_{-0.16}$	$4.10^{+2.55}_{-1.65}$	$17.05^{+4.77}_{-3.61}$	$1.37^{+0.10}_{-0.09}$	$2.68^{+1.79}_{-1.15}$	$11.86^{+2.78}_{-2.24}$	$2.12^{+0.20}_{-0.22}$	$4.55^{+4.05}_{-2.10}$	$17.54^{+5.45}_{-4.91}$	$1.39^{+0.10}_{-0.12}$	$2.99^{+2.85}_{-1.46}$	$12.47^{+2.85}_{-2.88}$
MACSJ1359.2-1929	$1.40^{+0.25}_{-0.28}$	$4.10^{+6.90}_{-2.55}$	$5.11^{+3.25}_{-2.49}$	$0.91^{+0.14}_{-0.16}$	$2.68^{+4.87}_{-1.76}$	$3.55^{+1.85}_{-1.57}$	$1.48^{+0.27}_{-0.28}$	$4.35^{+5.00}_{-2.50}$	$6.03^{+3.94}_{-2.82}$	$0.97^{+0.15}_{-0.17}$	$2.85^{+3.53}_{-1.73}$	$4.25^{+2.33}_{-1.85}$
A1835	$2.22^{+0.16}_{-0.16}$	$4.10^{+1.50}_{-0.90}$	$16.08^{+3.73}_{-3.23}$	$1.45^{+0.09}_{-0.09}$	$2.68^{+1.05}_{-0.63}$	$11.19^{+2.11}_{-1.99}$	$2.30^{+0.20}_{-0.20}$	$3.20^{+1.20}_{-0.90}$	$17.88^{+5.08}_{-4.27}$	$1.47^{+0.09}_{-0.11}$	$2.05^{+0.84}_{-0.62}$	$11.73^{+2.39}_{-2.34}$
RXJ1504	$1.75^{+0.18}_{-0.17}$	$4.10^{+2.10}_{-1.50}$	$7.56^{+2.58}_{-2.00}$	$1.14^{+0.09}_{-0.10}$	$2.68^{+1.48}_{-1.04}$	$5.26^{+1.39}_{-1.25}$	$1.80^{+0.21}_{-0.20}$	$3.80^{+2.45}_{-1.50}$	$8.22^{+3.23}_{-2.45}$	$1.17^{+0.11}_{-0.11}$	$2.47^{+1.72}_{-1.04}$	$5.62^{+1.72}_{-1.45}$
A2163	$2.96^{+0.43}_{-0.36}$	$1.40^{+0.75}_{-0.60}$	$36.10^{+18.13}_{-11.64}$	$1.74^{+0.16}_{-0.14}$	$0.82^{+0.50}_{-0.39}$	$18.27^{+5.68}_{-4.14}$	$3.06^{+1.00}_{-0.52}$	$1.05^{+0.95}_{-1.00}$	$39.89^{+53.28}_{-17.08}$	$1.73^{+0.13}_{-0.21}$	$0.59^{+0.63}_{-0.57}$	$18.08^{+4.48}_{-5.84}$
A2204	$2.12^{+0.27}_{-0.21}$	$3.05^{+1.05}_{-1.05}$	$12.57^{+5.44}_{-3.38}$	$1.35^{+0.13}_{-0.11}$	$1.95^{+0.73}_{-0.72}$	$8.15^{+2.56}_{-1.86}$	$2.07^{+0.29}_{-0.23}$	$2.40^{+1.15}_{-0.90}$	$11.70^{+5.64}_{-3.48}$	$1.29^{+0.13}_{-0.12}$	$1.50^{+0.80}_{-0.61}$	$7.09^{+2.29}_{-1.79}$
RXCJ2014.8-2430	$1.65^{+0.35}_{-0.31}$	$4.85^{+6.75}_{-2.70}$	$5.92^{+4.62}_{-2.75}$	$1.09^{+0.17}_{-0.18}$	$3.20^{+4.77}_{-1.88}$	$4.26^{+2.38}_{-1.79}$	$1.76^{+0.46}_{-0.38}$	$3.05^{+6.35}_{-2.00}$	$7.18^{+7.23}_{-3.72}$	$1.12^{+0.20}_{-0.20}$	$1.95^{+4.47}_{-1.35}$	$4.65^{+2.96}_{-2.03}$
RXCJ2151.0-0736	$1.41^{+0.19}_{-0.20}$	$6.20^{+5.70}_{-2.70}$	$4.29^{+1.98}_{-1.58}$	$0.94^{+0.11}_{-0.12}$	$4.15^{+4.03}_{-1.90}$	$3.22^{+1.29}_{-1.10}$	$1.42^{+0.22}_{-0.23}$	$5.50^{+7.30}_{-2.85}$	$4.38^{+2.37}_{-1.80}$	$0.95^{+0.13}_{-0.14}$	$3.66^{+5.16}_{-1.99}$	$3.23^{+1.51}_{-1.25}$
A2390	$2.06^{+0.12}_{-0.10}$	$4.85^{+1.20}_{-1.05}$	$12.50^{+2.31}_{-1.73}$	$1.36^{+0.07}_{-0.06}$	$3.20^{+0.84}_{-0.74}$	$9.00^{+1.39}_{-1.08}$	$2.03^{+0.12}_{-0.11}$	$5.05^{+1.35}_{-1.10}$	$11.96^{+2.25}_{-1.84}$	$1.34^{+0.07}_{-0.07}$	$3.34^{+0.95}_{-0.77}$	$8.68^{+1.36}_{-1.20}$
MACS J2214.9-1359	$1.68^{+0.20}_{-0.19}$	$7.55^{+7.35}_{-3.30}$	$9.28^{+3.73}_{-2.81}$	$1.14^{+0.11}_{-0.11}$	$5.11^{+5.20}_{-2.32}$	$7.17^{+2.34}_{-1.94}$	$1.49^{+0.24}_{-0.18}$	$11.90^{+4.10}_{-6.80}$	$6.47^{+3.66}_{-2.07}$	$1.02^{+0.14}_{-0.12}$	$8.18^{+2.91}_{-4.80}$	$5.26^{+2.37}_{-1.60}$
MACS J2243.3-0935	$2.07^{+0.22}_{-0.23}$	$3.35^{+6.45}_{-1.80}$	$16.25^{+5.75}_{-4.84}$	$1.33^{+0.12}_{-0.14}$	$2.15^{+4.54}_{-1.23}$	$10.79^{+3.09}_{-3.03}$	$1.92^{+0.23}_{-0.24}$	$5.55^{+10.45}_{-3.65}$	$12.97^{+5.24}_{-4.28}$	$1.28^{+0.13}_{-0.15}$	$3.70^{+7.40}_{-2.54}$	$9.57^{+3.10}_{-2.99}$
RXCJ2248.7-4431	$2.13^{+0.15}_{-0.14}$	$2.60^{+0.90}_{-0.75}$	$15.78^{+3.57}_{-2.91}$	$1.34^{+0.08}_{-0.08}$	$1.63^{+0.62}_{-0.51}$	$9.79^{+1.75}_{-1.58}$	$2.07^{+0.16}_{-0.17}$	$2.50^{+1.10}_{-0.80}$	$14.49^{+3.63}_{-3.28}$	$1.30^{+0.09}_{-0.09}$	$1.57^{+0.76}_{-0.54}$	$8.88^{+1.87}_{-1.79}$
A2537	$1.98^{+0.13}_{-0.13}$	$3.80^{+1.65}_{-1.05}$	$11.97^{+2.52}_{-2.21}$	$1.29^{+0.06}_{-0.07}$	$2.47^{+1.16}_{-0.73}$	$8.19^{+1.22}_{-1.18}$	$1.92^{+0.15}_{-0.15}$	$3.65^{+2.35}_{-1.35}$	$10.91^{+2.76}_{-2.36}$	$1.24^{+0.07}_{-0.08}$	$2.36^{+1.65}_{-0.93}$	$7.40^{+1.39}_{-1.29}$
RXCJ2337.6+0016	$1.89^{+0.18}_{-0.17}$	$2.00^{+1.20}_{-0.75}$	$10.14^{+3.18}_{-2.50}$	$1.16^{+0.08}_{-0.09}$	$1.22^{+0.83}_{-0.50}$	$5.80^{+1.31}_{-1.20}$	$1.92^{+0.19}_{-0.18}$	$2.80^{+1.60}_{-1.10}$	$10.63^{+3.48}_{-2.72}$	$1.22^{+0.09}_{-0.09}$	$1.77^{+1.12}_{-0.75}$	$6.73^{+1.59}_{-1.41}$

Table 13: Intrinsic scatter using the masses from the conservative background selection.

Cluster sample	APEX-SZ		Planck
	β-profile	GNFW-profile	Arnaud-profile
All			
$\sigma_{log(Y\|M)}$	0.21 ± 0.08	0.13 ± 0.07	0.12 ± 0.04
$\sigma_{log(M\|Y)}$	0.07 ± 0.03	0.06 ± 0.03	0.09 ± 0.03
w.o. A1689 and Bullet			
$\sigma_{log(Y\|M)}$	0.18 ± 0.09	0.1 ± 0.06	0.07 ± 0.04
$\sigma_{log(M\|Y)}$	0.06 ± 0.03	0.06 ± 0.03	0.04 ± 0.03
Relaxed			
$\sigma_{log(Y\|M)}$	0.19 ± 0.09	0.11 ± 0.06	
$\sigma_{log(M\|Y)}$	0.06 ± 0.03	0.06 ± 0.04	

B

CLUSTER IMAGES

This chapter shows color composite images of the central cluster regions with convergence contours in white. Listed are only those clusters not discussed in detail in Chapter 9. If available, the contours from the SZ maps, based on the BOA pipeline are overlaid in green, and X-ray surface brightness contours are overplayed in magenta. When both X-ray and SZ data are available, two images are shown, to avoid confusion with too many different contours. For A907 and RXC1347 the convergence contours based on Suprime-Cam are drawn as a white continuous line, whereas the WFI-based contours are highlighted as white dashed lines.

The convergence and SZ contour levels are equally spaced in linear space, X-ray contours in log space. Contour levels are allowed to change for visualization purposes. Images and contours are for qualitative purposes only. The filters used for the color channels are listed in Table 3.

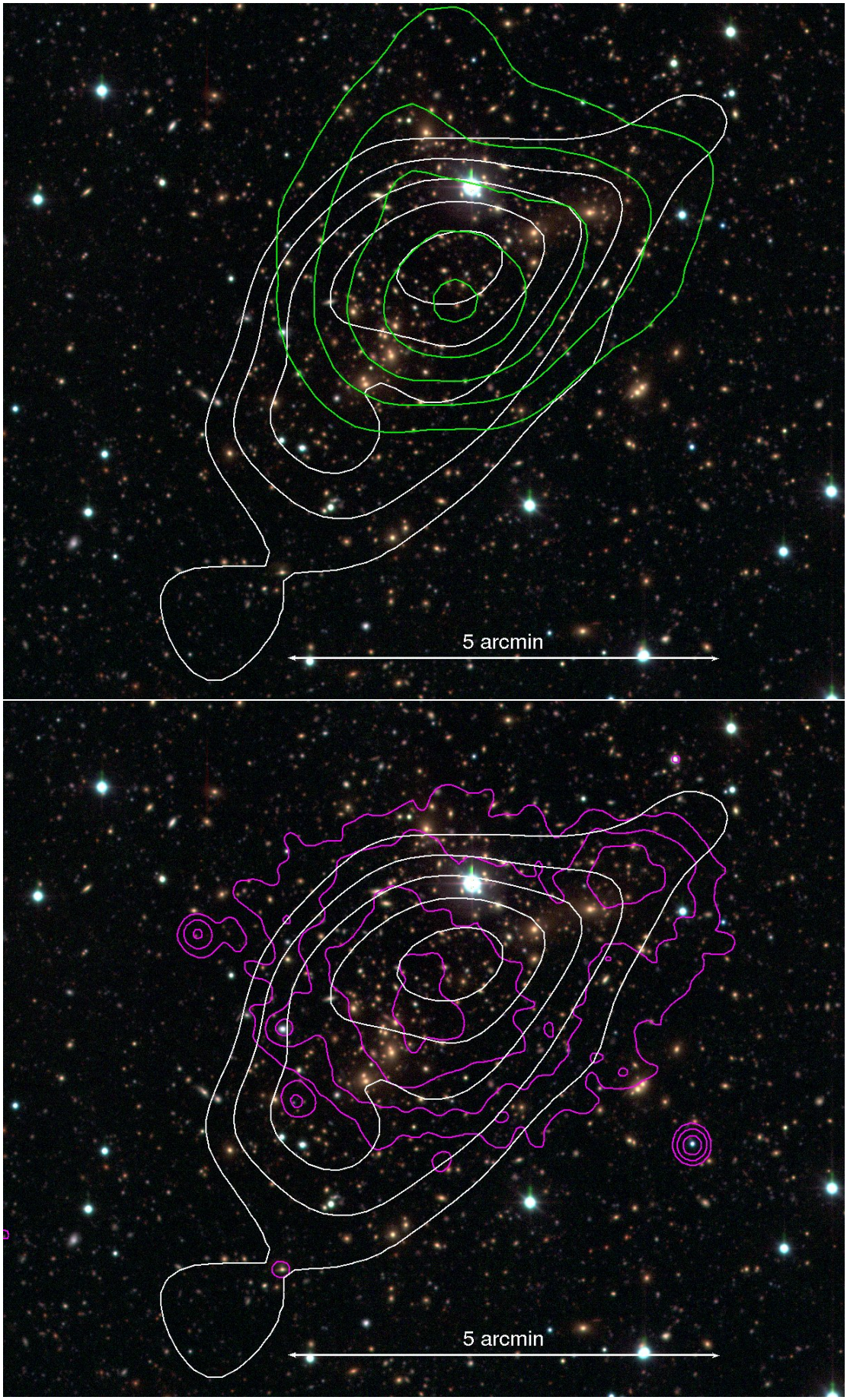

Figure 75: A2744

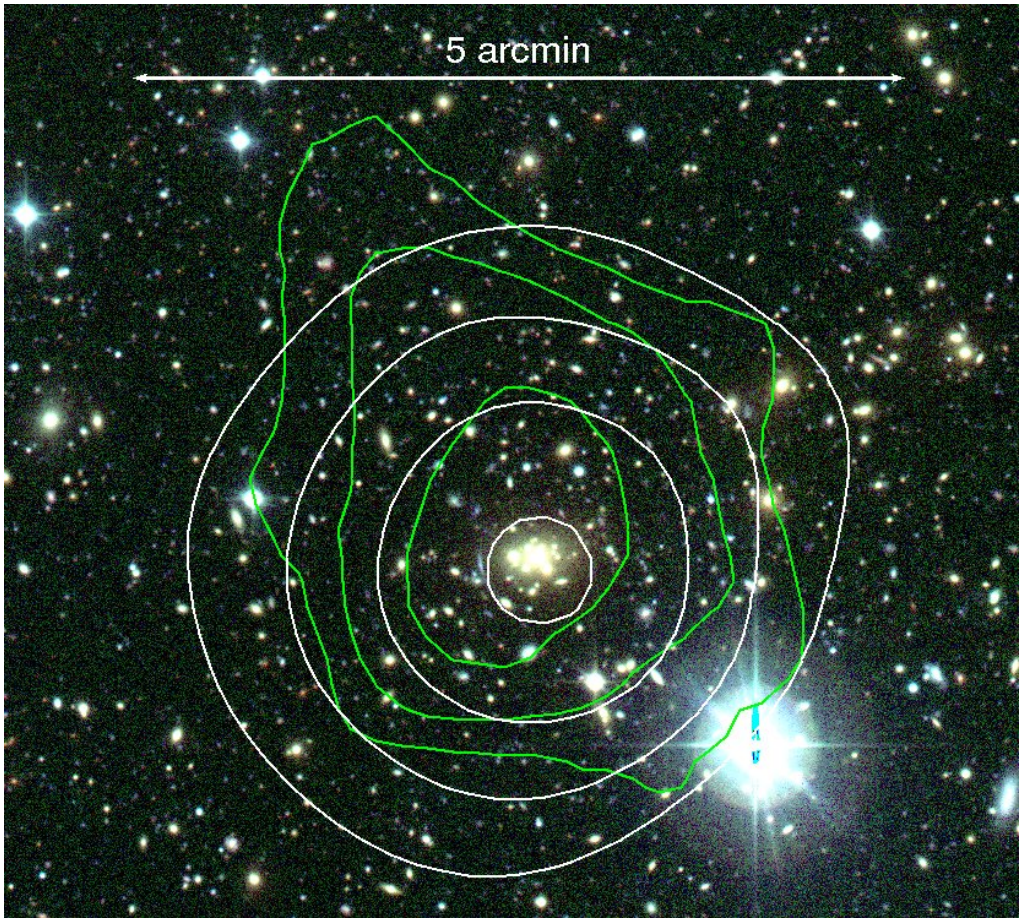

Figure 76: RXC0019

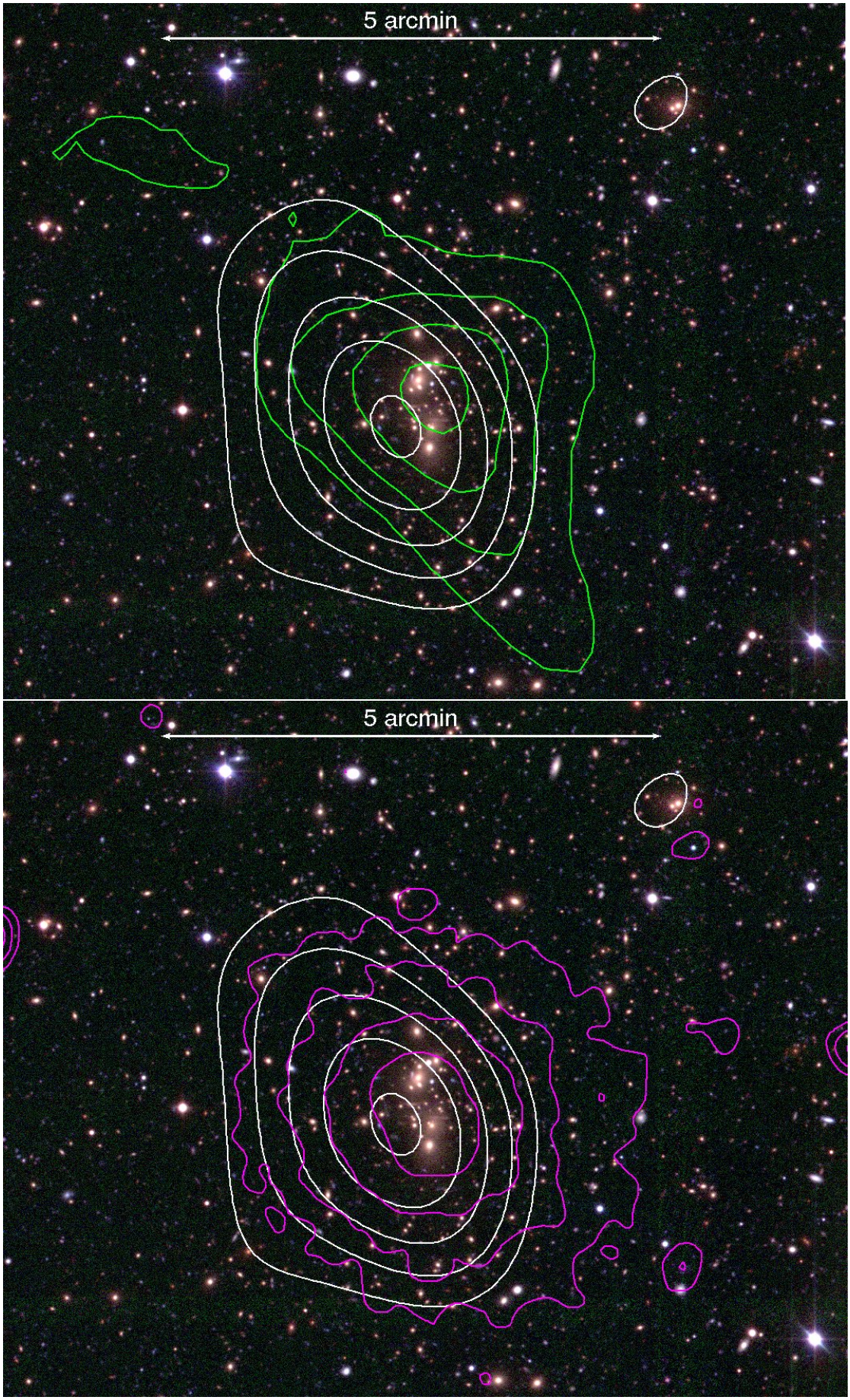

Figure 77: A2813

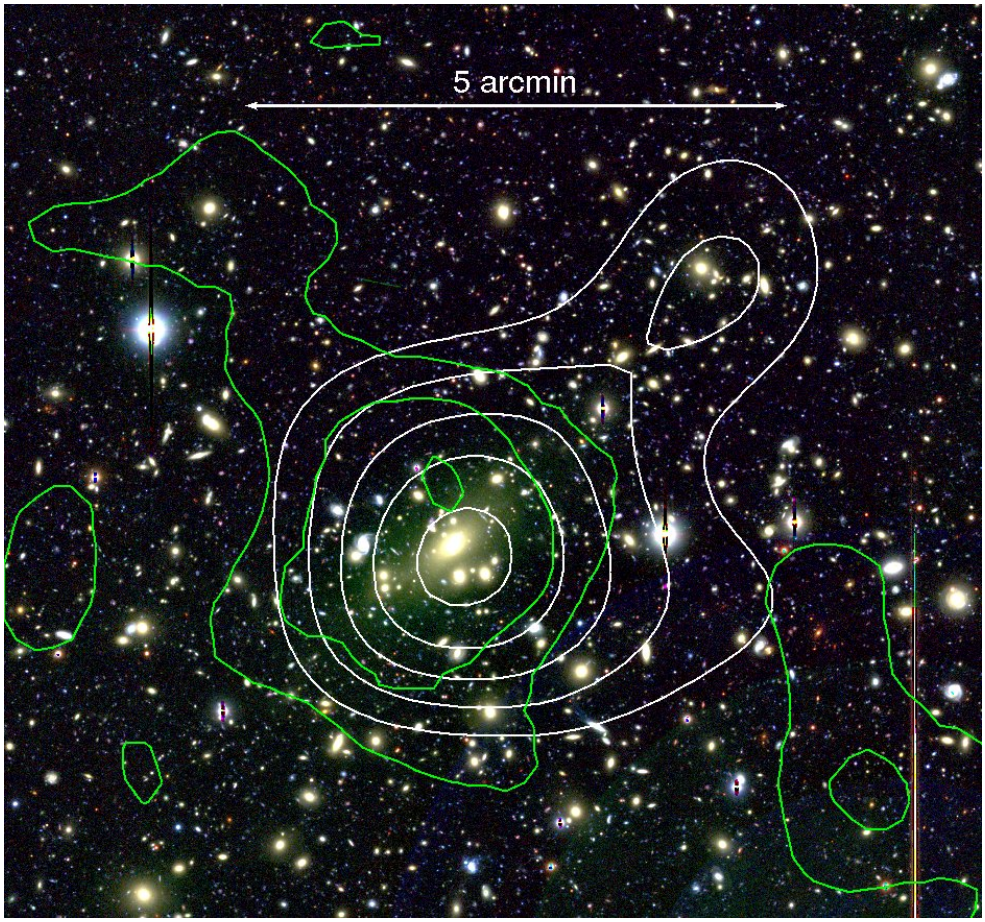

Figure 78: A209

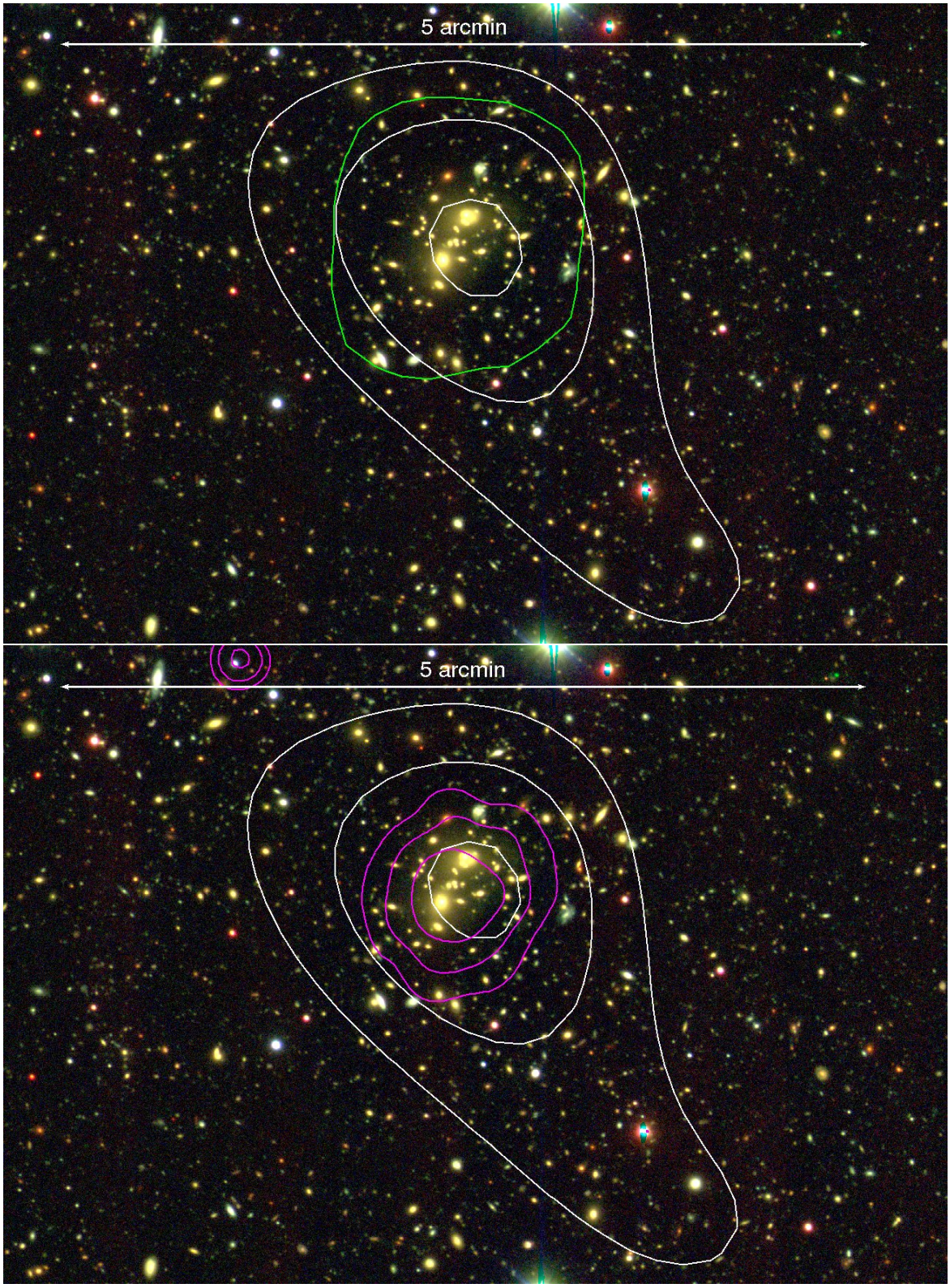

Figure 79: XLSSC006

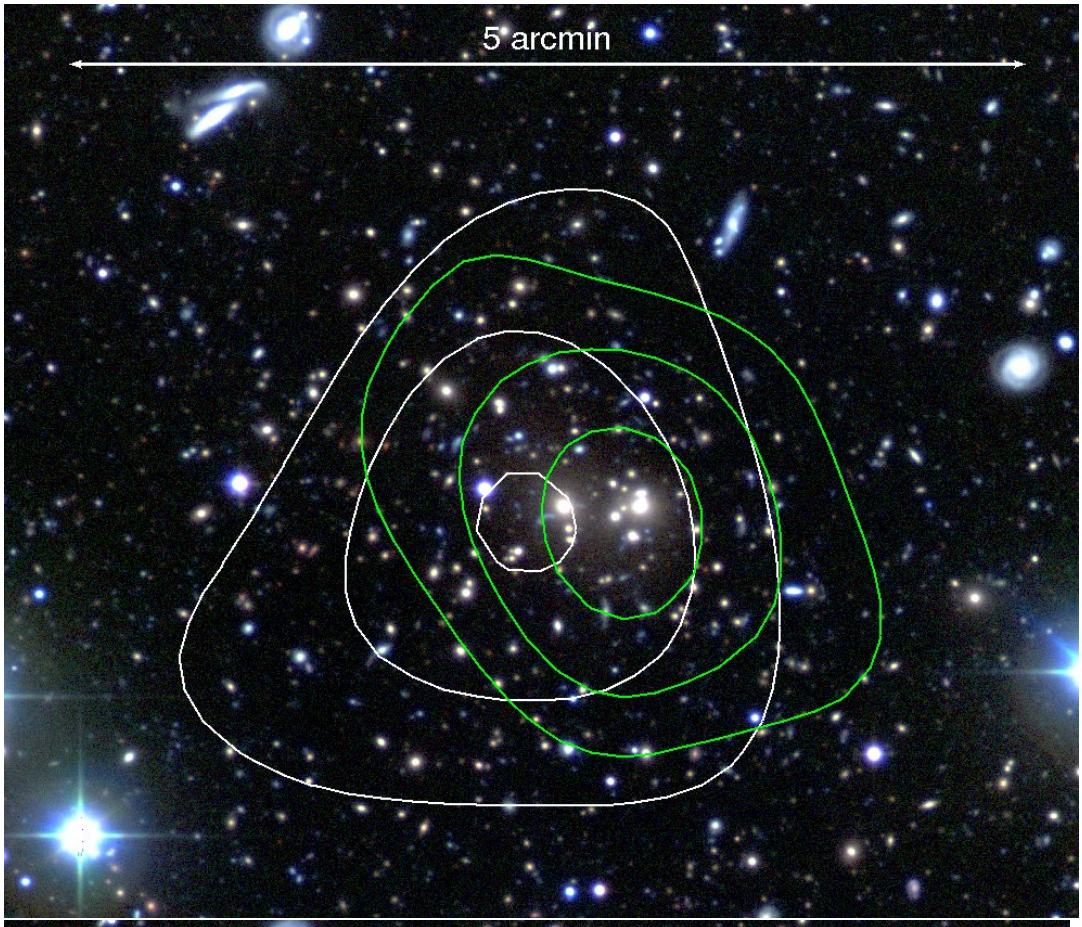

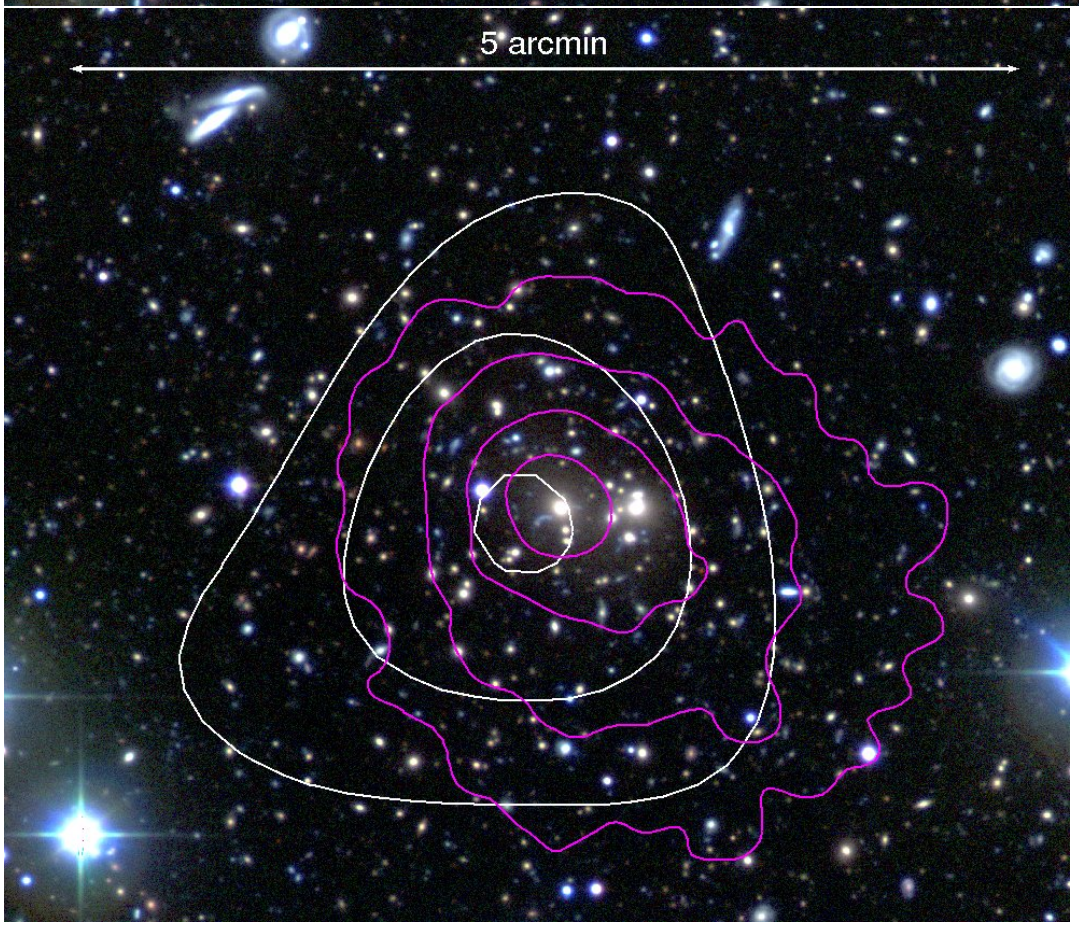

Figure 80: RXC0232

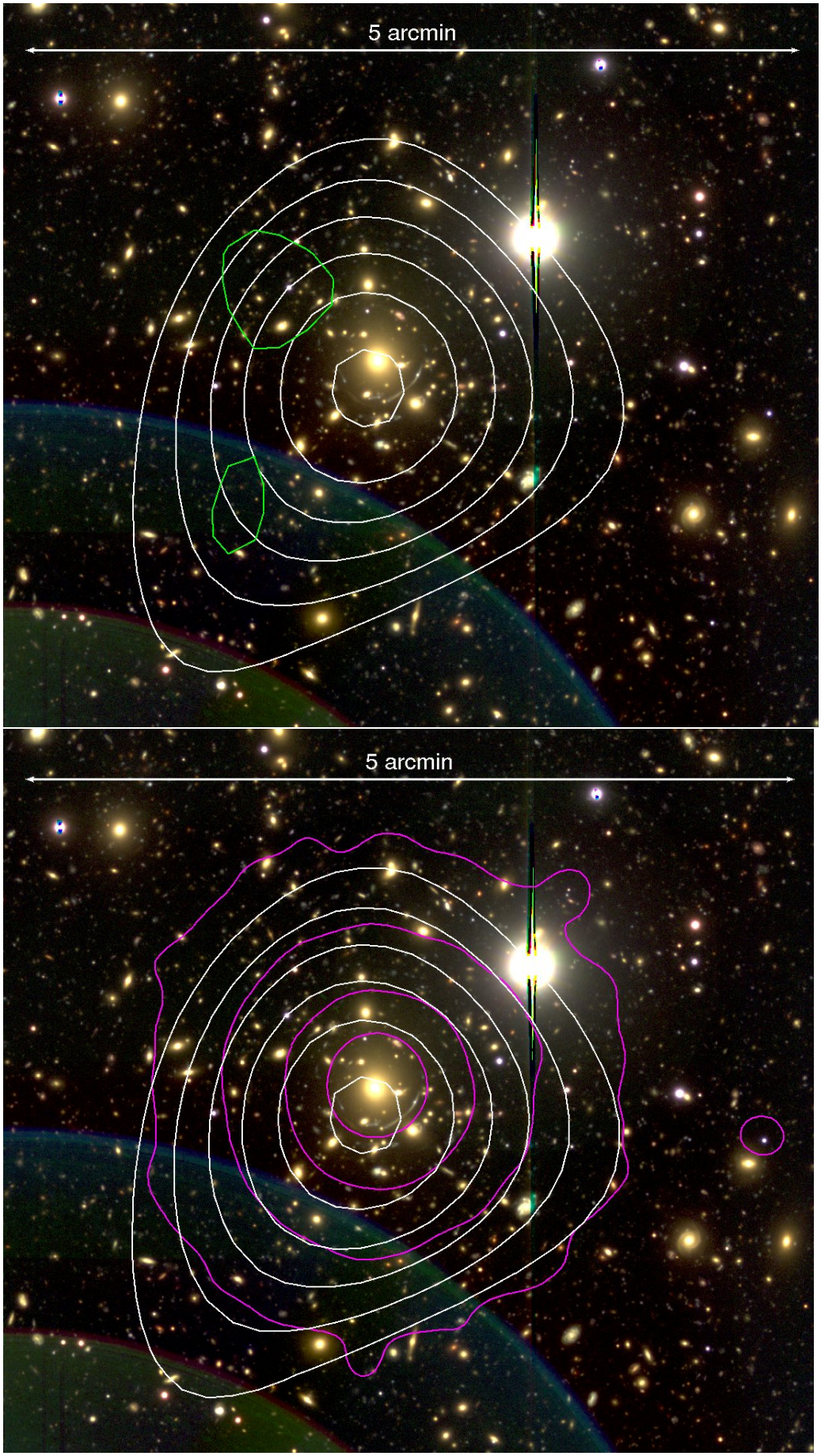

Figure 81: A383

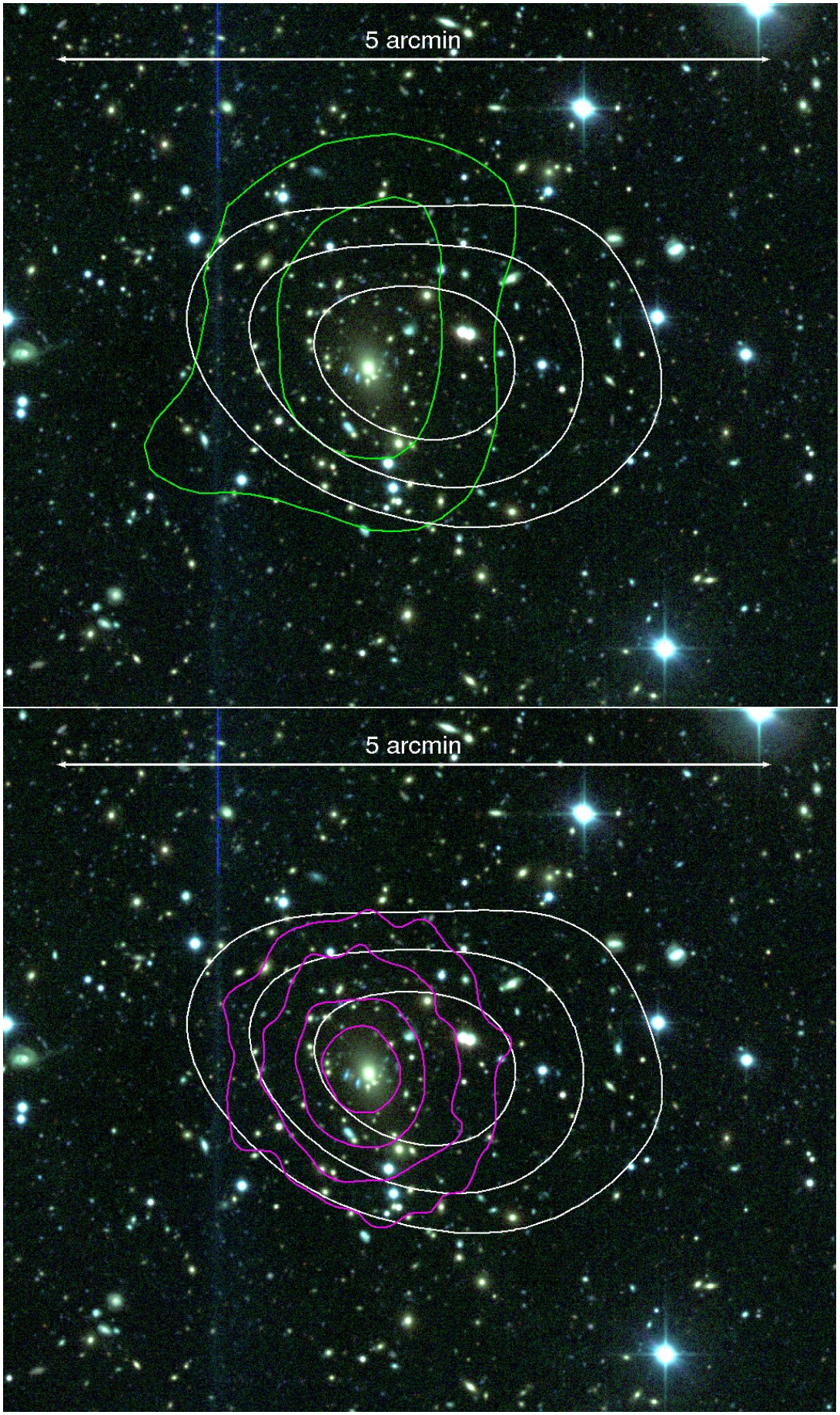

Figure 82: RXC0437

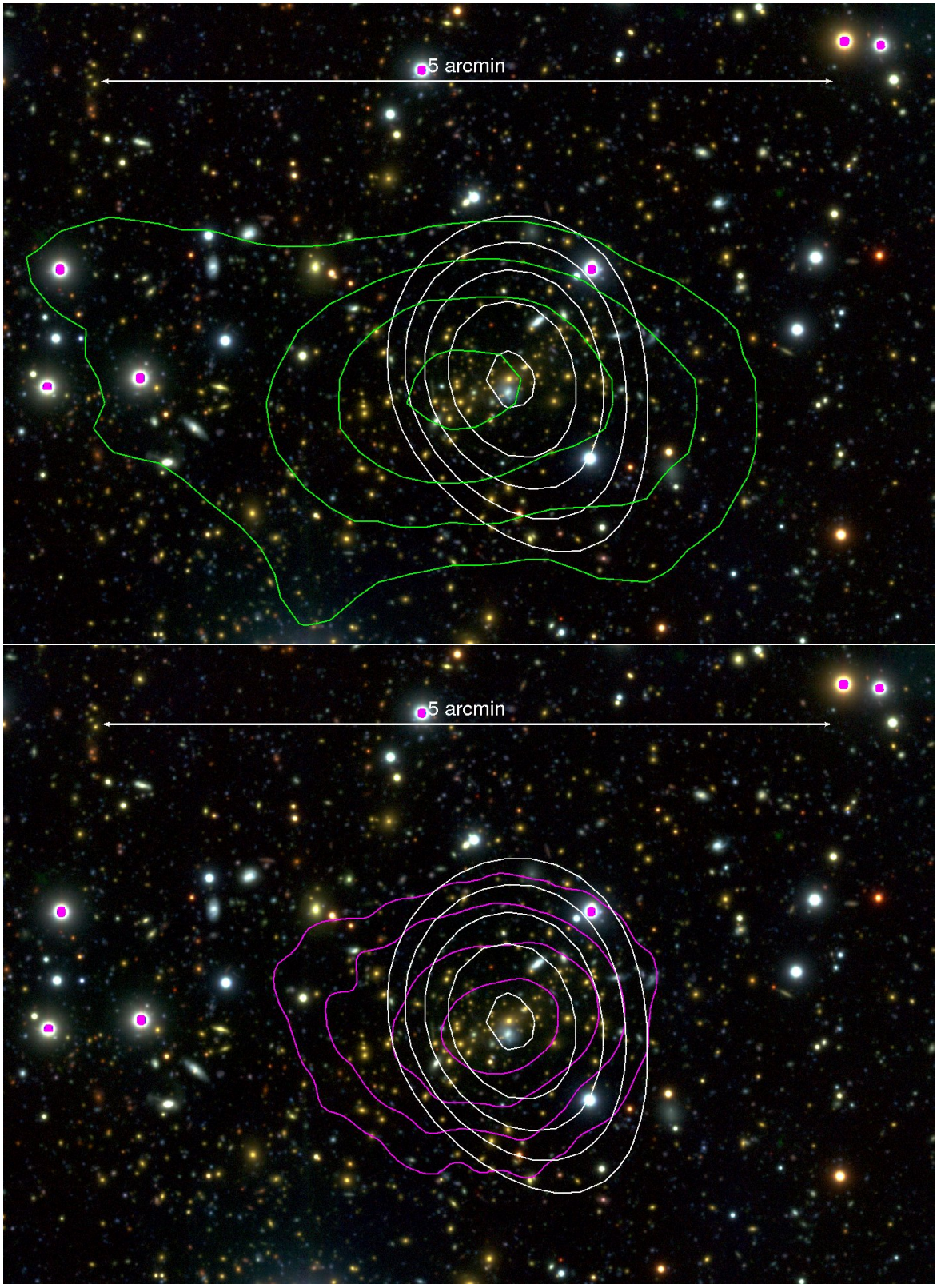

Figure 83: MS0451

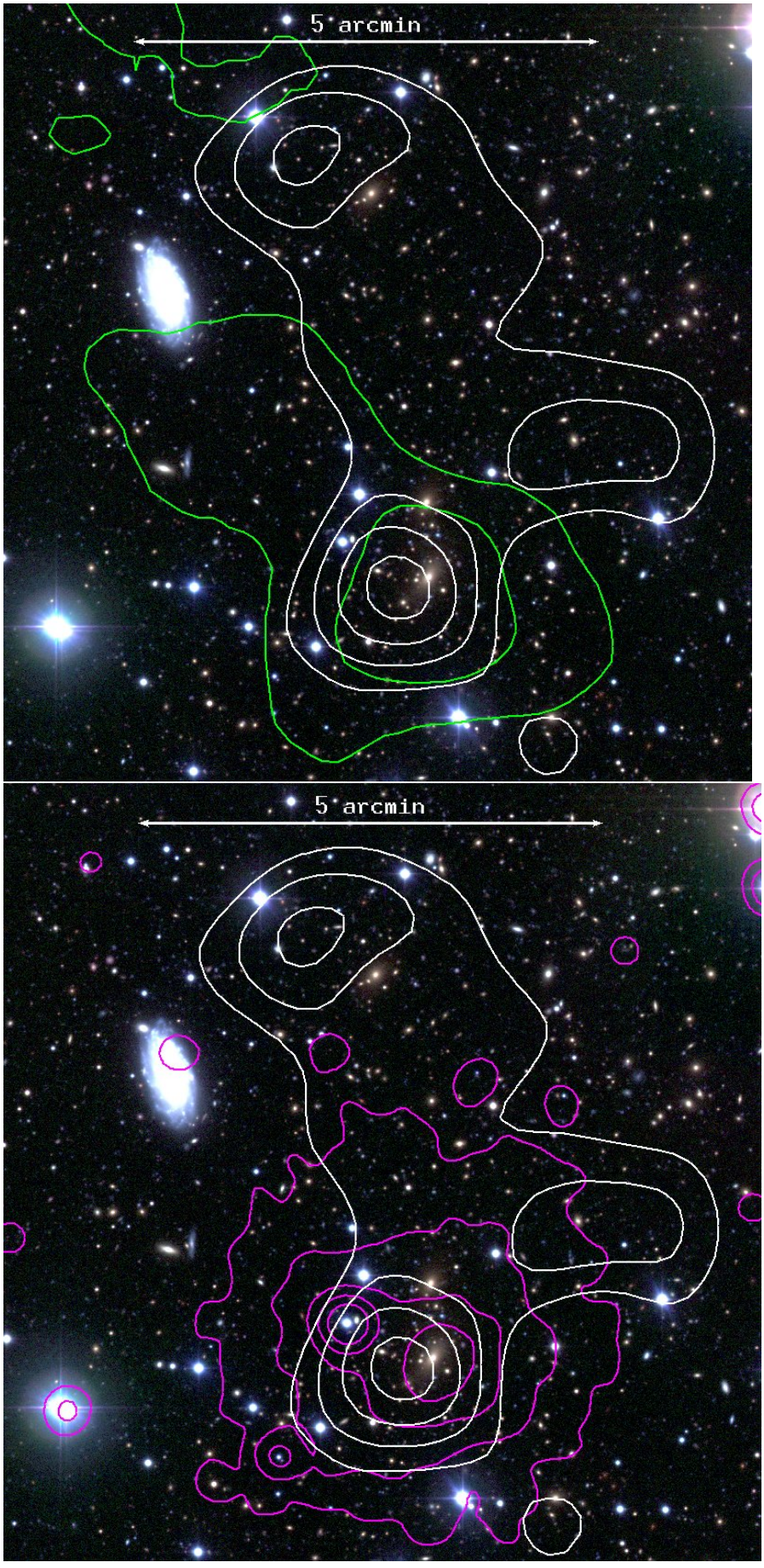

Figure 84: RXC0528

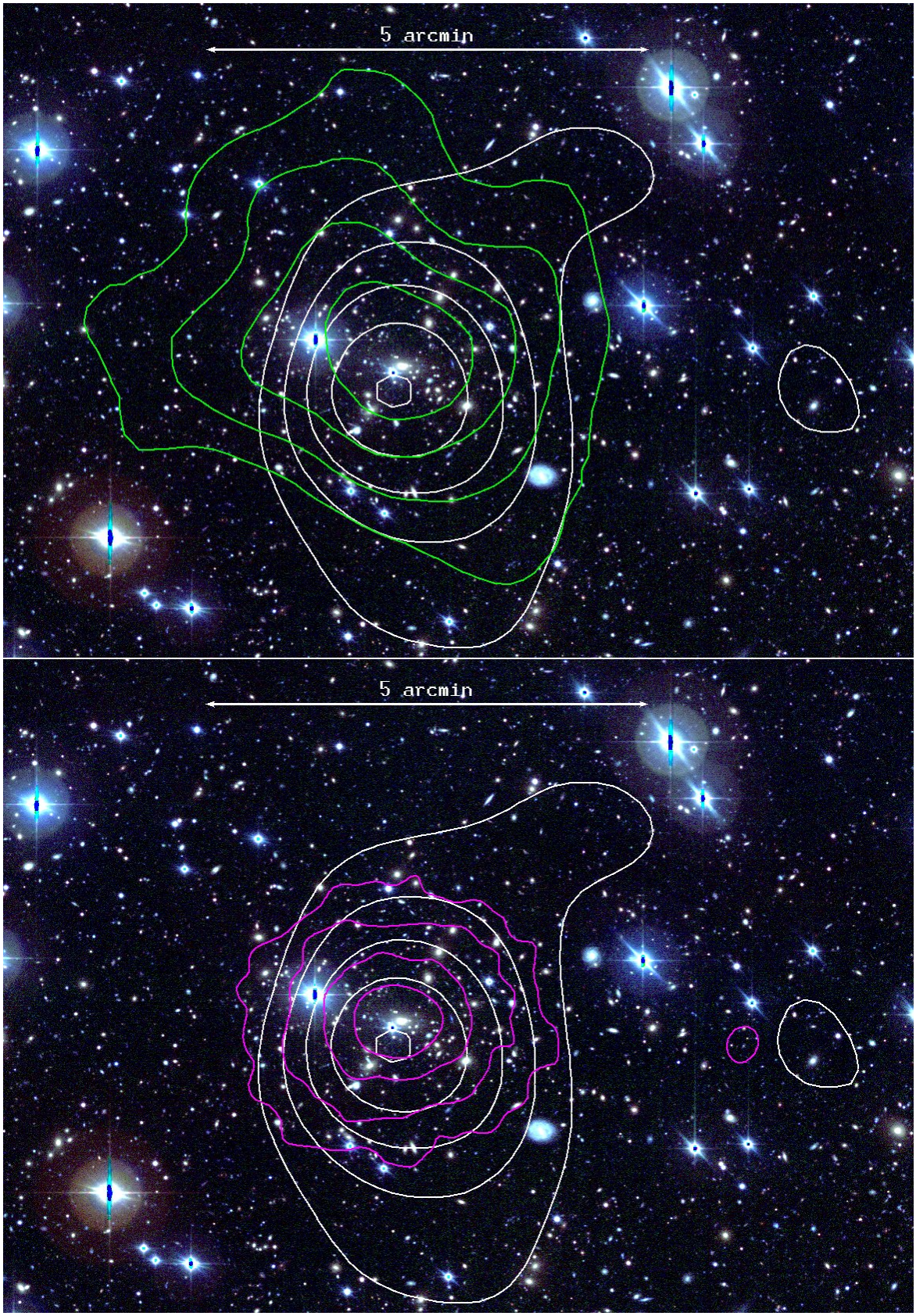

Figure 85: RXC0532

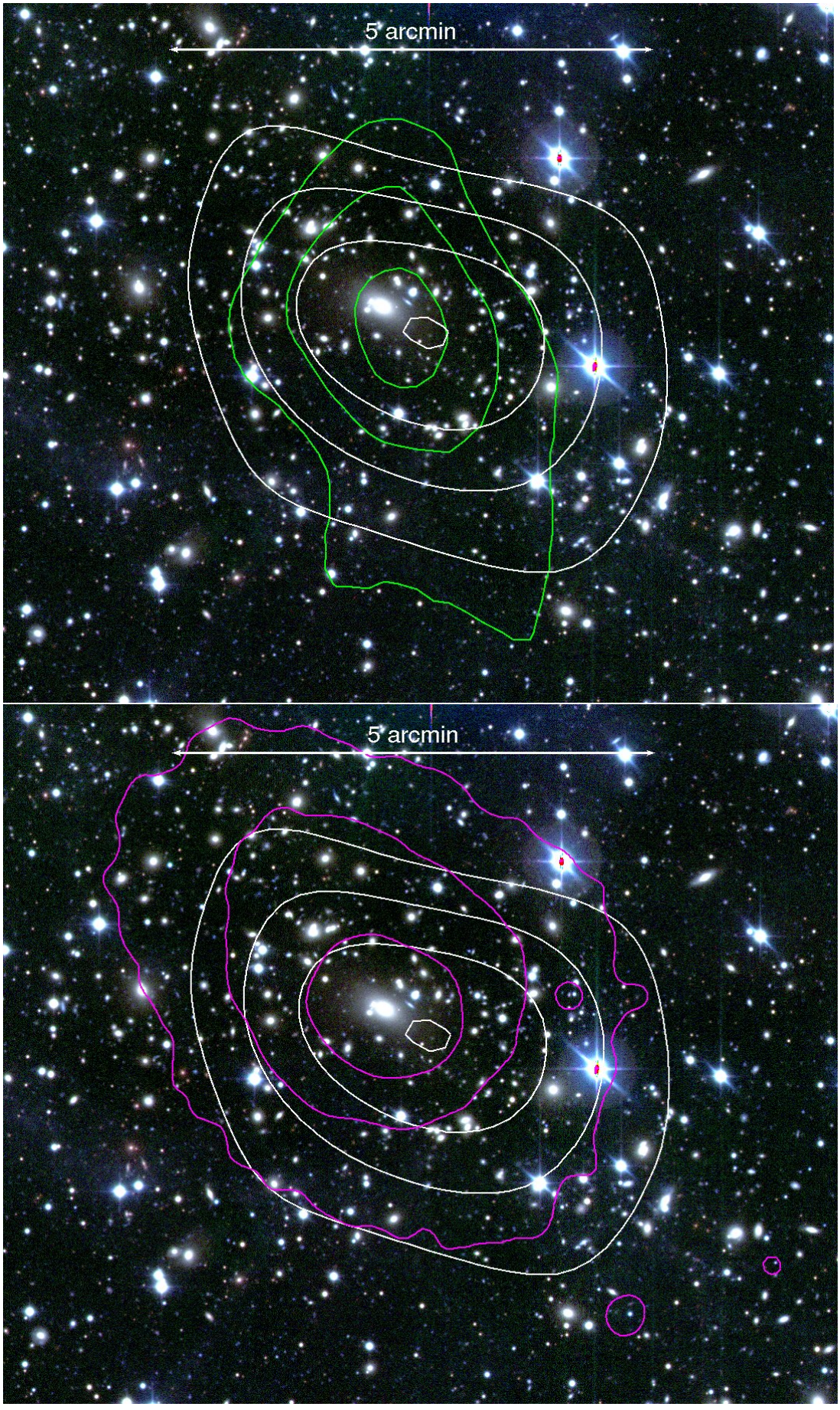

Figure 86: A3404

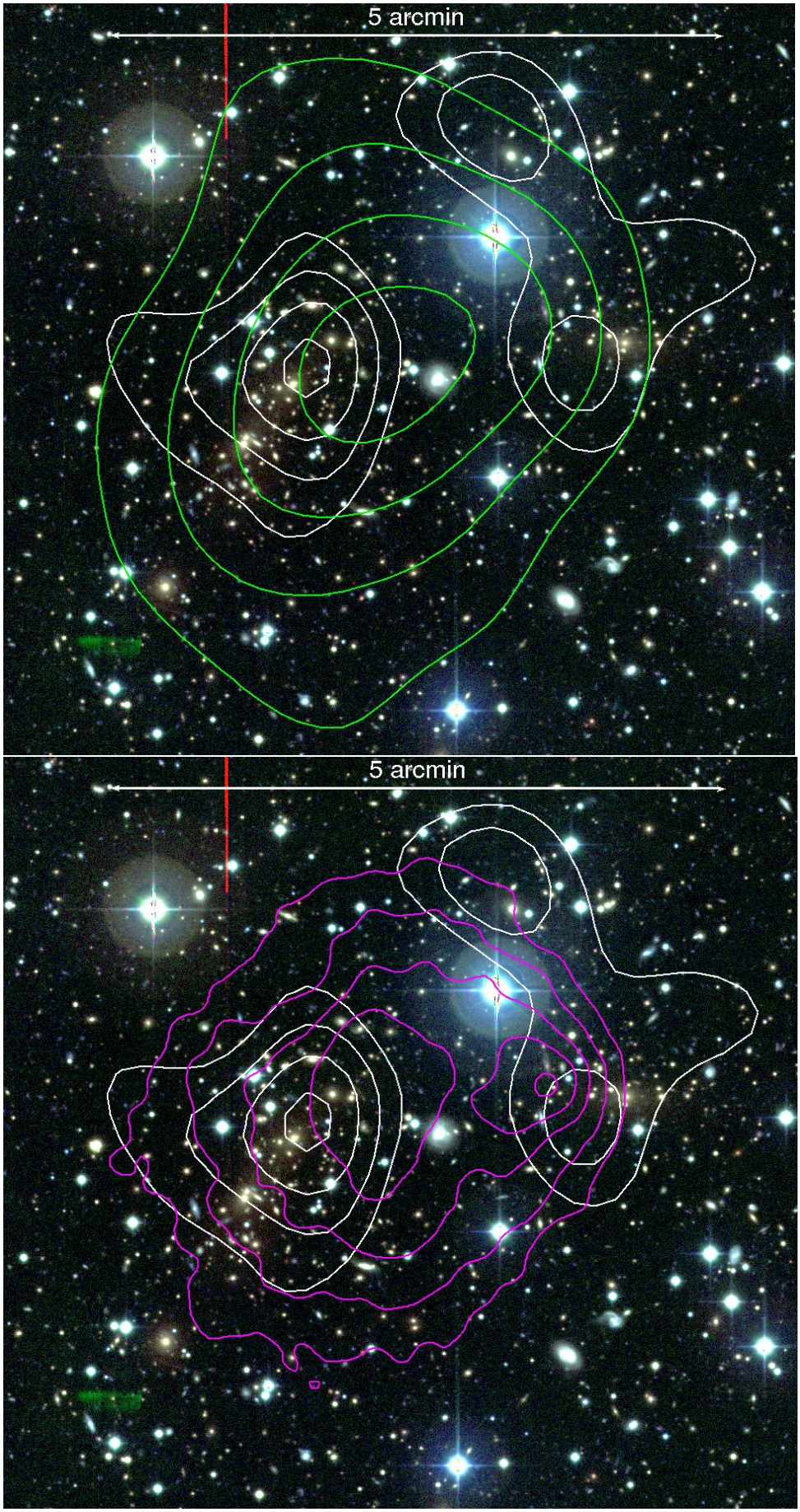

Figure 87: Bullet

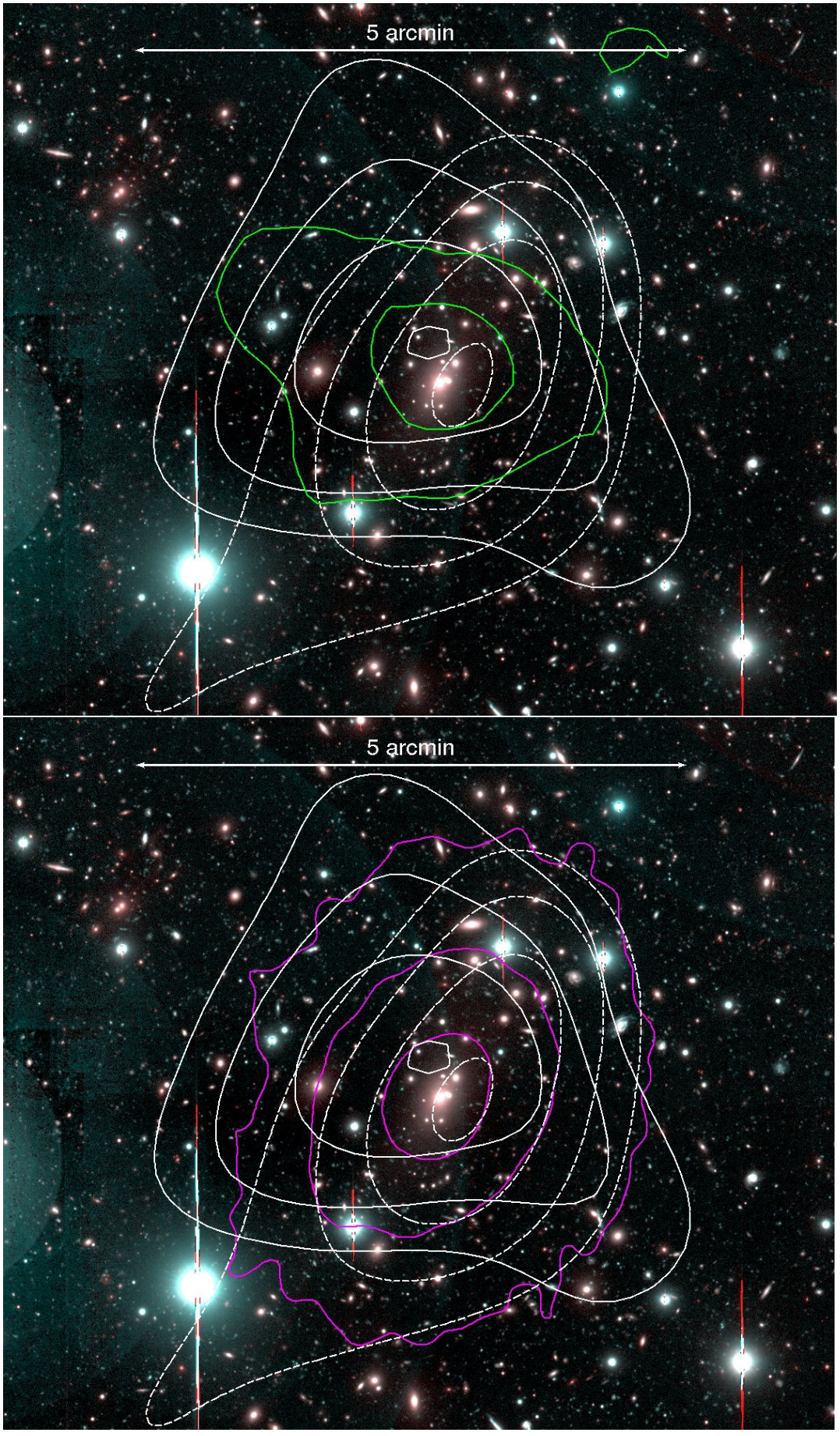

Figure 88: A907

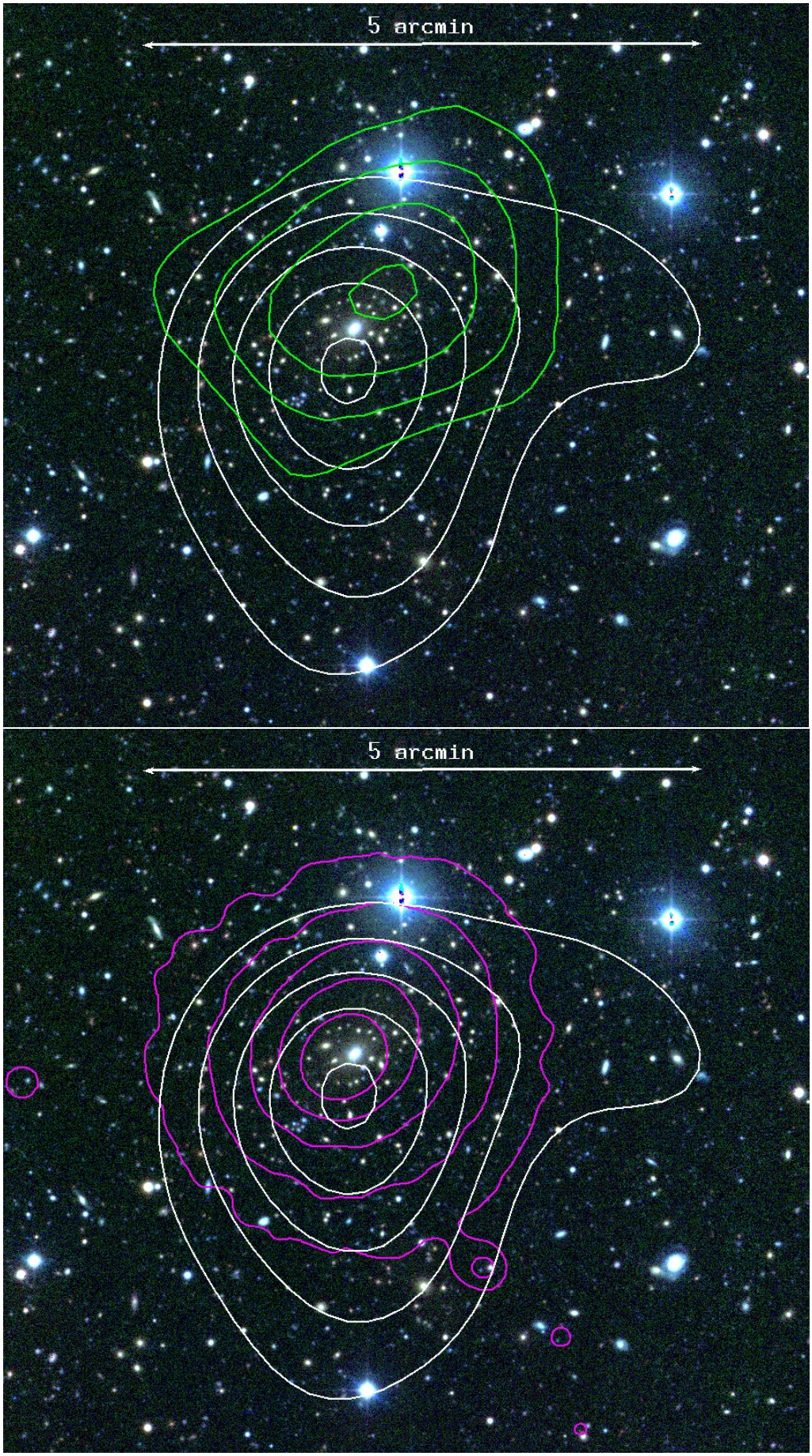

Figure 89: RXC1023

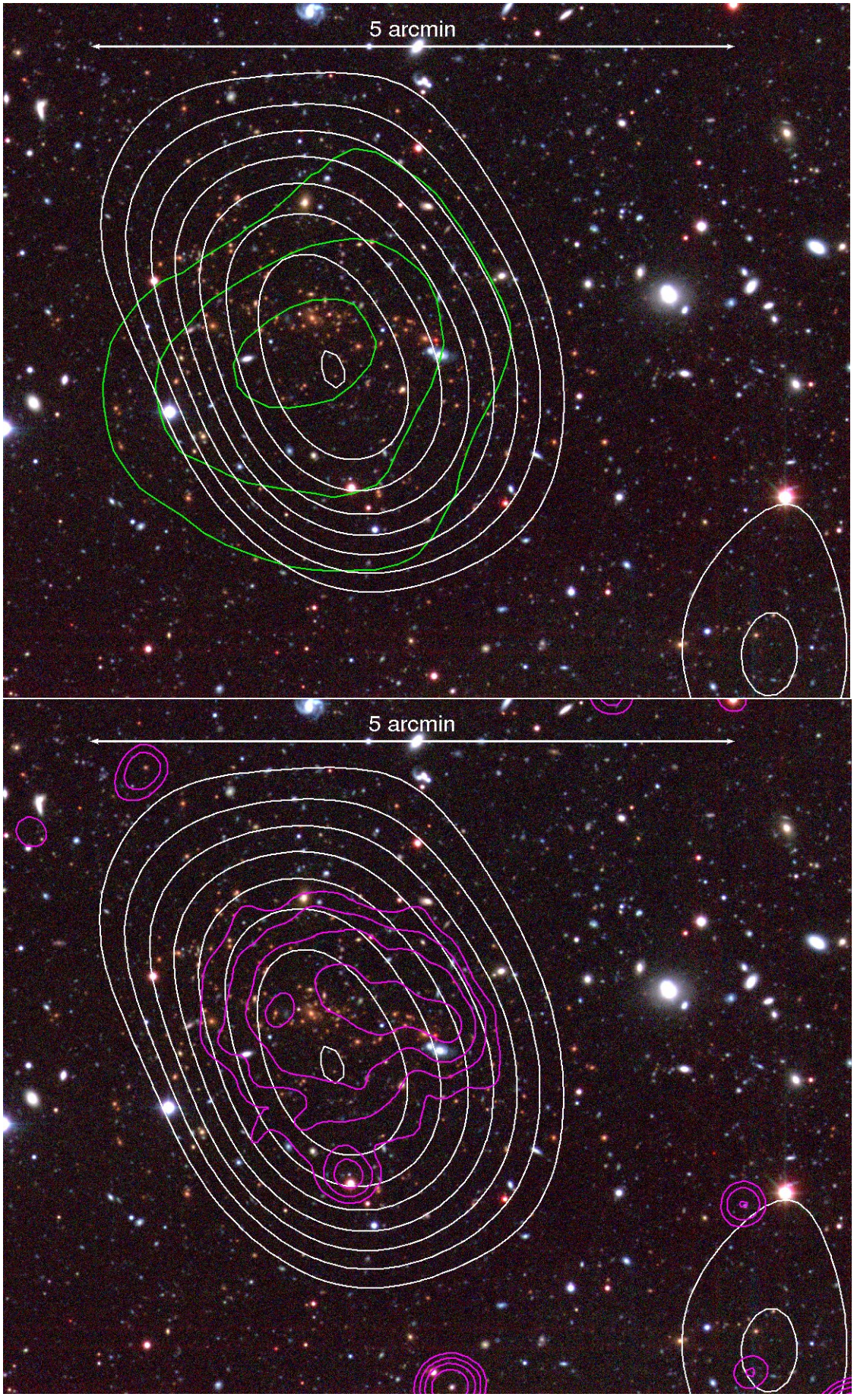

Figure 90: MS1054

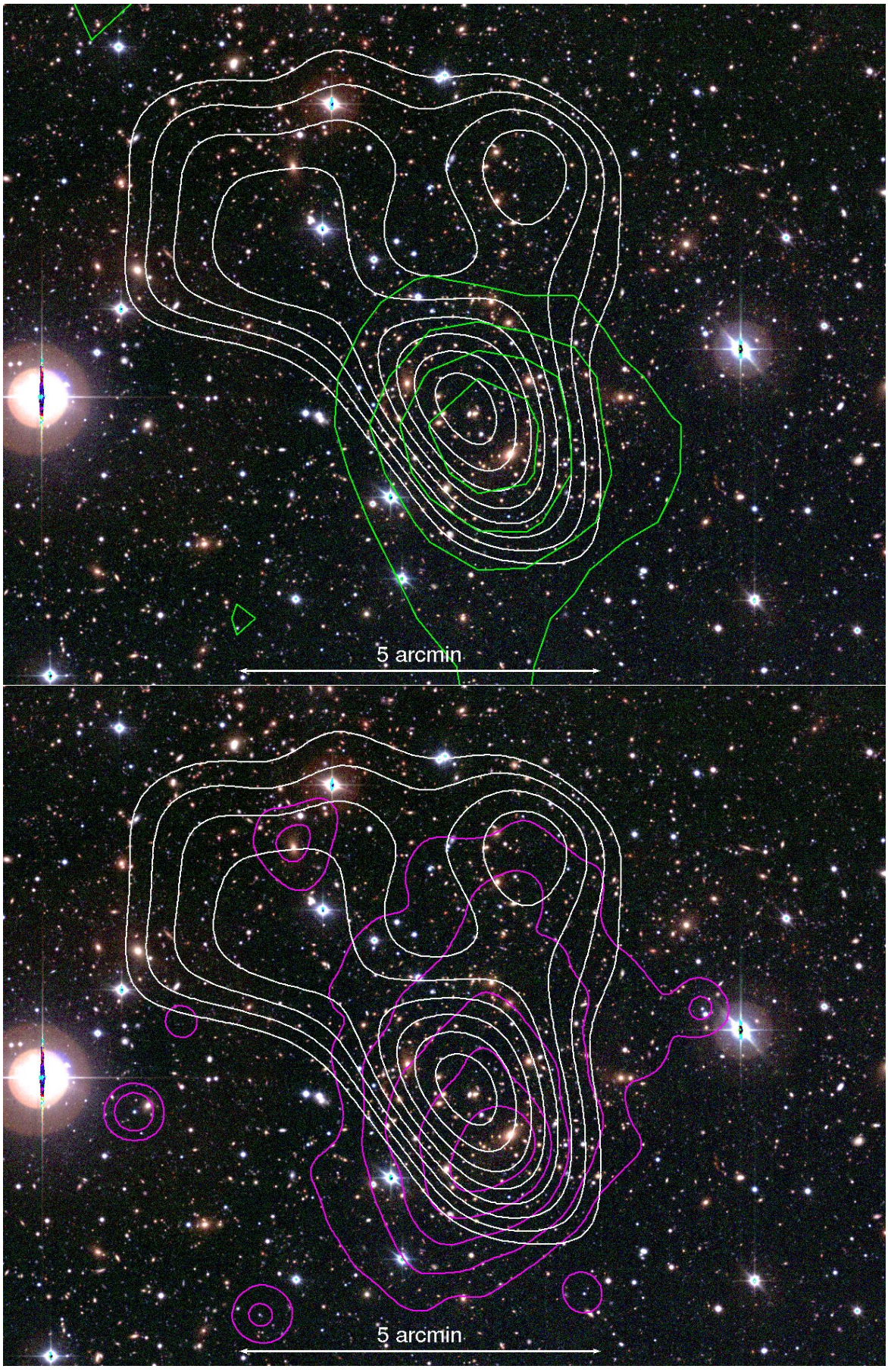

Figure 91: A1300

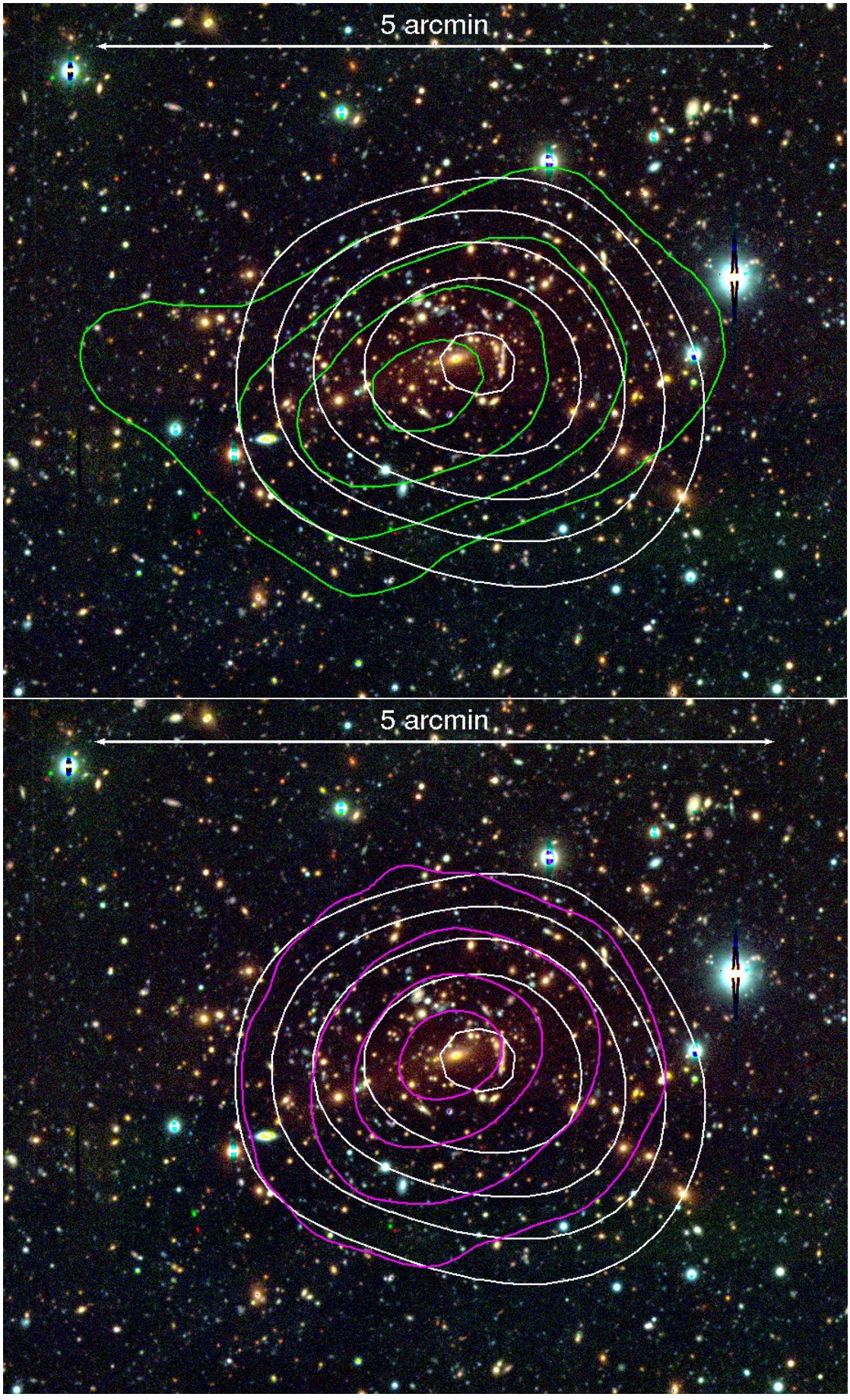

Figure 92: RXC1206

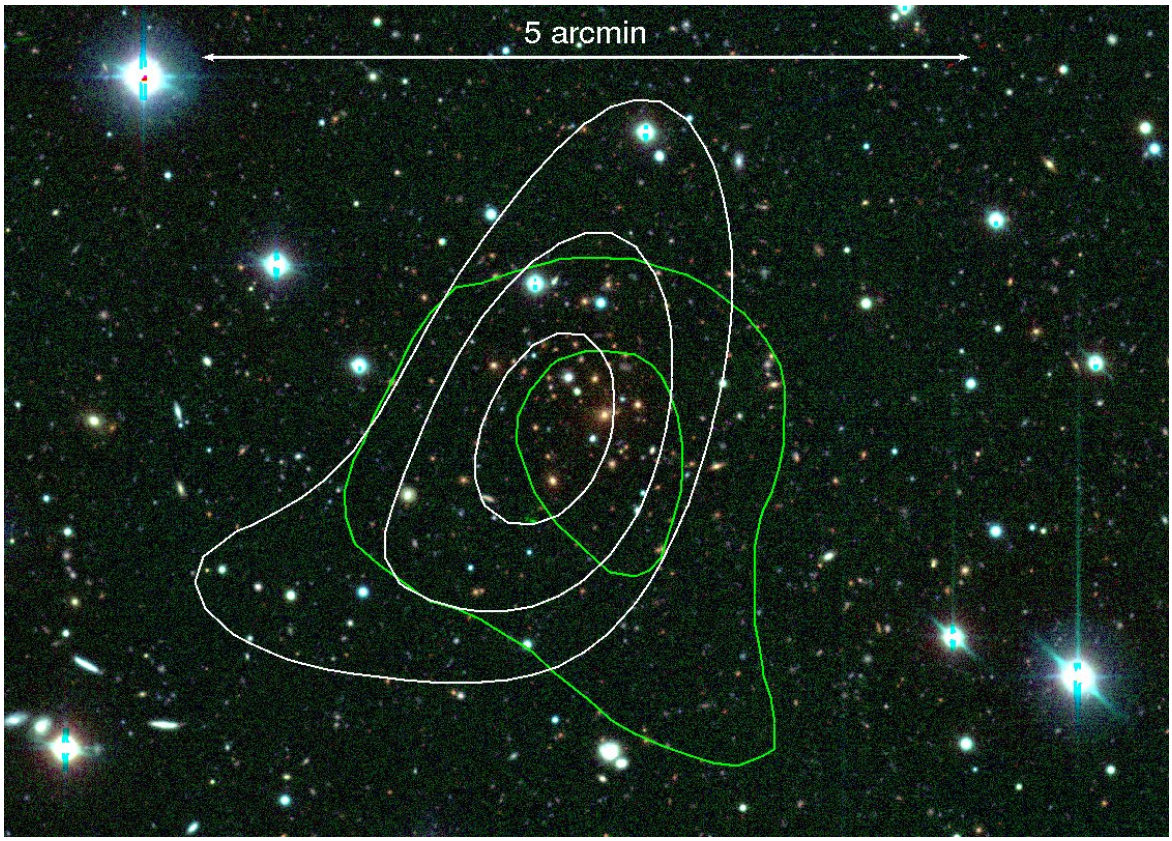

Figure 93: MCS1311

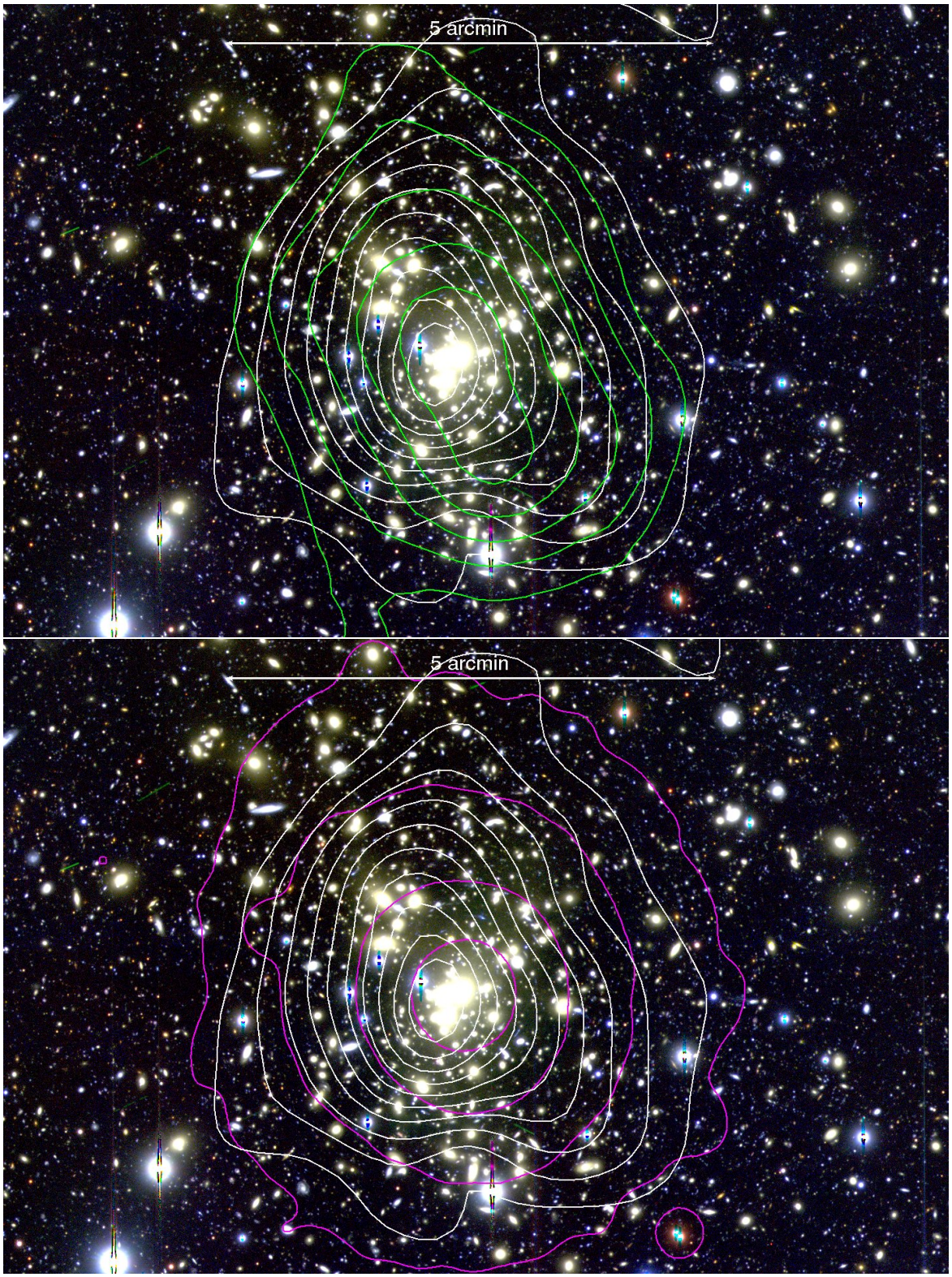

Figure 94: A1689

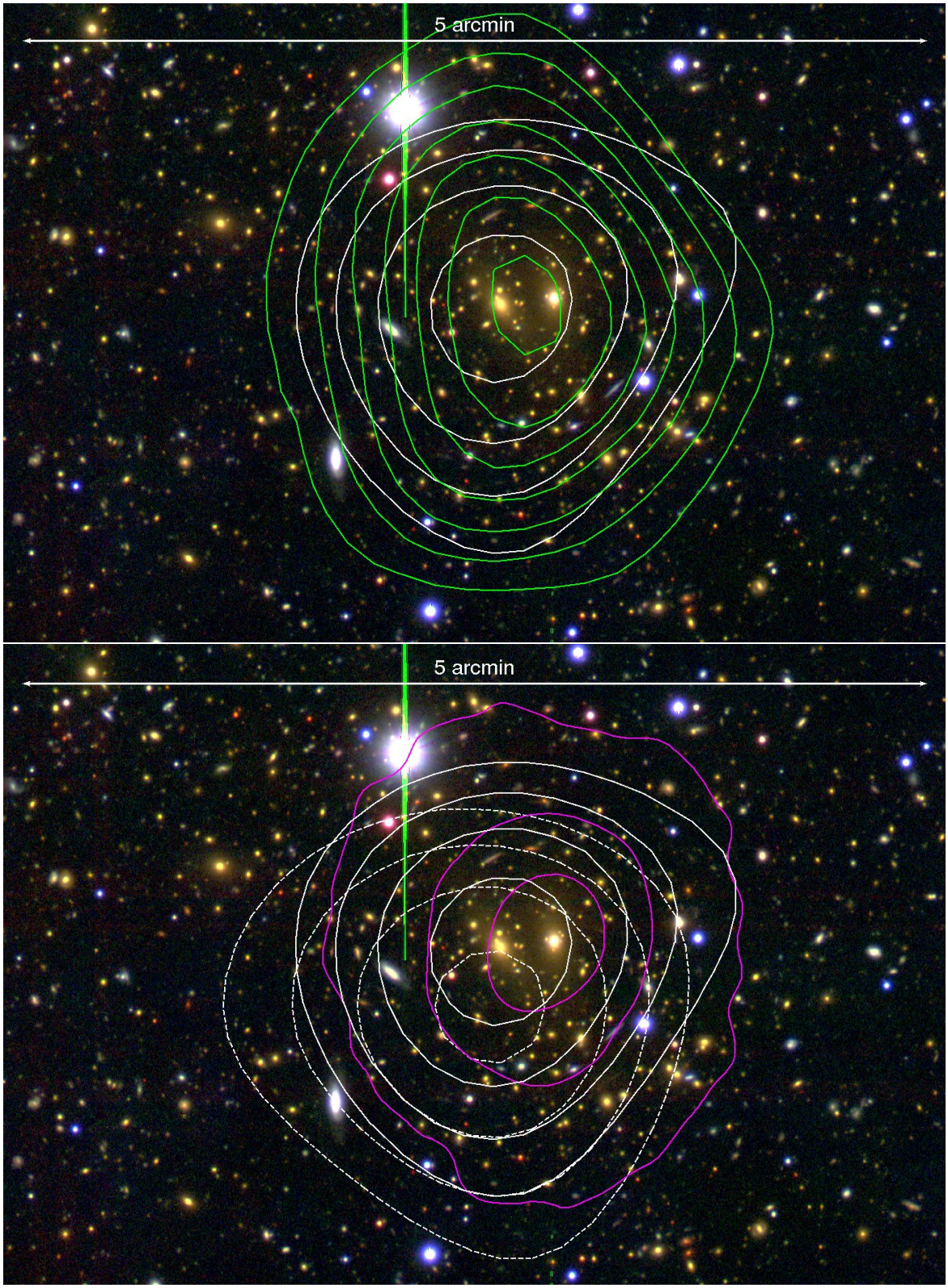

Figure 95: RXC1347

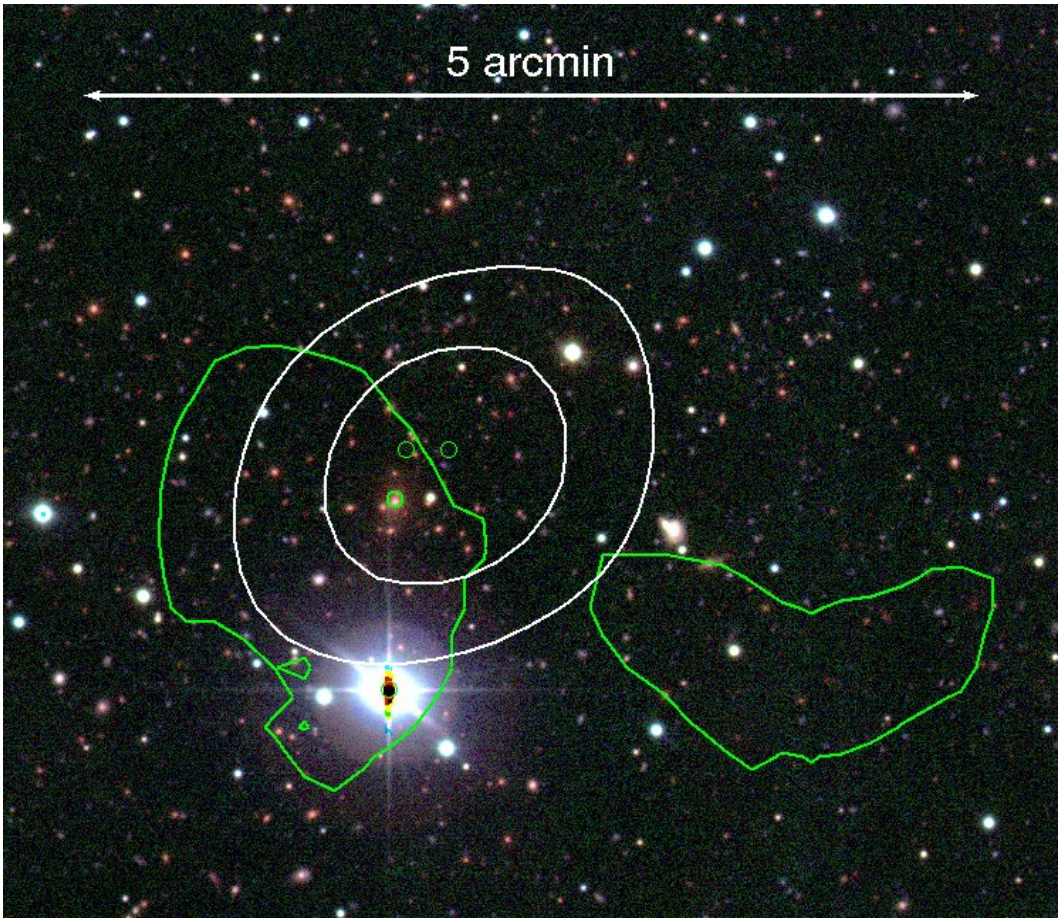

Figure 96: RXC1359

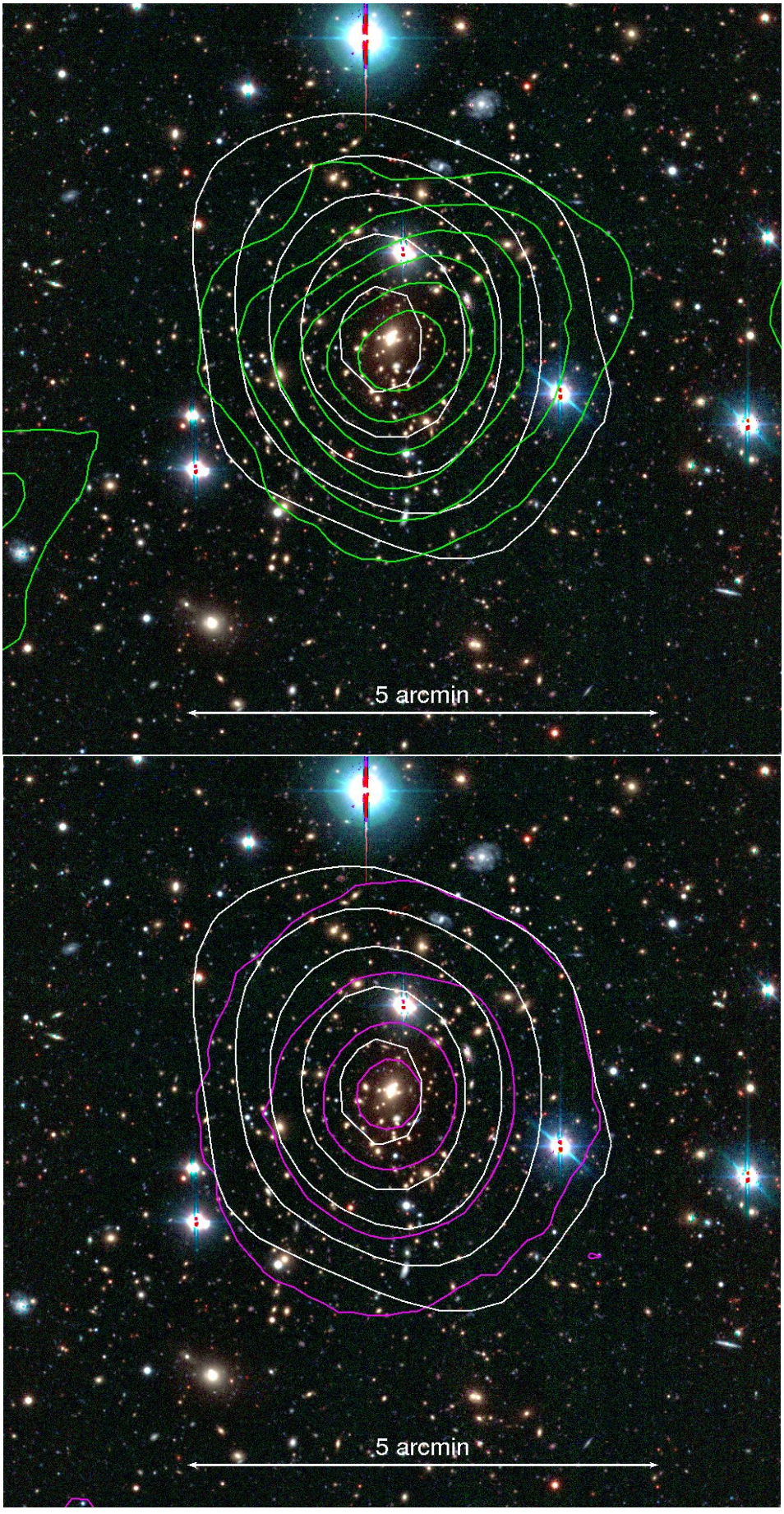

Figure 97: A1835

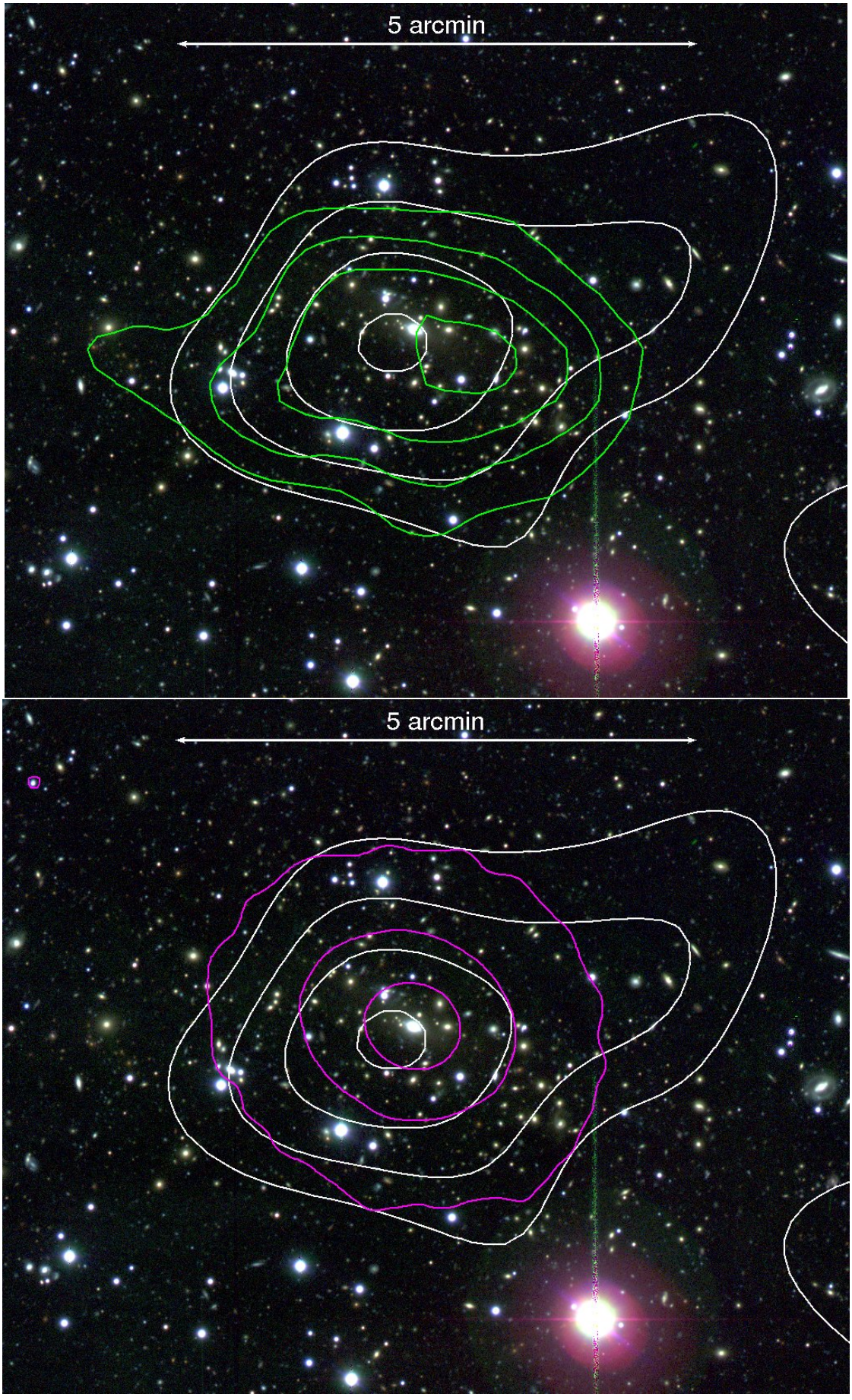

Figure 98: RXC1504

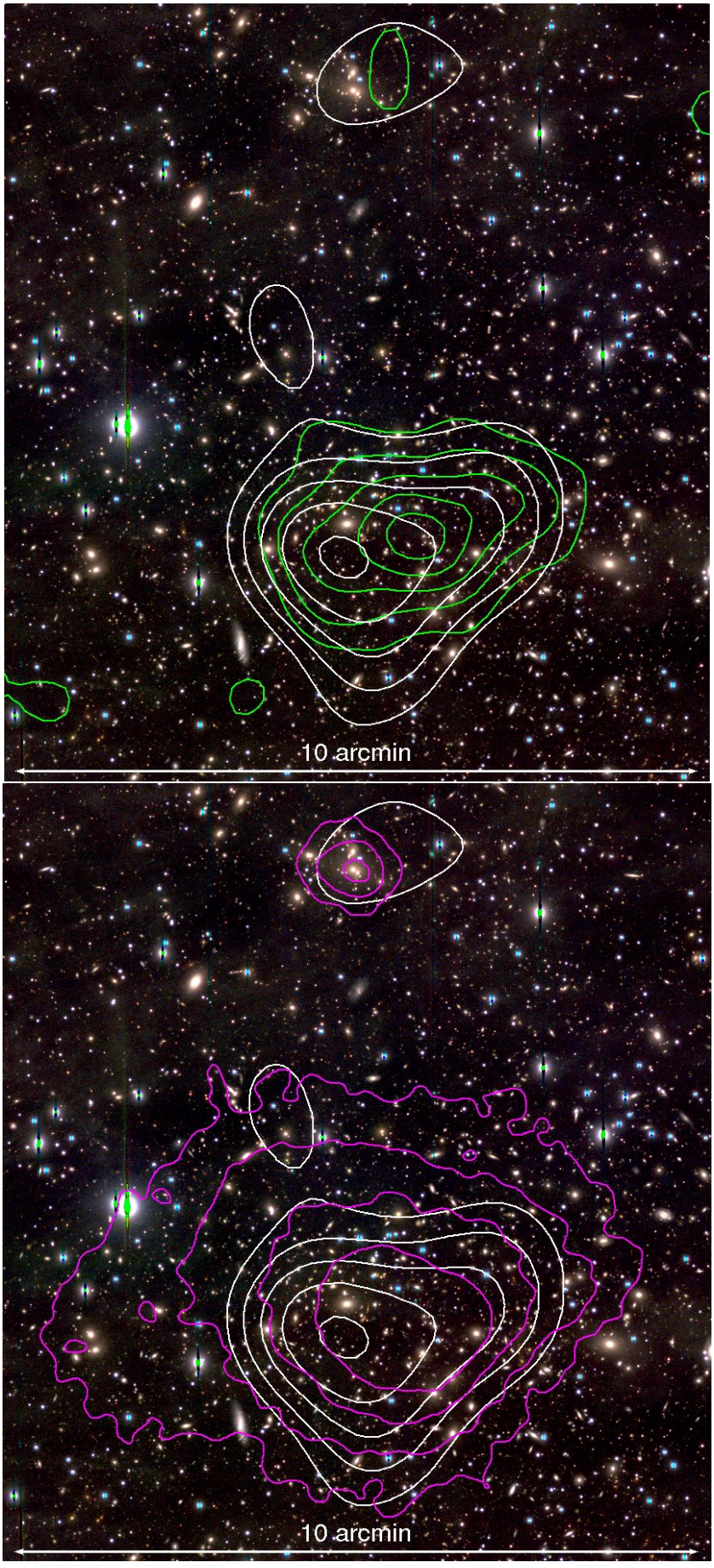

Figure 99: A2163

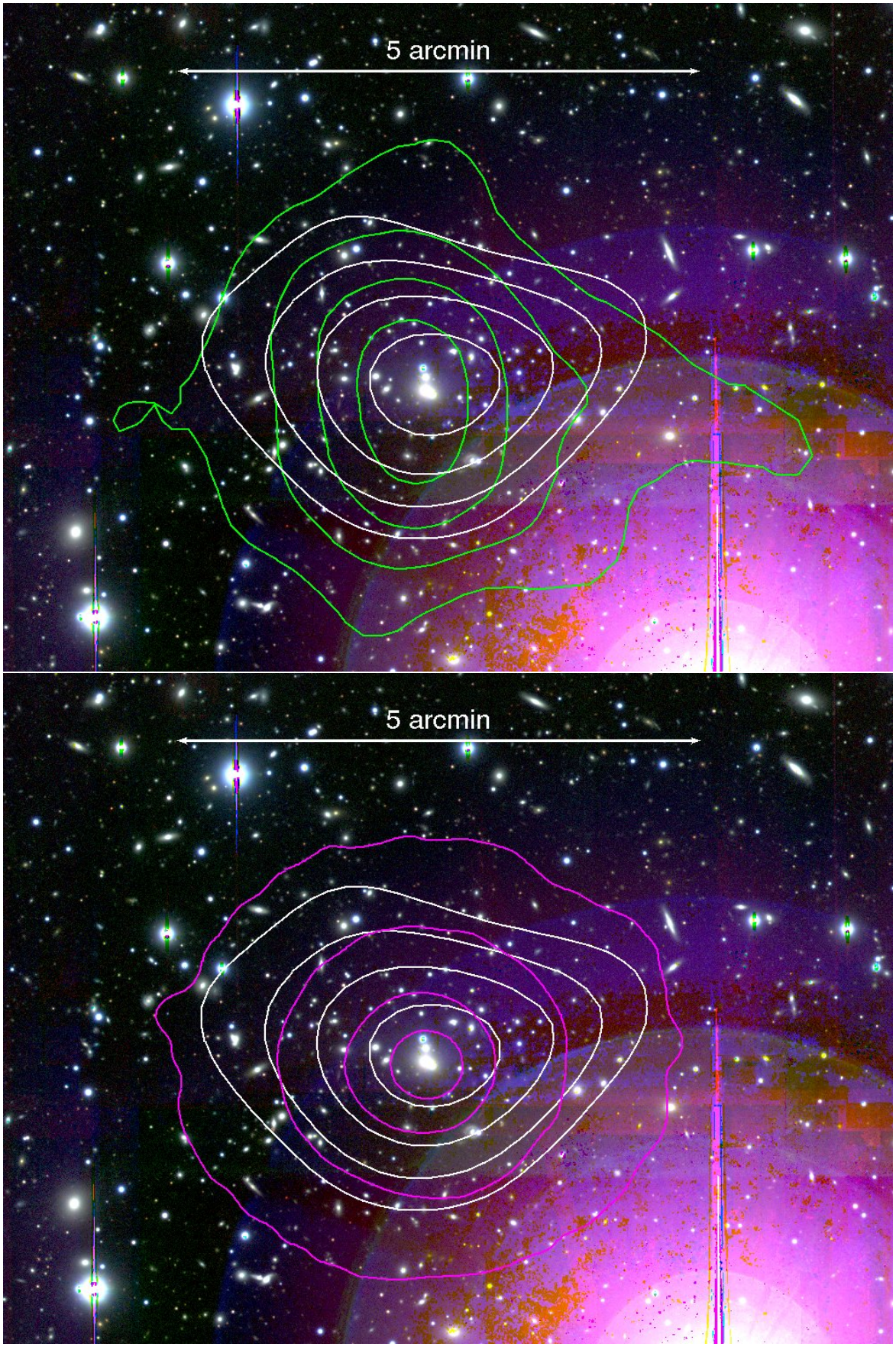

Figure 100: A2204

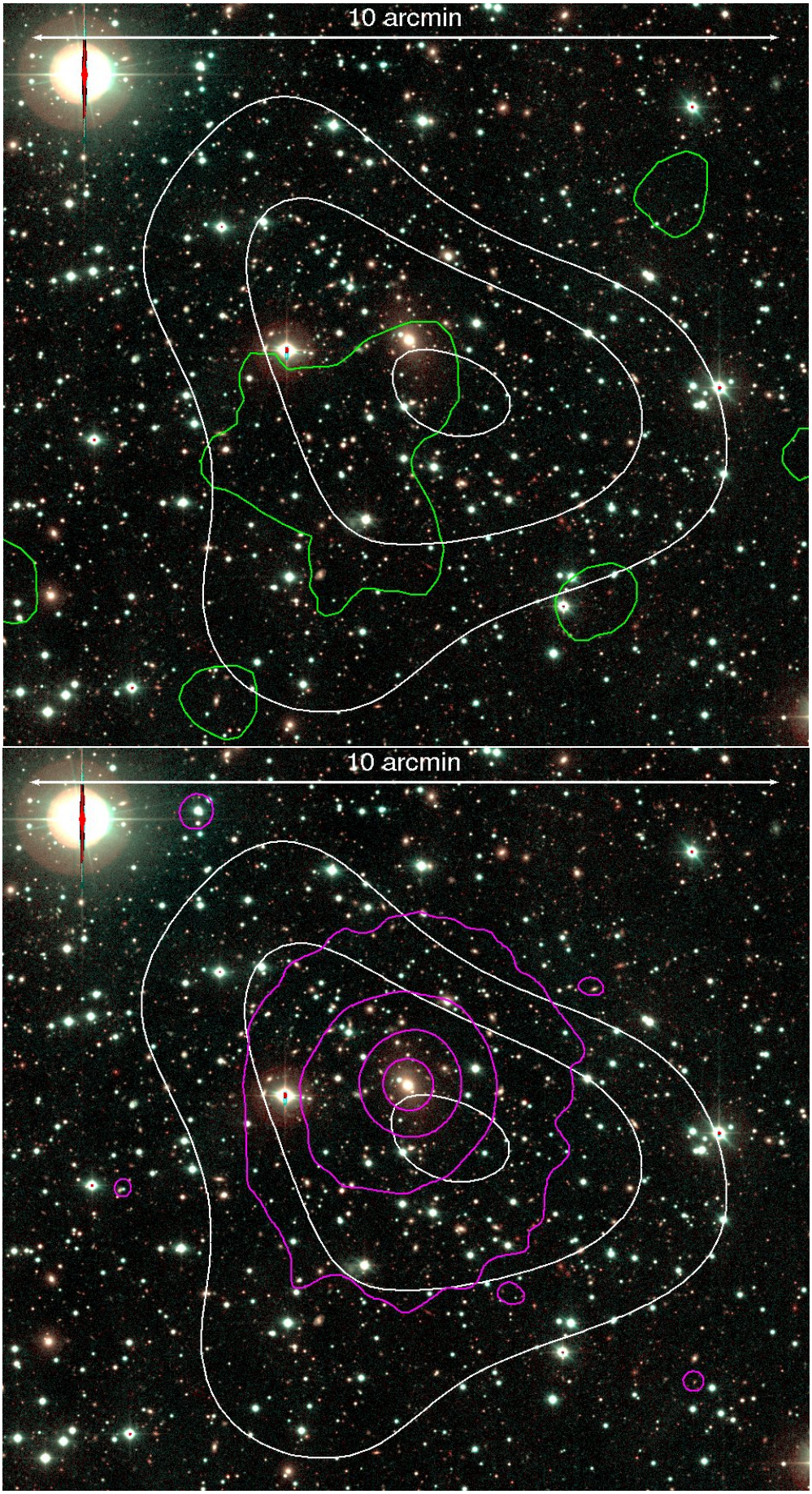

Figure 101: RXC2014

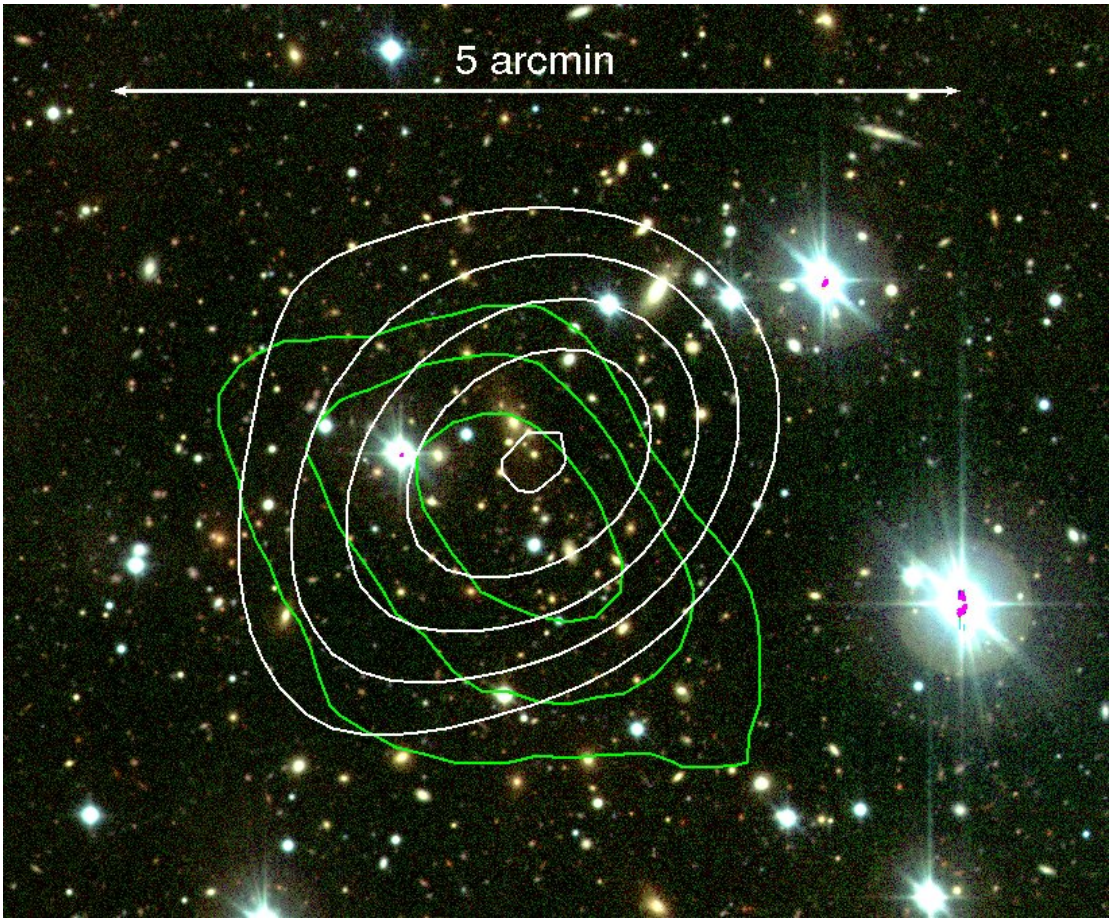

Figure 102: RXC2151

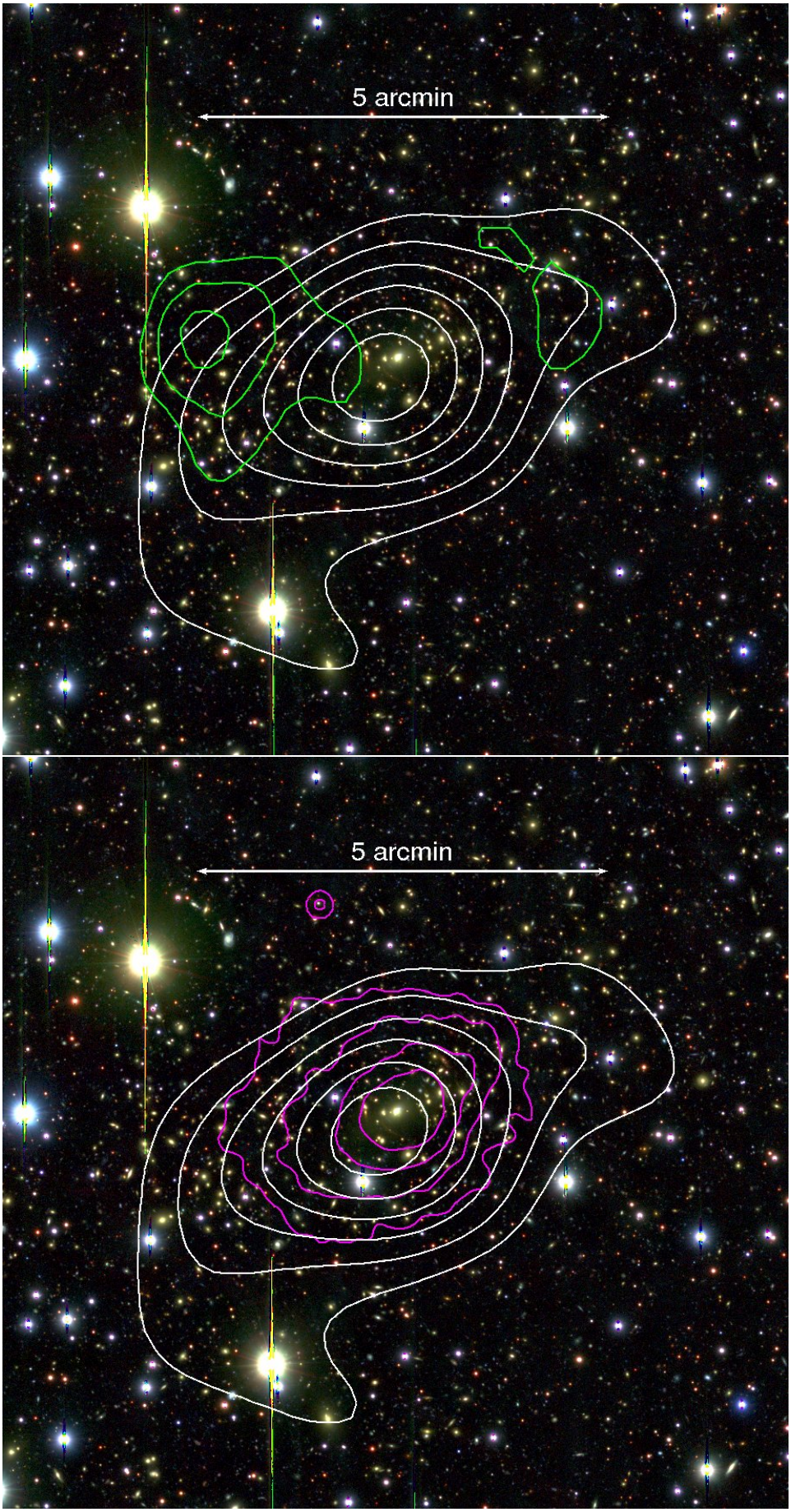

Figure 103: A2390

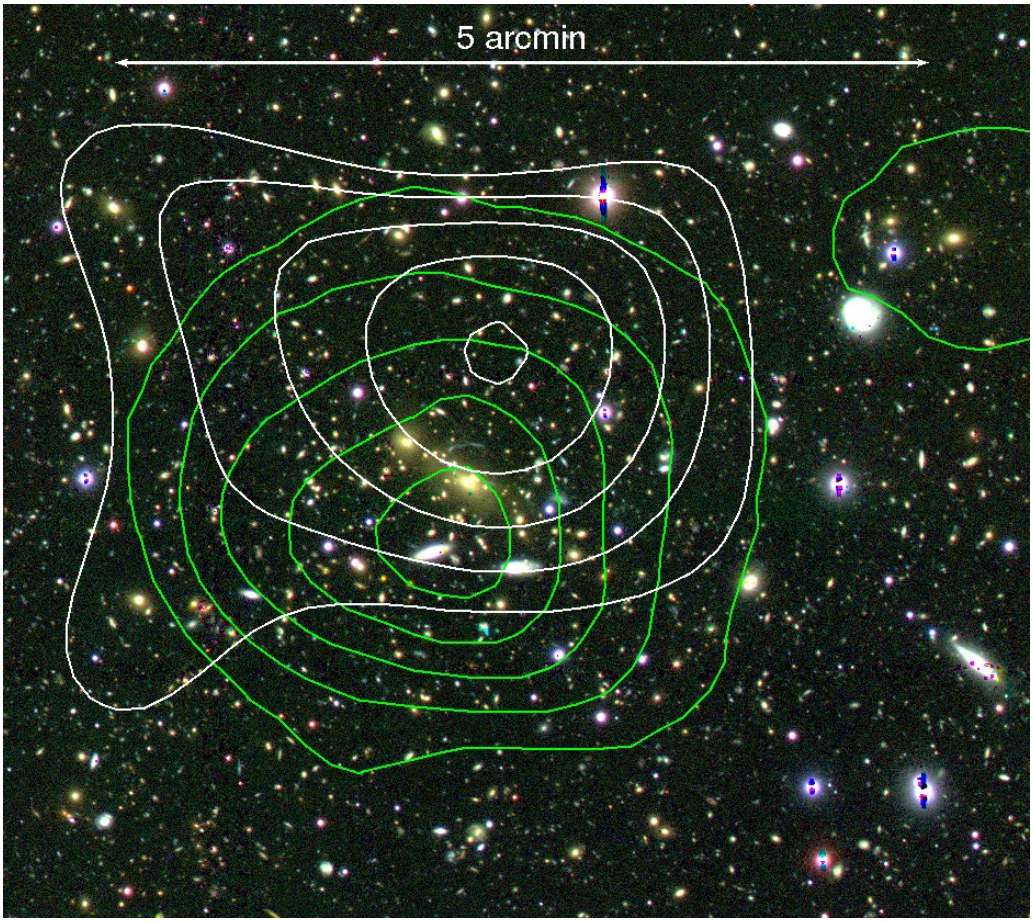

Figure 104: MCS2214

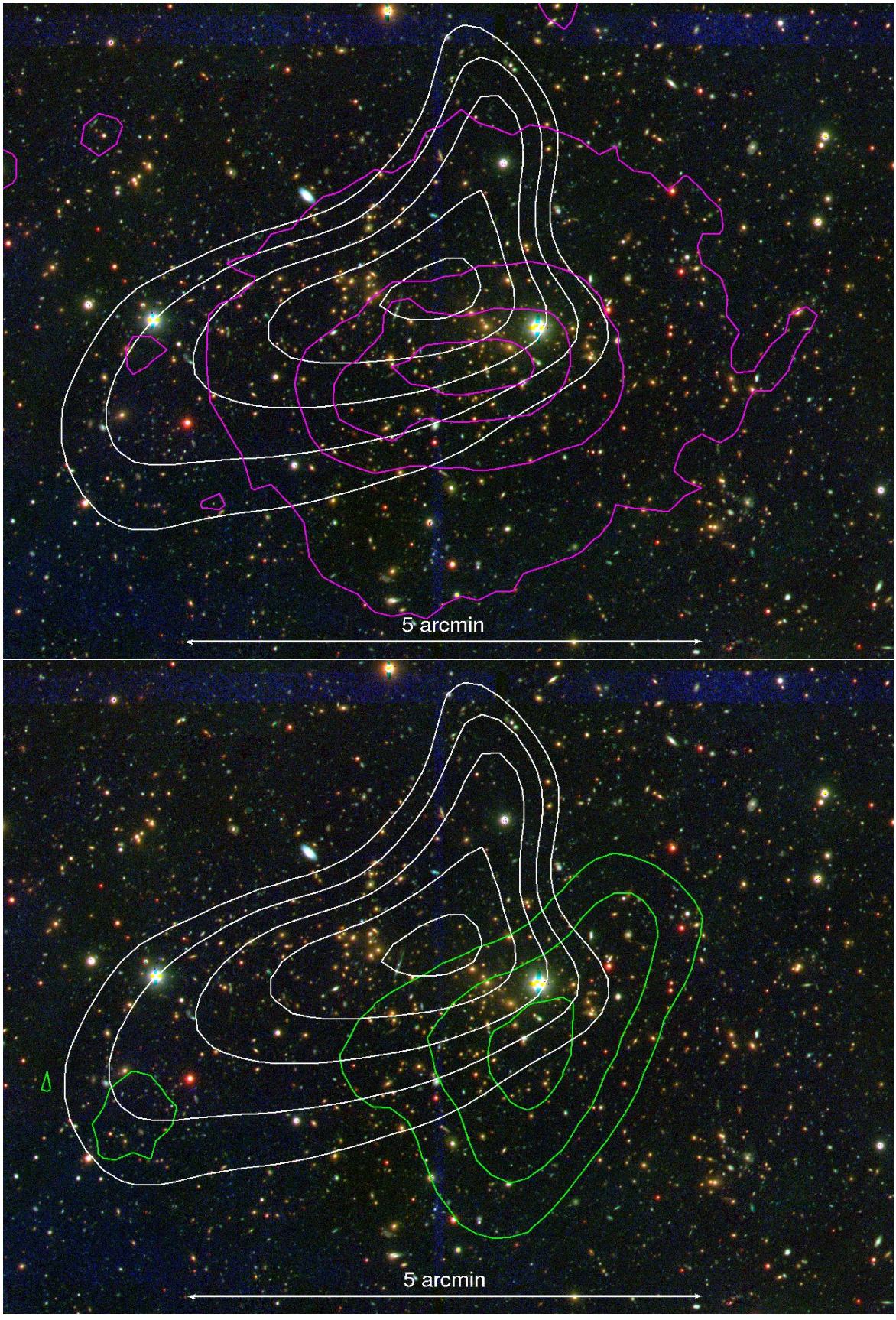

Figure 105: MCS2243

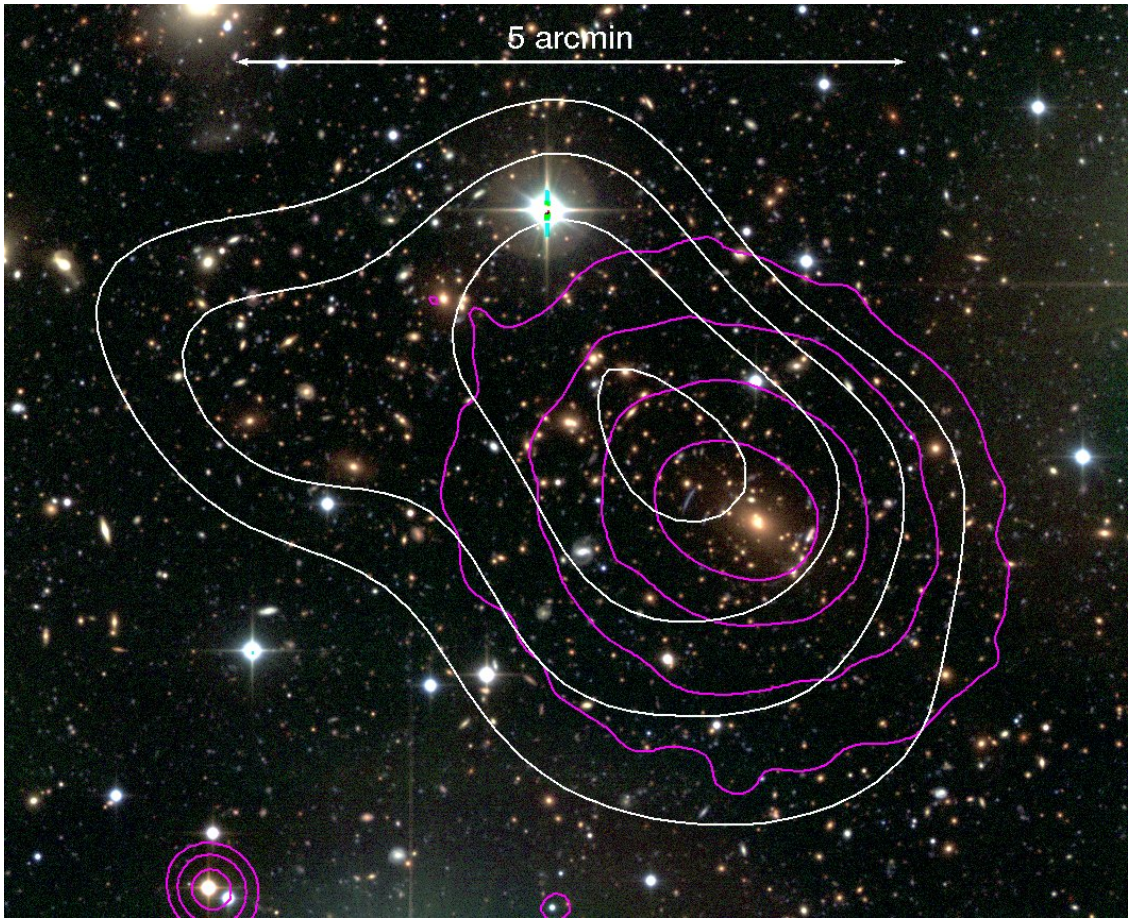

Figure 106: RXC2248

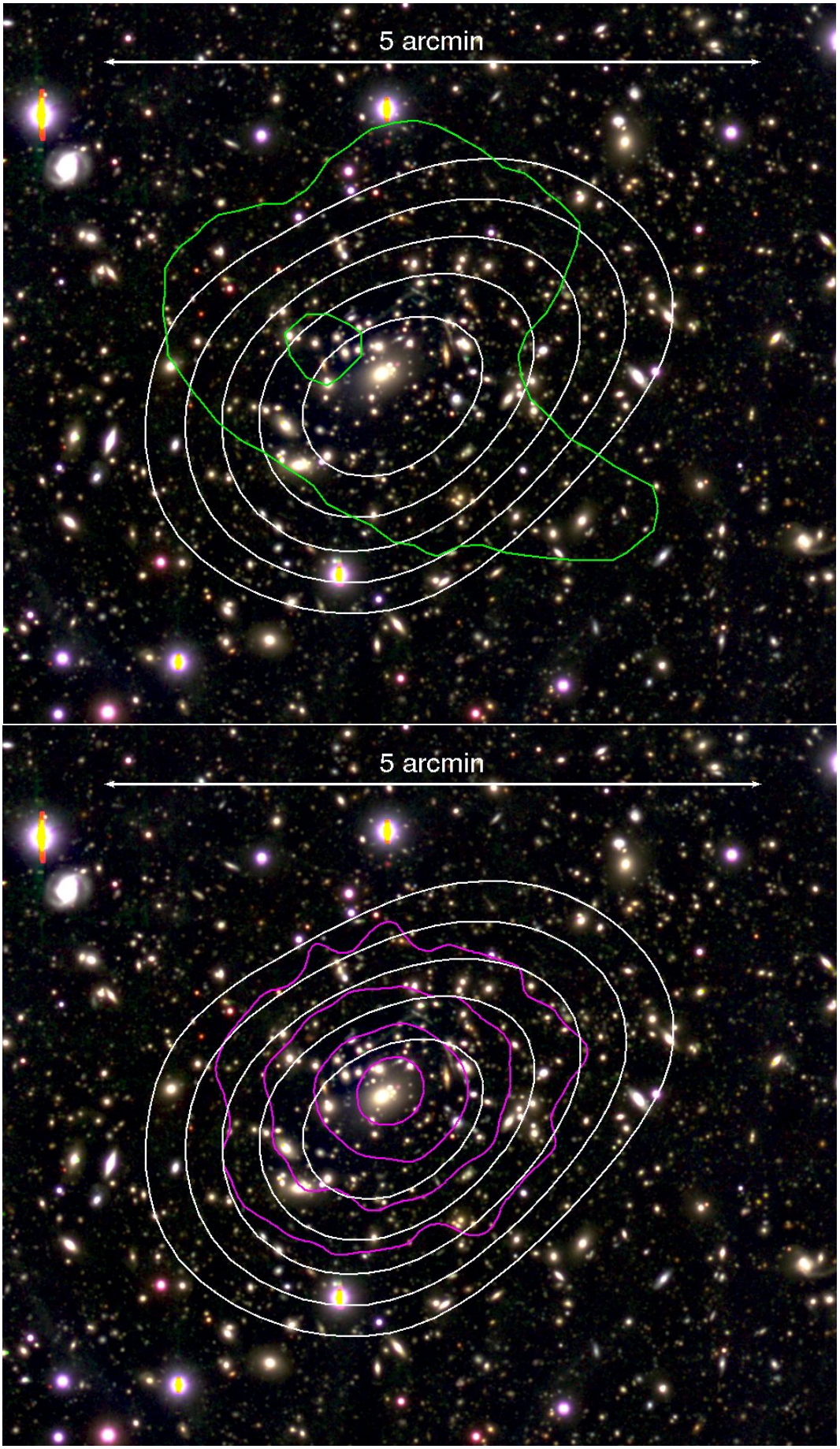

Figure 107: A2537

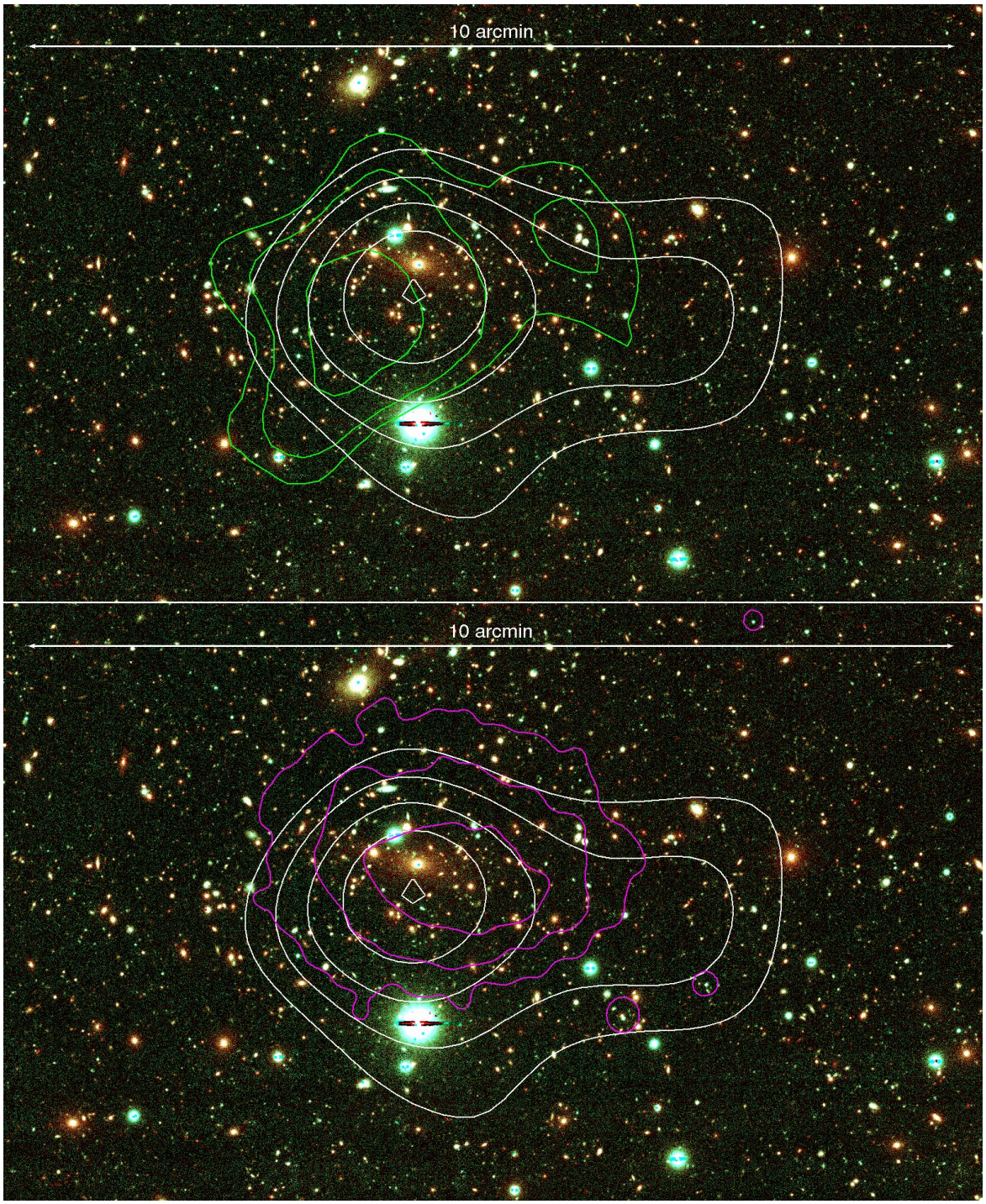

Figure 108: RXC2337

BIBLIOGRAPHY

G. O. Abell. The Distribution of Rich Clusters of Galaxies. ApJS, 3:211, May 1958. doi: 10.1086/190036.

G. O. Abell, H. G. Corwin, Jr., and R. P. Olowin. A catalog of rich clusters of galaxies. ApJS, 70:1–138, May 1989. doi: 10.1086/191333.

J. K. Adelman-McCarthy, M. A. Agüeros, S. S. Allam, C. Allende Prieto, K. S. J. Anderson, S. F. Anderson, J. Annis, N. A. Bahcall, C. A. L. Bailer-Jones, I. K. Baldry, J. C. Barentine, B. A. Bassett, A. C. Becker, T. C. Beers, E. F. Bell, A. A. Berlind, M. Bernardi, M. R. Blanton, J. J. Bochanski, W. N. Boroski, J. Brinchmann, J. Brinkmann, R. J. Brunner, T. Budavári, S. Carliles, M. A. Carr, F. J. Castander, D. Cinabro, R. J. Cool, K. R. Covey, I. Csabai, C. E. Cunha, J. R. A. Davenport, B. Dilday, M. Doi, D. J. Eisenstein, M. L. Evans, X. Fan, D. P. Finkbeiner, S. D. Friedman, J. A. Frieman, M. Fukugita, B. T. Gänsicke, E. Gates, B. Gillespie, K. Glazebrook, J. Gray, E. K. Grebel, J. E. Gunn, V. K. Gurbani, P. B. Hall, P. Harding, M. Harvanek, S. L. Hawley, J. Hayes, T. M. Heckman, J. S. Hendry, R. B. Hindsley, C. M. Hirata, C. J. Hogan, D. W. Hogg, J. B. Hyde, S.-i. Ichikawa, Ž. Ivezić, S. Jester, J. A. Johnson, A. M. Jorgensen, M. Jurić, S. M. Kent, R. Kessler, S. J. Kleinman, G. R. Knapp, R. G. Kron, J. Krzesinski, N. Kuropatkin, D. Q. Lamb, H. Lampeitl, S. Lebedeva, Y. S. Lee, R. F. Leger, S. Lépine, M. Lima, H. Lin, D. C. Long, C. P. Loomis, J. Loveday, R. H. Lupton, O. Malanushenko, V. Malanushenko, R. Mandelbaum, B. Margon, J. P. Marriner, D. Martínez-Delgado, T. Matsubara, P. M. McGehee, T. A. McKay, A. Meiksin, H. L. Morrison, J. A. Munn, R. Nakajima, E. H. Neilsen, Jr., H. J. Newberg, R. C. Nichol, T. Nicinski, M. Nieto-Santisteban, A. Nitta, S. Okamura, R. Owen, H. Oyaizu, N. Padmanabhan, K. Pan, C. Park, J. J. Peoples, J. R. Pier, A. C. Pope, N. Purger, M. J. Raddick, P. Re Fiorentin, G. T. Richards, M. W. Richmond, A. G. Riess, H.-W. Rix, C. M. Rockosi, M. Sako, D. J. Schlegel, D. P. Schneider, M. R. Schreiber, A. D. Schwope, U. Seljak, B. Sesar, E. Sheldon, K. Shimasaku, T. Sivarani, J. A. Smith, S. A. Snedden, M. Steinmetz, M. A. Strauss, M. SubbaRao, Y. Suto, A. S. Szalay, I. Szapudi, P. Szkody, M. Tegmark, A. R. Thakar, C. A. Tremonti, D. L. Tucker, A. Uomoto, D. E. Vanden Berk, J. Vandenberg, S. Vidrih, M. S. Vogeley, W. Voges, N. P. Vogt, Y. Wadadekar, D. H. Weinberg, A. A. West, S. D. M. White, B. C. Wilhite, B. Yanny, D. R. Yocum, D. G. York, I. Zehavi, and D. B. Zucker. The Sixth Data Release of the Sloan Digital Sky Survey. ApJS, 175:297–313, April 2008. doi: 10.1086/524984.

M. G. Akritas and M. A. Bershady. Linear Regression for Astronomical Data with Measurement Errors and Intrinsic Scatter. ApJ, 470:706, October 1996. doi: 10.1086/177901.

S. W. Allen, D. A. Rapetti, R. W. Schmidt, H. Ebeling, R. G. Morris, and A. C. Fabian. Improved constraints on dark energy from Chandra X-ray observations of the largest relaxed galaxy clusters. MNRAS, 383:879–896, January 2008. doi: 10.1111/j.1365-2966.2007.12610.x.

K. Andersson, J. R. Peterson, G. Madejski, and A. Goobar. Characterizing the Properties of Clusters of Galaxies as a Function of Luminosity and Redshift. ApJ, 696:1029–1050, May 2009. doi: 10.1088/0004-637X/696/1/1029.

K. Andersson, B. A. Benson, P. A. R. Ade, K. A. Aird, B. Armstrong, M. Bautz, L. E. Bleem, M. Brodwin, J. E. Carlstrom, C. L. Chang, T. M. Crawford, A. T. Crites, T. de

Haan, S. Desai, M. A. Dobbs, J. P. Dudley, R. J. Foley, W. R. Forman, G. Garmire, E. M. George, M. D. Gladders, N. W. Halverson, F. W. High, G. P. Holder, W. L. Holzapfel, J. D. Hrubes, C. Jones, M. Joy, R. Keisler, L. Knox, A. T. Lee, E. M. Leitch, M. Lueker, D. P. Marrone, J. J. McMahon, J. Mehl, S. S. Meyer, J. J. Mohr, T. E. Montroy, S. S. Murray, S. Padin, T. Plagge, C. Pryke, C. L. Reichardt, A. Rest, J. Ruel, J. E. Ruhl, K. K. Schaffer, L. Shaw, E. Shirokoff, J. Song, H. G. Spieler, B. Stalder, Z. Staniszewski, A. A. Stark, C. W. Stubbs, K. Vanderlinde, J. D. Vieira, A. Vikhlinin, R. Williamson, Y. Yang, O. Zahn, and A. Zenteno. X-Ray Properties of the First Sunyaev-Zel'dovich Effect Selected Galaxy Cluster Sample from the South Pole Telescope. ApJ, 738:48, September 2011. doi: 10.1088/0004-637X/738/1/48.

S. Andreon and J. Bergé. Richness-mass relation self-calibration for galaxy clusters. A&A, 547:A117, November 2012. doi: 10.1051/0004-6361/201220115.

S. Andreon, J. Willis, H. Quintana, I. Valtchanov, M. Pierre, and F. Pacaud. Galaxy evolution in clusters up to z= 1.0. MNRAS, 353:353–368, September 2004. doi: 10.1111/j.1365-2966.2004.08089.x.

I. Appenzeller, K. Fricke, W. Fürtig, W. Gässler, R. Häfner, R. Harke, H.-J. Hess, W. Hummel, P. Jürgens, R.-P. Kudritzki, K.-H. Mantel, W. Meisl, B. Muschielok, H. Nicklas, G. Rupprecht, W. Seifert, O. Stahl, T. Szeifert, and K. Tarantik. Successful commissioning of FORS1 - the first optical instrument on the VLT. *The Messenger*, 94:1–6, December 1998.

D. E. Applegate, A. von der Linden, P. L. Kelly, M. T. Allen, S. W. Allen, P. R. Burchat, D. L. Burke, H. Ebeling, A. Mantz, and R. G. Morris. Weighing the Giants III: Methods and Measurements of Accurate Galaxy Cluster Weak-Lensing Masses. *ArXiv e-prints*, August 2012.

M. Arnaud, G. W. Pratt, R. Piffaretti, H. Böhringer, J. H. Croston, and E. Pointecouteau. The universal galaxy cluster pressure profile from a representative sample of nearby systems (REXCESS) and the Y_{SZ} - M_{500} relation. A&A, 517:A92, July 2010. doi: 10.1051/0004-6361/200913416.

D. Baade, K. Meisenheimer, O. Iwert, J. Alonso, T. Augusteijn, J. Beletic, H. Bellemann, W. Benesch, A. Böhm, H. Böhnhardt, J. Brewer, S. Deiries, B. Delabre, R. Donaldson, C. Dupuy, P. Franke, R. Gerdes, A. Gilliotte, B. Grimm, N. Haddad, G. Hess, G. Ihle, R. Klein, R. Lenzen, J.-L. Lizon, D. Mancini, N. Münch, A. Pizarro, P. Prado, G. Rahmer, J. Reyes, F. Richardson, E. Robledo, F. Sanchez, A. Silber, P. Sinclaire, R. Wackermann, and S. Zaggia. The Wide Field Imager at the 2.2-m MPG/ESO telescope: first views with a 67-million-facette eye. *The Messenger*, 95:15–16, March 1999.

Y. M. Bahé, I. G. McCarthy, and L. J. King. Mock weak lensing analysis of simulated galaxy clusters: bias and scatter in mass and concentration. MNRAS, 421:1073–1088, April 2012. doi: 10.1111/j.1365-2966.2011.20364.x.

S. Bardeau, G. Soucail, J.-P. Kneib, O. Czoske, H. Ebeling, P. Hudelot, I. Smail, and G. P. Smith. A CFH12k lensing survey of X-ray luminous galaxy clusters. II. Weak lensing analysis and global correlations. A&A, 470:449–466, August 2007. doi: 10.1051/0004-6361:20077443.

M. Bartelmann. Cluster mass estimates from weak lensing. A&A, 303:643–+, November 1995.

M. Bartelmann. Arcs from a universal dark-matter halo profile. A&A, 313:697–702, September 1996.

M. Bartelmann and P. Schneider. Weak gravitational lensing. Phys. Rep., 340:291–472, January 2001. doi: 10.1016/S0370-1573(00)00082-X.

K. Basu. A Sunyaev-Zel'dovich take on cluster radio haloes - I. Global scaling and bimodality using Planck data. MNRAS, 421:L112–L116, March 2012. doi: 10.1111/j.1745-3933.2012.01217.x.

M. R. Becker and A. V. Kravtsov. On the Accuracy of Weak-lensing Cluster Mass Reconstructions. ApJ, 740:25, October 2011. doi: 10.1088/0004-637X/740/1/25.

A. N. Bender. *Galaxy Cluster Scaling Relations with APEX-SZ*. PhD thesis, University of Colorado at Boulder, 2011.

E. Bertin. Automatic Astrometric and Photometric Calibration with SCAMP. In C. Gabriel, C. Arviset, D. Ponz, and S. Enrique, editors, *Astronomical Data Analysis Software and Systems XV*, volume 351 of *ASP Conference Series*, page 112, July 2006.

E. Bertin and S. Arnouts. SExtractor: Software for source extraction. A&AS, 117:393–404, June 1996.

E. Bertin, Y. Mellier, M. Radovich, G. Missonnier, P. Didelon, and B. Morin. The TERAPIX Pipeline. In D. A. Bohlender, D. Durand, and T. H. Handley, editors, *Astronomical Data Analysis Software and Systems XI*, volume 281 of *Astronomical Society of the Pacific Conference Series*, page 228, 2002.

S. Bhattacharya, S. Habib, K. Heitmann, and A. Vikhlinin. Dark Matter Halo Profiles of Massive Clusters: Theory versus Observations. ApJ, 766:32, March 2013. doi: 10.1088/0004-637X/766/1/32.

M. Birkinshaw, S. F. Gull, and K. J. E. Northover. Measurements of the gas contents of clusters of galaxies by observations of the background radiation at 10.6 GHz. MNRAS, 185:245–262, October 1978.

H. Boehringer, G. Chon, C. A. Collins, L. Guzzo, N. Nowak, and S. Bobrovskyi. The extended ROSAT-ESO flux limited X-ray galaxy cluster survey (REFLEX II) II. Construction and properties of the survey. A&A, 555:A30, July 2013. doi: 10.1051/0004-6361/201220722.

H. Böhringer, W. Voges, J. P. Huchra, B. McLean, R. Giacconi, P. Rosati, R. Burg, J. Mader, P. Schuecker, D. Simiç, S. Komossa, T. H. Reiprich, J. Retzlaff, and J. Trümper. The Northern ROSAT All-Sky (NORAS) Galaxy Cluster Survey. I. X-Ray Properties of Clusters Detected as Extended X-Ray Sources. ApJS, 129:435–474, August 2000. doi: 10.1086/313427.

H. Böhringer, P. Schuecker, L. Guzzo, C. A. Collins, W. Voges, R. G. Cruddace, A. Ortiz-Gil, G. Chincarini, S. De Grandi, A. C. Edge, H. T. MacGillivray, D. M. Neumann, S. Schindler, and P. Shaver. The ROSAT-ESO Flux Limited X-ray (REFLEX) Galaxy cluster survey. V. The cluster catalogue. A&A, 425:367–383, October 2004. doi: 10.1051/0004-6361:20034484.

H. Böhringer, V. Burwitz, Y.-Y. Zhang, P. Schuecker, and N. Nowak. Chandra Reveals Galaxy Cluster with the Most Massive Nearby Cooling Core: RXC J1504.1-0248. ApJ, 633:148–153, November 2005. doi: 10.1086/444584.

H. Böhringer, P. Schuecker, G. W. Pratt, M. Arnaud, T. J. Ponman, J. H. Croston, S. Borgani, R. G. Bower, U. G. Briel, C. A. Collins, M. Donahue, W. R. Forman, A. Finoguenov, M. J. Geller, L. Guzzo, J. P. Henry, R. Kneissl, J. J. Mohr, K. Matsushita, C. R. Mullis, T. Ohashi, K. Pedersen, D. Pierini, H. Quintana, S. Raychaudhury, T. H. Reiprich, A. K. Romer, P. Rosati, K. Sabirli, R. F. Temple, P. T. P. Viana, A. Vikhlinin, G. M. Voit, and Y.-Y. Zhang. The representative XMM-Newton cluster structure survey (REXCESS) of an X-ray luminosity selected galaxy cluster sample. A&A, 469:363–377, July 2007. doi: 10.1051/0004-6361:20066740.

M. Bonamente, M. K. Joy, S. J. LaRoque, J. E. Carlstrom, E. D. Reese, and K. S. Dawson. Determination of the Cosmic Distance Scale from Sunyaev-Zel'dovich Effect and Chandra X-Ray Measurements of High-Redshift Galaxy Clusters. ApJ, 647:25–54, August 2006. doi: 10.1086/505291.

M. Bonamente, M. Joy, S. J. LaRoque, J. E. Carlstrom, D. Nagai, and D. P. Marrone. Scaling Relations from Sunyaev-Zel'dovich Effect and Chandra X-Ray Measurements of High-Redshift Galaxy Clusters. ApJ, 675:106–114, March 2008. doi: 10.1086/525517.

W. Boschin. A deep cluster survey in Chandra archival data. First results. A&A, 396: 397–409, December 2002. doi: 10.1051/0004-6361:20021393.

G. Brunetti, G. Setti, L. Feretti, and G. Giovannini. Particle reacceleration in the Coma cluster: radio properties and hard X-ray emission. MNRAS, 320:365–378, January 2001. doi: 10.1046/j.1365-8711.2001.03978.x.

G. Brunetti, T. Venturi, D. Dallacasa, R. Cassano, K. Dolag, S. Giacintucci, and G. Setti. Cosmic Rays and Radio Halos in Galaxy Clusters: New Constraints from Radio Observations. ApJ, 670:L5–L8, November 2007. doi: 10.1086/524037.

R. J. Brunner, A. J. Connolly, and A. S. Szalay. The Statistical Approach to Quantifying Galaxy Evolution. ApJ, 516:563–581, May 1999. doi: 10.1086/307146.

G. L. Bryan and M. L. Norman. Statistical Properties of X-Ray Clusters: Analytic and Numerical Comparisons. ApJ, 495:80, March 1998. doi: 10.1086/305262.

J. S. Bullock, T. S. Kolatt, Y. Sigad, R. S. Somerville, A. V. Kravtsov, A. A. Klypin, J. R. Primack, and A. Dekel. Profiles of dark haloes: evolution, scatter and environment. MNRAS, 321:559–575, March 2001. doi: 10.1046/j.1365-8711.2001.04068.x.

R. A. Burenin, A. Vikhlinin, A. Hornstrup, H. Ebeling, H. Quintana, and A. Mescheryakov. The 400 Square Degree ROSAT PSPC Galaxy Cluster Survey: Catalog and Statistical Calibration. ApJS, 172:561–582, October 2007. doi: 10.1086/519457.

H. Butcher and A. Oemler, Jr. The evolution of galaxies in clusters. II - The galaxy content of nearby clusters. ApJ, 226:559–565, December 1978. doi: 10.1086/156640.

J. E. Carlstrom, G. P. Holder, and E. D. Reese. Cosmology with the Sunyaev-Zel'dovich Effect. ARA&A, 40:643–680, 2002. doi: 10.1146/annurev.astro.40.060401.093803.

A. Cavaliere and R. Fusco-Femiano. The Distribution of Hot Gas in Clusters of Galaxies. A&A, 70:677, November 1978.

S. M. Chung, A. H. Gonzalez, D. Clowe, M. Markevitch, and D. Zaritsky. Star Formation in the Bullet Cluster. I. The Infrared Luminosity Function and Star Formation Rate. ApJ, 725:1536–1549, December 2010. doi: 10.1088/0004-637X/725/2/1536.

M. Cirelli, G. Corcella, A. Hektor, G. Hütsi, M. Kadastik, P. Panci, M. Raidal, F. Sala, and A. Strumia. PPPC 4 DM ID: a poor particle physicist cookbook for dark matter indirect detection. J. Cosmology Astropart. Phys., 3:051, March 2011. doi: 10.1088/1475-7516/2011/03/051.

D. Clowe and P. Schneider. Wide field weak lensing observations of A1835 and A2204. A&A, 395:385–397, November 2002. doi: 10.1051/0004-6361:20021137.

D. Clowe, M. Bradač, A. H. Gonzalez, M. Markevitch, S. W. Randall, C. Jones, and D. Zaritsky. A Direct Empirical Proof of the Existence of Dark Matter. ApJ, 648:L109–L113, September 2006. doi: 10.1086/508162.

D. Clowe, M. Markevitch, M. Bradač, A. H. Gonzalez, S. M. Chung, R. Massey, and D. Zaritsky. On Dark Peaks and Missing Mass: A Weak-lensing Mass Reconstruction of the Merging Cluster System A520. ApJ, 758:128, October 2012. doi: 10.1088/0004-637X/758/2/128.

R. G. Clowes, K. A. Harris, S. Raghunathan, L. E. Campusano, I. K. Söchting, and M. J. Graham. A structure in the early Universe at z 1.3 that exceeds the homogeneity scale of the R-W concordance cosmology. MNRAS, 429:2910–2916, March 2013. doi: 10.1093/mnras/sts497.

D. Coe, N. Benítez, T. Broadhurst, and L. A. Moustakas. A High-resolution Mass Map of Galaxy Cluster Substructure: LensPerfect Analysis of A1689. ApJ, 723:1678–1702, November 2010. doi: 10.1088/0004-637X/723/2/1678.

R. Cruddace, W. Voges, H. Böhringer, C. A. Collins, A. K. Romer, H. MacGillivray, D. Yentis, P. Schuecker, H. Ebeling, and S. De Grandi. The ROSAT All-Sky Survey: a Catalog of Clusters of Galaxies in a Region of 1 steradian around the South Galactic Pole. ApJS, 140:239–264, June 2002. doi: 10.1086/324519.

T. M. Davis, E. Mörtsell, J. Sollerman, A. C. Becker, S. Blondin, P. Challis, A. Clocchiatti, A. V. Filippenko, R. J. Foley, P. M. Garnavich, S. Jha, K. Krisciunas, R. P. Kirshner, B. Leibundgut, W. Li, T. Matheson, G. Miknaitis, G. Pignata, A. Rest, A. G. Riess, B. P. Schmidt, R. C. Smith, J. Spyromilio, C. W. Stubbs, N. B. Suntzeff, J. L. Tonry, W. M. Wood-Vasey, and A. Zenteno. Scrutinizing Exotic Cosmological Models Using ESSENCE Supernova Data Combined with Other Cosmological Probes. ApJ, 666:716–725, September 2007. doi: 10.1086/519988.

K. S. Dawson, G. Aldering, R. Amanullah, K. Barbary, L. F. Barrientos, M. Brodwin, N. Connolly, and et al. An Intensive Hubble Space Telescope Survey for z>1 Type Ia Supernovae by Targeting Galaxy Clusters. AJ, 138:1271–1283, November 2009. doi: 10.1088/0004-6256/138/5/1271.

W. A. Dawson, D. Wittman, M. J. Jee, P. Gee, J. P. Hughes, J. A. Tyson, S. Schmidt, P. Thorman, M. Bradač, S. Miyazaki, B. Lemaux, Y. Utsumi, and V. E. Margoniner. Discovery of a Dissociative Galaxy Cluster Merger with Large Physical Separation. ApJ, 747:L42, March 2012. doi: 10.1088/2041-8205/747/2/L42.

S. de Grandi, H. Böhringer, L. Guzzo, S. Molendi, G. Chincarini, C. Collins, R. Cruddace, D. Neumann, S. Schindler, P. Schuecker, and W. Voges. A Flux-limited Sample of Bright Clusters of Galaxies from the Southern Part of the ROSAT All-Sky Survey: The Catalog and LOG N-LOG S. ApJ, 514:148–163, March 1999. doi: 10.1086/306939.

B. Dennison. Formation of radio halos in clusters of galaxies from cosmic-ray protons. ApJ, 239:L93–L96, August 1980. doi: 10.1086/183300.

A. R. Duffy, J. Schaye, S. T. Kay, and C. Dalla Vecchia. Dark matter halo concentrations in the Wilkinson Microwave Anisotropy Probe year 5 cosmology. MNRAS, 390:L64–L68, October 2008. doi: 10.1111/j.1745-3933.2008.00537.x.

H. Ebeling, W. Voges, H. Bohringer, A. C. Edge, J. P. Huchra, and U. G. Briel. Properties of the X-ray-brightest Abell-type clusters of galaxies (XBACs) from ROSAT All-Sky Survey data - I. The sample. MNRAS, 281:799–829, August 1996.

H. Ebeling, A. C. Edge, S. W. Allen, C. S. Crawford, A. C. Fabian, and J. P. Huchra. The ROSAT Brightest Cluster Sample - IV. The extended sample. MNRAS, 318:333–340, October 2000. doi: 10.1046/j.1365-8711.2000.to1-1-03549.x.

H. Ebeling, E. Barrett, D. Donovan, C.-J. Ma, A. C. Edge, and L. van Speybroeck. A Complete Sample of 12 Very X-Ray Luminous Galaxy Clusters at z>0.5. ApJ, 661:L33–L36, May 2007. doi: 10.1086/518603.

H. Ebeling, A. C. Edge, A. Mantz, E. Barrett, J. P. Henry, C. J. Ma, and L. van Speybroeck. The X-ray brightest clusters of galaxies from the Massive Cluster Survey. MNRAS, 407: 83–93, September 2010a. doi: 10.1111/j.1365-2966.2010.16920.x.

H. Ebeling, A. C. Edge, A. Mantz, E. Barrett, J. P. Henry, C. J. Ma, and L. van Speybroeck. The X-ray brightest clusters of galaxies from the Massive Cluster Survey. *ArXiv astro-ph/1004.4683*, April 2010b.

A. C. Edge, H. Boehringer, L. Guzzo, C. A. Collins, D. Neumann, G. Chincarini, S. de Grandi, R. Duemmler, H. Ebeling, S. Schindler, W. Seitter, P. Vettolani, U. Briel, R. Cruddace, R. Gruber, H. Gursky, G. Hartner, H. T. MacGillivray, P. Schuecker, P. Shaver, W. Voges, J. Wallin, A. Wolter, and G. Zamorani. A giant arc in a ROSAT-detected cluster of galaxies. A&A, 289:L34–L36, September 1994.

T. Erben, L. van Waerbeke, E. Bertin, Y. Mellier, and P. Schneider. How accurately can we measure weak gravitational shear? A&A, 366:717–735, February 2001. doi: 10.1051/0004-6361:20010013.

T. Erben, M. Schirmer, J. P. Dietrich, O. Cordes, L. Haberzettl, M. Hetterscheidt, H. Hildebrandt, O. Schmithuesen, P. Schneider, P. Simon, E. Deul, R. N. Hook, N. Kaiser, M. Radovich, C. Benoist, M. Nonino, L. F. Olsen, I. Prandoni, R. Wichmann, S. Zaggia, D. Bomans, R. J. Dettmar, and J. M. Miralles. GaBoDS: The Garching-Bonn Deep Survey. IV. Methods for the image reduction of multi-chip cameras demonstrated on data from the ESO Wide-Field Imager. *Astronomische Nachrichten*, 326:432–464, July 2005. doi: 10.1002/asna.200510396.

S. Ettori, F. Gastaldello, A. Leccardi, S. Molendi, M. Rossetti, D. Buote, and M. Meneghetti. Mass profiles and c-M_{DM} relation in X-ray luminous galaxy clusters. A&A, 524:A68, December 2010. doi: 10.1051/0004-6361/201015271.

S. Ettori, F. Gastaldello, A. Leccardi, S. Molendi, M. Rossetti, D. Buote, and M. Meneghetti. Mass profiles and c - M_{DM} relation in X-ray luminous galaxy clusters (Corrigendum). A&A, 526:C1, February 2011. doi: 10.1051/0004-6361/201015271e.

R. Fassbender, H. Böhringer, J. S. Santos, G. W. Pratt, R. Šuhada, J. Kohnert, M. Lerchster, E. Rovilos, D. Pierini, G. Chon, A. D. Schwope, G. Lamer, M. Mühlegger, P. Rosati, H. Quintana, A. Nastasi, A. de Hoon, S. Seitz, and J. J. Mohr. A pan-chromatic view of the galaxy cluster XMMU J1230.3+1339 at z = 0.975. Observing the assembly of a massive system. A&A, 527:A78, March 2011. doi: 10.1051/0004-6361/201015204.

L. Feretti and G. Giovannini. Clusters of Galaxies in the Radio: Relativistic Plasma and ICM/Radio Galaxy Interaction Processes. In M. Plionis, O. López-Cruz, and D. Hughes, editors, *A Pan-Chromatic View of Clusters of Galaxies and the Large-Scale Structure*, volume 740 of *Lecture Notes in Physics, Berlin Springer Verlag*, page 143, 2008. doi: 10.1007/978-1-4020-6941-3_5.

L. Feretti, R. Fusco-Femiano, G. Giovannini, and F. Govoni. The giant radio halo in Abell 2163. A&A, 373:106–112, July 2001. doi: 10.1051/0004-6361:20010581.

C. Ferrari, C. Benoist, S. Maurogordato, A. Cappi, and E. Slezak. Dynamical state and star formation properties of the merging galaxy cluster Abell 3921. A&A, 430:19–38, January 2005. doi: 10.1051/0004-6361:20041811.

C. Ferrari, M. Arnaud, S. Ettori, S. Maurogordato, and J. Rho. Chandra observation of the multiple merger cluster Abell 521. A&A, 446:417–428, February 2006. doi: 10.1051/0004-6361:20053946.

T. S. Fetisova, D. Y. Kuznetsov, V. A. Lipovetskij, A. A. Starobinskij, and R. P. Olowin. Characteristics of the spatial distribution of rich clusters of galaxies in the northern and southern galactic hemispheres. *Astronomy Letters*, 19:198–202, June 1993.

A. Finoguenov, L. Guzzo, G. Hasinger, N. Z. Scoville, H. Aussel, H. Böhringer, M. Brusa, P. Capak, N. Cappelluti, A. Comastri, S. Giodini, R. E. Griffiths, C. Impey, A. M. Koekemoer, J.-P. Kneib, A. Leauthaud, O. Le Fèvre, S. Lilly, V. Mainieri, R. Massey, H. J. McCracken, B. Mobasher, T. Murayama, J. A. Peacock, I. Sakelliou, E. Schinnerer, J. D. Silverman, V. Smolčić, Y. Taniguchi, L. Tasca, J. E. Taylor, J. R. Trump, and G. Zamorani. The XMM-Newton Wide-Field Survey in the COSMOS Field: Statistical Properties of Clusters of Galaxies. ApJS, 172:182–195, September 2007. doi: 10.1086/516577.

D. G. Gilbank, H. K. C. Yee, E. Ellingson, A. K. Hicks, M. D. Gladders, L. F. Barrientos, and B. Keeney. A z = 0.9 Supercluster of X-Ray Luminous, Optically Selected, Massive Galaxy Clusters. ApJ, 677:L89–L92, April 2008. doi: 10.1086/588138.

S. Giodini, L. Lovisari, E. Pointecouteau, S. Ettori, T. H. Reiprich, and H. Hoekstra. Scaling Relations for Galaxy Clusters: Properties and Evolution. Space Sci. Rev., 177:247–282, August 2013. doi: 10.1007/s11214-013-9994-5.

M. D. Gladders and H. K. C. Yee. A New Method For Galaxy Cluster Detection. I. The Algorithm. AJ, 120:2148–2162, October 2000. doi: 10.1086/301557.

F. Govoni, M. Markevitch, A. Vikhlinin, L. van Speybroeck, L. Feretti, and G. Giovannini. Chandra Temperature Maps for Galaxy Clusters with Radio Halos. ApJ, 605:695–708, April 2004. doi: 10.1086/382674.

N. W. Halverson, T. Lanting, P. A. R. Ade, K. Basu, A. N. Bender, B. A. Benson, F. Bertoldi, H.-M. Cho, G. Chon, J. Clarke, M. Dobbs, D. Ferrusca, R. Güsten, W. L. Holzapfel, A. Kovács, J. Kennedy, Z. Kermish, R. Kneissl, A. T. Lee, M. Lueker, J. Mehl, K. M. Menten, D. Muders, M. Nord, F. Pacaud, T. Plagge, C. Reichardt, P. L. Richards, R. Schaaf,

P. Schilke, F. Schuller, D. Schwan, H. Spieler, C. Tucker, A. Weiss, and O. Zahn. Sunyaev-Zel'Dovich Effect Observations of the Bullet Cluster (1E 0657-56) with APEX-SZ. ApJ, 701:42–51, August 2009. doi: 10.1088/0004-637X/701/1/42.

N. Hand, G. E. Addison, E. Aubourg, N. Battaglia, E. S. Battistelli, D. Bizyaev, J. R. Bond, H. Brewington, J. Brinkmann, B. R. Brown, S. Das, K. S. Dawson, M. J. Devlin, J. Dunkley, R. Dunner, D. J. Eisenstein, J. W. Fowler, M. B. Gralla, A. Hajian, M. Halpern, M. Hilton, A. D. Hincks, R. Hlozek, J. P. Hughes, L. Infante, K. D. Irwin, A. Kosowsky, Y.-T. Lin, E. Malanushenko, V. Malanushenko, T. A. Marriage, D. Marsden, F. Menanteau, K. Moodley, M. D. Niemack, M. R. Nolta, D. Oravetz, L. A. Page, N. Palanque-Delabrouille, K. Pan, E. D. Reese, D. J. Schlegel, D. P. Schneider, N. Sehgal, A. Shelden, J. Sievers, C. Sifón, A. Simmons, S. Snedden, D. N. Spergel, S. T. Staggs, D. S. Swetz, E. R. Switzer, H. Trac, B. A. Weaver, E. J. Wollack, C. Yeche, and C. Zunckel. Evidence of Galaxy Cluster Motions with the Kinematic Sunyaev-Zel'dovich Effect. *Physical Review Letters*, 109(4):041101, July 2012. doi: 10.1103/PhysRevLett.109.041101.

J. Hartlap, T. Schrabback, P. Simon, and P. Schneider. The non-Gaussianity of the cosmic shear likelihood - or: How odd is the Chandra Deep Field South? *ArXiv astro-ph/0901.3269*, January 2009.

A. Hektor, M. Raidal, and E. Tempel. Evidence for Indirect Detection of Dark Matter from Galaxy Clusters in Fermi γ-Ray Data. ApJ, 762:L22, January 2013. doi: 10.1088/2041-8205/762/2/L22.

T. J. Henry. The Mass-Luminosity Relation from End to End. In R. W. Hilditch, H. Hensberge, and K. Pavlovski, editors, *Spectroscopically and Spatially Resolving the Components of the Close Binary Stars*, volume 318 of *Astronomical Society of the Pacific Conference Series*, pages 159–165, December 2004.

C. Heymans, L. van Waerbeke, D. Bacon, J. Berge, G. Bernstein, E. Bertin, S. Bridle, M. L. Brown, D. Clowe, H. Dahle, T. Erben, M. Gray, M. Hetterscheidt, H. Hoekstra, P. Hudelot, M. Jarvis, K. Kuijken, V. Margoniner, R. Massey, Y. Mellier, R. Nakajima, A. Refregier, J. Rhodes, T. Schrabback, and D. Wittman. The Shear Testing Programme - I. Weak lensing analysis of simulated ground-based observations. MNRAS, 368:1323–1339, May 2006. doi: 10.1111/j.1365-2966.2006.10198.x.

F. W. High, C. W. Stubbs, A. Rest, B. Stalder, and P. Challis. Stellar Locus Regression: Accurate Color Calibration and the Real-Time Determination of Galaxy Cluster Photometric Redshifts. AJ, 138:110–129, July 2009. doi: 10.1088/0004-6256/138/1/110.

F. W. High, H. Hoekstra, N. Leethochawalit, T. de Haan, L. Abramson, K. A. Aird, R. Armstrong, M. L. N. Ashby, M. Bautz, M. Bayliss, G. Bazin, B. A. Benson, L. E. Bleem, M. Brodwin, J. E. Carlstrom, C. L. Chang, H. M. Cho, A. Clocchiatti, M. Conroy, T. M. Crawford, A. T. Crites, S. Desai, M. A. Dobbs, J. P. Dudley, R. J. Foley, W. R. Forman, E. M. George, M. D. Gladders, A. H. Gonzalez, N. W. Halverson, N. L. Harrington, G. P. Holder, W. L. Holzapfel, S. Hoover, J. D. Hrubes, C. Jones, M. Joy, R. Keisler, L. Knox, A. T. Lee, E. M. Leitch, J. Liu, M. Lueker, D. Luong-Van, A. Mantz, D. P. Marrone, M. McDonald, J. J. McMahon, J. Mehl, S. S. Meyer, L. Mocanu, J. J. Mohr, T. E. Montroy, S. S. Murray, T. Natoli, D. Nurgaliev, S. Padin, T. Plagge, C. Pryke, C. L. Reichardt, A. Rest, J. Ruel, J. E. Ruhl, B. R. Saliwanchik, A. Saro, J. T. Sayre, K. K. Schaffer, L. Shaw, T. Schrabback, E. Shirokoff, J. Song, H. G. Spieler, B. Stalder, Z. Staniszewski, A. A. Stark, K. Story, C. W. Stubbs, R. Šuhada, S. Tokarz, A. van Engelen, K. Vanderlinde, J. D. Vieira, A. Vikhlinin, R. Williamson, O. Zahn, and A. Zenteno. Weak-lensing

Mass Measurements of Five Galaxy Clusters in the South Pole Telescope Survey Using Magellan/Megacam. ApJ, 758:68, October 2012. doi: 10.1088/0004-637X/758/1/68.

H. Hildebrandt, J. Pielorz, T. Erben, P. Schneider, T. Eifler, P. Simon, and J. P. Dietrich. GaBoDS: the Garching-Bonn deep survey. VIII. Lyman-break galaxies in the ESO deep public survey. A&A, 462:865–873, February 2007. doi: 10.1051/0004-6361:20065880.

M. Hilton, C. A. Collins, S. A. Stanford, C. Lidman, K. S. Dawson, M. Davidson, S. T. Kay, A. R. Liddle, R. G. Mann, C. J. Miller, R. C. Nichol, A. K. Romer, K. Sabirli, P. T. P. Viana, and M. J. West. The XMM Cluster Survey: The Dynamical State of XMMXCS J2215.9-1738 at z = 1.457. ApJ, 670:1000–1009, December 2007. doi: 10.1086/522827.

H. Hoekstra, M. Franx, K. Kuijken, and G. Squires. Weak Lensing Analysis of CL 1358+62 Using Hubble Space Telescope Observations. ApJ, 504:636–+, September 1998. doi: 10.1086/306102.

H. Hoekstra, A. Mahdavi, A. Babul, and C. Bildfell. The Canadian Cluster Comparison Project: weak lensing masses and SZ scaling relations. MNRAS, 427:1298–1311, December 2012. doi: 10.1111/j.1365-2966.2012.22072.x.

C.-L. Hung and H. Ebeling. Galaxy alignments in very X-ray luminous clusters at z>0.5. MNRAS, 421:3229–3237, April 2012. doi: 10.1111/j.1365-2966.2012.20546.x.

H. S. Hwang and M. G. Lee. Galaxy activity in merging binary galaxy clusters. MNRAS, 397:2111–2122, August 2009. doi: 10.1111/j.1365-2966.2009.15100.x.

O. Ilbert, P. Capak, M. Salvato, H. Aussel, H. J. McCracken, D. B. Sanders, N. Scoville, J. Kartaltepe, S. Arnouts, E. LeFloc'h, B. Mobasher, Y. Taniguchi, F. Lamareille, A. Leauthaud, S. Sasaki, D. Thompson, M. Zamojski, G. Zamorani, S. Bardelli, M. Bolzonella, A. Bongiorno, M. Brusa, K. I. Caputi, C. M. Carollo, T. Contini, R. Cook, G. Coppa, O. Cucciati, S. de la Torre, L. de Ravel, P. Franzetti, B. Garilli, G. Hasinger, A. Iovino, P. Kampczyk, J.-P. Kneib, C. Knobel, K. Kovac, J. F. LeBorgne, V. LeBrun, O. LeFèvre, S. Lilly, D. Looper, C. Maier, V. Mainieri, Y. Mellier, M. Mignoli, T. Murayama, R. Pellò, Y. Peng, E. Pérez-Montero, A. Renzini, E. Ricciardelli, D. Schiminovich, M. Scodeggio, Y. Shioya, J. Silverman, J. Surace, M. Tanaka, L. Tasca, L. Tresse, D. Vergani, and E. Zucca. Cosmos Photometric Redshifts with 30-BANDS for $2 - deg^2$. ApJ, 690:1236–1249, January 2009. doi: 10.1088/0004-637X/690/2/1236.

H. Israel, T. Erben, T. H. Reiprich, A. Vikhlinin, H. Hildebrandt, D. S. Hudson, B. A. McLeod, C. L. Sarazin, P. Schneider, and Y.-Y. Zhang. The 400d Galaxy Cluster Survey Weak Lensing Programme: I: MMT/Megacam Analysis of CL0030+2618 at z=0.50. A&A, *in press*, November 2010a.

H. Israel, T. Erben, T. H. Reiprich, A. Vikhlinin, H. Hildebrandt, D. S. Hudson, B. A. McLeod, C. L. Sarazin, P. Schneider, and Y.-Y. Zhang. The 400d Galaxy Cluster Survey weak lensing programme. I. MMT/Megacam analysis of CL0030+2618 at z = 0.50. A&A, 520:A58, September 2010b. doi: 10.1051/0004-6361/200913667.

H. Israel, T. Erben, T. H. Reiprich, A. Vikhlinin, C. L. Sarazin, and P. Schneider. The 400d Galaxy Cluster Survey weak lensing programme. II. Weak lensing study of seven clusters with MMT/MegaCam. A&A, 546:A79, October 2012. doi: 10.1051/0004-6361/201118676.

N. Jarosik, C. L. Bennett, J. Dunkley, B. Gold, M. R. Greason, M. Halpern, R. S. Hill, G. Hinshaw, A. Kogut, E. Komatsu, D. Larson, M. Limon, S. S. Meyer, M. R. Nolta, N. Odegard, L. Page, K. M. Smith, D. N. Spergel, G. S. Tucker, J. L. Weiland, E. Wollack, and

E. L. Wright. Seven-year Wilkinson Microwave Anisotropy Probe (WMAP) Observations: Sky Maps, Systematic Errors, and Basic Results. ApJS, 192:14, February 2011. doi: 10.1088/0067-0049/192/2/14.

M. J. Jee, A. Mahdavi, H. Hoekstra, A. Babul, J. J. Dalcanton, P. Carroll, and P. Capak. A Study of the Dark Core in A520 with the Hubble Space Telescope: The Mystery Deepens. ApJ, 747:96, March 2012. doi: 10.1088/0004-637X/747/2/96.

B. Joachimi and P. Schneider. The removal of shear-ellipticity correlations from the cosmic shear signal. Influence of photometric redshift errors on the nulling technique. A&A, 507:105–129, November 2009. doi: 10.1051/0004-6361/200912420.

I. Jørgensen and K. Chiboucas. Stellar Populations and Evolution of Early-type Cluster Galaxies: Constraints from Optical Imaging and Spectroscopy of z = 0.5-0.9 Galaxy Clusters. AJ, 145:77, March 2013. doi: 10.1088/0004-6256/145/3/77.

M. Jurić, Ž. Ivezić, A. Brooks, R. H. Lupton, D. Schlegel, D. Finkbeiner, N. Padmanabhan, N. Bond, B. Sesar, C. M. Rockosi, G. R. Knapp, J. E. Gunn, T. Sumi, D. P. Schneider, J. C. Barentine, H. J. Brewington, J. Brinkmann, M. Fukugita, M. Harvanek, S. J. Kleinman, J. Krzesinski, D. Long, E. H. Neilsen, Jr., A. Nitta, S. A. Snedden, and D. G. York. The Milky Way Tomography with SDSS. I. Stellar Number Density Distribution. ApJ, 673: 864–914, February 2008. doi: 10.1086/523619.

N. Kaiser. Evolution and clustering of rich clusters. MNRAS, 222:323–345, September 1986.

N. Kaiser and G. Squires. Mapping the dark matter with weak gravitational lensing. ApJ, 404:441–450, February 1993. doi: 10.1086/172297.

N. Kaiser, G. Squires, and T. Broadhurst. A Method for Weak Lensing Observations. ApJ, 449:460–+, August 1995. doi: 10.1086/176071.

B. C. Kelly. Some Aspects of Measurement Error in Linear Regression of Astronomical Data. ApJ, 665:1489–1506, August 2007. doi: 10.1086/519947.

P. L. Kelly, A. von der Linden, D. E. Applegate, M. T. Allen, S. W. Allen, P. R. Burchat, D. L. Burke, H. Ebeling, P. Capak, O. Czoske, D. Donovan, A. Mantz, and R. G. Morris. Weighing the Giants II: Improved Calibration of Photometry from Stellar Colors and Accurate Photometric Redshifts. *ArXiv e-prints*, August 2012.

E. Komatsu, J. Dunkley, M. R. Nolta, C. L. Bennett, B. Gold, G. Hinshaw, N. Jarosik, D. Larson, M. Limon, L. Page, D. N. Spergel, M. Halpern, R. S. Hill, A. Kogut, S. S. Meyer, G. S. Tucker, J. L. Weiland, E. Wollack, and E. L. Wright. Five-Year Wilkinson Microwave Anisotropy Probe Observations: Cosmological Interpretation. ApJS, 180:330–376, February 2009. doi: 10.1088/0067-0049/180/2/330.

A. V. Kravtsov, A. Vikhlinin, and D. Nagai. A New Robust Low-Scatter X-Ray Mass Indicator for Clusters of Galaxies. ApJ, 650:128–136, October 2006. doi: 10.1086/506319.

P. Kroupa, B. Famaey, K. S. de Boer, J. Dabringhausen, M. S. Pawlowski, C. M. Boily, H. Jerjen, D. Forbes, G. Hensler, and M. Metz. Local-Group tests of dark-matter concordance cosmology . Towards a new paradigm for structure formation. A&A, 523:A32, November 2010. doi: 10.1051/0004-6361/201014892.

M. Lerchster, S. Seitz, F. Brimioulle, R. Fassbender, M. Rovilos, H. Böhringer, D. Pierini, M. Kilbinger, A. Finoguenov, H. Quintana, and R. Bender. The massive galaxy cluster XMMU J1230.3+1339 at z 1: colour-magnitude relation, Butcher-Oemler effect, X-ray and weak lensing mass estimates. MNRAS, 411:2667–2694, March 2011. doi: 10.1111/j.1365-2966.2010.17874.x.

H. Liang. Diffuse Cluster-wide Radio Halos. *ArXiv Astrophysics e-prints*, December 2000.

M. Lima, C. E. Cunha, H. Oyaizu, J. Frieman, H. Lin, and E. S. Sheldon. Estimating the redshift distribution of photometric galaxy samples. MNRAS, 390:118–130, October 2008. doi: 10.1111/j.1365-2966.2008.13510.x.

E. J. Lloyd-Davies, A. K. Romer, N. Mehrtens, M. Hosmer, M. Davidson, K. Sabirli, R. G. Mann, M. Hilton, A. R. Liddle, P. T. P. Viana, H. C. Campbell, C. A. Collins, E. N. Dubois, P. Freeman, C. D. Harrison, B. Hoyle, S. T. Kay, E. Kuwertz, C. J. Miller, R. C. Nichol, M. Sahlén, S. A. Stanford, and J. P. Stott. The XMM Cluster Survey: X-ray analysis methodology. MNRAS, 418:14–53, November 2011. doi: 10.1111/j.1365-2966.2011.19117.x.

A. Mahdavi, H. Hoekstra, A. Babul, D. D. Balam, and P. L. Capak. A Dark Core in Abell 520. ApJ, 668:806–814, October 2007. doi: 10.1086/521383.

M. Markevitch, A. H. Gonzalez, D. Clowe, A. Vikhlinin, W. Forman, C. Jones, S. Murray, and W. Tucker. Direct Constraints on the Dark Matter Self-Interaction Cross Section from the Merging Galaxy Cluster 1E 0657-56. ApJ, 606:819–824, May 2004. doi: 10.1086/383178.

D. P. Marrone, G. P. Smith, N. Okabe, M. Bonamente, J. E. Carlstrom, T. L. Culverhouse, M. Gralla, C. H. Greer, N. Hasler, D. Hawkins, R. Hennessy, M. Joy, J. W. Lamb, E. M. Leitch, R. Martino, P. Mazzotta, A. Miller, T. Mroczkowski, S. Muchovej, T. Plagge, C. Pryke, A. J. R. Sanderson, M. Takada, D. Woody, and Y. Zhang. LoCuSS: The Sunyaev-Zel'dovich Effect and Weak-lensing Mass Scaling Relation. ApJ, 754:119, August 2012. doi: 10.1088/0004-637X/754/2/119.

R. Massey, C. Heymans, J. Bergé, G. Bernstein, S. Bridle, D. Clowe, H. Dahle, R. Ellis, T. Erben, M. Hetterscheidt, F. W. High, C. Hirata, H. Hoekstra, P. Hudelot, M. Jarvis, D. Johnston, K. Kuijken, V. Margoniner, R. Mandelbaum, Y. Mellier, R. Nakajima, S. Paulin-Henriksson, M. Peeples, C. Roat, A. Refregier, J. Rhodes, T. Schrabback, M. Schirmer, U. Seljak, E. Semboloni, and L. van Waerbeke. The Shear Testing Programme 2: Factors affecting high-precision weak-lensing analyses. MNRAS, 376:13–38, March 2007. doi: 10.1111/j.1365-2966.2006.11315.x.

B. McLeod, J. Geary, M. Ordway, S. Amato, M. Conroy, and T. Gauron. The MMT Megacam. In J. E. Beletic, J. W. Beletic, & P. Amico, editor, *Scientific Detectors for Astronomy 2005*, page 337, March 2006.

B. A. McLeod, M. Conroy, T. M. Gauron, J. C. Geary, and M. P. Ordway. Megacam: A Wide-field Imager for the MMT Observatory. In M. B. Denton, editor, *Further Developments in Scientific Optical Imaging*, page 11, 2000.

E. Medezinski, T. Broadhurst, K. Umetsu, M. Oguri, Y. Rephaeli, and N. Benítez. Detailed cluster mass and light profiles of A1703, A370 and RXJ1347-11 from deep Subaru imaging. MNRAS, 405:257–273, June 2010. doi: 10.1111/j.1365-2966.2010.16491.x.

J.-B. Melin, J. G. Bartlett, and J. Delabrouille. Catalog extraction in SZ cluster surveys: a matched filter approach. A&A, 459:341–352, November 2006. doi: 10.1051/0004-6361:20065034.

F. Menanteau, J. P. Hughes, L. F. Barrientos, A. J. Deshpande, M. Hilton, L. Infante, R. Jimenez, A. Kosowsky, K. Moodley, D. Spergel, and L. Verde. Southern Cosmology Survey. II. Massive Optically Selected Clusters from 70 Square Degrees of the Sunyaev-Zel'dovich Effect Common Survey Area. ApJS, 191:340–351, December 2010. doi: 10.1088/0067-0049/191/2/340.

S. Miyazaki, Y. Komiyama, M. Sekiguchi, S. Okamura, M. Doi, H. Furusawa, M. Hamabe, K. Imi, M. Kimura, F. Nakata, N. Okada, M. Ouchi, K. Shimasaku, M. Yagi, and N. Yasuda. Subaru Prime Focus Camera – Suprime-Cam. PASJ, 54:833–853, December 2002.

C. R. Mullis, P. Rosati, G. Lamer, H. Böhringer, A. Schwope, P. Schuecker, and R. Fassbender. Discovery of an X-Ray-luminous Galaxy Cluster at z=1.4. ApJ, 623:L85–L88, April 2005. doi: 10.1086/429801.

M. T. Murphy, J. K. Webb, and V. V. Flambaum. Further evidence for a variable fine-structure constant from Keck/HIRES QSO absorption spectra. MNRAS, 345:609–638, October 2003. doi: 10.1046/j.1365-8711.2003.06970.x.

D. Nagai, A. V. Kravtsov, and A. Vikhlinin. Effects of Galaxy Formation on Thermodynamics of the Intracluster Medium. ApJ, 668:1–14, October 2007a. doi: 10.1086/521328.

D. Nagai, A. Vikhlinin, and A. V. Kravtsov. Testing X-Ray Measurements of Galaxy Clusters with Cosmological Simulations. ApJ, 655:98–108, January 2007b. doi: 10.1086/509868.

J. F. Navarro, C. S. Frenk, and S. D. M. White. The Structure of Cold Dark Matter Halos. ApJ, 462:563–+, May 1996. doi: 10.1086/177173.

M. Nord. *Observations of the Sunyaev-Zel'dovich Effect towards Clusters of Galaxies with the APEX Telescope*. PhD thesis, University of Bonn, http://hss.ulb.uni-bonn.de/2009/1873/1873.htm, 2009.

M. Nord, K. Basu, F. Pacaud, P. A. R. Ade, A. N. Bender, B. A. Benson, F. Bertoldi, H.-M. Cho, G. Chon, J. Clarke, M. Dobbs, D. Ferrusca, N. W. Halverson, W. L. Holzapfel, C. Horellou, D. Johansson, J. Kennedy, Z. Kermish, R. Kneissl, T. Lanting, A. T. Lee, M. Lueker, J. Mehl, K. M. Menten, T. Plagge, C. L. Reichardt, P. L. Richards, R. Schaaf, D. Schwan, H. Spieler, C. Tucker, A. Weiss, and O. Zahn. Multi-frequency imaging of the galaxy cluster Abell 2163 using the Sunyaev-Zel'dovich effect. A&A, 506:623–636, November 2009. doi: 10.1051/0004-6361/200911746.

M. C. Novicki, M. Sornig, and J. P. Henry. The Evolution of the Galaxy Cluster Luminosity-Temperature Relation. AJ, 124:2413–2424, November 2002. doi: 10.1086/344162.

S. Nozawa, N. Itoh, Y. Kawana, and Y. Kohyama. Relativistic Corrections to the Sunyaev-Zeldovich Effect for Clusters of Galaxies. IV. Analytic Fitting Formula for the Numerical Results. ApJ, 536:31–35, June 2000. doi: 10.1086/308938.

M. Oguri and T. Hamana. Detailed cluster lensing profiles at large radii and the impact on cluster weak lensing studies. MNRAS, 414:1851–1861, July 2011. doi: 10.1111/j.1365-2966.2011.18481.x.

M. Oguri, M. B. Bayliss, H. Dahle, K. Sharon, M. D. Gladders, P. Natarajan, J. F. Hennawi, and B. P. Koester. Combined strong and weak lensing analysis of 28 clusters from the Sloan Giant Arcs Survey. MNRAS, 420:3213–3239, March 2012. doi: 10.1111/j.1365-2966.2011.20248.x.

N. Okabe and K. Umetsu. Subaru Weak Lensing Study of Seven Merging Clusters: Distributions of Mass and Baryons. PASJ, 60:345–375, April 2008.

N. Okabe, M. Takada, K. Umetsu, T. Futamase, and G. P. Smith. LoCuSS: Subaru Weak Lensing Study of 30 Galaxy Clusters. *ArXiv astro-ph/0903.1103*, March 2009.

W. J. Percival, S. Cole, D. J. Eisenstein, R. C. Nichol, J. A. Peacock, A. C. Pope, and A. S. Szalay. Measuring the Baryon Acoustic Oscillation scale using the Sloan Digital Sky Survey and 2dF Galaxy Redshift Survey. MNRAS, 381:1053–1066, November 2007. doi: 10.1111/j.1365-2966.2007.12268.x.

M. J. Pereira and J. R. Kuhn. Radial Alignment of Cluster Galaxies. ApJ, 627:L21–L24, July 2005. doi: 10.1086/432089.

V. Petrosian. On the Nonthermal Emission and Acceleration of Electrons in Coma and Other Clusters of Galaxies. ApJ, 557:560–572, August 2001. doi: 10.1086/321557.

A. Pillepich, C. Porciani, and O. Hahn. Halo mass function and scale-dependent bias from N-body simulations with non-Gaussian initial conditions. MNRAS, 402:191–206, February 2010. doi: 10.1111/j.1365-2966.2009.15914.x.

K. A. Pimbblet, I. Smail, A. C. Edge, E. O'Hely, W. J. Couch, and A. I. Zabludoff. The Las Campanas/Anglo-Australian Telescope Rich Cluster Survey - III. Spectroscopic studies of X-ray bright galaxy clusters at z˜ 0.1. MNRAS, 366:645–666, February 2006. doi: 10.1111/j.1365-2966.2005.09892.x.

T. Plagge, B. A. Benson, P. A. R. Ade, K. A. Aird, L. E. Bleem, J. E. Carlstrom, C. L. Chang, H.-M. Cho, T. M. Crawford, A. T. Crites, T. de Haan, M. A. Dobbs, E. M. George, N. R. Hall, N. W. Halverson, G. P. Holder, W. L. Holzapfel, J. D. Hrubes, M. Joy, R. Keisler, L. Knox, A. T. Lee, E. M. Leitch, M. Lueker, D. Marrone, J. J. McMahon, J. Mehl, S. S. Meyer, J. J. Mohr, T. E. Montroy, S. Padin, C. Pryke, C. L. Reichardt, J. E. Ruhl, K. K. Schaffer, L. Shaw, E. Shirokoff, H. G. Spieler, B. Stalder, Z. Staniszewski, A. A. Stark, K. Vanderlinde, J. D. Vieira, R. Williamson, and O. Zahn. Sunyaev-Zel'dovich Cluster Profiles Measured with the South Pole Telescope. ApJ, 716:1118–1135, June 2010. doi: 10.1088/0004-637X/716/2/1118.

Planck Collaboration, P. A. R. Ade, N. Aghanim, M. Arnaud, M. Ashdown, J. Aumont, C. Baccigalupi, A. Balbi, A. J. Banday, R. B. Barreiro, and et al. Planck early results. XI. Calibration of the local galaxy cluster Sunyaev-Zeldovich scaling relations. A&A, 536: A11, December 2011. doi: 10.1051/0004-6361/201116458.

Planck Collaboration, P. A. R. Ade, N. Aghanim, C. Armitage-Caplan, M. Arnaud, M. Ashdown, F. Atrio-Barandela, J. Aumont, C. Baccigalupi, A. J. Banday, and et al. Planck 2013 results. XVI. Cosmological parameters. *ArXiv e-prints*, March 2013a.

Planck Collaboration, P. A. R. Ade, N. Aghanim, C. Armitage-Caplan, M. Arnaud, M. Ashdown, F. Atrio-Barandela, J. Aumont, C. Baccigalupi, A. J. Banday, and et al. Planck 2013 results. XX. Cosmology from Sunyaev-Zeldovich cluster counts. *ArXiv e-prints*, March 2013b.

B. M. Poggianti, T. J. Bridges, Y. Komiyama, M. Yagi, D. Carter, B. Mobasher, S. Okamura, and N. Kashikawa. A Comparison of the Galaxy Populations in the Coma and Distant Clusters: The Evolution of k+a Galaxies and the Role of the Intracluster Medium. ApJ, 601:197–213, January 2004. doi: 10.1086/380195.

G. W. Pratt, J. H. Croston, M. Arnaud, and H. Böhringer. Galaxy cluster X-ray luminosity scaling relations from a representative local sample (REXCESS). A&A, 498:361–378, May 2009. doi: 10.1051/0004-6361/200810994.

W. H. Press and P. Schechter. Formation of Galaxies and Clusters of Galaxies by Self-Similar Gravitational Condensation. ApJ, 187:425–438, February 1974. doi: 10.1086/152650.

A. G. Riess, L.-G. Strolger, J. Tonry, S. Casertano, H. C. Ferguson, B. Mobasher, P. Challis, A. V. Filippenko, S. Jha, W. Li, R. Chornock, R. P. Kirshner, B. Leibundgut, M. Dickinson, M. Livio, M. Giavalisco, C. C. Steidel, T. Benítez, and Z. Tsvetanov. Type Ia Supernova Discoveries at z > 1 from the Hubble Space Telescope: Evidence for Past Deceleration and Constraints on Dark Energy Evolution. ApJ, 607:665–687, June 2004. doi: 10.1086/383612.

S. Roeser, M. Demleitner, and E. Schilbach. The PPMXL Catalog of Positions and Proper Motions on the ICRS. Combining USNO-B1.0 and the Two Micron All Sky Survey (2MASS). AJ, 139:2440–2447, June 2010. doi: 10.1088/0004-6256/139/6/2440.

P. Rosati, S. Borgani, and C. Norman. The Evolution of X-ray Clusters of Galaxies. ARA&A, 40:539–577, 2002. doi: 10.1146/annurev.astro.40.120401.150547.

P. Rosati, P. Tozzi, S. Ettori, V. Mainieri, R. Demarco, S. A. Stanford, C. Lidman, M. Nonino, S. Borgani, R. Della Ceca, P. Eisenhardt, B. P. Holden, and C. Norman. Chandra and XMM-Newton Observations of RDCS 1252.9-2927, A Massive Cluster at z=1.24. AJ, 127:230–238, January 2004. doi: 10.1086/379857.

S. Schindler, L. Guzzo, H. Ebeling, H. Boehringer, G. Chincarini, C. A. Collins, S. de Grandi, D. M. Neumann, U. G. Briel, P. Shaver, and G. Vettolani. Discovery of an arc system in the brightest ROSAT cluster of galaxies. A&A, 299:L9, July 1995.

M. Schirmer, T. Erben, M. Hetterscheidt, and P. Schneider. GaBoDS: the Garching-Bonn Deep Survey. IX. A sample of 158 shear-selected mass concentration candidates. A&A, 462:875–887, February 2007. doi: 10.1051/0004-6361:20065955.

P. Schneider. Detection of (dark) matter concentrations via weak gravitational lensing. MNRAS, 283:837–853, December 1996.

P. Schneider. *Einführung in die extragalaktische Astronomie und Kosmologie*. Springer-Verlag Berlin Heidelberg, 2006a.

P Schneider. *"Weak Gravitational Lensing" in: Gravitational Lensing: Strong, Weak and Micro: Saas-Fee Advanced Courses, Volume 33* . Springer-Verlag Berlin Heidelberg, 2006b. doi: 10.1007/978-3-540-30310-7.

P. Schneider. *"Introduction to Gravitational Lensing and Cosmology" in: Gravitational Lensing: Strong, Weak and Micro, Saas-Fee Advanced Courses, Volume 33*, page 1ff. Springer-Verlag Berlin Heidelberg, 2006c. doi: 10.1007/978-3-540-30310-7_1.

P. Schneider, L. King, and T. Erben. Cluster mass profiles from weak lensing: constraints from shear and magnification information. A&A, 353:41–56, January 2000.

T. Schrabback, T. Erben, P. Simon, J.-M. Miralles, P. Schneider, C. Heymans, T. Eifler, R. A. E. Fosbury, W. Freudling, M. Hetterscheidt, H. Hildebrandt, and N. Pirzkal. Cosmic shear analysis of archival HST/ACS data. I. Comparison of early ACS pure parallel data to the HST/GEMS survey. A&A, 468:823–847, June 2007. doi: 10.1051/0004-6361:20065898.

P. Schuecker, R. R. Caldwell, H. Böhringer, C. A. Collins, L. Guzzo, and N. N. Weinberg. Observational constraints on general relativistic energy conditions, cosmic matter density and dark energy from X-ray clusters of galaxies and type-Ia supernovae. A&A, 402: 53–63, April 2003. doi: 10.1051/0004-6361:20030197.

C. Seitz and P. Schneider. Steps towards nonlinear cluster inversion through gravitational distortions. III. Including a redshift distribution of the sources. A&A, 318:687–699, February 1997.

S. Seitz and P. Schneider. Cluster lens reconstruction using only observed local data: an improved finite-field inversion technique. A&A, 305:383–+, January 1996.

M. Sereno, S. Ettori, K. Umetsu, and A. Baldi. Mass, shape and thermal properties of Abell 1689 using a multiwavelength X-ray, lensing and Sunyaev-Zel'dovich analysis. MNRAS, 428:2241–2254, January 2013. doi: 10.1093/mnras/sts186.

G. F. Snyder, M. Brodwin, C. M. Mancone, G. R. Zeimann, S. A. Stanford, A. H. Gonzalez, D. Stern, P. R. M. Eisenhardt, M. J. I. Brown, A. Dey, B. Jannuzi, and S. Perlmutter. Assembly of the Red Sequence in Infrared-selected Galaxy Clusters from the IRAC Shallow Cluster Survey. ApJ, 756:114, September 2012. doi: 10.1088/0004-637X/756/2/114.

M. W. Sommer and K. Basu. A comparative study of radio halo occurrence in SZ and X-ray selected galaxy cluster samples. *ArXiv e-prints*, July 2013.

D. N. Spergel, L. Verde, H. V. Peiris, E. Komatsu, M. R. Nolta, C. L. Bennett, M. Halpern, G. Hinshaw, N. Jarosik, A. Kogut, M. Limon, S. S. Meyer, L. Page, G. S. Tucker, J. L. Weiland, E. Wollack, and E. L. Wright. First-Year Wilkinson Microwave Anisotropy Probe (WMAP) Observations: Determination of Cosmological Parameters. ApJS, 148:175–194, September 2003. doi: 10.1086/377226.

V. Springel, S. D. M. White, A. Jenkins, C. S. Frenk, N. Yoshida, L. Gao, J. Navarro, R. Thacker, D. Croton, J. Helly, J. A. Peacock, S. Cole, P. Thomas, H. Couchman, A. Evrard, J. Colberg, and F. Pearce. Simulations of the formation, evolution and clustering of galaxies and quasars. Nature, 435:629–636, June 2005. doi: 10.1038/nature03597.

P. B. Stetson. Homogeneous Photometry for Star Clusters and Resolved Galaxies. II. Photometric Standard Stars. PASP, 112:925–931, July 2000. doi: 10.1086/316595.

M. F. Struble and H. J. Rood. A compilation of redshifts and velocity dispersions for Abell clusters. ApJS, 63:543–553, March 1987. doi: 10.1086/191173.

M. F. Struble and H. J. Rood. A Compilation of Redshifts and Velocity Dispersions for ACO Clusters. ApJS, 125:35–71, November 1999. doi: 10.1086/313274.

M. Sun, M. Donahue, and G. M. Voit. Hα Tail, Intracluster H II Regions, and Star Formation: ESO 137-001 in Abell 3627. ApJ, 671:190–202, December 2007. doi: 10.1086/522690.

R. A. Sunyaev and Y. B. Zel'dovich. The Spectrum of Primordial Radiation, its Distortions and their Significance. *Comments on Astrophysics and Space Physics*, 2:66, March 1970.

A. N. Taylor, D. J. Bacon, M. E. Gray, C. Wolf, K. Meisenheimer, S. Dye, A. Borch, M. Kleinheinrich, Z. Kovacs, and L. Wisotzki. Mapping the 3D dark matter with weak lensing in COMBO-17. MNRAS, 353:1176–1196, October 2004. doi: 10.1111/j.1365-2966.2004.08138.x.

J. Tinker, A. V. Kravtsov, A. Klypin, K. Abazajian, M. Warren, G. Yepes, S. Gottlöber, and D. E. Holz. Toward a Halo Mass Function for Precision Cosmology: The Limits of Universality. ApJ, 688:709–728, December 2008. doi: 10.1086/591439.

J. L. Tonry, B. P. Schmidt, B. Barris, P. Candia, P. Challis, A. Clocchiatti, A. L. Coil, A. V. Filippenko, P. Garnavich, C. Hogan, S. T. Holland, S. Jha, R. P. Kirshner, K. Krisciunas, B. Leibundgut, W. Li, T. Matheson, M. M. Phillips, A. G. Riess, R. Schommer, R. C. Smith, J. Sollerman, J. Spyromilio, C. W. Stubbs, and N. B. Suntzeff. Cosmological Results from High-z Supernovae. ApJ, 594:1–24, September 2003. doi: 10.1086/376865.

K.-V. H. Tran, M. Franx, G. D. Illingworth, P. van Dokkum, D. D. Kelson, J. P. Blakeslee, and M. Postman. A Keck Spectroscopic Survey of MS 1054-03 (z = 0.83): Forming the Red Sequence. ApJ, 661:750–767, June 2007. doi: 10.1086/513738.

W. Tucker, P. Blanco, S. Rappoport, L. David, D. Fabricant, E. E. Falco, W. Forman, A. Dressler, and M. Ramella. 1E 0657-56: A Contender for the Hottest Known Cluster of Galaxies. ApJ, 496:L5, March 1998. doi: 10.1086/311234.

K. Umetsu, T. Broadhurst, A. Zitrin, E. Medezinski, and L.-Y. Hsu. Cluster Mass Profiles from a Bayesian Analysis of Weak-lensing Distortion and Magnification Measurements: Applications to Subaru Data. ApJ, 729:127, March 2011. doi: 10.1088/0004-637X/729/2/127.

L. van Waerbeke, M. White, H. Hoekstra, and C. Heymans. Redshift and shear calibration: Impact on cosmic shear studies and survey design. *Astroparticle Physics*, 26:91–101, September 2006. doi: 10.1016/j.astropartphys.2006.05.008.

A. Vikhlinin, A. Kravtsov, W. Forman, C. Jones, M. Markevitch, S. S. Murray, and L. Van Speybroeck. Chandra Sample of Nearby Relaxed Galaxy Clusters: Mass, Gas Fraction, and Mass-Temperature Relation. ApJ, 640:691–709, April 2006. doi: 10.1086/500288.

A. Vikhlinin, A. V. Kravtsov, R. A. Burenin, H. Ebeling, W. R. Forman, A. Hornstrup, C. Jones, S. S. Murray, D. Nagai, H. Quintana, and A. Voevodkin. Chandra Cluster Cosmology Project III: Cosmological Parameter Constraints. ApJ, 692:1060–1074, February 2009. doi: 10.1088/0004-637X/692/2/1060.

M. Viola, P. Melchior, and M. Bartelmann. Biases in, and corrections to, KSB shear measurements. MNRAS, 410:2156–2166, February 2011. doi: 10.1111/j.1365-2966.2010.17589.x.

A. von der Linden, M. T. Allen, D. E. Applegate, P. L. Kelly, S. W. Allen, H. Ebeling, P. R. Burchat, D. L. Burke, D. Donovan, R. G. Morris, R. Blandford, T. Erben, and A. Mantz. Weighing the Giants I: Weak Lensing Masses for 51 Massive Galaxy Clusters - Project Overview, Data Analysis Methods, and Cluster Images. *ArXiv e-prints*, August 2012.

J. Wambsganss. *"Gravitational Microlensing" in: Gravitational Lensing: Strong, Weak and Micro, Saas-Fee Advanced Courses, Vol. 33*, page 453 ff. Springer-Verlag Berlin Heidelberg, 2006. doi: 10.1007/978-3-540-30310-7_4.

J. K. Webb, M. T. Murphy, V. V. Flambaum, V. A. Dzuba, J. D. Barrow, C. W. Churchill, J. X. Prochaska, and A. M. Wolfe. Further Evidence for Cosmological Evolution of the Fine Structure Constant. *Physical Review Letters*, 87(9):091301, August 2001. doi: 10.1103/PhysRevLett.87.091301.

C. O. Wright and T. G. Brainerd. Gravitational Lensing by NFW Halos. ApJ, 534:34–40, May 2000. doi: 10.1086/308744.

Y.-Y. Zhang, A. Finoguenov, H. Böhringer, Y. Ikebe, K. Matsushita, and P. Schuecker. Temperature gradients in XMM-Newton observed REFLEX-DXL galaxy clusters at z 0.3. A&A, 413:49–63, January 2004. doi: 10.1051/0004-6361:20031531.

Y.-Y. Zhang, H. Böhringer, A. Finoguenov, Y. Ikebe, K. Matsushita, P. Schuecker, L. Guzzo, and C. A. Collins. X-ray properties in massive galaxy clusters: XMM-Newton observations of the REFLEX-DXL sample. A&A, 456:55–74, September 2006. doi: 10.1051/0004-6361:20053650.

Y.-Y. Zhang, A. Finoguenov, H. Böhringer, J.-P. Kneib, G. P. Smith, R. Kneissl, N. Okabe, and H. Dahle. LoCuSS: comparison of observed X-ray and lensing galaxy cluster scaling relations with simulations. A&A, 482:451–472, May 2008. doi: 10.1051/0004-6361:20079103.

F. Zwicky. Die Rotverschiebung von extragalaktischen Nebeln. *Helvetica Physica Acta*, 6:110–127, 1933.

LIST OF FIGURES

LIST OF TABLES

ACRONYMS

BAO Baryonic Acoustic Oscillation

CC color-color

CCM color-color-magnitude

CMB Cosmic Microwave Background

SN Supernova

SUP Suprime-Cam

SZ Sunyaev-Zel'dovich

WFI Wide Field Imager

WMAP Wilkinson Microwave Anisotropy Probe

ACKNOWLEDGEMENTS

I would like to thank my supervisor Prof. Dr. Frank Bertoldi for providing me with the opportunity to work on my PhD thesis within the APEX-SZ team at the Argelander-Institute for Astronomy. I appreciate that he strongly supported my work, which included several trips to Chile. I am also very thankful for the encouragement to attend international conferences, such as those in Huntsville and Beijing, which greatly motivated and inspired my work.

I am also very grateful to my second supervisor Prof. Dr. Peter Schneider, who provided me with important and helpful feedback on my work and talks I gave in the "Lens Seminar". I was positively surprised how quickly I received the comments from him on the thesis and the following discussion was the most invigorating discussion about mistakes I ever had.

Not at the last place, I also want to thank Dr. Holger Israel for his great support on the data reduction and the basic software tools. The discussions with him in the beginning of my PhD time helped me a lot in understanding the basic techniques of the weak lensing analysis. Later in the PhD, our discussions helped to improve the details of the lensing work.

I am happy to know, work and discuss with Dr. Florian Pacaud. The conversations with him led me to do a closer analysis of some clusters in this thesis and beyond.

I would like to thank also my office-mates Aarti, Sandra and Sameera, as well as Miriam, and all the other colleagues, who became my friends during my time as a PhD student. I will never forget all the happy moments and trips with all of them.

I also thank Dr. Martin Sommer, Dr. Kaustuv Basu and the complete APEX-SZ collaboration around Prof. Dr. Adrian Lee for the interesting and inspiring work within this collaboration. My work would never have been possible without the sufficient amount of financial support. Therefore, I thank the University of Bonn, the Transregional Collaborative Research Center TRR 33 "The Dark Universe" and the SFB 956 "Conditions and Impact of Star Formation" for financial support.

I would like to thank my family, my parents and my grandfather for the moral support, love, care and understanding during these years of my thesis and before. I am extraordinarily happy about the birth of my little nice Nele-Lena and that of my nephew Paul-Willi, which gave me the best energy and enthusiasm to carry on and to finish this thesis work.

Last, but not least, I want to thank my fiancee, Snezhanka, for the courage and for believing in me in the moments of difficulty, in which it was hard for me to carry on with the writing of this work. I am very happy to have her by my side.